Imperial College London
Department of Physics

Cold, slow YbF molecules for measuring the electron's electric dipole moment

Stefan Popa

Submitted in partial fulfilment of the requirements for the degree of
Doctor of Philosophy in Physics of Imperial College London
June 2024

Declaration

I declare that the work presented in this thesis is my own. Where needed, I have acknowledged the work of others or referenced the correct sources.

Abstract

The Standard Model (SM), our current best framework of physics, has notable failings including its inability to account for the observed asymmetry of anti-matter to matter in the universe. This motivates theories beyond the SM. These beyond the SM theories introduce increased charge, parity (CP) symmetry breaking, as well as time symmetry violating effects. An electron with an electric dipole moment (eEDM) is an example of time symmetry violation, making eEDM searches crucial tests of these theories. The SM predicts that the eEDM is below 10^{-35} $e\,$cm, while extensions to the SM predict higher values, in the range 10^{-32} to 10^{-24} $e\,$cm. The current best limit, set by the JILA group in 2023, is $|d_E| < 4.1 \times 10^{-30}$ $e\,$cm.

Currently, molecular eEDM searches are often limited by short coherence times or low molecule numbers. To increase both, we propose measuring the eEDM using cooled YbF molecules, trapped in an optical lattice. In this thesis, we present the progress towards such a measurement with which an uncertainty of 10^{-32} $e\,$cm should be achievable, testing most extensions to the SM. We use a two-stage cryogenic buffer gas source to produce a high flux molecular beam whose forward velocity is 49 m/s. We use radiation pressure slowing to decelerate this beam so that it can be captured in a magneto-optical trap, which we have built. We measure a leak out of the cooling cycle at a few parts in 10^4, which we attribute to low-lying states arising from inner-shell excitations which we call $4f$-hole states. The electronic character and rotational structure of these $4f$-hole states is studied.

Acknowledgements

First, I would like to thank my supervisors - Mike, Jongseok and Ben. Your expertise, understanding and patience were invaluable to my PhD experience. Thank you for your willingness to meet and discuss physics, I have learnt a lot from your explanations, comments and insights. Mike, thank you also for your guidance and feedback in writing this thesis.

During my PhD, I've been very fortunate to work with some amazing people at CCM. I have especially benefited from working with all those who call the Huxley lab their home. Thank you to all in team Ultracold and Lattice EDM. In particular I would like to thank Andy and Jorge. Your assistance and guidance in the lab, especially during the early years of my PhD, were invaluable. Thank you also to Jon and Dave for their support in the workshop and to Sanja for keeping CCM running.

I was also very fortunate to spend some time at the Fritz-Haber Institute in Berlin and I would like to extend a thank you to all those who supported me during my time there. Gerard, Andre and Sascha thank you for welcoming me into your research group and for making my time at the Fritz so enjoyable, and to Luca for carrying the YbF baton after I left. I learnt a lot and our results have significantly contributed to the depth of my thesis.

I am also indebted to my family. Your support and encouragement has been a great source of strength during this journey. To my parents, thank you for your help, especially during my writing spells at home, and for the countless effort you have made to ensure my success. To Alex, thank you for the quick F1 breaks/chats whilst I was writing and you were sitting exams. And to Rachel, thank you for your support and heartfelt encouragement, and for sharing both the joys and frustrations of my PhD.

Finally, I would like to thank my friends outside of academia, for providing a necessary distraction from my research and for their constant encouragement and their willingness to listen to me talk about my laser woes.

Dedication

Pentru familia mea.

Contents

Declaration **i**

Abstract **iii**

Acknowledgements **v**

1 Introduction **1**

1.1 Symmetry and the electron's electric dipole moment 2

1.1.1 A general eEDM experiment 4

1.2 Molecules as eEDM test vessels 7

1.3 State of the field 8

1.4 eEDM with laser-coolable molecules 10

1.4.1 Lattice EDM 11

1.5 Thesis outline 12

2 Molecular structure **14**

2.1 Gross molecular structure 14

2.2 Rotational structure and Hund's cases 17

2.3 Hyperfine structure 20

2.4 Molecular transitions 20

2.4.1 Rotational branches 21

2.4.2 Optical cycling 23

3 Source **26**

3.1 Introduction 26

3.1.1 Background 27

3.2 Experimental setup 28

3.2.1 Experimental apparatus for beam characterisation 31

3.2.2 Laser induced fluorescence detector 33

3.3 Beam characterisation 35

3.3.1 Absorption measurements and extraction characteristics 35

3.3.2 Laser induced fluorescence 39

3.4 Doppler velocimetry 41

3.4.1 One-stage and two-stage cells 43

3.4.2 Exit times 46

3.4.3 Temperature dependence 48

3.4.4 Optimisation 50

3.5 Summary 52

4 Optical cycling and slowing **53**

4.1 Introduction . . . 53

4.1.1 Optical cycling scheme in YbF . . . 55

4.2 Simulating longitudinal laser slowing . . . 56

4.2.1 Multi-level rate equations . . . 57

4.2.2 Monte-Carlo simulation . . . 60

4.2.3 Leaks to $v = 2$ and $v = 3$ . . . 64

4.3 Photon scattering . . . 67

4.3.1 Photon scattering on $A^2\Pi_{1/2}(v = 0) \leftrightarrow X^2\Sigma^+(v = 0)$ . . . 67

4.3.2 Adding repump lasers. Scattering rate with $v = 0$, $v = 1$, $v = 2$ . . . 72

4.4 Laser slowing . . . 75

4.5 Vibrational leak to $v = 3$ . . . 77

4.5.1 Branching ratio to $v = 3$ . . . 80

4.6 Possible remaining loss channels . . . 83

4.7 Summary . . . 85

5 Inner-shell excitations in YbF **87**

5.1 Introduction . . . 87

5.2 Experimental configuration . . . 90

5.2.1 Relevant energy levels . . . 90

5.2.2 REMPI methods . . . 91

5.2.3 Beamline and experimental setup . . . 92

5.3 Spectroscopic model: Hund's case (c) . . . 93

5.4 The high-lying state: [31.05] . . . 97

5.4.1 Assignment of spectral lines . . . 99

5.4.2 Fitting to the spectrum . . . 100

5.4.3 Lifetime of [31.05] . . . 102

5.5 The autoionising states: [48.72] and [48.73] . . . 104

5.6 The leak states: $4f_{7/2}^{-1}$ . . . 108

5.6.1 Assignment of rotational lines: "fingerprinting" . . . 109

5.6.2 Fitting to the spectra . . . 110

5.7 The mixed character repump states: [18.58] and [18.71] . . . 113

5.7.1 Lifetimes of [18.58] and [18.71] . . . 114

5.8 Summary and discussion . . . 115

6 Setting up the MOT **120**

6.1 Introduction . . . 120

6.1.1 Background . . . 121

6.2 MOT hardware . . . 124

6.2.1 Magnetic field coils . . . 125

6.3 Frequency configuration and MOT optics . . . 127

6.3.1 Sideband structure . . . 127

6.3.2 MOT laser system and optics . . . 130

6.4 Molecule detection in the MOT . . . 131

6.4.1 Reducing background noise 132

6.4.2 MOT detection optics 132

6.4.3 Smallest detectable signal in the MOT 133

6.4.4 Molecule detection in the MOT chamber 134

6.5 Summary 135

7 Conclusion **137**

7.1 Summary of this thesis 137

7.2 Outlook towards an eEDM measurement in a lattice 139

A Line lists **142**

B Energy level diagrams **149**

Bibliography **149**

List of Tables

2.1 Selection rules for electric dipole transitions in molecules. 20

2.2 Spectroscopic constants for the $X^2\Sigma^+$ and $A^2\Pi_{1/2}$ states in ^{174}YbF. 24

4.1 Hyperfine splitting in the P(1) rotational line of $[557] \leftarrow X^2\Sigma^+(v = 3)$ 79

5.1 Spectroscopic parameters of $4f$ hole states. 104

5.2 Frequencies (in cm^{-1}) required to repump population from the relevant $4f$ hole states through either the [18.58] or [18.71] states. 117

A.1 Rotational lines in $[31.05] \leftarrow X^2\Sigma^+(v = 0)$. 143

A.2 Rotational lines in $[31.05] \leftarrow 4f^{-1}_{7/2,1/2}(v = 0)$. 144

A.3 Rotational lines in $[31.05] \leftarrow 4f^{-1}_{7/2,1/2}(v = 1)$. 146

A.4 Rotational lines in $[31.05] \leftarrow 4f^{-1}_{7/2,3/2}(v = 0)$. 147

A.5 Energy levels of [48.72]. 148

A.6 Energy levels of [48.73]. 148

List of Figures

1.1 T-violation and P-violation in an electron with an electric dipole moment. . . . 2

1.2 Upper limits on d_e over the years. 3

1.3 A general depiction of en EDM measurement. 5

1.4 Laser-coolable molecules as candidates for an eEDM measurement. 10

1.5 Proposed experiment to measure the eEDM using YbF molecules trapped in an optical lattice. 11

2.1 Hund's cases (a) and (b). 18

2.2 Allowed rotational transitions from $X^2\Sigma^+(N = 1)$. 21

2.3 The rotational spectrum for $A^2\Pi_{1/2} \leftarrow X^2\Sigma^+$ in ^{174}YbF. 23

3.1 Schematic of the cryogenic buffer gas source. 29

3.2 A schematic of the experimental setup used in this to characterise the molecular beam. 31

3.3 Optical table configuration for the molecular probe laser. 32

3.4 A schematic of the apparatus used to detect LIF. 34

3.5 Example time-of-flight and absorption profiles. 35

3.6 Fluorescence spectrum showing the P(1) transition with a single frequency laser and a laser that has sidebands applied to the laser. 39

3.7 Doppler sensitive laser-induced fluorescence spectroscopy to determine the longitudinal velocity distribution of molecules in the cryogenic buffer gas beam. . . 42

3.8 Forward velocity distributions for the one-stage and two-stage cells. 43

3.9 Velocity distributions for different gap sizes between the first and second stages. 46

3.10 Exit time from the cell versus velocity. 47

3.11 Relative thermal population distribution in the first five rotational levels of $X\,^2\Sigma^+$ at 1.55 K. 48

3.12 Temperature dependence of velocity distributions. 49

3.13 Molecular beam characteristics as a function of ablation pulse energy and helium flow rate. 51

4.1 Relevant energy levels for lasing slowing of YbF. 55

4.2 Energy levels for simulating laser slowing. 58

4.3 Monte-Carlo trajectory simulation of longitudinal laser slowing of YbF. 62

4.4 Energy levels for simulating laser slowing. 64

4.5 Simulated saturation curves of repump lasers. 66

4.6 Setup used to measure photon cycling rates. 67

4.7 Magnetic field configuration on our beamline used to destabilise dark states. . . 69

4.8 Effect of a magnetic field and polarisation modulation to destabilise dark states. 70

4.9 The left-over population in $X^2\Sigma^+(v = 0, N = 1)$ as a function of interaction time with a red-detuned counter propagating slowing laser addressing the $A^2\Pi_{1/2}(v = 0) \leftarrow X^2\Sigma^+(v = 0)$ transition. 71

4.10 Sideband frequencies used to address hyperfine transitions in $X^2\Sigma^+(v = 0, 1, 2)$. 72

4.11 Photon cycling rates with the addition of vibrational repump lasers. 74

4.12 Laser slowing setup. 75

4.13 Forward velocity change of the molecular beam by radiation pressure from a counter-propagating laser. 76

4.14 The mean deceleration from a counter-propagating laser beam as a function of gate center. 77

4.15 Experimental setup and timing sequence for pump-probe spectroscopy of $X^2\Sigma^+(v = 3)$. 78

4.16 Hyperfine structure of the $[557] \leftarrow X^2\Sigma^+(v = 3)$ P(1) transition 79

4.17 Experimental setup used to measure the branching ratio to $X^2\Sigma^+(v = 3)$. 80

4.18 Branching ratio to $X^2\Sigma^+(v = 3)$ 81

4.19 Slowing with v0,v1,v2,v3 82

5.1 ^{174}YbF energy levels and transitions relevant to our study of $4f$ hole states. . . . 90

5.2 Illustration of photo-ionisation schemes. 91

5.3 Schematic of the supersonic source at the Fritz-Haber Institute. 92

5.4 Vector diagram for Hund's case (c). 94

5.5 Rotational energy levels in Hund's case (c). 96

5.6 Study of [31.05]. 98

5.7 Fitting procedure and residuals for the $[31.05] \leftarrow X^2\Sigma^+(v = 0)$ spectrum. 100

5.8 Lifetime measurement of [31.05]. 103

5.9 Spectroscopic study of [48.72] and [48.73]. 105

5.10 Residuals of fit to [48.72] and [48.73]. 107

5.11 The rotational spectrum of the [31.05] $\leftarrow 4f^{-1}_{7/2,1/2}(v=0)$ transition. 108

5.12 Selective ionisation for assignment of rotational lines in the spectrum [31.05] $\leftarrow$ $4f^{-1}_{7/2,1/2}(v=0)$. 109

5.13 Spectra of the [31.05] $\leftarrow 4f^{-1}_{7/2,1/2}(v=1)$ and [31.05] $\leftarrow 4f^{-1}_{7/2,3/2}(v=0)$ transitions.111

5.14 Rotational line frequencies as a function of quantum number J for the low-lying $4f$ hole states. 112

5.15 Summary of the energy level structures of the low-lying $4f$ hole states. 113

5.16 Lifetime measurements of [18.58], [18.71] and $A^2\Pi_{1/2}(v=0)$ states of ^{174}YbF. . . 114

6.1 Operating principle of a magneto-optical trap. 121

6.2 Angular momentum cases where magneto-optical trapping is difficult to achieve. 122

6.3 MOT hardware. 124

6.4 The in-vacuum MOT coils. 125

6.5 Magnetic field coil calibration. 126

6.6 Proposed sideband configurations and polarisations for a dual frequency MOT of YbF. 127

6.7 Simulated acceleration in the MOT. 128

6.8 One dimensional phase-space trajectories of YbF in the MOT. 129

6.9 Proposed MOT optics. 130

6.10 Imaging optics for the CCD. 132

6.11 Smallest detectable signal in the MOT. 134

6.12 The molecular beam measured in the MOT chamber. 135

7.1 Illustration of the proposed beamline to measure the eEDM in an optical lattice. 139

B.1 Rotational levels of $X^2\Sigma^+(v=0)$. 150

B.2 Rotational levels of $A^2\Pi_{1/2}$. 151

B.3 Rotational levels of [31.05]. 152

B.4 Rotational levels of [48.72]. 153

B.5 Rotational levels of [48.73]. 154

B.6 Rotational levels of $4f^{-1}_{7/2,1/2}(v=0)$. 155

B.7 Rotational levels of $4f^{-1}_{7/2,1/2}(v=1)$. 156

B.8 Rotational levels of $4f^{-1}_{7/2,3/2}(v=0)$. 157

Chapter 1

Introduction

The Standard Model, the theory classifying all known particles in the universe and the forces between them, is known to have notable failings. These include its inability to account for the observed asymmetry of antimatter to matter and the existence of dark matter - an unexplained form of matter with very weak or non existent interactions with light. This motivates theories beyond the Standard Model. These beyond Standard Model theories introduce new sources of charge, parity (CP) symmetry breaking, equivalent to a violation of time-reversal (T) symmetry. While large-scale particle accelerators such as the Large Hadron Collider can search for direct evidence of physics beyond the SM, an electron with an electric dipole moment (eEDM) is an example of T-violation. As such, searches for a permanent electric dipole moment of the electron are also tests of beyond Standard Model theories and can be carried out on a smaller scale (for example in a basement of a South Kensington building). The sensitivity of these eEDM searches can be greatly improved by making use of laser cooled molecules. The work in this thesis represents the first steps towards a measurement of the eEDM using cold, slow and, ultimately, trapped YbF molecules.

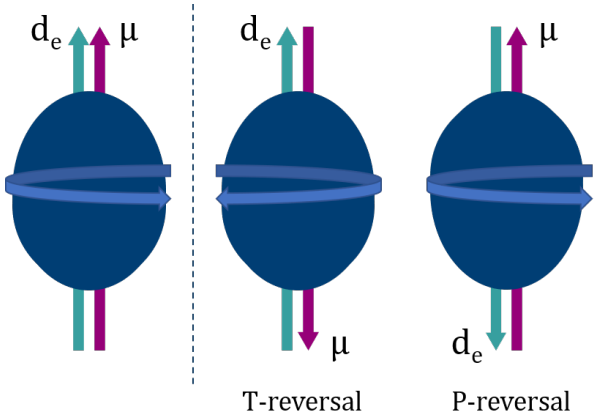

Figure 1.1: A particle with an electric dipole moment, d_e and a magnetic dipole, μ, violates both parity and time reversal symmetries.

1.1 Symmetry and the electron's electric dipole moment

The Standard Model of particle physics, our best understanding of the fundamental building blocks of our universe, is symmetric under the combination of three symmetries: charge, parity and time. Charge symmetry reversal exchanges anti-particles and particles, parity symmetry refers to the exchange of spatial coordinates, $(x, y, z) \rightarrow (-x, -y, -z)$, and time symmetry reversal refers to the flow of time being reversed, $t \rightarrow -t$. If a system remains unchanged after applying all three transformations, it is said to have a CPT symmetry. CPT symmetry is a requirement of all Lorentz-invariant field theories and no evidence has been found to support CPT symmetry violation [1, 2]. Ramsey and Purcell were the first to suggest that electrons could have permanent electric dipole moments [3]. Such an eEDM would violate P and T symmetry. Consider a non-zero electric dipole moment of the electron. The electron's spin creates a magnetic moment, μ, which is shown alongside the electric dipole moment, d_e, in figure 1.1. As per the Wigner-Eckhart theorem, the electric dipole moment must be orientated in the same axis as the spin. The eEDM could, however, be orientated in any parallel/antiparallel combination relative to the spin and require its own quantum number. However from atomic structure, we know that the electron can only occupy two states which suggests that the spin is their only allowed degree of freedom. If this were not the case, atomic electrons would have four spin/eEDM projection states rather than just the two we observe. The eEDM orientation is therefore constrained relative to the spin e.g. if the spin points up so must the eEDM. Figure 1.1

shows the eEDM as affected by parity and time reversal operations. Under a parity operation the direction of d_e is reversed but the direction of μ remains the same. Under time reversal, d_e remains unchanged but the direction of μ reverses. From the argument given above, only one of these relative orientations is observed in nature. Since both parity and time-reversal reverse the relative orientations of d_e and μ, the electron EDM, should it have a non-zero value, would therefore provide evidence of both parity and time symmetry violation. Parity violation was first observed in the beta decay of Co^{60} [4] and further symmetry breaking has been observed in the combined violation of charge and parity symmetry, CP, in the decay of K, B and D mesons [5–8]. T violation has so far only been observed in two cases, the decay of neutral kaons and that of B mesons [5, 9]. CP symmetry violation can be treated as equivalent to T symmetry violation provided the combined CPT symmetry is upheld.

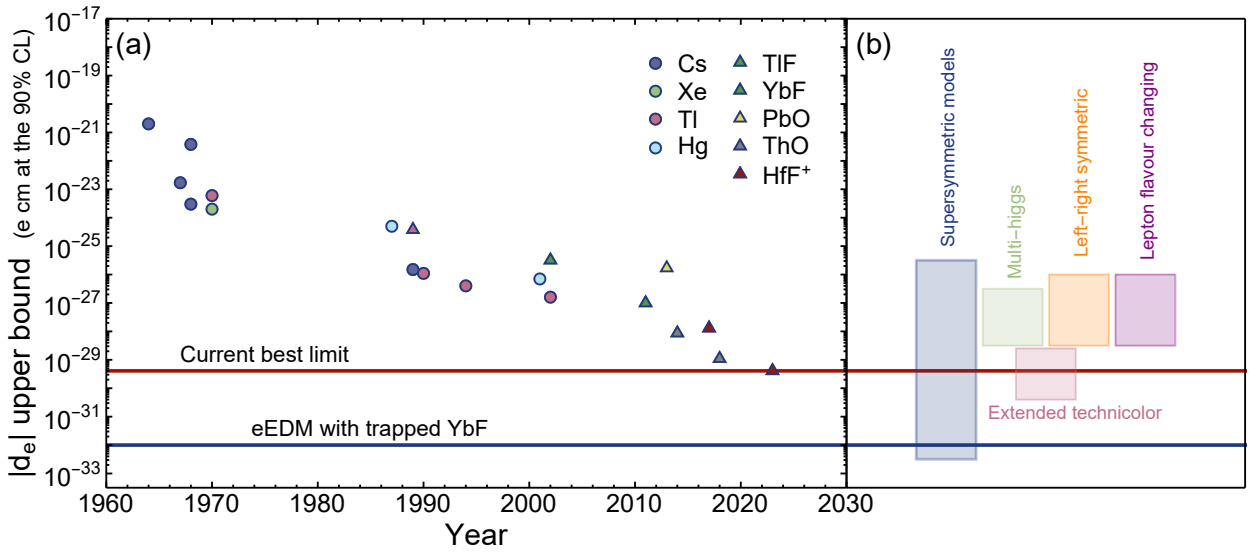

Figure 1.2: (a) upper limits on the magnitude of d_e over the years. Measured with atoms are indicated by circles, those with molecules by triangles. All values are quoted at the 90% confidence level. A predicted sensitivity of 10^{-32} e cm is possible using trapped YbF molecules. (b) Range of $|d_e|$ values predicted by theories beyond the Standard Model. Figure adapted from [10, 11].

CP violation is a requirement of the observed matter-antimatter asymmetry in the universe. The universe consists of many more baryons than anti-baryons. This imbalance, known as the baryon asymmetry of the universe (BAU), often has its origin attributed to the *baryogenesis* process of the universe where the BAU formed from initial symmetric conditions by some

asymmetric baryon production process, shortly after the Big Bang. The BAU can be estimated from the number of photons in the universe. Since no significant amount of antimatter remains in the universe it is assumed it must have annihilated with matter to produce photons. The estimated BAU is then the ratio of observed baryons, N_B, to photons, N_γ, today $\eta = N_B/N_\gamma \approx 10^{-10}$ [12, 13]. The Standard Model itself also allows for CP violating processes via quark-mixing terms in the Cabibbo-Kobayashi-Maskawa (CKM) matrix [14] and via the strong interaction through a term in the QCD Langrangian [15]. The Pontecorvo-Maki-Nakagawa-Sakata (PMNS) neutrino mixing matrix, which accounts for neutrino oscillations, also introduces an additional potential source of CP violation [16]. Nevertheless, the Standard Model can only account for a small fraction of the observed imbalance. To overcome this problem, beyond Standard Model theories (BSM) have been developed [17, 18]. As well as generating further sources of CP violation needed to explain the BAU, these theories also predict T violation phenomena such as an eEDM. The values these BSM theories predict for the eEDM are many orders of mangitude larger than that predicted by the Standard Model. While the SM predicts an eEDM of $\left|d_e^{\mathrm{SM}}\right| \simeq 10^{-35} - 10^{-38}\ e\,\mathrm{cm}$ [15, 19], various BSM theories increase this to $\left|d_e^{\mathrm{BSM}}\right| \simeq 10^{-25} - 10^{-32}\ e\,\mathrm{cm}$. A zero measurement of the eEDM can therefore constrain or discount BSM theories, whilst a non-zero measurement would provide evidence of T-violating effects. Figure 1.2 shows predicted values of $|d_e|$ alongside experimental measurements. All measurements of the eEDM have so far been consistent with zero and therefore set upper limits on the value of $|d_e|$. The current best limit was set by the Cornell group at JILA who have made a measurement of $|d_e| < 4.1 \times 10^{-30}\ e\,\mathrm{cm}$.

1.1.1 A general eEDM experiment

To measure the eEDM we would like to see the interaction of the eEDM, denoted $\mathbf{d_e}$ below, with an electric field, $\boldsymbol{\mathcal{E}}$. The effective Hamiltonian for such an interaction is given by,

$$H_{\mathrm{EDM}} = -\boldsymbol{d}_e \cdot \boldsymbol{\mathcal{E}} = -d_e \boldsymbol{\sigma} \cdot \mathcal{E}\hat{\boldsymbol{z}}, \tag{1.1}$$

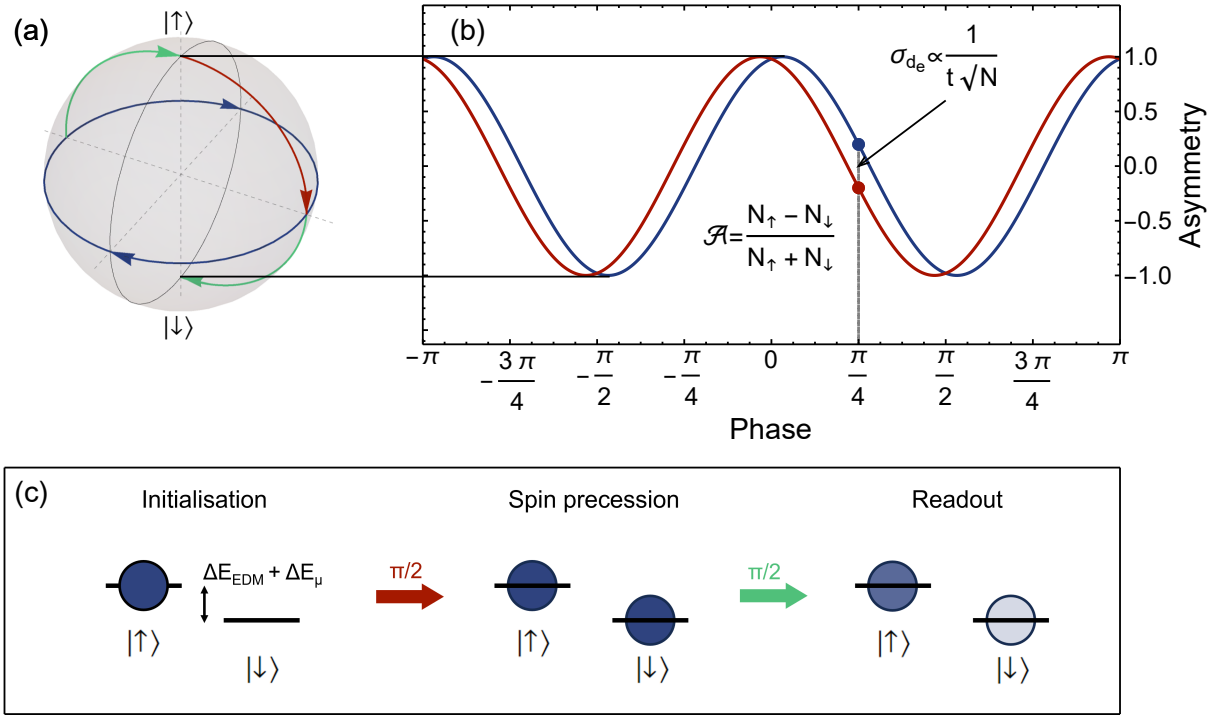

Figure 1.3: A Ramsey-type interferometer is used to measure the electron's electric dipole moment. (a): A Bloch sphere representation of a Ramsey interferometer. (b): The normalised population difference after state projection, called the asymmetry, as a function of accumulated phase. An eEDM will introduce a phase shift correlated with the direction of the electric field, depicted by the red and blue lines. The change in asymmetry produced by small changes in phase is maximised by operating around a phase of $\pi/4$, where the slope is greatest. (c): A pictorial representation of the Ramsey interferometer. ΔE_{EDM} and ΔE_μ are the energy shifts induced by $H_{\mathrm{EDM}}$and H_μ.

where $\hat{\boldsymbol{z}}$ is the unit vector along the quantisation axis set by the direction of the electric field. We remind ourselves that the only degree of freedom for $\mathbf{d_e}$ is the spin, where $\boldsymbol{\sigma}$ is the unit vector in the direction of the electron spin. An electron has, in addition to a potential eEDM, a magnetic dipole moment due to its spin. If in addition to the electric field, $\boldsymbol{\mathcal{E}}$, a magnetic field, $\boldsymbol{\mathcal{B}}$, is applied, then there will be an additional interaction, H_μ, between the magnetic moment of the electron, with magnitude denoted μ, and the magnetic field,

$$H_e = H_{\mathrm{EDM}} + H_\mu = -d_e \boldsymbol{\sigma} \cdot \mathcal{E}\hat{\boldsymbol{z}} + \mu \boldsymbol{\sigma} \cdot \mathcal{B}\hat{\boldsymbol{z}}. \tag{1.2}$$

To measure the small Stark shift induced by the eEDM, experiments in general use a Ramsey-type interferometer. Such a setup is shown in figure 1.3. Particles are prepared in a pure spin state, say spin-up $|\uparrow\rangle$, then excited to a superposition, $\frac{1}{\sqrt{2}}(|\uparrow\rangle + |\downarrow\rangle)$ by a $\frac{\pi}{2}$ pulse. There

will be an energy splitting between spin-up and spin-down levels due to H_e such that this superposition state evolves in uniform magnetic and electric fields at a rate ω for time τ. The phase difference, 2ϕ, acquired between the two spin states is proportional to the difference in the energies of the spin states, ΔE, with

$$\phi = \omega\tau = \frac{\tau \Delta E}{\hbar} = (\mu B + d_e \mathcal{E})\frac{\tau}{\hbar}. \tag{1.3}$$

To retrieve the accumulated phase ϕ, the state is mapped back onto one of the two spin states. This can be achieved by a second $\frac{\pi}{2}$ pulse. The probability for the particle to be in the spin-up and spin-down state is then $\cos^2(\phi)$ and $\sin^2(\phi)$ respectively. By counting the number of particles in each of the two spin states one can form the asymmetry,

$$\mathcal{A} = (N_\uparrow - N_\downarrow) / (N_\uparrow + N_\downarrow) = \mathcal{C} \cos 2\phi \tag{1.4}$$

where $N_\uparrow$ and $N_\downarrow$ represent the number in the $|\uparrow\rangle$ and $|\downarrow\rangle$ states respectively. $\mathcal{C}$ is the contrast and characterises imperfections in the interferometer. The value of the eEDM can be obtained by reversing the direction of the electric field and measuring the resultant shift in the asymmetry. Figure 1.3(b) shows an example of an asymmetry curve as a function of magnetic phase. An eEDM causes a displacement in the asymmetry curve that reverses with the direction of the electric field. This is shown by red and blue curves. The largest change in the asymmetry between the two curves occurs at $\pi/4$ and represents the most sensitive part of the interferometer. The statistical uncertainty on the eEDM given by such an interferometer can be estimated by

$$\sigma_{d_e} = \frac{\hbar}{2\mathcal{E}\mathcal{C}\tau\sqrt{N_{\text{det}}}} \tag{1.5}$$

where N_{det} is the number of detected particles, $\mathcal{C}$ the interferometer contrast, $\mathcal{E}$ the electric field strength, and τ is the total precession time. This is the uncertainty that arises from the particle counting error in forming the asymmetry and is known as the shot-noise [11]. It describes the fundamental limit on the statistical precision. Equation 1.5 motivates several experimental improvements to achieve the lowest shot noise. A large electric field, a large precession time and a large number of particles.

1.2 Molecules as eEDM test vessels

Although early EDM measurements have been made using free electrons [20, 21], electrons accelerate in an electric field. This makes measuring the EDM challenging and prone to uncertainty. Instead, modern measurement techniques search for the eEDM in the valence electron of a paramagnetic atom or molecule. One might expect that the charges in a neutral atom or molecule would rearrange themselves such that each electron experiences no net electric field and that therefore the expectation value of the eEDM interaction is $\langle \mathbf{d_e} \cdot \boldsymbol{\mathcal{E}} \rangle = \mathbf{d_e} \cdot \langle \boldsymbol{\mathcal{E}} \rangle = 0$. This is known as Schiff's theorem [22] and states that any interactions of the eEDM with an externally applied electric field, $\boldsymbol{\mathcal{E}}_{\text{app}}$, will be screened by the internal polarising field of the atom or molecule, $\boldsymbol{\mathcal{E}}_{\text{int}}$. Schiff's theorem, however, neglects relativistic effects. When these are taken into account, an eEDM interaction is restored [23]. An intuitive understanding of why Schiff's theorem breaks down in heavy atoms/molecules can be gained by considering a moving electron in the center of mass frame of an atom [24, 25]. In the rest frame of the electron, it has an eEDM, d_e. Due to relativistic length contraction, the eEDM in the atom frame will be

$$d_e^{\text{atom}} = \frac{d_e}{\gamma} = d_e \sqrt{1 - \frac{v_z^2}{c^2}}, \tag{1.6}$$

where γ is the Lorentz factor, v_z, the velocity of the electron along the direction of the applied electric field in the atom frame and c, the speed of light. The expectation value of the eEDM interaction will therefore be

$$\langle H_{EDM} \rangle = \langle \psi_e | \, d_e \sqrt{1 - \frac{v_z^2}{c^2}} (\mathcal{E}_{\text{int}} + \mathcal{E}_{\text{app}}) \, | \psi_e \rangle \, , \tag{1.7}$$

where ψ_e is the electronic wavefunction, which itself will be distorted due to the application of the external field. The interaction of the eEDM now additionally depends on the spatially dependent velocity so even though $\langle \mathcal{E} \rangle = \langle \psi_e | \, \mathcal{E}_{\text{int}} + \mathcal{E}_{\text{app}} \, | \psi_e \rangle = 0$, $\langle H_{EDM} \rangle$ does not. In fact, the interaction can be enhanced by orders of magnitude by using an atom or molecule. The size of this enhancement comes from the introduced distortion (or polarisability) of the electron distribution. An applied electric field will mix states of opposite parity. For example an electron

in an s orbital will mix with a nearby p orbital when an electric field is applied. The degree of polarisation (how much of the p orbital is mixed in) will depend on the energy difference between the opposite parity states and the magnitude of the applied electric field. In atoms, the energy spacing between opposite parity s and p states is relatively large and can only be weakly polarised in laboratory achievable fields. In contrast, molecules, in addition to electronic structure, also have quantised vibrational and rotational states. The spacing between adjacent rotational states of opposite parity in molecules is much smaller than that between electronic states in atoms. A polar molecule can be fully polarised in only a small applied electric field. The enhancement of the molecular eEDM as a result of the polarisability can then be written as

$$\Delta E_{\mathrm{EDM}} = -\eta\left(\mathcal{E}_{\mathrm{app}}\right) d_e \mathcal{E}_{\mathrm{eff}}, \tag{1.8}$$

where η is the polarisation factor of the atom or molecule and $\mathcal{E}_{\mathrm{eff}}$ an effective electric field.

1.3 State of the field

All of the most recent limits on the eEDM have been set using heavy polar molecules. The last five were set by three groups, each using a different molecule - the ACME collaboration's ThO experiment, JILA's HfF^+ experiment and Imperial College London's YbF experiment.

The current best limit on the eEDM was set using HfF^+ molecular ions by the Cornell group at JILA. Their measurement constrained the eEDM to $|d_e| < 4.1 \times 10^{-30} e$ cm [26] at the 90% confidence level. JILA's EDM search is the only such experiment to utilise molecular ions. By trapping the ions, the team at JILA has been able to achieve very large interrogation times of 2.1 s [27]. This generally comes at the cost of the number of ions in the trap and current measurements are space-charge limited. The eEDM measurement makes use of two measuring states of opposite parity for which the Stark shift is in opposite directions. This removes the need to switch the direction of the electric field and allows for common mode rejection of system noise. Work has already begun on the third generation experiment that plans to use ThF^+ ions which have a higher effective field of $E_{\mathrm{eff}} = 37$ GV/cm compared to $E_{\mathrm{eff}} = 24$ GV/cm in HfF^+

[28] and permit a longer coherence time because the eEDM state is the ground state.

The ACME collaboration between Harvard, the University of Chicago and Northwestern University are using a beam of ThO molecules to measure the eEDM. Their second generation experiment constrained the eEDM to $|d_e| < 1.1 \times 10^{-29}$ e cm in 2018 [29]. ThO has several advantages conducive to obtaining eEDM measurements. First, it has an effective field of 80 GV/cm, the highest of any molecule currently used for eEDM searches. In addition to this, the eEDM measurement occurs in two opposite parity states that have equal but opposite eEDM shifts. This is the same case as for HfF^+. Finally, the experiment benefits from being able to produce a large number of molecules. The group use a cryogenic buffer gas source which produces a cold intense beam of over 10^{13} molecules $sr^{-1}state^{-1}s^{-1}$ with a forward velocity of around 170 m s^{-1}. The ACME experiment is currently undergoing its next generation of developments. There are plans to include an electric lens in order to collimate the molecular beam to further improve the number of molecules in the beamline. They also hope to increase the length of the interaction time with the electric field by a factor of four in order to increase the precession time.

In 2011, the Imperial College London YbF experiment was the first molecular experiment to outperform atomic searches, setting the best limit at the time of $|d_e| < 10.5 \times 10^{-28}$ e cm [30]. Since then, developments have been under way to construct the second and third generation of Imperial YbF EDM experiment. YbF has a more modest effective field of 26 GV/cm but comes with the benefit that YbF is laser-coolable. YbF has been generated in large numbers in buffer gas sources and presents the possibility of large coherence times by collimating and trapping the molecules using optical techniques. In addition to this, the eEDM sensitive state is the ground state allowing for an almost unlimited lifetime. Two eEDM experiments are currently under development in our group. The first is a beamline experiment in which transverse laser-cooling is used to collimate the molecular beam. This reduces its divergence and together with a slower cryogenic source of molecules is expected to increase spin-precession times to around 30 ms. This experiment recently recorded its first interferometer fringes. The third generation of experiment aims to trap the molecules in an optical lattice where the localised molecules can have a spin precession time on the order of seconds. This thesis describes the progress of this

third generation experiment.

1.4 eEDM with laser-coolable molecules

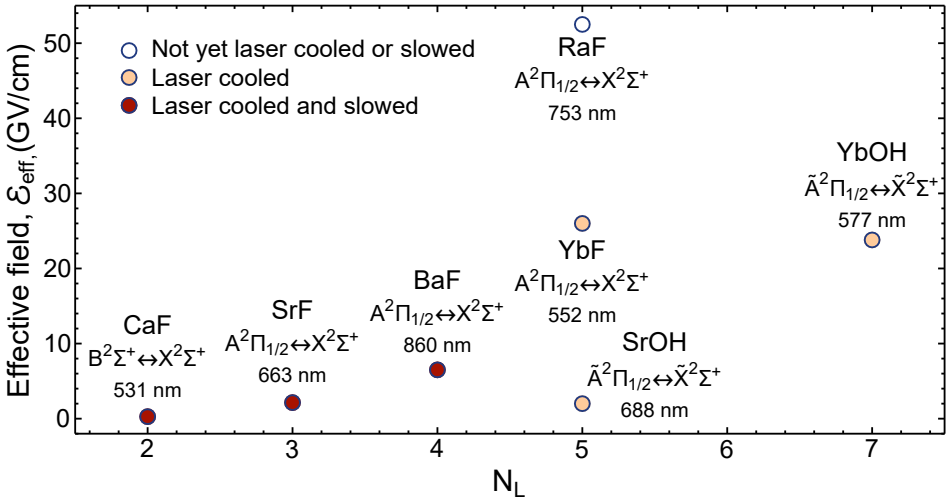

Figure 1.4: The effective electric field, $\mathcal{E}_{\text{eff}}$, of selected laser-coolable molecules alongside the estimated number of lasers, N_L, required to induce a velocity change of 100 m/s. This figure collates data presented in [31–38].

In addition to the proposed measurement with YbF mentioned above, there are further experiments under development that aim to utilise laser-cooled molecules for a measurement of the eEDM. Laser cooling relies on the repeated absorption and emission of photons. This requires a closed cycling transition. Due to the existence of vibrational levels in molecules, closed cycling transitions can only be established if the vibrational wavefunction of both the ground and excited state overlap. This overlap is known as the Franck-Condon factor and is described in greater detail in the next chapter. If the Franck-Condon factor is unfavourable, a molecule may end up in a different vibrational state after scattering only a few photons. Losses to other vibrational states can be brought back to the main cycling transition by means of additional lasers.

Figure 1.4 shows the value of the effective field alongside the estimated number of lasers required to slow selected laser-coolable molecules by 100 m/s. BaF, YbOH, SrOH and RaF have all been suggested as possible candidates for an eEDM measurement. The NL-eEDM collaboration

in the Netherlands is working towards using a laser cooled, Stark-decelerated beam of BaF molecules to measure the eEDM [39]. BaF has a smaller effective field than YbF but is lighter and has more favourable Franck-Condon factors. A similar sensitivity to the eEDM as YbF could be reached if the number of molecules trapped is increased. Polyatomic molecules, such as YbOH, combine the opposite parity levels so useful in ThO and HfF^+ with an optical cycling transition needed for laser cooling. YbOH could provide near full polarisation ($\eta = 1$) due to the small splitting in near-degenerate opposite parity levels as well as good control over systematics. Polyatomic molecules, however have additional degrees of freedom due to the extra vibrational modes. This leads to additional laser requirements. RaF combines a large effective field with favourable Franck-Condon factors that make it amenable to laser cooling and has an eEDM sensitive ground state but faces similar technical challenges as other heavy molecular species. Heavier molecules will require many more scattering events than lighter species. RaF also has the added complication of working with radioactive Radium.

1.4.1 Lattice EDM

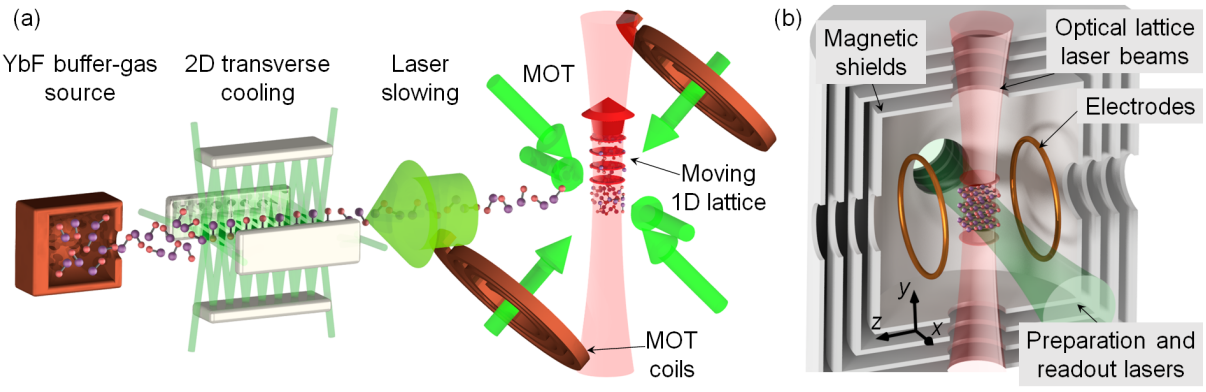

Figure 1.5: Proposed experiment to measure the eEDM using YbF molecules trapped in an optical lattice. The molecules are transversely cooled, decelerated and trapped in a MOT. An optical lattice can then be loaded. The magnetically shielded region where the eEDM measurement can take place is shown in (b). Figure produced by J. Lim.

The current limits on the eEDM were set using experiments which either provide large coherence times, τ, or large number of detected molecules, N_{det}. YbF provides a promising platform towards an eEDM experiment that has both a large τ and large N_{det}. Figure 1.5 illustrates the proposed experiment which we call Lattice EDM. YbF molecules are generated inside a

cryogenically cooled buffer gas cell. Through design choice of the cell as well as advances in closed-circuit cryocoolers, we aim to produce an intense beam of molecules at already low forward velocities. Further deceleration of the molecular beam by radiation pressure slowing from counter-propagating laser light will bring the molecules to sufficiently low velocities that they can be captured into a magneto-optical trap (MOT). The number of molecules in the MOT can likely be improved by transversely cooling the molecular beam to reduce its divergence. The molecules in the MOT will be cooled to a temperature of around 10 mK and confined to an area of a few mm. Further sub-Doppler cooling will reduce their temperature to around 10 μK. The molecules will then be loaded into an optical lattice formed by a 1D standing wave of far detuned laser light creating a series of potential wells about 200 μK deep. Once in the lattice, the molecules are prepared in the lowest rotational and hyperfine state, and then the lattice is translated in order to move the molecules into the magnetically shielded eEDM interaction region. Here the eEDM measurement can begin. 10^4 molecules loaded into the lattice with a coherence time of around 4 s is expected to give a statistical sensitivity of $\sigma_{d_e} = 8 \times 10^{-29}\, e\,\text{cm}$ in a single shot of the experiment [40]. With careful control of systematic errors, it seems possible to reach a sensitivity of $10^{-32}\, e\,\text{cm}$. At this level, should the eEDM be zero, large parameter spaces of many BSM theories will be excluded, leading theoretical work in new directions.

1.5 Thesis outline

This thesis describes the progress towards an eEDM measurement using cold, trapped molecules in an optical lattice. When I first joined, the experiment consisted of an empty optical table and so this thesis describes the ground-up construction of the project we call LatticeEDM. The outline of this thesis is as follows. We begin in the next chapter with a description of the molecular structure of YbF. We introduce the energy level structure, spectroscopic notation and constants required for subsequent sections.

In chapter 3 we discuss our molecular source. The source makes two improvements to previous cryogenic buffer gas sources in our group. A closed-circuit cryocooler allows us to reach

temperatures below 2 K and the chosen design of the cell is such that the number of molecules exiting the source at slow velocities is increased. The molecular beam from this new source is characterised and the number of molecules and their velocities are measured.

Chapter 4 investigates the optical cycling rate and losses from a counter-propagating laser beam. Such scattering is needed for radiation pressure slowing and we demonstrate some modest laser slowing. We find that there remain significant losses out of our optical cycle.

In chapter 5 we perform a spectroscopic study of a series of electronic states arising from the excitation of an inner-shell electron in YbF. One such manifold of states lies in-between the ground and excited states in our optical cycling transition, and decays to these states are predicted to be a loss channel. In addition to recording the rotational structure of these states we also study a high-lying state in the UV and a pair of states that lie *above* the ionisation limit of the molecule.

Chapter 6 describes the technical progress towards building a MOT of YbF. The experimental hardware, laser and imaging setups are described and we make a careful characterisation of background noise in order to establish efficient detection techniques for molecules in the MOT.

Finally, in chapter 7 we reflect on the results of the thesis and describe the outlook of the project.

Chapter 2

Molecular structure

2.1 Gross molecular structure

YbF is formed when an ytterbium atom, with electronic configuration [Xe]$4f^{14}6s^2$, donates one of its $6s$ electrons to a fluorine atom, [He]$2s^2 2p^5$. The molecule can then be seen as an Yb^+ ion with a single valence electron, bonded ionically to an F^- ion. The molecular ground state has, to some approximation, [Xe]$4f^{14}6s^1$ structure with the first excited state being mostly an excitation of the valence electron to [Xe]$4f^{14}6p^1$ structure, analogous to the alkali atom equivalent.

Unlike atoms however, in addition to their electronic structure, molecules also have rotational and vibrational structure due to the nuclear motion. A full treatment of the Hamiltonian would require summing over the many constituent electrons, nuclei and their interactions in a fully relativistic setting. This leads to a lengthy and complicated Hamiltonian. See chapter 3 in Ref. [41]. Instead we construct an effective Hamiltonian that allows us to understand spectroscopic observations of the energy level structure. The rotational, vibrational and electronic structure can be separated by making use of the Born-Oppenheimer approximation. This approximation allows the wavefunction of a diatomic molecule, Ψ_{mol}, to be separated into three parts: electronic, vibrational and rotational $\Psi_{\mathrm{mol}} \simeq \psi_{\mathrm{elec}}\, \psi_{\mathrm{vib}} \psi_{\mathrm{rot}}$. The gross molecular structure can then be described by the effective Hamiltonian $H_{\mathrm{eff}} = H_{\mathrm{elec}} + H_{\mathrm{vib}} + H_{\mathrm{rot}}$.

Electronic structure

The quantum numbers that we are familiar with when working with atoms are the principal quantum number n, the orbital angular momentum quantum number l, and the spin angular momentum quantum number s. In a diatomic molecule the presence of two nuclei causes a breaking in the spherical symmetry of the potential found in atoms that makes l a good quantum number. Instead, in diatomic molecules, there is a strong internal electric field along the internuclear axis $\hat{\boldsymbol{n}}$. For some electronic states, those in Hund's case (a) (see section 2.2), the coupling between the orbital angular momentum $\mathbf{L}$ and the internuclear axis is strong such that L is no longer a good quantum number but instead the projection of L along the internuclear axis is. This is denoted Λ. For sufficiently strong coupling strengths the total electron spin $\mathbf{S}$ also couples to the internuclear axis. It also proves convenient to define a quantum number for the projection of the electronic spin onto the internuclear axis, which is denoted Σ.

For a state with orbital angular momentum L, Λ can take on values $0, \pm1, \pm2, ..., \pm L$. The sign of Λ corresponds to the direction of the orbital angular momentum being either clockwise (positive) or anti-clockwise (negative) about $\hat{\boldsymbol{n}}$. A reflection operator acting on an eigenfunction with eigenvalue Λ will convert it to the same eigenfunction with eigenvalue $-\Lambda$. Both of these eigenfunctions have the same energy, to first order, and so are degenerate for $\Lambda \neq 0$. The states corresponding to $|\Lambda| = 0, 1, 2, ...$ are hence denoted by convention as a $\Sigma, \Pi, \Delta...$ state. For states that have $\Lambda \neq 0$ an internal magnetic field is generated along $\hat{\boldsymbol{n}}$, which the magnetic moment of the electrons (arising from their spin, $\mathbf{S}$,) can couple to. This is known as spin-orbit coupling. Like in atoms $\mathbf{L}$ and $\mathbf{S}$ couple to give $\mathbf{J_a}$, the projection of $\mathrm{J_a}$ onto the internuclear axis is then defined as $\Omega = \Lambda + \Sigma$. The electronic state of a diatomic molecule where $\Lambda \neq 0$ is given a term symbol analogous to that in atoms, ${}^{2S+1}\Lambda_{\Omega}$.

For states that have $\Lambda = 0$, there is no spin-orbit coupling and Ω is not defined. These states are given the term symbol ${}^{2S+1}\Lambda^{+/-}$ where the superscript denotes whether the electronic wavefunction is symmetric/anti-symmetric upon reflection about an arbitrary plane containing the internuclear axis.

The electronic contribution to the molecular energy, including spin-orbit coupling, is then,

$$E_{\text{elec}} = T_0 + A\Lambda\Sigma, \tag{2.1}$$

where T_0 is the electrostatic energy relative to the ground state and A parametrises the spin-orbit coupling term in the Hamiltonian, $A\mathbf{L}\cdot\mathbf{S}$.

Vibrational structure

The electronic energy is a function of the internuclear separation of the constituent atoms. The atoms can vibrate around the equilibrium position of this near harmonic potential. This is then analogous to a harmonic oscillator with quantum number v plus higher order corrections to account for the anharmonicity in the potential. The vibrational energy eigenstates can then be expressed as,

$$E_{\text{vib}} = \omega_e\left(v+\frac{1}{2}\right) - \omega_e x_e\left(v+\frac{1}{2}\right)^2 + \omega_e y_e\left(v+\frac{1}{2}\right)^3 + \ldots \tag{2.2}$$

Here, ω_e is the vibrational constant and x_e, y_e, are anharmonic constants of decreasing size. For low vibrational levels it is usually sufficient to consider the series to second order.

Rotational structure

The rotational motion of the molecule can be approximated as a rigid rotor, where the two nuclei rotate about their centre of mass at a fixed distance from each other. The energies of the rotor are

$$E_{\text{rot}} = BR(R+1) - DR^2(R+1)^2 + \ldots \tag{2.3}$$

where R is the rotational quantum number and B the rotational constant. The second term,

characterised by D is referred to as the centrifugal distortion and is a correction due to the stretching of the bond from the rotational motion.

The gross energy level structure of a diatomic molecule can then be summarised to first order as

$$E = E_{\text{elec}} + E_{\text{vib}} + E_{\text{rot}} = T_0 + A\Lambda\Sigma + \omega_e \left(v + \frac{1}{2} \right) + BR(R+1). \tag{2.4}$$

2.2 Rotational structure and Hund's cases

In our description above we've seen how the gross structure of molecules gives rise to various angular momenta. These angular momenta can couple with each other to produce different rotational spectra. Hund's coupling cases are idealised situations which help us to understand the pattern of rotational levels and the resulting spectra. They identify which quantum numbers are good for a certain system.

There are five cases, proposed by spectroscopist Friedrich Hund and traditionally denoted by the letters (a) through (e) [42]. Here we discuss cases (a) and (b) as these are most relevant to our optical cycle. We make an additional discussion of case (c) in chapter 5.

Case (a)

In Hund's case (a), illustrated in the vector diagram shown in figure 2.1(a), the orbital angular momentum **L** is strongly coupled to the internuclear axis. The electron spin angular momentum in turn is strongly coupled to **L** through spin–orbit coupling. The axial components of **L** and **S**, Λ and Σ are well defined as is their sum Ω. The angular momentum from the rotation of the nuclei, **R**, is coupled to **L** and **S** to form the resulting total angular momentum **J**. The precession of **L** and **S** about the internuclear axis is presumed to be much faster than the nutation of **R** about **J**. The good quantum numbers for this case are Λ, S, Σ, J and Ω. The rotational Hamiltonian is then given by,

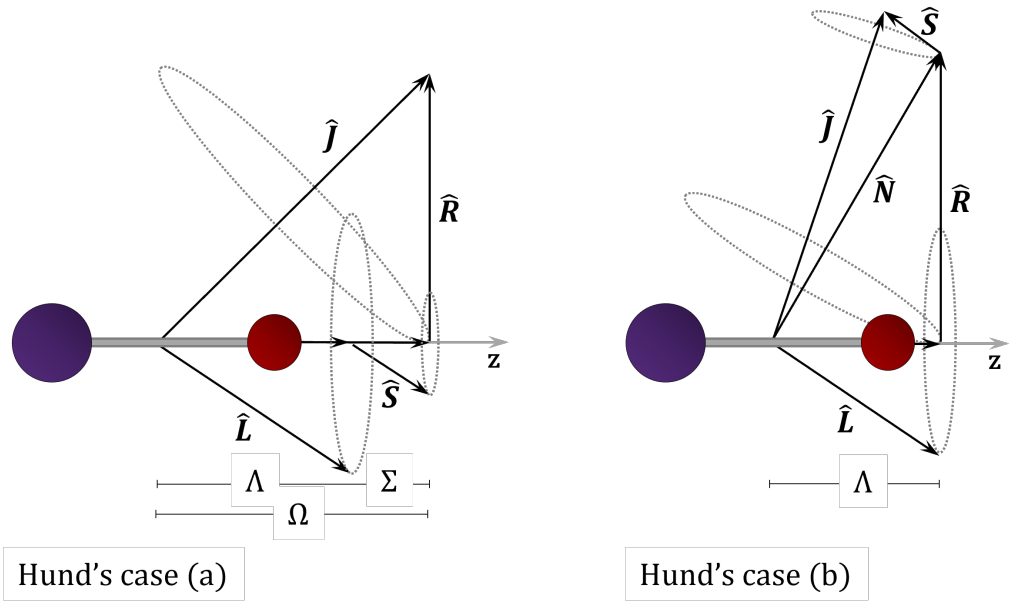

Figure 2.1: Diagram of Hund's angular momentum coupling cases (a) and (b) based on those in [41]. The internuclear axis is denoted **z**.

$$\begin{aligned} H_{\text{rot}} &= B\mathbf{R}^2 \\ &= B(\mathbf{J}-\mathbf{L}-\mathbf{S})^2 \end{aligned} \tag{2.5}$$

The first excited state of YbF is labelled $A^2\Pi$ and to a good approximation is well described by Hund's case (a). This state has $|\Omega| = 1/2, 3/2$. The spin-orbit splitting between these states is sufficiently large ($\sim$ 2THz) that the first electronic excited state is treated as two separate states, $A^2\Pi_{1/2}$ and $A^2\Pi_{3/2}$. In this work we only consider the $A^2\Pi_{1/2}$ state. The value of Ω for this state can take values $\pm 1/2$ corresponding to the projection of **J** pointing along or against the internuclear axis. The parity eigenstates are symmetric and antisymmetric combinations of these states. The degeneracy of the opposite parity combinations, called $\Omega-$doublets, is lifted due to mixing with a neighbouring Σ state. This splitting of the $\Omega-$doublets ,can also be referred to as $\Lambda-$doubling as it occurs for $|\Lambda| > 0$. The full treatment of $\Lambda-$doubling for $^2\Pi$ states in Hund's case (a) can be found in [43]. The $\Lambda-$doubling can be parameterised using two factors, p and q, such that the splitting between the symmetric and anti-symmetric $\Omega-$doublets is

$$\Delta E_\Lambda = \mp(p+2q)(J+1/2). \tag{2.6}$$

Case (b)

In Hund's case (b), illustrated in the vector diagram shown in figure 2.1, the spin-orbit coupling is weak or non-existent ($\Lambda = 0$). In this case the spin vector $\mathbf{S}$ is no longer coupled to the internuclear axis and Ω is not defined. $\mathbf{L}$ precesses very rapidly about the internuclear axis with a well-defined Λ. $\mathbf{L}$ is coupled to $\mathbf{R}$ to form $\mathbf{N}$. $\mathbf{N}$ is then coupled with $\mathbf{S}$ to form the total angular momentum $\mathbf{J}$. The good quantum numbers for this case are Λ, N, S, Σ and J. The rotational Hamiltonian is then given by,

$$\begin{aligned} H_{\text{rot}} =& B\mathbf{R}^2 \\ =& B\left(\mathbf{N}-\mathbf{L}\right)^2. \end{aligned} \tag{2.7}$$

YbF has a $X^2\Sigma^+$ ground state which is best described by Hund's case (b). The rotation of the molecule, $\mathbf{N}$, can also couple to the spin, $\mathbf{S}$. It is then convenient to form an intermediate angular momentum $\mathbf{J} = \mathbf{N} + \mathbf{S}$. The strength of this spin-rotation coupling, $\gamma_N \mathbf{S}\cdot\mathbf{N}$, can be characterised using a parameter γ_N. Each rotational level in the $X^2\Sigma^+$ state will be split into two states, labelled by their value of J. These are denoted F_1 and F_2 with energies [41, 44, 45]

$$F_1(N) = BN(N+1) + (1/2)\gamma_N N \tag{2.8}$$

$$F_2(N) = BN(N+1) - (1/2)\gamma_N (N+1), \tag{2.9}$$

where γ_N itself has a strong dependence on N and can be parameterised by [46, 47]

$$\gamma_N = \gamma_0 + \gamma_1 N(N+1) + \gamma_2 N^2(N+1)^2 + \cdots . \tag{2.10}$$

Here, F_1 has $J = N + 1/2$ and F_2 has $J = N - 1/2$. In addition to the spin-rotation coupling there is also hyperfine splitting due to the nuclear spin I (see the next section). For the case of the X state in YbF, the spin rotation splitting is comparable with the hyperfine splitting [48] and states of the same F have, in reality, mixed J character (see for example the Appendix of [48]). J is therefore only approximately a good quantum number. For the purposes of this

Vibration	no selection rules
Rotation	$\Delta J = 0, \pm 1, \Delta m_J = 0, \pm 1$ $J = 0 \not\leftrightarrow J' = 0$
Parity	$\Delta P = \pm 1$

Table 2.1: Selection rules for electric dipole transitions in molecules.

thesis, however, the above picture of the X state is sufficient.

2.3 Hyperfine structure

The ^{174}YbF molecule has nuclear spin $I = 1/2$ owing to the fluorine ^{19}F atom. The nuclear spin leads to a nuclear magnetic moment which interacts with the magnetic field produced by the electrons. This interaction splits J levels into hyperfine levels F, defined as $\mathbf{F} = \mathbf{J} + \mathbf{I}$. Each quantum state F is composed of $2F + 1$ projection sublevels labelled m_F.

2.4 Molecular transitions

Electric dipole transitions between two electronic states in molecules must follow the selection rules listed in table 2.1. The quantum number J changes according to the selection rules above. The parity of the state must also change. Vibrational state changes, however, have no selection rules. Instead the transition strengths for a vibrational state change within an electronic transition are called the Franck-Condon factors (FCFs) and are defined by

$$f_{v',v} = |\langle \psi_{v'} \mid \psi_v \rangle|^2 \tag{2.11}$$

where $\psi_{v'}$ and ψ_v are the vibrational eigenfunctions of the upper and lower electronic states. For two states whose electronic potentials are very similar the excited state is very likely to decay to the same vibrational state in the ground electronic state. In this situation $f_{0,0} \gg f_{0,1} \gg f_{0,2} \gg \ldots$ which is important for optical cycling.

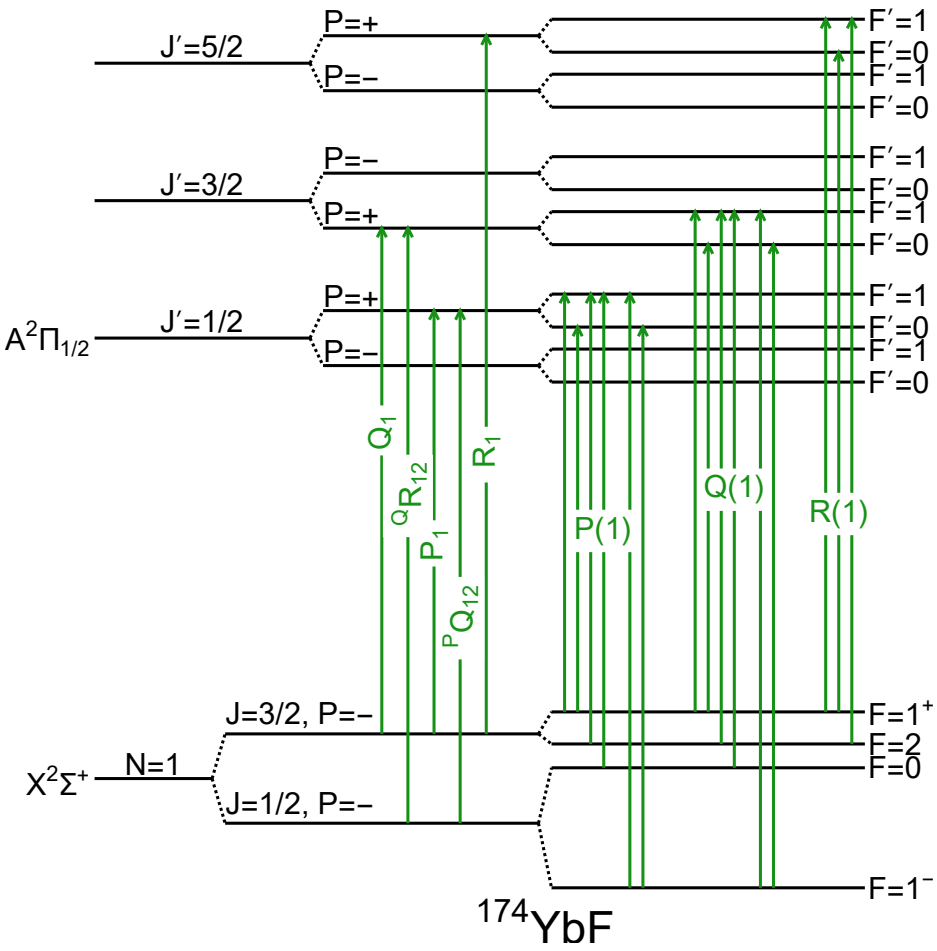

Figure 2.2: Allowed rotational transitions from $X^2\Sigma^+(N = 1)$. This diagram is not drawn to scale and energy splittings have been exaggerated. The $N = 1$ level does not have a P_{12} transition though these in general will also be present for $N > 1$.

2.4.1 Rotational branches

Figure 2.2 shows some allowed electric dipole transitions between the ground, $X^2\Sigma^+$ and excited state, $A^2\Pi_{1/2}$ of YbF. Transitions between two electronic states may change rotational quantum numbers as per the selection rules mentioned previously. The transitions are labelled in spectroscopic notation by their change in quantum numbers [49]. In the $X^2\Sigma^+$ state, N, labels the rotational level while for the $A^2\Pi_{1/2}$, the total angular momentum J provides the best label for the rotational state. The rotational transitions can then be labelled by ${}^{\Delta N}\Delta J_{F_i' F_i}$. Here, F_i' and F_i denote the spin multiplet component of the excited and ground states respectively. The transition is denoted by the letter P if $\Delta J = -1$, Q if $\Delta J = 0$ and R if $\Delta J = +1$. In Hund's case a), the spin component of lowest energy is denoted $_1$ and $_2$ for the next lowest

etc. All levels of a $^2\Pi_{1/2}$ state are assigned $F_i' = 1$. In Hund's case b), for each N, the total angular momentum in X can either be $J = N + 1/2$ or $J = N - 1/2$. The component with the higher $J = N + 1/2$ value is denoted $_1$ while that with the lower $J = N - 1/2$ value is denoted $_2$. In this labelling scheme, the superscript is dropped if $\Delta N = \Delta J$ and the second subscript is dropped if $F_i' = F_i$. For ease of reference the Q_1 and the $^QR_{12}$ lines are together referred to as the $Q(1)$ line and the P_1 and $^PQ_{12}$ lines are referred to as the $P(1)$ line, where the number in the bracket refers to the value of N of the ground state.

Rotational spectra and bandheads

Consider two electronic states with rotational splitting $E = BJ(J+1)$ and $B'J'(J'+1)$. The energy of the transition between them is given by

$$\Delta E = B'J'(J'+1) - BJ(J+1), \tag{2.12}$$

where ΔE denotes the energy splitting between two rotational states, J' and J. For each rotational level, J, there will be, in general, three allowed transitions, P, Q and R. Since there is a ladder of rotational levels this will give rise to a series of rotational branches, $P(J)$, $Q(J)$ and $R(J)$,

$$P(J) = B'(J-1)(J) - BJ(J+1), \tag{2.13}$$

$$Q(J) = B'(J)(J+1) - BJ(J+1), \tag{2.14}$$

$$R(J) = B'(J+1)(J+2) - BJ(J+1). \tag{2.15}$$

The spacing between successive transitions is then,

$$P(J+1) - P(J) = 2J(B' - B) - 2B, \tag{2.16}$$

$$Q(J+1) - Q(J) = 2J(B' - B) + 2(B' - B), \tag{2.17}$$

$$R(J+1) - R(J) = 2J(B' - B) + 4B' - 2B. \tag{2.18}$$

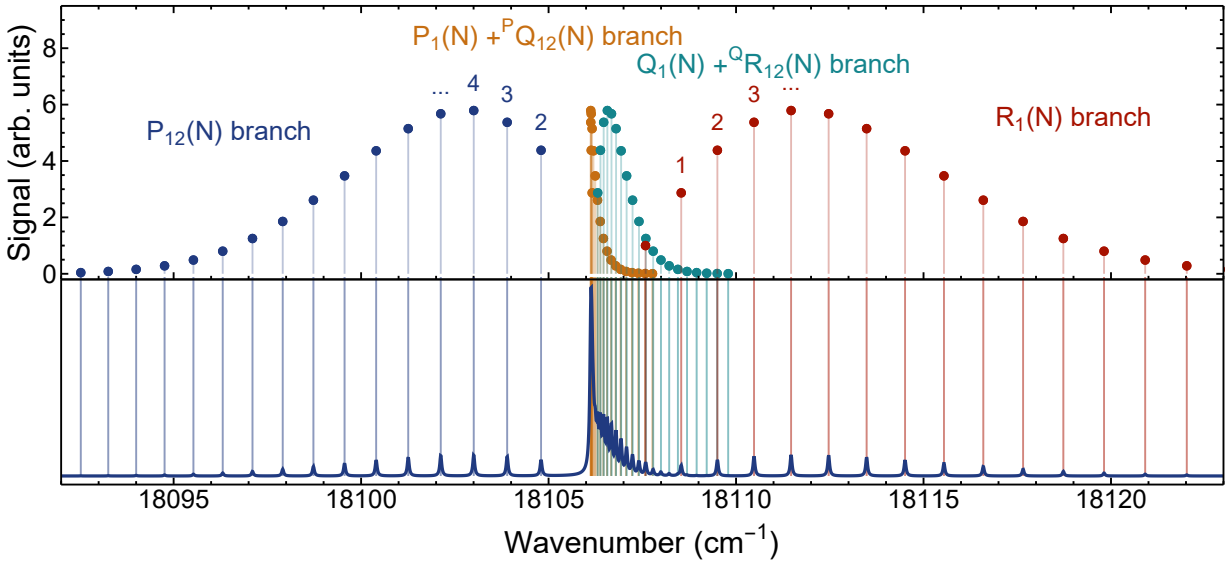

Figure 2.3: The rotational spectrum for $A^2\Pi_{1/2} \leftarrow X^2\Sigma^+$ in ^{174}YbF at 30 K plotted from the spectroscopic constants in table 2.2. The relative intensities between rotational lines are determined from the thermal population of states at 30 K. Stick spectra are shown in the top panel while the rotational lines in the bottom panel each have Lorentzian widths of 0.03 cm^{-1}.

When $B' \approx B$ we see that the spacing between R lines is $2B$ while that in P lines is $-2B$. When $B' > B$ the energy of the P lines decreases with increasing J at low J, but increases at high J. At the turning point, many P lines are clustered together in energy. This is known as a P-branch bandhead. Similarly, when $B' < B$, the energy of the R lines increases with increasing J at low J, but decreases at high J. The turning point, where many R lines are clustered together in energy, is known as a R-branch bandhead. Figure 2.3 shows the rotational spectrum for the $A^2\Pi_{1/2} \leftarrow X^2\Sigma^+$ transition in ^{174}YbF as plotted using the spectroscopic constants listed in table 2.2. The Q_1 and P_1 lines form narrow branches, while the spacing between P_{12} and R_1 lines is much larger. The P_{12} branch bandhead occurs at higher J than is shown in this spectrum.

2.4.2 Optical cycling

In this work we aim to slow down a beam of YbF to within the capture velocity of a magneto-optical trap. The basic principle of laser cooling is as follows. A photon carries momentum $p = \hbar k$. When a molecule absorbs a resonant photon it gains this momentum in the direction

Table 2.2: Spectroscopic constants for the $X^2\Sigma^+$ and $A^2\Pi_{1/2}$ states in ^{174}YbF. All values are in cm^{-1}. Constants are taken from [47, 50]. 1 cm^{-1} = 29.98 GHz.

Constant	$X^2\Sigma^+$ value (cm^{-1})	$A^2\Pi_{1/2}$ value (cm^{-1})
T_0	0	18106.1991
A	-	1365.2908
ω_e	506.6674	-
$\omega_e x_e$	2.2451	-
B	0.242191	0.247758
D	2.388×10^{-7}	2.453×10^{-7}
$p + 2q$	-	-0.39635
$\gamma_0(\times 10^4)$	-4.47776	-
$\gamma_1(\times 10^7)$	-1.267877	-
$\gamma_1(\times 10^{13})$	-8.3391	-

of light propagation. The excited molecule spontaneously decays by emitting a photon. This emitted photon has almost the same energy and momentum as the absorbed photon but is now released in a random direction. Over many absorption-emission cycles the momentum emitted cancels due to the random directions it's released in but the absorbed momentum does not such that the atom gains momentum in one direction. Our molecular beam can therefore be slowed by counter-propagating laser light resonant with the molecules. The laser frequency can either be broadened or chirped to account for the changing Doppler shift of the molecules as they slow.

We choose to slow on the P(1) line ($X^2\Sigma^+(v = 0, N = 1) \rightarrow A^2\Pi(v = 0, N = 0)$ transition). The selection rules for angular momentum and parity ensure that the excited state can only decay back to the $N = 1$ level of the $X^2\Sigma^+$ state, so the transition is rotationally closed. Decays out of the slowing cycle are still allowed however by decays to other vibrational levels since there are no selection rules for these decays. The P(1) transition has a linewidth of 5.7 MHz and a recoil velocity of 3.7 mm/s. In order to slow the molecules from the typical velocity of a cryogenic buffer gas source ($\sim$ 150 m/s) to within the typical capture velocity of a MOT ($\sim$ 10 m/s), a YbF molecule must scatter $\sim 10^4$ photons. This requires that vibrational leaks are reduced to below 10^{-4}. This is achieved by addressing each vibrational decay channel with a repump laser to bring molecules back into the slowing cycle.

Dark states

The consequence of choosing a rotationally closed transition is that the excited state will have smaller angular momentum than the ground state, $F' \leq F$. In this configuration there will be dark states. These are states that do not couple to the light field for a given laser polarisation. A molecule will be optically pumped into a dark state after scattering only a small number of photons and cease to scatter more photons. This is an impediment to laser cooling that has to be overcome by destabilising the dark states. This can be achieved either by modulating the polarisation of the laser or by applying a static magnetic field [51]. A further discussion of dark states and how to overcome them is made in chapter 4.

Chapter 3

Source

3.1 Introduction

The aim of the experiment is to create a dense cloud of trapped YbF molecules in an optical lattice. In order to facilitate this, we aim to produce an already cold, slow and high flux source of molecules as a starting point for direct laser slowing, cooling and ultimately trapping of the molecules. Similar atomic laser cooling experiments benefit from the ease of creation of a high density of atoms in the gas phase by evaporation in a vapour cell or a metal dispenser. Creation of a YbF vapour, however, requires a much larger temperature, typically around 1500 K [52]. At this temperature, molecules have a mean velocity of around 450 m/s and most of the molecules occupy high rotational states, near $N = 45$. This is a bad starting point for going ultracold. Instead, molecular laser cooling experiments often begin with the creation of a pulsed molecular beam. Molecules are produced inside a cell by ablating a target and extracted by an inert buffer gas. The form of the ablation target can be a mixture of reactants e.g. the direct creation of YbF from a mixed target of Yb and AlF_3 [53–56], the direct ablation of a ceramic target e.g. the production of ThO from a ceramic target of ThO_2 [57], or the ablation of a pure metal target and the introduction of a reactant gas e.g. the creation of CaF by ablation of a Ca target in the presence of SF_6 [58, 59] as well as many other species including YbF and AlF [60–62]. Molecular beams are generally produced in one of two types of

sources. In a supersonic source, the molecules, entrained in a buffer gas pulsed into the cell, are supersonically expanded through a narrow aperture. The energy of the random thermal motion is converted into translational energy in the forward direction by collisions. This rotationally and vibrationally cools the molecules but comes at the cost of increased forward velocity. Buffer gas sources operate by flowing a gas continuously into the cell, at much lower pressure than in a supersonic source. The buffer gas thermalises with the walls of the cell which is cryogenically cooled. Collisions with the buffer gas rotationally, vibrationally and translationally cool the molecule. Supersonic sources have found wide use in spectroscopy of molecules and metal clusters as well as for experiments loading Stark and Zeeman accelerators [63, 64]. The low forward velocity of molecules emerging from a cryogenic buffer gas source however means that it is the preferred starting point for molecular trapping experiments. Many experiments with cold or ultracold molecules start from a cryogenic buffer gas source. Some examples include CaF, BaF, AlF, SrF, YO, [60, 62, 65–70] as well as polyatomic molecules including YbOH, SrOH, CaOH [71–75]. Indeed, all molecular MOTs, so far, have started with a buffer gas source [31, 76]. This chapter demonstrates the production of a cold, slow, intense source of YbF produced in a cryogenic buffer gas source. Our cryogenic source consists in part of a copper cell based on the design by [77]. This design utilises a two chamber design to reduce the forward velocity of the molecular beam. We regularly produce $\sim 10^{10}$ mol/sr/pulse in a single rotational state with peak velocities as low as ~ 50 m/s. Our source is the first buffer gas source of YbF to operate at $\sim$2 K and presents a significant improvement over previous molecular sources of YbF, typically operating at 4 K and delivering beams with speeds of about 150 m/s.

3.1.1 Background

Molecular sources can be characterised into two regimes based on the distance a buffer gas atom can travel before colliding with another buffer gas atom. We describe the molecular source as an ideal atomic gas inside a box, where the beam is formed when the atoms exit the box through

an aperture. The mean free path, λ, of an atom is

$$\lambda = \frac{1}{\sqrt{2} n_0 \sigma} \tag{3.1}$$

where n_0 is the number density of helium atoms and σ is the elastic scattering cross-section of the buffer gas. The flow regime near the aperture of the cell is determined by the number of collisions that occur in this region. This is characterised by the Knudsen number, K,

$$K = \frac{\lambda}{L} = \frac{1}{\sqrt{2} n_0 \sigma L} \tag{3.2}$$

where L is the characteristic length of the system, assumed to be the radius of the aperture. In the case where $K > 1$ the gas is in the molecular flow regime. In this regime the molecules primarily collide with the walls of the container. This corresponds to an effusive beam and the kinetic theory of gases can be used to predict the properties of such a beam [78]. Molecules rarely collide with other molecules so the velocity distribution of an effusive beam tends to be broad. When $K < 0.01$ we are said to be in the hydrodynamic regime (supersonic regime if the pressure difference across the aperture is high enough). In this case, particles collide with each other much more often than with the walls of the container. Cryogenic buffer gas sources, such as that used in this work, operate between these two regimes and can benefit from both good thermalisation with the buffer gas as well as improved molecular yield by hydrodynamically enhanced extraction out of the cell. A more detailed discussion of this is made later in this chapter.

3.2 Experimental setup

Figure 3.1 shows a schematic of our cryogenic molecular beam source. The molecular beam is generated inside a buffer gas cell shown in figure 3.1(b-c). The buffer gas cell is cooled to 1.8 K. Cooling power is provided by a two-stage closed-circuit He cryocooler (Sumitomo RDE 418D4 with F-70 compressor). Each stage of the cryocooler is cooled to different temperature

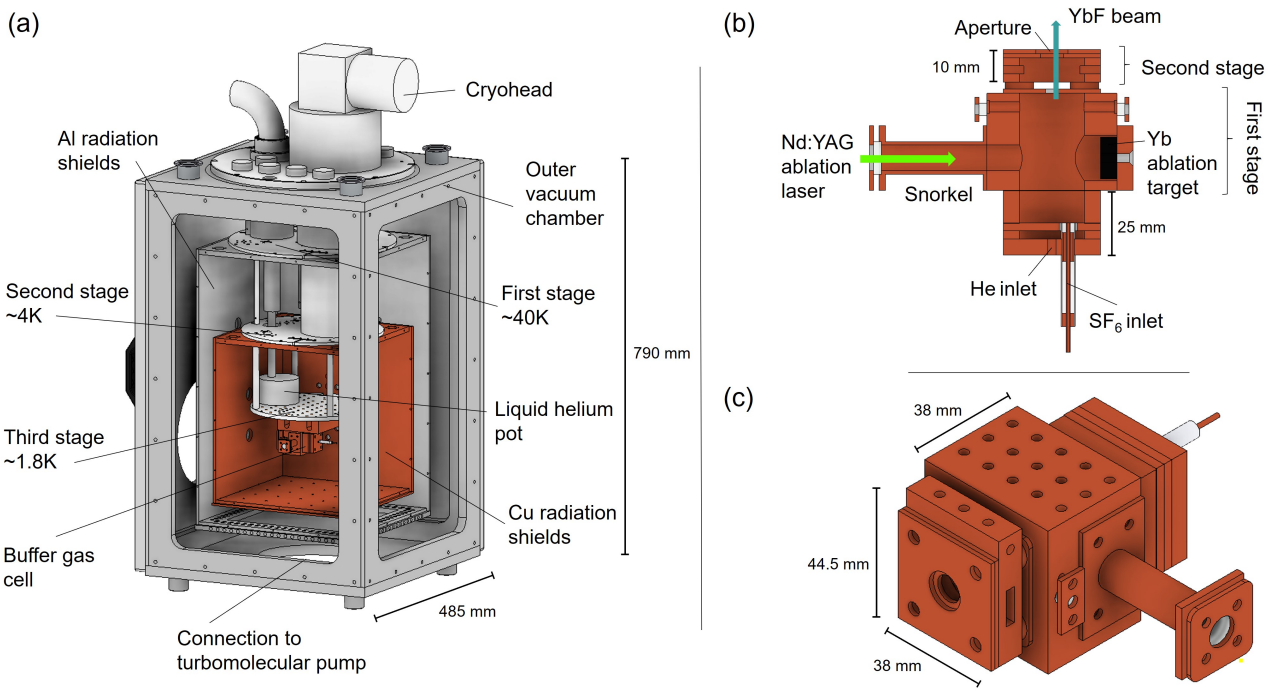

Figure 3.1: (a): A diagram of the molecular beam source. The chamber doors have been omitted. (b): Cut through of a bird's eye view of the two stage buffer gas cell. (c): Entire view of the two stage buffer gas cell.

and has different cooling power. To limit heating from the blackbody radiation of the room temperature environment the first stage is surrounded by aluminium radiation shields which are cooled to around 40 K. The second stage is surrounded by copper shields which are cooled to 3.6 K. A third stage, mounted beneath the two-stages of the cryocooler, is maintained at lower temperature by pumping on a reservoir filled with liquid helium that is mounted onto this stage. This stage has a base temperature of 1.2 K but during operation the cell is at 1.8 K, primarily due to the heat load from the ablation laser. The ablation laser can produce thermal loads of $\sim$ 200 mW, close to the quoted cooling power at 1.8 K ($\sim$300 mW). The operating pressure of the source chamber under cryogenic conditions is about 5×10^{-9} mbar, measured outside the radiation shields. To form a molecular beam we continuously flow helium gas into the buffer gas cell which increases the operating pressure. To minimise the pressure increase, the internal walls of the copper shields are coated with activated charcoal. The charcoal acts as an efficient sorption pump for helium gas at temperatures below 10 K. The pressure typically increases to 1×10^{-8} mbar when 2 standard cubic centimetres per minute (sccm) of helium is flowed through the cell. Holes in the radiation shields allow for optical access into the source

chamber. The source can be cooled from room temperature to 1.8 K in about 16 h. Cartridge heaters can be used on the third stage to control its temperature once cold. A second cartridge heater attached to the second stage is used in addition to the first to heat the set-up to room temperature overnight. When under normal operation we warm the source to 50 K at the end of every working day before cooling back down to 1.8 K in order to remove excess helium from the charcoal sorbs. A full warm-up to room temperature is carried out over the weekend.

A cross-section schematic of the buffer gas cell is shown in Figure 3.1(b). It is based on the design presented by the Doyle group [77, 79]. The buffer gas cell is anchored to the third stage maintained at 1.8 K during normal operation. YbF is produced by ablating a solid ytterbium target in the presence of a fluorine donor gas (SF_6) inside the cell and extracted by a helium buffer gas thermalised to the cell walls. The cell is machined from oxygen-free copper, has a circular bore with a 25 mm diameter, and length 38 mm. Windows near the aperture of the cell allow for in-cell absorption spectroscopy. The exit aperture of the cell has a diameter of 5 mm. A solid Yb target made out of a 9 mm disk is screwed into a removable plate which sits opposite a long tube for the ablation laser to travel through the so-called snorkel. The purpose of the snorkel is to prevent ablation products from coating the window. The output of a pulsed Nd:YAG laser with a pulse energy of up to 195mJ and a pulse length of 6 ns is gently focused onto the target. The Nd:YAG fires with a repetition rate of 2 Hz. A higher repetition rate leads to excess heat load on the third stage which the helium reservoir is unable to remove. Motorised kinematic mirrors allow us to translate the ablation laser beam to a fresh position on the target. We find we have to do this once a day to maintain good molecular flux. The helium buffer gas is pre-cooled in two copper pipe bobbins that are attached to each of the first two cooling stages and fed into the rear of the cell. A diffuser plate dissipates the helium in the cell. We introduce sulphur hexafluoride, SF_6, into the cell through a copper capillary that is thermally isolated from the cell. To prevent the SF_6 from freezing the temperature of the capillary is kept at about 230 K by a heater. The flow of He and SF_6 ino the cell is controlled by a pair of mass flow controllers. In order to reduce the forward velocity of the beam further, a second cell, is attached to the front of the first with a variable gap in between [76, 77]. The

second 'slowing' cell has internal dimensions of 25 mm diameter and 10 mm length with an exit aperture of 10 mm diameter. A copper mesh with a open area of 37% is placed over the aperture of the slowing cell. Collisions with back scattered molecules reduce the forward velocity of the beam, at the cost of flux. Two venting ports on the side of the slowing cell are fashioned to leak out some helium so as to control the density of gas. The density can further be tuned by varying the gap between the two cells.

3.2.1 Experimental apparatus for beam characterisation

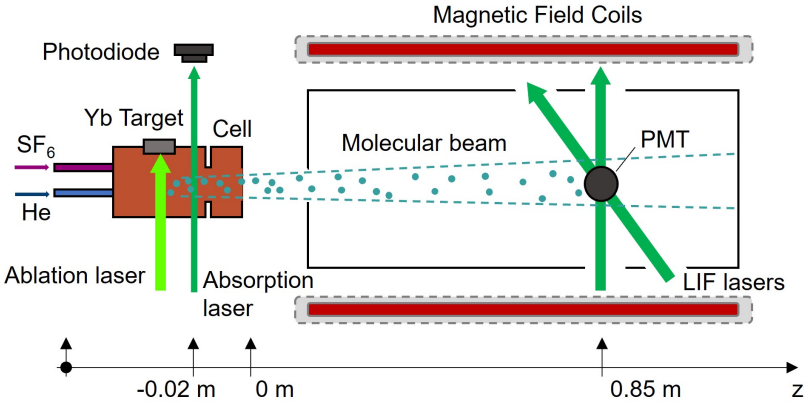

Figure 3.2: A schematic of the experimental setup used in this chapter. YbF molecules are produced in a cryogenic buffer gas cell by laser ablation of a solid Yb target in the presence of SF_6. The molecules can be detected inside the cell by an intersecting laser, incident on a photodiode. The molecules downstream of the source are imaged by laser induced fluorescence (LIF). One of two laser beams can be used for LIF measurements, a beam intersecting the path of the molecules orthogonally and another at 60° to the direction of propagation.

A schematic of the experimental configuration used to characterise the molecular beam is shown in figure 3.2. The molecules are probed on the P(1) cycling transition of $A\,^2\Pi_{1/2} \leftarrow X\,^2\Sigma^+$. The molecules can be probed at two positions along the beamline. First, absorption spectroscopy of molecules inside the cell is facilitated by an intersecting laser beam at approximately $z = -0.02$ m. A second detection point is at $z = 0.85$ m. Here, the molecules can be probed by two laser beams, one transverse and the other at 60° to the molecular path. Laser induced fluorescence (LIF) from the molecules is imaged onto a photomultiplier tube (PMT). This LIF detector is used to measure the molecular flux and longitudinal velocity of the molecular beam. To efficiently cycle photons on the P(1) line, a magnetic field is used to destabilise dark states.

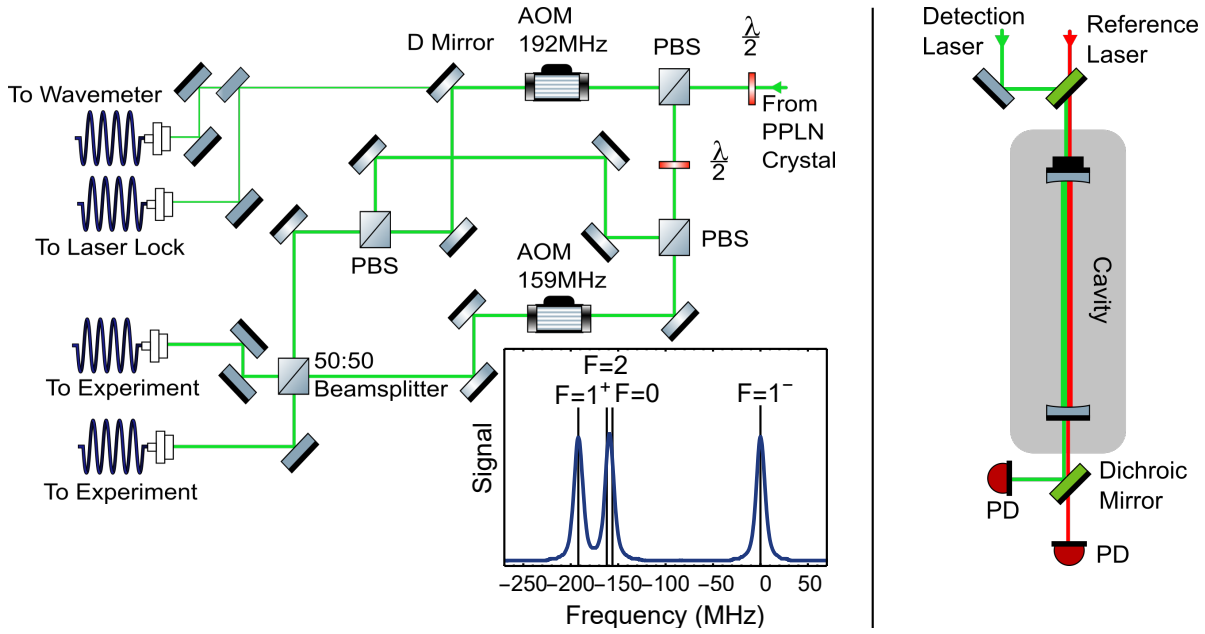

Figure 3.3: Optical table configuration for the molecular probe laser. AOMs are used to generate the frequency sidebands used for addressing the hyperfine structure in $X\,^2\Sigma^+(N=1)$ (left). The probe laser is locked to a stable reference laser using a transfer cavity lock (right).

This is formed by a pair of magnetic field coils mounted onto our beamline. Magnetic field destabilisation is discussed in greater detail in chapter 4.

The probe light is produced by a frequency doubled, 1104 nm, home build external cavity diode laser (ECDL). The ECDL seed laser is amplified using an ytterbium fiber amplifier and then frequency doubled to 552 nm using a PPLN crystal. In order to maximise detected signal it is convenient to drive all hyperfine components of the P(1) line simultaneously. $X\,^2\Sigma^+(N=1)$ has four hyperfine states with $F = 1, 0, 2, 1$. The hyperfine structure in $A\,^2\Pi_{1/2}(J = 1/2^+)$ has states with F = 0 and 1, however the splitting between these is 4 MHz so is not resolved in our experiments. Acousto-optic modulators (AOMs) are used to address the four hyperfine states in $X\,^2\Sigma^+$. The optical setup used to produce these RF sidebands is shown in figure 3.3. The laser light is split into three beams, one beam is left unaltered, the other two beams are each passed through an AOM driven at 159 MHz and 192 MHz respectively. We use the AOMs in a single-pass configuration and only use the first negative diffraction order beam to lower the frequency by 159 MHz and 192 MHz respectively. The 159 MHz sideband addresses both the $F = 0$ and $F = 2$ states which are split by less than the power broadened width of

the laser light. The sideband configuration used is shown by the inset in figure 3.3. The zero orders from the AOM are used to provide light for our frequency locking setup and a reading for a wavemeter. To stabilise the frequency of our probe laser the frequency is locked to that of a stable reference laser. The apparatus used to do this is shown on the right of figure 3.3. The reference laser is a commercial 780 nm laser (Moglabs Cateye ECDL Model CEL 002), frequency locked to the D2 line of Rb by Doppler-free Zeeman-modulated spectroscopy. Both the reference laser and the probe laser are combined through a single optical cavity (Thorlabs SA200-5B). The output light from the cavity is then separated again and each laser frequency monitored on a photodiode. As the cavity length is scanned, it comes into resonance with each of the laser wavelengths, giving a peak in transmission for that wavelength. A computer program maintains the position of the reference peak in the scan by feeding back to the cavity piezo. The relative distance (in volts scanned) between reference laser and the probe ECDL is kept constant by feeding back to the cavity length of the ECDL. We refer to this setup as transfer cavity lock since it transfers the stability of a stable reference laser to another laser.

3.2.2 Laser induced fluorescence detector

The molecular beam can be efficiently detected using laser induced fluorescence (LIF). Emitted photons are imaged onto a photo-multiplier tube (PMT). This allows for high-gain, low noise detection when, for example, the density of molecules is too low for absorption measurements. One could also use a CCD to record the molecular signal but one would forgo time resolution which is key for our laser slowing experiments.

Figure 3.4 shows a schematic of our laser induced fluorescence detector. A probe laser intersects the molecular beam inside a vacuum chamber. The probe laser enters and exits the vacuum chamber through two baffles which minimise the laser light scattered into the detection system from the entrance/exit windows. The inside of the vacuum chamber is coated in black soot (not shown in figure 3.4) to minimise stray laser scatter. The laser induced fluorescence is collected and collimated by a 43 mm focal length lens placed 43 mm from the crossing point of the molecular beam and laser. A mirror of 50 mm radius of curvature placed 50 mm from the

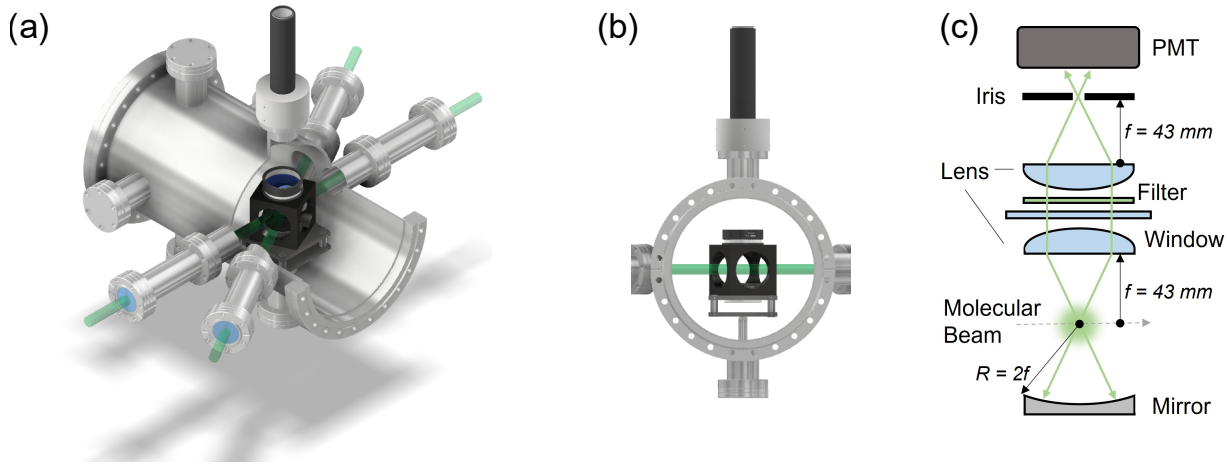

Figure 3.4: Laser induced fluorescence from the molecular beam is collected inside a vacuum chamber (a). Two laser beams intersecting the molecular beam transversely and at 60° can be used for imaging. A side on view is shown in (b). The imaging optics setup is shown in (c). Two lenses are used to create a 1:1 image onto a photomultiplier tube (PMT). A spherical mirror is used to increase the detection volume. The imaged area can be adjusted using an iris.

beam along the axis of the lens approximately doubles the number of photons collected. The photons are then focused by a second lens with focal length 43 mm to create a 1:1 image onto the PMT. An iris placed before the surface of the PMT allows reduction of the imaged area, and reduces scattered light from outside the probed volume from reaching the detector.

The incident photons are converted into electrons on the cathode of the PMT (Hamamatsu R928). Dynodes of the PMT sequentially multiply the number of electrons which are collected on the anode. This process provides low noise gain of around 10^6. The output current of the PMT is proportional to the number of incident photons of the PMT taking into account the quantum efficiency of the PMT which for wavelengths around 552 nm is 10%. The maximum number of counts the PMT can sustain is limited by the maximum output current the anode can tolerate. This is typically 0.1 mA corresponding to $\approx 10^8$ photons/s. The photo-current output by the PMT is converted to a voltage using a transimpedance amplifier. Under typical molecular signals we record photon count rates of a few 10^6 photons/s and have typical SNR of 50 - 100 in a single shot.

3.3 Beam characterisation

3.3.1 Absorption measurements and extraction characteristics

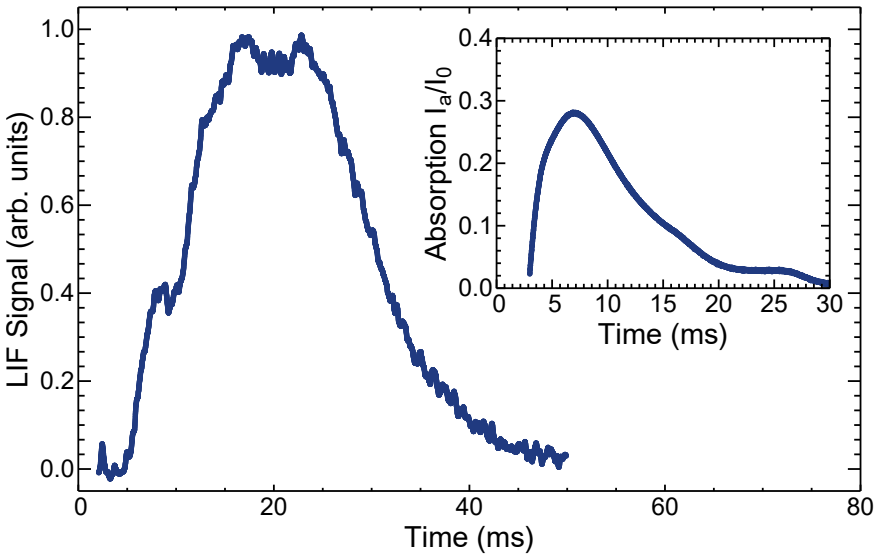

Figure 3.5: Laser induced fluorescence signal of the cryogenic buffer gas beam over time recorded using a two-stage cell at 2 sccm helium flow and 55 mJ ablation pulse energy. The absorption signal as a function of time inside the cell is shown in the inset. The time for the molecules to diffuse to the probing region can be estimated by the time to reach peak absorption. The extraction time is estimated by an exponential fit to the tail of the absorption signal.

The properties of the molecular beam are characterised by probing the P(1) rotational line of the $A\,^2\Pi_{1/2} \leftarrow X\,^2\Sigma^+$ transition. The molecule signal out of the buffer gas cell can be probed by laser induced fluorescence at a distance of 85 cm from the exit of the cell. In addition, the density of the YbF molecules inside the buffer gas cell can be probed via absorption spectroscopy. In both cases the laser is locked on resonance with the P(1) rotational line. Figure 3.5 shows a typical time of flight profile of the molecular beam. The inset in figure 3.5 depicts the absorption signal over time recorded inside the first stage of the cell, ≈ 0.02 m from the exit aperture. The laser intensity is reduced to limit pumping out of the ground vibrational level and ensure $n_1 \gg n_2$, where n_1 is the population in the ground state and n_2 is the population in the excited state. The beam brightness of molecules in the $N = 1$ rotational level can be estimated from the laser induced fluorescence of the molecules downstream of the cell whilst the the production yield in the cell and extraction characteristics such as the diffusion time, extraction time and

efficiency can be determined by absorption spectroscopy inside the cell.

We first turn our attention to the absorption profile. For a two-level system, the Beer-Lambert law relates the density of molecules in the ground level, n_1, and excited level, n_2, to the measured absorption,

$$-\ln\left(I_t(t,\omega)/I_0\right) = n(t)\sigma(\omega)z, \tag{3.3}$$

where $\sigma(\omega)$ is the absorption cross-section, z is the interaction length, and I_t and I_0 are the intensities transmitted with and without the molecules present. At low laser intensities we can approximate that $n_1 - n_2 \approx n_1 = n$. The absorption cross-section can be defined by [80],

$$\sigma(\omega) = \frac{\lambda^2}{4}\frac{g_2}{g_1}A_{21}s(\omega) \tag{3.4}$$

where $g_1 = 12$ and $g_2 = 4$ are the degeneracies of the ground and excited states respectively and $A_{21} = \Gamma$ is the linewidth of the transition. Here, $s(\omega)$ is a lineshape function normalised such that its integral over all angular frequencies is unity. In the absence of broadening mechanisms $s(\omega)$ is a Lorentzian whose width is the natural line width of the transition. In cases of absorption through a gas of molecules with a thermal velocity distribution, $s(\omega)$ is a Voigt profile whose Lorentzian width is equal to the natural linewidth of the transition[1] and a Doppler contribution due to the motion of the molecules. This broadening makes the spectral line wider but does not change the area under the curve. In our case the Lorentzian contribution is $2\pi \times 5$ MHz and we take the Doppler contribution to be that of YbF thermalised to 3 K to allow for imperfect thermalisation with the cell walls, $2\pi \times 50$ MHz. The resonant absorption cross section for the P(1) line is then $\sigma_0 = 2 \times 10^{-15}$ m^2. The interaction distance is taken as the width of the cell. We assume the density is uniform across the entire volume of the cell, V_{cell} and estimate the total number of molecules produced in the cell, N_{YbF}, from the peak density in the cell multiplied by the volume of the cell. The molecular parameters used to obtain figure 3.5 give a molecular yield of $N_{\text{YbF}} = 1.7 \times 10^{11}$ in the $N = 1$ rotational state.

[1] Provided the collision rate is much smaller than the natural linewidth.

A more complete estimate requires accounting for saturation of the absorption, collisions, and diffusion into the probe volume [55].

Diffusion time

Figure 3.5 shows that density in the cell peaks at around 6 ms. The signal decays with a similar time constant of 6 ms. The molecules are created at the target surface. The timescale for ablation and molecule creation occurs on a sub μs timescale, however the molecules will diffuse through the helium background through the cell. The timescale for diffusion across the cell can be estimated from the diffusion constant given by,

$$D = \frac{3}{16}\left(\frac{2\pi k_{\mathrm{B}} T}{\mu}\right)^{1/2} \frac{1}{n_0 \bar{\sigma}_{\mathrm{D}}} \tag{3.5}$$

where μ is the reduced mass of the helium and YbF molcules, $\mu = \frac{m_{\mathrm{YbF}} m_{\mathrm{He}}}{m_{\mathrm{YbF}} + m_{\mathrm{He}}}$, n_0 is the number density of buffer gas in the cell and $\bar{\sigma}_{\mathrm{D}}$ is the diffusion cross-section. To estimate the number density we consider the flow rate out of the cell. The molecular conductance of the aperture in effusive conditions is $f_{\mathrm{out}} = (1/4) n_0 \bar{v} A_{\mathrm{aperture}}$, where $\bar{v}$ is the mean thermal velocity of the buffer gas inside the cell [76]. In steady state, the flow rate out of the cell is equal to that into the cell. With a flow rate of 2 sccm into the cell, a thermal velocity of 137 m/s corresponding to helium at 3 K, we find a buffer gas density in our cell of 1×10^{21} m^{-3}, similar to that found in [77] for CaH production with a helium buffer gas for the same cell geometry and similar experimental parameters. At higher Knudsen number, the density inside the cell can be higher. Although this method assumes an effusive beam, the case for a hydrodynamic beam is in general no more than a factor 2 larger [81]. The YbF - He diffusion cross-section at 20 K was determined as $203 \pm 75 \times 10^{-20}$ m^2 in [55]. Assuming this value also applies at 3 K gives a diffusion coefficient 0.01 m^2/s.

The time constant for diffusion, τ_{diff}, through a cubic cell of length L is,

$$\tau_{\mathrm{diff}} = \frac{L^2}{3\pi^2 D}. \tag{3.6}$$

A diffusion time of 6 ms corresponds to a characteristic length of 41 mm, which is in reasonable agreement with the length of our cell.

Extraction time

The rate at which the buffer gas exits the cell is given by the molecular conductance of the cell aperture, $\dot{N}_{\mathrm{b}} = \frac{1}{4} N_{\mathrm{b}} \bar{v}_{0,\mathrm{b}} A_{\mathrm{aperture}} / V_{\mathrm{cell}}$, where $\dot{N}_{\mathrm{b}}$ is the rate of change in the number of buffer gas species, $\bar{v}_{0,\mathrm{b}}$ is the mean velocity of the buffer gas, A_{aperture} is the open area of the cell aperture and V_{cell} is the volume of the cell [76]. The solution to this equation is an exponential decay with a time constant given by,

$$\tau_{\mathrm{extract}} = \frac{4 V_{\mathrm{cell}}}{\bar{v}_{0,\mathrm{b}} A_{\mathrm{aperture}}}. \tag{3.7}$$

For the geometry of our cell and a helium temperature of 3 K we find $\tau_{\mathrm{extract}} = 12$ ms.

Under effusive conditions, extraction out of the cell occurs solely by diffusion of the species to the aperture of the cell. In this case, the extraction efficiency is given by the ratio of the aperture area to the total inner surface of the cell. In our cell this is approximately 1%. In the limit of a fully hydrodynamic beam, the molecules are swept out entirely by the flow of helium. Here, the extraction efficiency can be 100%. The extraction efficiency can be characterised by the dimensionless parameter

$$\gamma_{\mathrm{cell}} \equiv \frac{\tau_{\mathrm{diff}}}{\tau_{\mathrm{extract}}}, \tag{3.8}$$

where τ_{extract} and τ_{diff} are the extraction and diffusion times respectively. When $\gamma_{\mathrm{cell}} \ll 1$, the diffusion to the walls is faster than the extraction from the cell, so the majority of molecules will stick to the cell walls and be lost. This "diffusion limit" characterises effusive beams. For $\gamma_{\mathrm{cell}} \gtrsim 1$, molecules are extracted out of the cell before reaching the cell walls and characterises a hydrodynamical beam. In our case, $\gamma_{\mathrm{cell}} \approx 1$ representing a beam hydrodynamically enhanced beam. For such a beam, the angular divergence is closer to that of a hydrodynamic beam and the lower end of our extraction estimate is relevant.

We note that the extraction time, diffusion length and molecular yield can be significantly

influenced by the position of the ablation laser on the target which can promote ablation material towards or away from the aperture of the cell. To achieve an extraction time of 6 ms, the effective cell length would need to be approximately halved.

3.3.2 Laser induced fluorescence

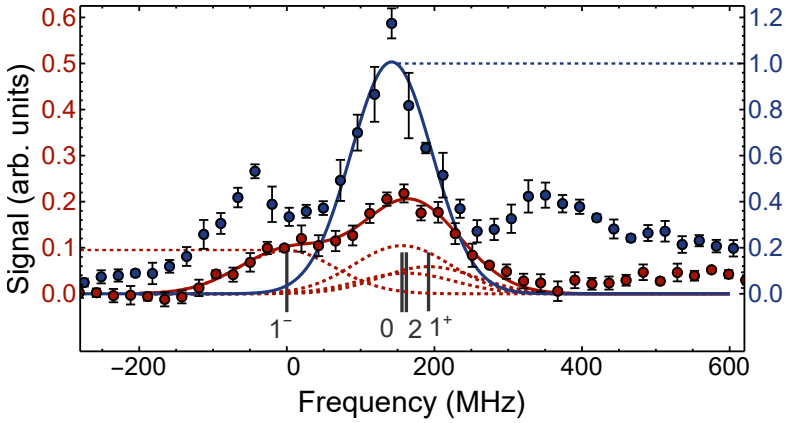

Figure 3.6: LIF fluorescence spectrum showing the P(1) transition with (red) a single frequency laser and (blue) sidebands applied to the laser to address the hyperfine structure.

Although absorption measurements inside the buffer gas cell provide a good estimate of the molecular yield inside the cell, the beam propagation further downstream can be altered by the large density of helium near the cell aperture as well as the second stage of the cell. It is therefore desirable to detect the molecules in a region further downstream where the trap will be located. Molecular sources, however, typically do not produce the required density to perform these absorption measurements far from the cell. Instead we detect molecules 85 cm away by laser induced fluorescence. The flux of molecules can be determined from the signal recorded by the PMT. The measured count rate on the PMT, $\dot{N}$, is related to the actual photon emission rate, $\dot{N}_0$, by

$$\dot{N}_0 = \frac{\dot{N}}{\mathcal{T}\eta\Pi} \tag{3.9}$$

where $\mathcal{T}$ is the loss in the collection optics, η is the quantum efficiency of the PMT (10%) and Π is the geometric collection probability (12%). Each molecule will on average emit $\mathcal{N}$ photons. The molecular beam diverges from the source and is very large by the time it reaches the detector, so we detect only a small part of it. The detected solid angle is determined by the

elliptical segment area restricted by the distance we image in one dimension (≈ 5 mm) and the laser diameter (3.5 mm $1/e^2$) in the other dimension. We estimate a solid angle of $\Omega = 10^{-5}$. The expression for the molecular flux, in units of molecules per steradian per second, is then

$$\dot{N}_m = \frac{\dot{N}_0}{\mathcal{N}\Omega}. \tag{3.10}$$

We detect the molecules on the P(1) line, and address all the hyperfine components simultaneously, so a molecule will scatter photons until it is optically pumped to $X^2\Sigma^+(v = 1)$, or until it leaves the laser beam. If the molecules are pumped to $X^2\Sigma^+(v = 1)$, the mean number of scattered photons is 14. This is the maximum value that $\mathcal{N}$ can take. The scattering rate may not be high enough to reach this maximum, so we determine the number of photons scattered per molecule, $\mathcal{N}$, by scanning a single frequency 552 nm laser across the P(1) rotational line and comparing the maximum signal to that obtained when the same rotational line is scanned with frequency sidebands addressing the hyperfine structure in the ground state. Figure 3.6 shows a frequency scan across the P(1) transition. The red curve is obtained using a single frequency. The blue curve is obtained with all hyperfine sidebands applied. The position of the hyperfine ground states are shown in grey. We estimate the number of photons scattered per molecule by comparing the signal obtained from $F = 1^-$ molecules scattering on resonance to that obtained with the laser resonant with all hyperfine components at once. The $F = 1^-$ state is sufficiently far from neighbouring hyperfine states that it can be resolved within the observed broadening. Additionally, it does not have dark states for linear polarisation - all m_F sublevels can be excited by our laser. The available laser power is sufficient to saturate the hyperfine transition from $F = 1^-$. The probability that a molecule excited to the $A\,^2\Pi_{1/2}$ state will decay back to the $F = 1^-$ state is 0.4. Each molecule in the $F = 1^-$ state will scatter on average $\frac{1}{1-0.4} \approx 1.7$ photons. The number of photons scattered per molecule, $\mathcal{N}$, with our laser beam when all sidebands are applied is then given by the ratio of the heights of the two peaks highlighted in figure 3.6 plus a factor to account for the ratio increase in population. We assume that the molecules are distributed equally among all m_F sublevels such that the ratio of molecules in $F = 1^-$ is 1/4 of the total ground state population. We therefore find the

number of photons scattered as $\mathcal{N} = \frac{1.7}{4} * 11 \approx 5$ photons per molecule. This is smaller than the maximum fluorescence yield, showing that we are not saturating the transition.

The flux of molecules per shot can then be obtained by integrating Eq. 3.10 over the time of flight profile. The parameters used to obtain the time of flight profile in figure 3.5 give a molecular flux of 1.5×10^{10} molecules $\mathrm{sr}^{-1}\mathrm{pulse}^{-1}$ as measured 0.85 m downstream. The angular divergence for an effusive beam is 120° giving a subtended solid angle of 0.75π [76]. For a hydrodynamic beam the divergence will approach $\approx 2\sqrt{\frac{m_{\mathrm{He}}}{m_{\mathrm{YbF}}}}$ and a solid angle $\approx \pi\frac{m_{\mathrm{He}}}{m_{\mathrm{YbF}}} = 0.07$ sr. Assuming an angular divergence of 0.1-1 sr, the number of molecules in the beam is in the range 1.5×10^9 - 1.5×10^{10}. Earlier, we estimated via in-cell absorption that the number of molecules produced in the cell is about 1.7×10^{11}, implying an extraction efficiency in the range 0.9% - 9%.

3.4 Doppler velocimetry

We now turn our attention to determining the forward velocity of the beam. Doppler sensitive LIF spectroscopy with an angled probe laser allows velocity selective detection of molecules arriving at our detector. Figure 3.7 displays our method for determining the longitudinal velocity distribution. The time of flight profile (figure 3.7(a)) is gated into 1 ms wide time bins. We correlate the arrival times of the molecules in these time bins with their mean velocity by comparing the Doppler shifted resonance of a probe laser angled at 60° to the direction of motion compared to that of a perpendicular probe laser. The two probe lasers are scanned about 300 MHz. Two examples of these spectra from different time bins are shown in figure 3.7(b,c)). The blue/red line indicates the scan obtained with the perpendicular/angled probe laser. The frequency shift, $\Delta\nu$, between the two probe beam scans can be related to a velocity, v by

$$v = \frac{\Delta\nu\, c}{\nu_0 \cos(60°)}, \tag{3.11}$$

where ν_0 is the orthogonal resonant frequency and c is the speed of light. The arrival time t as a function of the mean forward velocity, v, is shown by the points in figure 3.7(d). Assuming the molecules all leave the cell at the same time t_0 and travel at constant velocity once they have left

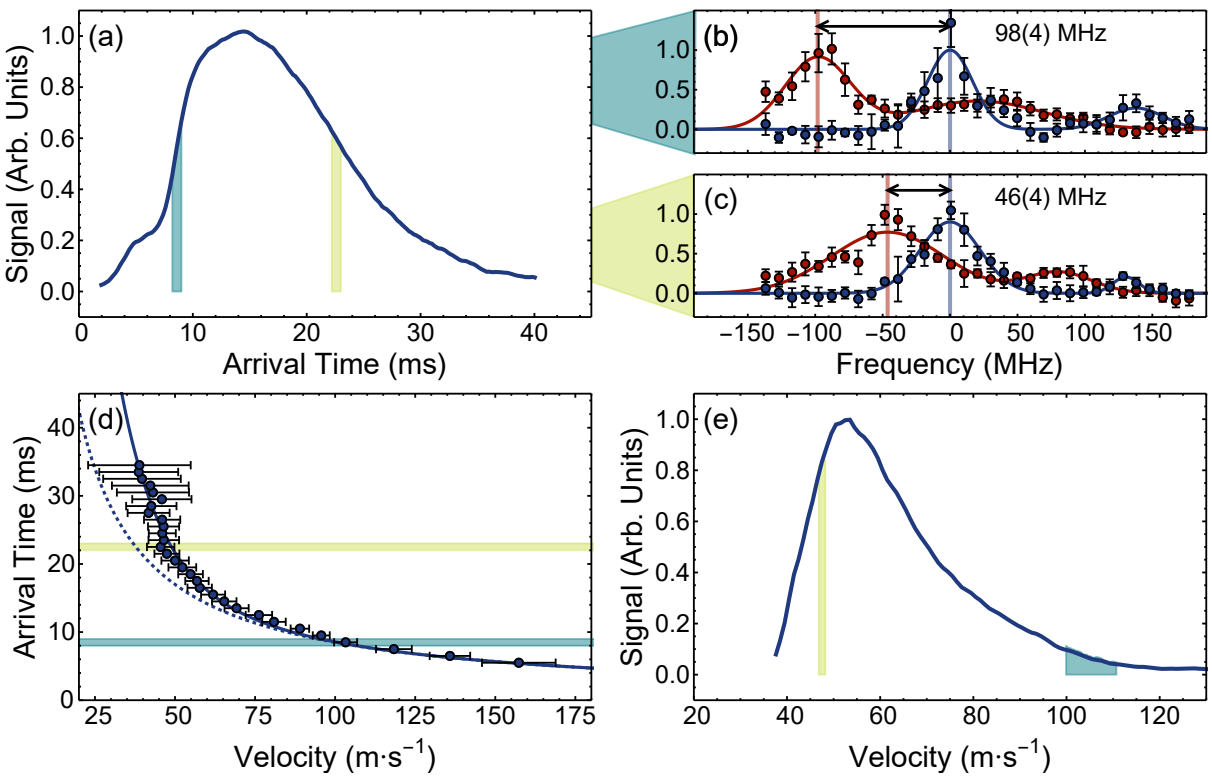

Figure 3.7: Doppler sensitive laser-induced fluorescence spectroscopy to determine the longitudinal velocity distribution of molecules in the cryogenic buffer gas beam. (a) A time-of-flight profile is divided into equal time bins. (b,c) An angled/perpendicular probe laser is scanned across the P(1) resonance, shown in red/blue for two example time gates. The lines are fits to a sum of two Gaussians. (d) Points: velocity (v) of molecules as a function of their arrival time (t). Dashed line: fit to $t = d/v$. Solid line: fit to $t = d/v + t_0(v)$ where $t_0(v) = A\exp(-v/\tau_v)$. (e) Velocity distribution.

the cell, we can write $t = d/v + t_0$ where $d = 85$ cm is the distance from the exit of the cell to the detector. A fit of the data to this model is shown as a dashed blue line in figure 3.7(d) with t_0 set to zero. In reality, we observe a strong velocity dependence on the exit times (see section 3.4.2). This can be seen from figure 3.7(d) where the data points at low velocity lie systematically above the model. To account for this, we model t_0 as $t_0(v) = A\exp(-v/\tau_v)$, where A and τ_v are free fitting parameters. This model was chosen on its empirical performance in fitting the observed data. A fit of the data to this updated model is shown as a solid blue line in figure 3.7(d). To construct the velocity distribution, we take velocity bin v of width δv, determine the width δt of the equivalent time bin using the fit, count the number of molecules arriving within this time interval, and assign them all to this velocity bin. This is an approximate procedure that works well when the range of velocities in each time bin is small. Figure 3.7(e) shows the velocity

distribution determined this way. It peaks at 53 m s^{-1} and has a full width at half maximum (FWHM) of around 28 m s^{-1}.

3.4.1 One-stage and two-stage cells

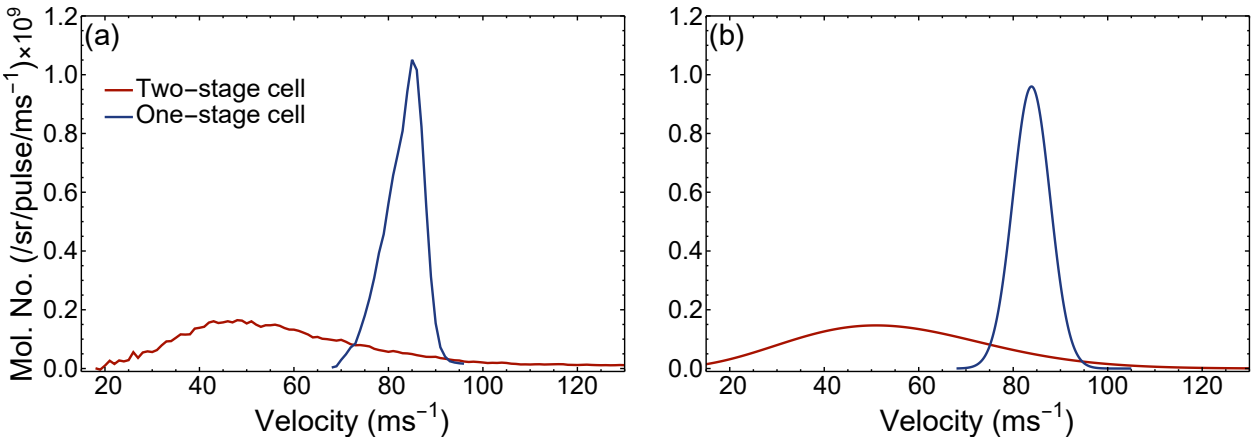

Figure 3.8: (a) Measured velocity distributions for the one-stage and two-stage cells. Ablation energy is 49 mJ and helium flow rate is 2 sccm. (b) Result of fitting Eq. (3.12) to the one-stage data and Eq. (3.13) to the two-stage data.

In the effusive regime, there are no collisions near the aperture of the cell and the forward velocity of the YbF molecular beam just samples the velocity distribution of the YbF molecules thermalised to the temperature of the buffer gas. The most probable forward velocity, $v_{f,\mathrm{eff}}$, of the molecular beam is given by $v_{f,\mathrm{eff}} = \sqrt{2k_B T_{\mathrm{He}}/m_{\mathrm{YbF}}}$, where T_{He} is the temperature of the buffer gas and m_{YbF} is the mass of a YbF molecule. In the intermediate regime, the molecules undergo collisions with the buffer gas. Collisions near the aperture are primarily in the forward direction (since there is near vacuum on one side of the aperture). This increases the longitudinal velocity of the heavy YbF molecules to that of the light buffer gas species. The YbF molecules then have a velocity close to that of the helium atoms, $v_{f,\mathrm{hydro}} = \sqrt{2k_B T_{\mathrm{He}}/m_{\mathrm{He}}}$, where m_{He} is the mass of the buffer gas atom. At a temperature of 1.8 K, the most probable velocity for YbF is $v_f = 13$ m/s compared to $v_f = 87$ m/s for He. A hydrodynamic beam has greater extraction efficiency but also higher velocity. Herein lies the principle behind the two stage cell. A first stage cell operating near hydrodynamically extracts the molecules. This gives high extraction efficiencies but also increased velocity due to collisional boosting near the

aperture of the cell. A second 'slowing stage' is therefore added in front of the first stage to slow down the boosted molecules. The density of buffer gas in the second stage can be controlled through two venting ports on the side of the cell, the open area of the mesh at the front of the cell and the gap between the first and second stages of the cell. These parameters are tuned such that the mean free path in the second stage is on the order of a couple mm such that molecules undergo just enough collisions to thermalise the boosted molecules and produce a near effusive beam.

A comparison of the longitudinal velocity distribution of our cryogenic buffer gas cell with and without the second 'slowing cell' is shown in figure 3.8(a) when the ablation energy is 49 mJ and the helium flow rate is 2 sccm. The distribution from the one-stage cell peaks at 86 m s^{-1} and has a width of only 7.9 m s^{-1}. The addition of the second stage reduces the peak of the velocity distribution to 49 m s^{-1} and increases its width to 38 m s^{-1}.

The single stage source peak velocity is close to the case we would expect for a near 'fully boosted' effusive beam (assuming the buffer gas atoms have thermalised to 1.8 K). Lu et al observed a similarly 'fully boosted' beam for the case of CaH with the same cell design [82]. The distribution of the velocities, however is remarkably narrow and much more characteristic of a supersonic beam. It is common to model the velocity distribution of a supersonic beam as

$$f_{\mathrm{ss}}(v) = Av^3 \exp\left(-\frac{M(v-v_0)^2}{2k_{\mathrm{B}}T_{\mathrm{trans}}}\right), \tag{3.12}$$

where A is a normalization constant, M is the mass of the molecule, v_0 is the central velocity and T_{trans} is the translation temperature of the beam [76]. The blue distribution shown in figure 3.8(b) is the best fit of the one-stage data to this model. The best fit parameters are $v_0 = 83.3 \pm 0.2$ m s^{-1} and $T_{\mathrm{trans}} = 0.36 \pm 0.04$ K. The translational temperature is below the cell temperature, which is typical for supersonic beams which cool as they expand from the higher-pressure region of the cell to the low pressure region beyond. We have checked the width of the distribution by examining the widths of the spectral features (like those in figure 3.7(b,c)) after integrating over the entire time-of-flight profile (instead of taking narrow time windows). The rms width is 16.9 ± 0.6 MHz for the 90° probe and 16.8 ± 0.7 MHz for

the 60° probe, showing that there is no measurable Doppler broadening. The uncertainties on this measurement translate to an upper limit of 15.6 m s^{-1} for the FWHM of the velocity distribution.

The addition of the second stage reduces the peak of the velocity distribution to 49 m s^{-1}. This is in a regime that is not at the effusive limit but lower nevertheless than that expected from a hydrodynamic beam. The width of the distribution is 38 m s^{-1} and there is a substantial flux of molecules with speeds below 30 m s^{-1}. We model this near-effusive beam, with the velocity distribution

$$f_{\text{eff}}(v) = Bv^3 \exp\left(-\frac{m^* v^2}{2k_{\text{B}}T}\right), \tag{3.13}$$

where B is a normalization constant, T is the cell temperature and m^* is an effective mass [76]. The red distribution in figure 3.8(b) is the best fit of the two-stage data to this model. The fit gives $m^* = 17.3 \pm 0.2$ u, reflecting the observation that the beam is slower than an effusive beam of He but faster than an effusive beam of YbF, and implying that there are still collisions between the two species in the vicinity of the exit aperture. Surprisingly, the two sources produce similar fluxes in $N = 1$: $(9.8 \pm 1.6) \times 10^9$ molecules/sr/pulse for the one-stage cell and $(8.0 \pm 1.3) \times 10^9$ molecules/sr/pulse for the two stage cell as measured 0.85 m downstream. The reduced divergence and increased extraction efficiency that accompanies more hydrodynamic beams would lead to a higher expected beam intensity from the one-stage cell compared to that of the two stage cell. A possible explanation for this discrepancy is that, in addition to translational cooling, there may be substantial rotational cooling in the one-stage cell. This is typical of hydrodynamic sources operating near supersonically [76]. The majority of the flux from the one-stage cell may therefore be in the ground rotational state, $N = 0$. We also make note that the uncertainties on the fluxes are estimated by averaging shots taken on the same day. We tend to find that the total flux decreases and the peak velocity increases on a timescale of 2-3 weeks. Source parameters are typically recovered when the source is opened, cleaned and re-assembled. The measurements reported here and in subsequent sections required a complete disassembly of the source, and some source properties can vary between one assembly and the next. Nevertheless, we believe all trends reported here are reproducible.

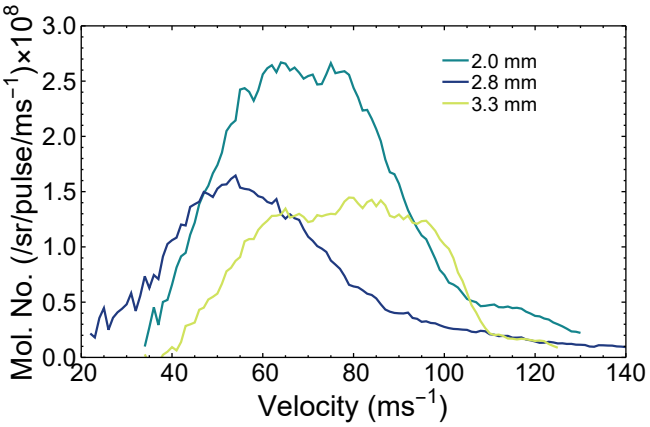

Figure 3.9: Velocity distributions for three different gaps between the first and second stages. Ablation energy is 49 mJ and helium flow is 2 sccm.

The parameters of the beam depend on the size of the gap between the first and second stages of the cell. Helium flows out of this gap, so the gap size is a parameter that controls the relative helium density in the two cells. A smaller gap gives a higher helium density, and thus a shorter mean free path, in the second stage. Figure 3.9 shows the velocity profiles for three different gap sizes. The slowest beams are formed when the gap is 2.8 mm. With a smaller gap (2 mm) the helium beam tends more towards the supersonic regime and the molecules are partly entrained in this helium flow, giving a faster beam. At larger gap sizes (3.3 mm) there are not enough collisions in the second stage to slow down the molecules coming out of the first stage, again giving a faster beam. Note that, of the three gaps used, the 2.8 mm gap gives the lowest total beam flux, but gives the highest flux of molecules below 40 m s^{-1}. Thus, the best choice of gap depends on the quantity to be optimised. The data shown in figure 3.9 is for a particular choice of ablation energy and helium flow, but we found that these general trends hold for all flows between 1 and 10 sccm and all ablation energies between 49 and 88 mJ (see 3.4.4).

3.4.2 Exit times

We saw from figure 3.7(d) that the data points at low velocity lie systematically above a best-fit model where the molecules are assumed to exit at the same time t_0. This suggests that this model is not quite accurate. Since we measure v for each value of t, and the distance $d = 0.85$ m is known, we can determine the exit time as a function of velocity from the measured data,

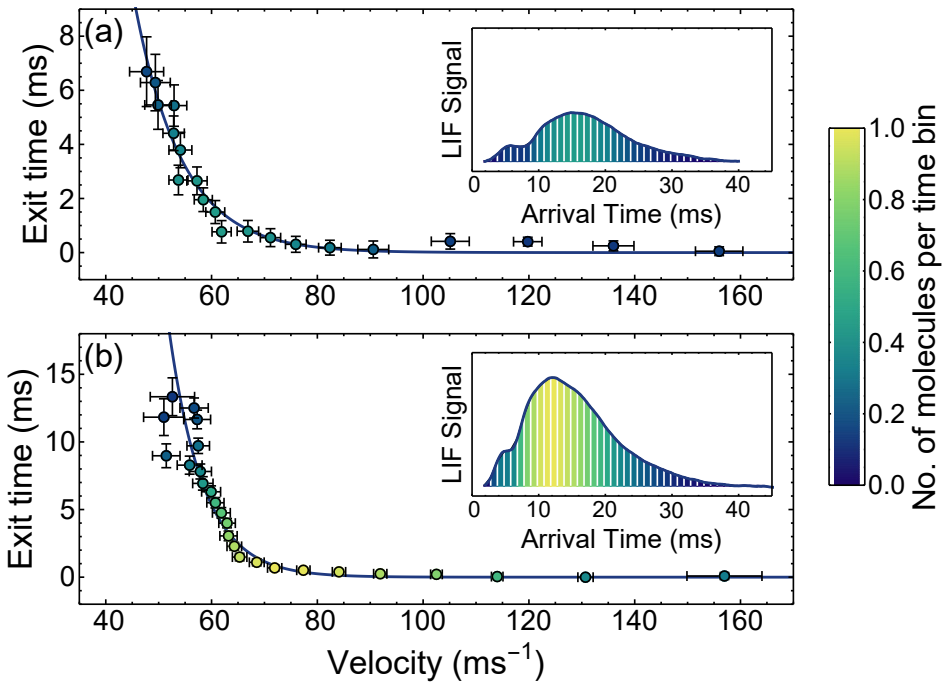

Figure 3.10: Exit time from the cell versus velocity. (a) Ablation energy: 69 mJ, helium flow: 8 sccm. (b) Ablation energy: 88 mJ, helium flow: 10 sccm. Insets show the corresponding time-of-flight profiles and colour indicates the relative number of molecules in each time bin. The solid line is a fit to the data of the form $A\exp(-v/\tau_v)$.

using $t_0(v) = t - d/v$.

Figure 3.10 shows $t_0(v)$ determined this way for 1 ms wide time bins. The the time-of-flight profiles are shown as insets. The colour coding indicates the number of molecules at each velocity or arrival time. In figure 3.10(a) the ablation energy is 69 mJ and the helium flow is 8 sccm, which produces a velocity distribution peaked at 63 m s^{-1}. In figure 3.10(b) the ablation energy is increased to 88 mJ and the helium flow increased to 10 sccm, producing a more intense beam with a peak velocity at 80 m s^{-1}. In both cases, the exit times fall into two distinct groups. For molecules in the beam with speeds between 45 and 65 m s^{-1}, the exit time correlates strongly with speed with the slower molecules exiting later. The exit times are systematically longer at the higher flow rate where the helium density is higher. Molecules travelling faster than 65 m s^{-1} leave the cell quickly ($t_0 < 1$ ms) and there is little correlation between the velocity and the exit time. The solid lines in figure 3.10(a)(b) are fits to $A\exp(-v/\tau_v)$.

3.4.3 Temperature dependence

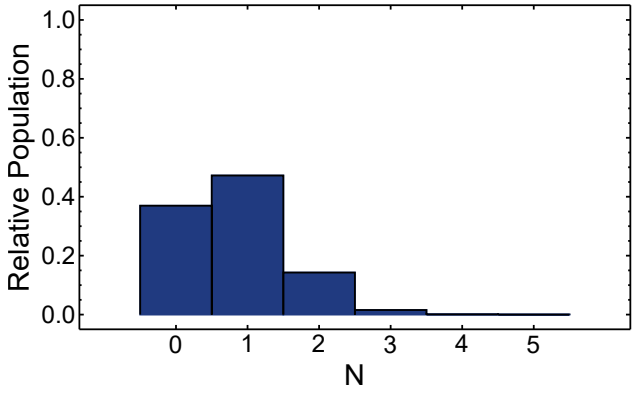

Figure 3.11: Relative thermal population distribution in the first five rotational levels of $X\,^2\Sigma^+$ at 1.55 K.

Cooling the internal degrees of freedom through collisions with the buffer gas inside the cell is critical for achieving a high flux beam of molecules in the same quantum state. Our laser cycling transition is the P(1) line of the $A^2\Pi_{1/2} \leftarrow X^2\Sigma^+$ transition. We therefore wish to maximise the rotational population in the $N = 1$ state. The distribution of population amongst rotational states in the $X^2\Sigma^+$ state of YbF is determined by the Maxwell-Boltzmann equation

$$P(N) = \frac{2N+1}{Z} \exp\left[-\frac{E_{\text{rot}}(N)}{k_B T}\right], \tag{3.14}$$

$$Z = \sum_N (2N+1) \exp\left[-\frac{E_{\text{rot}}(N)}{k_B T}\right], \tag{3.15}$$

where $E_{\text{rot}}(N)$ is the energy of the Nth rotational level, T is the temperature, k_B is the Boltzmann constant and Z denotes the partition function. The population in $X^2\Sigma^+(N = 1)$ is maximised at a temperature $T = 1.55\ K$. This represents our desired operational temperature. Figure 3.11 shows the relative populations of rotational levels at 1.55 K. Approximately 50% of the total population occupies the $N = 1$ level. In this section we describe the effect that the temperature of our buffer gas cell has on the parameters of the molecular beam.

Our two stage buffer gas cell is anchored to a copper plate that is cooled by a helium pumped reservoir to a base temperature of 1.8 K (see figure 3.1). The cell, together with the copper plate it's mounted on, are thermally separated from the remainder of the cryocooler such that the

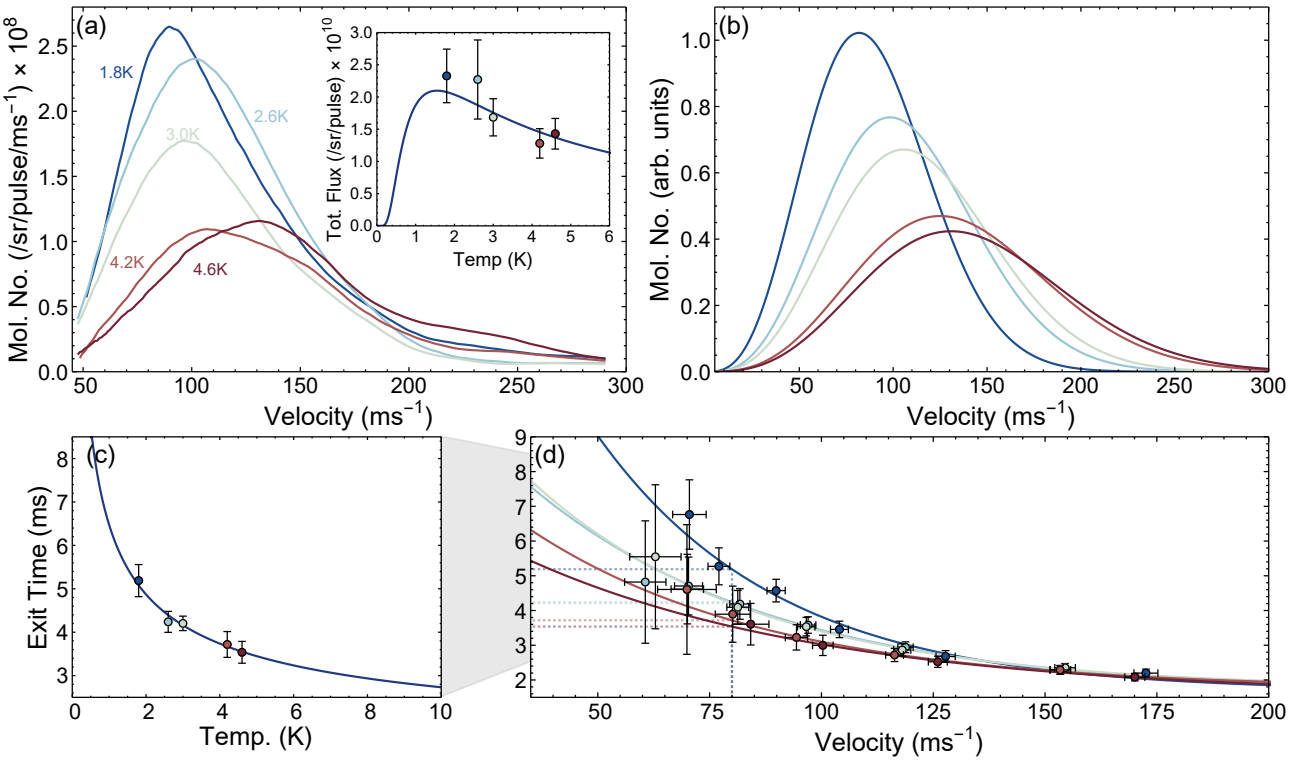

Figure 3.12: Temperature dependence of velocity distributions. (a) Measured YbF velocity distributions for various cell temperatures, T. Inset, points: total molecular flux. Inset, line: fit to a Maxwell-Boltzmann distribution for the population in $N = 1$. (b) Modelled velocity distributions at each cell temperature, assuming an effusive beam with an effective mass of $m^* = 6.7$ u. (c) Points: Exit times as a function of temperature for molecules travelling at 80 m/s. Line: Fit to $t_0 = t_{00} + A/\sqrt{T}$. (d) Points: Exit times as a function of velocity for different cell temperatures. Lines: Single exponential decays.

temperature of the cell can be independently controlled without affecting the temperature of the 4 K or 50 K stages of the cryocooler. The temperature of the cell is therefore independent of the temperature of the charcoal shields which are attached to the 4 K stage of the cryocooler. This allows us to decouple effects of the cell temperature with those of the charcoal shields which absorb more efficiently at lower temperatures. A heater and thermocouple placed on the copper plate and connected to a feedback loop stabilise the temperature within 0.2 K of a target value. Figure 3.12(a) shows velocity distributions measured at five different cell temperatures. For these measurements, the ablation energy is 80 mJ, resulting in faster beams than the one shown in figure 3.8. The ablation power and gas flow settings into the cell were chosen such that there was still significant molecular flux at temperatures around 4 K. Lowering the temperature shifts the peak of the velocity distribution to lower values, increases the total flux of molecules

in $N = 1$, and additionally increases the flux at low velocity. The inset in Figure 3.12(a) shows the total flux of molecules in $N = 1$ determined by integrating the velocity distributions. The line is a fit to the population expected in $N = 1$ according to a Maxwell-Boltzmann distribution (Eq. 3.14), where the amplitude is a free fitting parameter. This fits well, implying that the total flux across all rotational states is independent of cell temperature. Figure 3.12(b) shows velocity distributions calculated for effusive beams (Eq. 3.13) at each of these cell temperatures, where we have fixed the effective mass to $m^* = 6.7$ u in all cases and assumed the population in $N = 1$ follows the Maxwell-Boltzmann distribution for each cell temperature. We see that this simple model provides a reasonably good description of the velocity distribution for all the cell temperatures studied. Figure 3.12(d) shows the exit times as a function of velocity at each temperature. We fit single exponential decays to the data as in section 3.4.2. As the cell temperature increases, the exit times get shorter. This can be seen more clearly in figure 3.12(c) which plots the exit time as a function of temperature for molecules travelling at 80 m s^{-1}. The time taken to extract molecules from the cell should scale inversely with the velocity of the buffer gas (Eq. 3.7), which in turn is proportional to the square root of the cell temperature, T. Thus, we fit the model $t_0 = t_{00} + A/\sqrt{T}$ to the data. This fits well, as shown by the line in figure 3.12(c).

3.4.4 Optimisation

The velocity distribution and total flux of molecules in the beam can be influenced by many parameters in the cryogenic buffer gas source. Here, for the two-stage cell, we have measured velocity distributions across a wide range of parameters: helium flows in the range 1-10 sccm, ablation energies in the range 49-88 mJ and three gap sizes from 2.8 to 3.3 mm. Figure 3.13 summarizes the results of these measurements. The figure shows the total flux in $N = 1$, the peak velocity, and the flux of molecules below 30 m s^{-1}, all as functions of ablation energy and helium flow, and for three different gap sizes. For all gap sizes, the total flux is near linearly proportional to the ablation energy, and in general we do not reach a maximum within the ablation energies used here. Extrapolating the ablation energy to zero yield, we find a

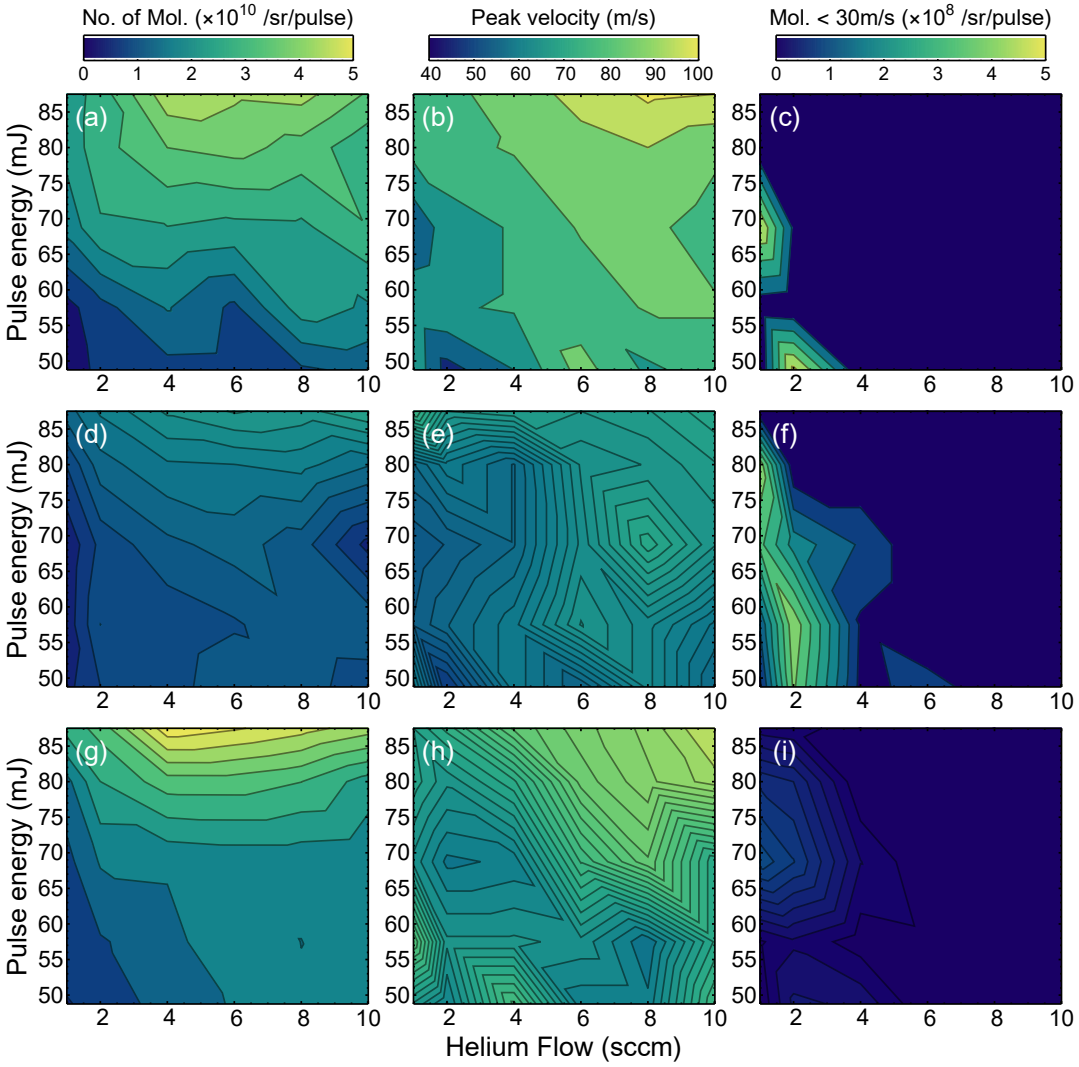

Figure 3.13: Molecular flux, peak velocity and flux of molecules with speeds below 30 m/s, as a function of ablation pulse energy and helium flow rate. (a)-(c) 2.0 mm gap between two stages of the cell. (d)-(f) 2.8 mm gap. (g)-(i) 3.3 mm gap.

threshold energy of around 10-15 mJ. For the 2.0 mm gap, the total flux and the peak velocity both increase with ablation energy. The flux does not depend strongly on the helium flow, whereas the peak velocity tends to increase with helium flow. The flux of molecules below 30 m s^{-1} is only substantial in the corner of the parameter space where both the flow and ablation energy are low. For the 2.8 mm gap the total flux has only a weak dependence on helium flow and is relatively constant for ablation energies up to 70 mJ, but then increases for higher energies. The peak velocity has little dependence on the ablation energy but tends to increase with flow, though less steeply than for the 2 mm gap. For flows below 3 sccm there is a substantial flux with speeds below 30 m s^{-1} at all ablation energies below 80 mJ. The trends

for the 3.3 mm gap are similar to those for the 2.8 mm gap. The total flux can be larger, but the peak velocity is significantly higher and there are very few molecules below 30 m s^{-1} across the entire parameter range. To maximize the flux below 30 m s^{-1}, we find it best to use a gap of 2.8 mm, a flow of 2 sccm and an ablation energy of 55 mJ. Under these conditions we have $\approx 4 \times 10^8$ molecules/sr/pulse travelling at less than 30 m/s.

3.5 Summary

The aim of this chapter was to produce a buffer gas cooled, high-flux, slow-velocity beam of YbF molecules suitable for laser slowing. In order to determine the flux of molecules in the beam, laser induced fluorescence from a transversely intersecting laser beam was used to image molecules 0.85 m away from the cell. The density of molecules inside the cell was also probed using absorption spectroscopy. We find a density of 1.7×10^{11} molecules inside the cell. The longitudinal velocity distribution of the molecules was measured using a Doppler sensitive angled probe laser to record laser induced fluorescence. The velocity distributions of the molecules can be used to calculate exit times out of the source. We observe typical exit times between 5-10 ms depending on the source parameters used, consistent with those determined from absorption measurements. Our cryogenic buffer gas source is the first such source for YbF that includes a second slowing stage and operates at 1.8 K. We characterised both the temperature dependence on the total flux, the forward velocity distribution as well as exit times in the cell. A study of part of the parameter space for this cell was made. We find operating the source at 2 sccm and 55 mJ pulse energy produces 1.5×10^{10} molecules/sr/pulse with a peak velocity of 50 m/s with more than 4×10^8 molecules/sr/pulse travelling at less than 30 m/s. The expected capture velocity of a YbF MOT is around 10 m/s. The measured velocities of our molecules out of the cryogenic buffer gas source remain above the limit where direct loading of a MOT would be possible but represent a significant improvement on supersonic sources as well as all other cryogenic buffer gas sources of YbF [62] which typically produce beams with much higher velocities in the range 150 - 350 m/s and, unlike our source, have no significant population at velocities below 30 m/s.

Chapter 4

Optical cycling and slowing

4.1 Introduction

In order to efficiently trap molecules in a magneto-optical trap (MOT), we wish to maximise the number of molecules below the capture velocity of the MOT, typically 10-20 m/s [83–85]. State of the art molecular MOTs typically capture $\sim 10^5$ molecules [86, 87]. We generally detect between 10^5 and 10^6 molecules downstream of the cryogenic buffer gas source. In order to capture a similar number of molecules in the MOT, high efficiency laser slowing is needed.

Atomic MOTs, typically containing 10^8 atoms, can be loaded from background gas in cases where sufficient atoms in the gas travel below the capture velocity of the MOT [88, 89]. Where the vapour pressure is insufficient, radiation pressure from a counter propagating laser beam can be used to reduce the velocity of a beam of atoms. To account for the changing Doppler shift as the velocity is reduced, a Zeeman slower can be used to bring the atoms back into resonance or the frequency of the laser itself can be changed, either by chirping or frequency broadening. The density of molecular MOTs achieved so far is much lower than that of their atomic counterparts [90, 91]. This is in part because of inefficiencies in bringing the molecular beam to velocities which are slow enough to capture. For molecules, optical cycling requires a rotationally closed transition. Successful MOTs of CaF, SrF, YO and BaF as well as the proposed YbF MOT, all cycle photons on the P(1) rotational line of $A\,^2\Pi_{1/2} \leftarrow X\,^2\Sigma^+$ [38, 90, 91]. This transition has

smaller angular momentum in the excited state than the ground state, therefore the number of magnetic sublevels in the excited state, n_e, is smaller than that in the ground state, n_g. The scattering rate, R_{scat}, for such a system is given by [31]

$$R_{\text{scat}} = \frac{\Gamma_{\text{eff}}}{2} \frac{s}{1 + s + 4\delta^2/\Gamma^2}, \tag{4.1}$$

where δ is the detuning of the laser and Γ the linewidth of the transition. The saturation parameter, s, is defined as $s = I/I_{\text{sat}}$ where I is the intensity of the laser driving the transition and $I_{\text{sat}} = \pi hc\Gamma/(3\lambda^3)$, where λ is the wavelength of the transition. Γ_{eff} is the effective spontaneous decay rate, which is given by

$$\Gamma_{\text{eff}} = \frac{2n_e}{n_e + n_g}\Gamma. \tag{4.2}$$

For zero laser detuning and high laser intensity, the scattering rate has a maximum value

$$R_{\text{scat}}^{\text{max}} = \frac{\Gamma_{\text{eff}}}{2} = \frac{n_e}{n_e + n_g}\Gamma. \tag{4.3}$$

Even before considering losses to other vibrational states, the maximum scattering rate is reduced to $\Gamma/4$ for ^{174}YbF and even lower for isotopologues with higher nuclear spin [92]. Comparatively, for atomic rubidium on the D2 line $R_{\text{scat}}^{\text{max}} = \Gamma/2$. The need to repump losses to other vibrational states further reduces the scattering rate. The low scattering rate can lead to large slowing distances and a reduced capture velocity compared to that for atoms. Nevertheless, molecules have been both efficiently slowed and trapped in MOTs. Zeeman slowers for molecules are challenging and so far have low efficiencies compared to frequency chirping or frequency broadening [93, 94]. SrF, CaF, YO and CaOH have all been slowed by radiation pressure and captured in a MOT [68, 84, 90, 95–98]. An alternative to radiation pressure slowing is Zeeman-Sisyphus slowing which only requires scattering a small number of photons [99]. This technique was first demonstrated for polyatomic CaOH [100]. Zeeman-Sysiphus deceleration has also been demonstrated for YbOH and is a promising option for slowing complex molecules which can only scatter a few photons [101].

4.1.1 Optical cycling scheme in YbF

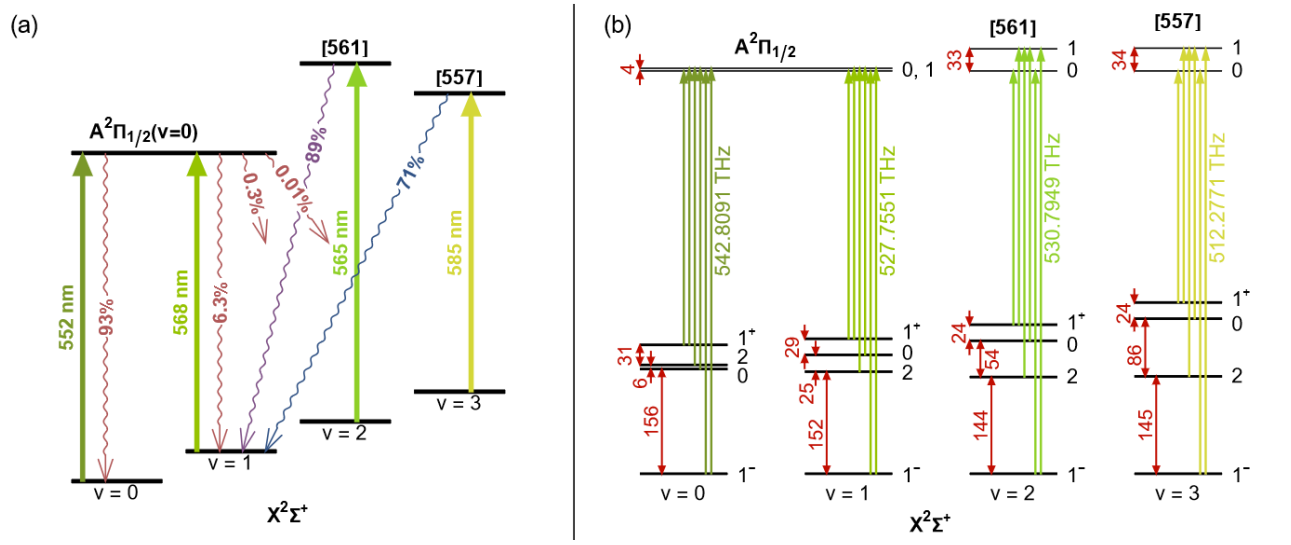

Figure 4.1: Relevant energy levels for lasing slowing of YbF. [557] and [561] are mixtures of the $A\,^2\Pi_{1/2}(v' = 1)$ state and a different electronic state arising from inner-shell excitation of the molecule. Solid arrows indicate repump lasers in use on our experiment along with their wavelengths. Squiggly lines represent spontaneous emission with the relevant branching ratios indicated. The hyperfine structure is shown in (b). The splittings between levels (in MHz) are indicated in red. Transition frequencies from $F = 1^-$ to $F' = 1$ are quoted in THz.

Figure 4.1 shows the relevant energy levels for optical cycling of YbF. The main optical cycling transition is $A\,^2\Pi_{1/2}(v' = 0, J' = 1/2) \leftarrow X\,^2\Sigma^+(v = 0, N = 1)$ which has a natural linewidth of $\Gamma = 2\pi \times 5.7$ MHz [102], a saturation intensity of $I_{\text{sat}} = \pi hc\Gamma/(3\lambda^3) = 4.4\ \text{mW/cm}^2$ and a photon emission recoil velocity of 3.7 mm/s. In order to reduce the forward velocity of a molecule travelling at 80 m/s to within 10 m/s it has to undergo $\approx 10^4$ photon scattering events. Although the angular momentum and parity selection rules mean that our optical cycling transition is rotationally closed, losses to other vibrational states have to be addressed. The relevant branching ratios are indicated in figure 4.1 [102–104]. To keep molecules in the scattering cycle, repump lasers are used to drive equivalent rotational lines from $X\,^2\Sigma^+(v = 1, 2, 3)$. With the omission of a $X\,^2\Sigma^+(v = 3)$ repump, this photon cycling scheme has been successfully used to demonstrate 1D and 2D transverse cooling of YbF [105, 106]. The $X\,^2\Sigma^+(v = 3)$ repump, although available, was found to not make significant difference in that work. However, far more photons need to be scattered for radiation pressure slowing than for transverse cooling. To reach the anticipated capture velocity of a MOT, all leaks greater than 10^{-5} have to be closed.

In this chapter we begin by simulating radiation pressure slowing using multi-level rate equations and demonstrate frequency chirped slowing of YbF as a viable method to bring molecules from our cryogenic buffer gas source to within the capture velocity of a MOT. We then start by investigating optical cycling on the P(1) transition of the 0-0 band of $A\,^2\Pi_{1/2}(v' = 0) \leftarrow X\,^2\Sigma^+(v = 0)$. We compare dark state destabilisation by magnetic field and polarisation modulation by measuring longitudinal pumping out of $X\,^2\Sigma^+(v = 0)$. We then proceed to add repump lasers sequentially and measure scattering rates with each laser. Finally, we demonstrate a measurable change in the longitudinal velocity of the molecular beam. This also provides an unambiguous measurement of our current photon cycling rate. We end this chapter with a discussion of remaining losses out of the optical cycle and consider methods to improve the observed slowing.

4.2 Simulating longitudinal laser slowing

Due to the complex structure of molecules, laser slowing involves multiple transitions driven by several frequencies. The success of laser slowing can therefore depend on many parameters, including the specific frequencies used to drive the transitions, the polarisation of the light, the dark state remixing rate, the frequency chirp rate (or frequency broadened spectrum) used as well as the phase space distribution of the molecules exiting the molecular source. In order to build an understanding of this parameter space, we test these ideas using Monte-Carlo trajectory simulations based on scattering rate equations. A semi-classical scattering rate model, such as that used here, does not take into account the evolution of dark states. A more complete but complicated picture can be obtained by using optical Bloch equations (OBEs) with the downside that the number of equations and parameters scale with the square of the number of considered levels [107]. Nevertheless, the rate equation model gives a good estimate of the scattering rate where the dark state remixing rate is near or larger than the scattering rate and cross-excitation from nearby transitions is negligible [31]. Simulations based on multi-level rate equations have been used to predict scattering rates in MOTs of SrF and

CaF[1] [95, 108].

Our approach therefore is as follows. We employ multilevel rate equations (MLREs) to predict the scattering rate as a function of laser intensity and detuning. A Monte-Carlo simulation of 10,000 molecules is then carried out to simulate laser slowing from a counterpropagating laser beam. In this section we begin with the construction of the MLREs and then present results of the Monte-Carlo simulations for the case of frequency chirped slowing.

4.2.1 Multi-level rate equations

We consider a molecule consisting of N_e excited states and N_g ground states. The scattering rate in this system is given by

$$R_{\text{scat}} = \Gamma n^e, \tag{4.4}$$

where n^e is the fraction of population that is in an excited state with lifetime Γ. To maximise the number of spontaneous scattering events, the population of molecules that are in the excited state should be maximised. The value of n^e depends on the intensity of the driving laser light, its detuning, its polarisation and the rate at which dark states are remixed. We now construct rate equations taking these parameters into account. Figure 4.2 shows the relevant energy levels in our MLRE model of the optical cycle in YbF. We consider both the $A\,^2\Pi_{1/2}(v = 0, J' = 1/2^+) \leftarrow X\,^2\Sigma^+(v = 0, N = 1)$ transition and the $A\,^2\Pi_{1/2}(v = 0, J' = 1/2^+) \leftarrow X\,^2\Sigma^+(v = 1, N = 1)$ repump but neglect further vibrational leaks. A discussion of the effect of leaks to $X\,^2\Sigma^+(v = 2)$ and $X\,^2\Sigma^+(v = 3)$ on the scattering rate is given later on. Our system contains a total of 28 states, 4 hyperfine excited states and 24 hyperfine ground states. The fraction of population in each excited state, u, is given by n^e_u. Similarly for each ground state, l, we label populations as n^g_l. Decay channels to $X\,^2\Sigma^+(v = 0)$ and $X\,^2\Sigma^+(v = 1)$ have different wavelengths, λ, and we allow the hyperfine structure in each transition to be driven by different frequency components so we further make the distinction $n^{g,0}_l$ and $n^{g,1}_l$ as states belonging to $X\,^2\Sigma^+(v = 0)$ and $X\,^2\Sigma^+(v = 1)$ respectively. We allow every hyperfine transition within the $A\,^2\Pi_{1/2}(v = 0, J' = 1/2^+) \leftarrow X\,^2\Sigma^+(v = 0, N = 1)$ transition and the

[1]Experimental values match simulations but with Γ_{eff} about half that predicted.

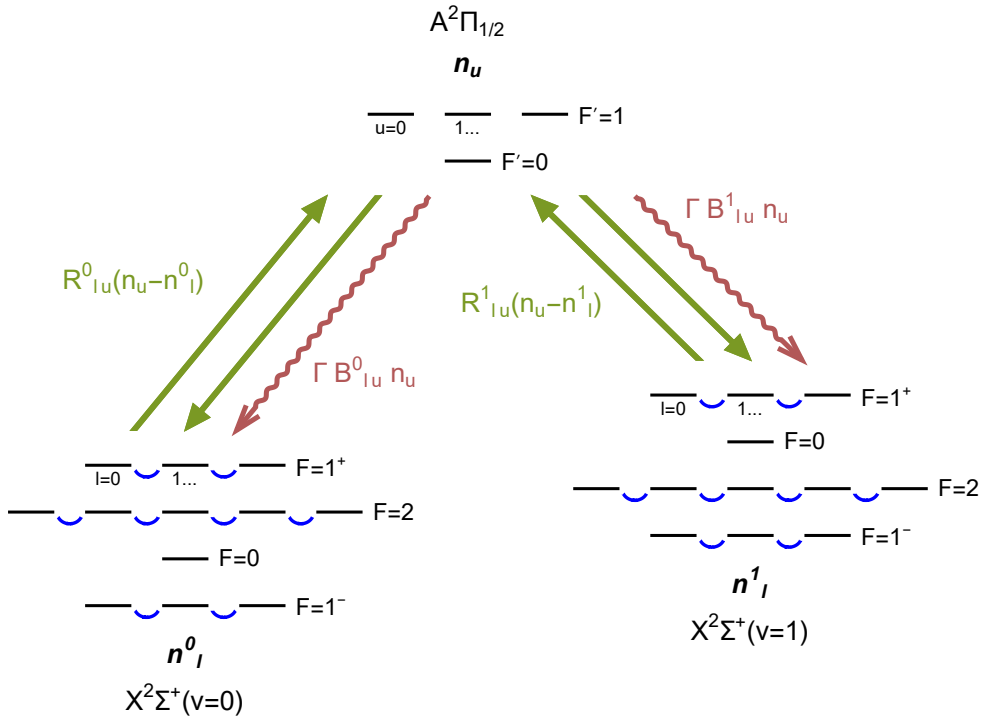

Figure 4.2: Energy levels considered in modelling the scattering rate in our slowing cycle. Stimulated absorption/emission between two states with populations n_u and n_l occurs at a rate R^0_{lu} and R^1_{lu} for $X^2\Sigma^+(v=0)$ and $X^2\Sigma^+(v=1)$ respectively. Similarly, spontaneous emission occurs at a rate ΓB^0_{lu} and ΓB^1_{lu}. Magnetic remixing is modelled as a population mixing between adjacent m_F states.

$A\,^2\Pi_{1/2}(v=0, J'=1/2^+) \leftarrow X\,^2\Sigma^+(v=1, N=1)$ to be driven by every component of the light addressing that band, each with its own Rabi frequency and detuning. However, light addressing the (0-1) band is entirely decoupled from that of the (0-0) band. For such coupling of energy states the rate of change of the population of a single ground state $\dot{n}_l$ is given by

$$\dot{n}^i_l = \underbrace{\sum_u R^i_{lu}\left(n^i_u - n^i_l\right)}_{\text{stimulated emission + absorption}} + \underbrace{\sum_u \Gamma B^i_{lu} n^i_u}_{\text{spontaneous decay}} + \underbrace{\sum_{l'} \frac{\omega^i_{l,l'}}{2\pi}\left(n^i_{l'} - n^i_l\right)}_{\text{magnetic field remixing}}, \tag{4.5}$$

where R_{lu} is the excitation rate between ground state l and excited state u, Γ is the total spontaneous emission rate of the $A\,^2\Pi_{1/2}(v=0, J'=1/2^+)$ state and B_{lu} is the branching ratio between ground state l and excited state u. The superscript, i, indicates the vibrational level in the $X\,^2\Sigma^+$ state and can be either 0 or 1. Although coherent dark states cannot be modelled with MLRE, the magnetic field remixing is added into the rate equation model as an extra term that varies populations between two ground states proportionally to their Larmor frequency,

$\omega_{l,l'}$. Similarly, for a single excited state the rate of change of the population is given by,

$$\dot{n}_u = \underbrace{-\Gamma n_u}_{\text{spontaneous decay}} + \underbrace{\sum_{i=0,1}\sum_{l} R^i_{lu}\left(n^i_l - n^i_u\right)}_{\text{stimulated absorption + emission}} \quad . \tag{4.6}$$

The excitation rate, R_{lu}, between two states l and u of either the (0-0) or (1-0) transition is given by,

$$R^{0/1}_{lu} = \frac{\Gamma}{2}\frac{I/I_{\text{sat}}}{1+4\delta^2/\Gamma^2}T^{0/1}_{lu} \tag{4.7}$$

where I/I_{sat} is the saturation parameter and is given by the ratio of the laser intensity, I, to the saturation intensity of the transition, I_{sat}; δ is the laser detuning and $T^{0/1}_{lu}$ is the normalised transition strength between two states. Here, I/I_{sat} is defined for a single sideband frequency. For multiple sidebands we sum over the different laser frequencies. This allows us to evaluate the scattering rate equations with arbitrary frequencies in the laser light addressing the (0-0) and (0-1) transitions. The transition strengths are calculated by finding the eigenvectors of the Hamiltonian for the rotational, hyperfine and Zeeman interactions in both the ground and excited states, and then calculating the transition dipole moments between these two sets of eigenvectors. The total scattering rate is obtained by numerically solving for the steady state excited populations and is given by

$$R_{\text{scat}} = \sum_u \Gamma n_u. \tag{4.8}$$

In the following, we solve the scattering rate equations for the system described in figure 4.2. Two lasers are used to drive our system. One is for the main optical cycling transition and another for the first repump transition. We wish to evaluate the case where the main laser is chirped but the vibrational repump is frequency broadened. Such a scheme has been successfully implemented in the laser slowing of CaF. The laser driving the (0-0) transition consists of three sideband frequencies. These are the same that have been used to address the hyperfine structure in the X state in the previous sections. The laser driving the (1-0) transition is frequency broadened to ∼300 MHz. Such a broadening, in practice, could be achieved by

two or more over-driven EOMs. Here, we model 10 sidebands of equal intensity spaced by 30 MHz. The laser light is assumed to be linearly polarised. Using these frequency configurations we solve the MLREs for laser intensities from 0 mW/cm^2 to 4000 mW/cm^2 and detunings of -300 MHz to 300 MHz sufficient to cover the Doppler shift of the molecules and any sideband broadening. This produces a scattering rate 'map' that is a function of four variables - the detuning of the (0-0) laser, the detuning of the (1-0) laser and their respective intensities.

4.2.2 Monte-Carlo simulation

To simulate the longitudinal slowing of a molecular beam caused by the interaction with counter-propagating laser light, we use a Monte-Carlo approach. For this purpose, we generate 10,000 molecules whose trajectories, influenced by the laser light, are tracked as they propagate. The simulation sequence is as follows:

1. We generate 10,000 molecules. The three-dimensional positions (x, y, z) and velocities (v_x, v_y, v_z) are tracked during the simulation. The initial phase space of the molecules is sampled from that experimentally observed such that in the absence of interactions with laser light the 10,000 molecules reproduce experimentally observed velocity and time of flight profiles (see chapter 3). This includes the exit times of molecules with faster molecules exiting earlier than later ones.

2. For a given laser power, beam size and focus, a three dimensional laser intensity map is produced for both the (0-0) and (0-1) laser. This intensity map relates the intensity from each laser experienced by a molecule with the molecules position along the beamline.

3. The simulation propagates the molecules in time steps of $d\tau = 10$ ns. At each time step the following procedure is evaluated for each molecule:

   (a) The local intensity at the current position of the molecule is determined from the laser intensity map.

(b) The Doppler shift due to the forward velocity of the molecule leads to a detuning of the laser frequency seen by the molecules. The frequency shift of this detuning is evaluated based on the current forward velocity and summed to any detuning due to a laser chirp.

(c) The two determined laser intensities and the total detuning is fed into the scattering rate 'map' obtained in the previous section. The probability of a molecule getting excited is determined by $P_{\text{scat}} = R_{\text{scat}} d\tau$. A random number between 0 and 1 is generated and compared to P_{scat} to decide if an excitation event takes place. If an excitation event has occurred, the recoil velocity $\hbar k/m = 3.7$ mm/s is removed from the forward velocity of the molecule.

(d) To incorporate the momentum kicks from photon emission, a random direction for photon emission is chosen and the velocity is adjusted accordingly.

(e) The position of the molecule is updated by the distance travelled in a time equal to the time step at the velocity it now has.

4. The simulation is terminated for a molecule if it reaches the distance of the detector, $z = 0.8$ m, has a transverse position greater than 5 mm, the forward velocity is negative (i.e. the molecule has turned around) or the molecule has reached the end of the simulated time, 40 ms.

Figure 4.3 summarises the results of such a Monte-Carlo simulation. The initial conditions of the simulated molecules are chosen to match the properties of a typical molecular beam from our buffer gas source. We match the forward velocity distributions to those observed and correlate the exit times and velocities of molecules out of our source to match those observed in figure 2.8 such that the time of flight profile obtained at a detector at $z = 0.8$ m replicates the experimental profile. Figure 4.3(a-b) show the simulated initial conditions in red with the experimental data in grey. The laser slowed distributions are shown in blue. The simulated molecular beam matches our experimental data well under free flight.

Both the laser addressing the (0-0) transition as well as the laser addressing the (1-0) transition are assumed to have 300 mW and are collimated with a $1/e^2$ diameter of 4 mm. In these

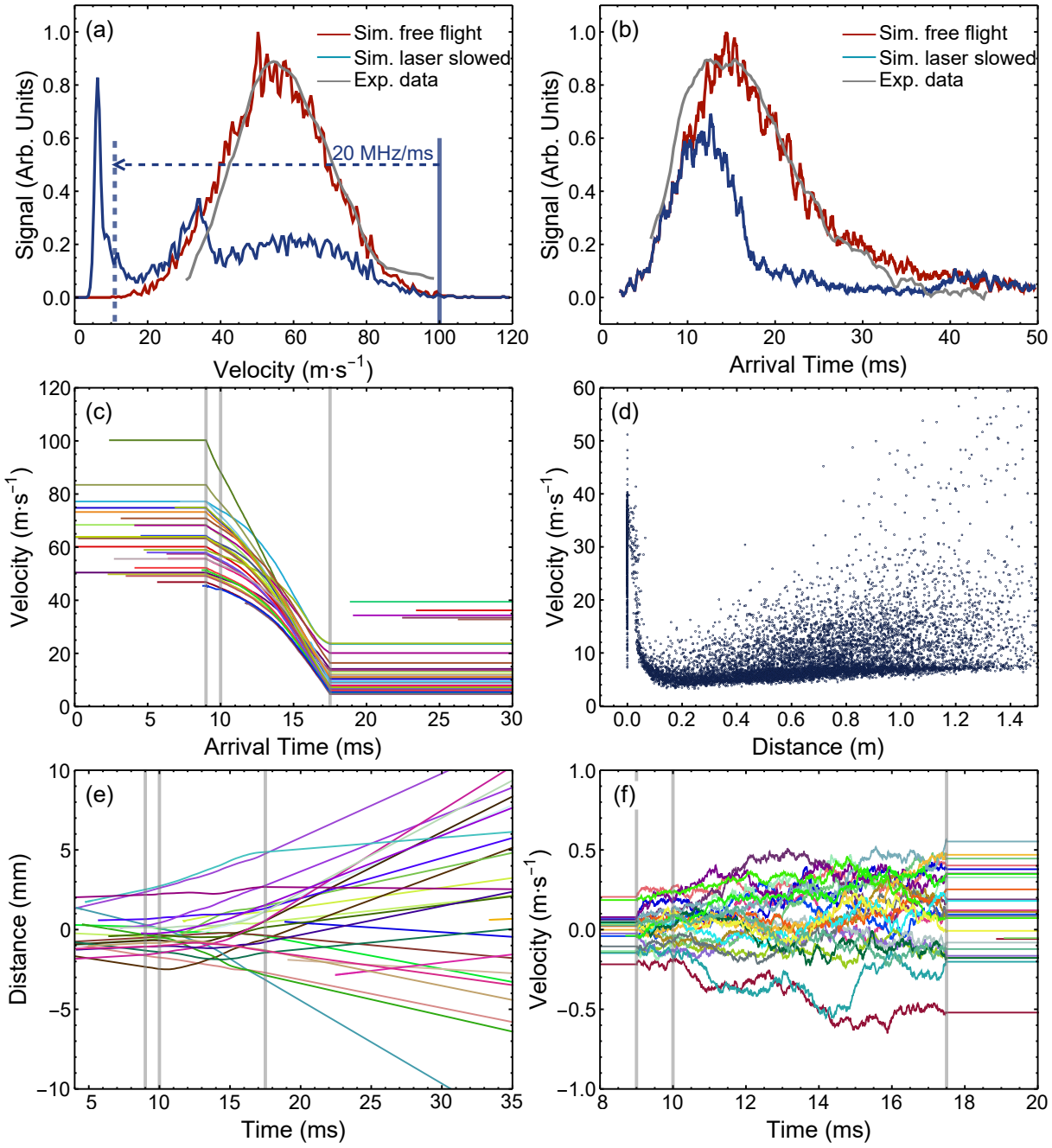

Figure 4.3: Monte-Carlo trajectory simulation of longitudinal laser slowing of YbF. The initial phase space of the molecules is chosen such that it replicates experimental velocity and time of flight profiles (a)-(b). A chirp rate of 20 MHz/ms is used for the main laser addressing the (0-0) transition whilst the first vibrational repump laser is frequency broadened. A selection of simulated trajectories is shown in (c)-(f). (c) Trajectories of individual molecules during slowing. Vertical lines indicate the times when the slowing laser is turned on, begins the chirp, and turns off. (d) Phase space distribution of molecules after slowing. (e) Transverse radial distances of molecules during slowing. (f) Transverse velocities of molecules during slowing.

simulations only the laser addressing the (0-0) transition is chirped. The (1-0) laser addressing the leak to $X\,^2\Sigma^+$ is frequency broadened but not chirped. This laser also has a power of

300 mW but is spread equally among 10 sidebands spaced by 30 MHz. Under these conditions, the model gives a maximum scattering rate of 4×10^6 photons/s.

The (0-0) laser is initially detuned by -180 MHz corresponding to molecules travelling at 100 m/s. This is shown with a solid blue line in figure 4.3(a). The laser is chirped to -20 MHz corresponding to molecules travelling at 10 m/s, indicated by a dashed line. The slowing laser is turned on 9 ms after the start of the beam pulse, which is late enough that nearly all molecules have exited the buffer gas cell. The slowing sequence consists of holding the laser frequency fixed for 1 ms in order to reduce the forward velocity spread, then chirping the frequency at 20 MHz/ms for 7.5 ms to track the changing Doppler shift, at which point the laser is turned off. There are three regions of interest in figure 4.3(a-b). The first is molecules slowed to below 10 m/s. These molecules have successfully followed the chirp and scatter an average of 12,000 photons. These are identified by a sharp peak in signal below 10 m/s in figure 4.3(a). These slowed molecules arrive at the detector between 17.5 ms and around 40 ms but the time of flight profile, figure 4.3(b), does not give a clear signature of their presence. The second is the molecules leaving the cell after the slowing laser has turned off. These molecules travel at 20-40 m/s and arrive at the detector $\sim$40 ms. The third region corresponds to the fast molecules that exit the cell first, these molecules have already reached a distance close to or exceeding 0.8 m, where the detector is located, in the time before the slowing laser turns on. These molecules arrive at the detector before 15 ms, largely unaffected by the slowing light.

Figure 4.3(c) illustrates how the forward velocities of a set of molecules change over time. The timings of the slowing sequence are shown as vertical lines in the figure. We see that molecules with initial speeds between 40 and 100 m/s are brought into the desired velocity range at nearly the same time. Some molecules travelling below $\sim$40 m/s exit the cell after the laser has already turned off and are unaffected by it.

The frequency chirped slowing method results in molecules slowed within very similar forward speeds but at a wide range of longitudinal positions, as shown in figure 4.3(d). Here, the longitudinal phase-space distribution after slowing indicates that slow molecules are distributed across a region greater than 1 m wide. This makes capturing molecules in a MOT challenging

since some molecules will need to travel distances ∼0.5 m after slowing in order to reach the MOT. The slowed molecules will diverge transversely in this time, beyond the capture volume of the MOT. Only molecules that arrive within a 5mm transverse circle are counted. Figures 4.3(e)-(f) show the transverse positions and velocities of molecules during slowing. The photon emission events during slowing lead to transverse heating of the molecules which further accentuates this problem. Nevertheless, the simulations show that successful slowing of 12% of our total molecular signal is possible. Given the molecular flux observed in chapter 3, we anticipate being able to produce 20,000 molecules within both the capture velocity and volume of a MOT. This number could be improved with the addition of transverse laser cooling to collimate the molecular beam.

4.2.3 Leaks to $v = 2$ and $v = 3$

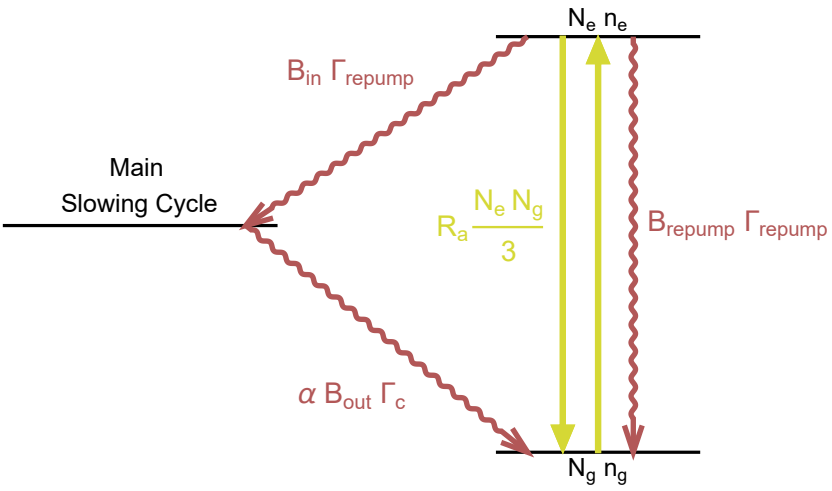

Figure 4.4: Model for determining required laser intensity in repump transitions. The model is based on that presented in [109].

Although losses to vibrational states higher than $X\,^2\Sigma^+(v = 1)$ have so far been neglected, the maximum scattering rate will be close to that predicted above since population in $v > 1$ is repumped via a different excited state. Put differently, there is no stimulated emission from $A^2\Pi_{1/2}(v' = 0)$ to $X\,^2\Sigma^+(v = 2)$ or $X\,^2\Sigma^+(v = 3)$. These states are only populated by spon-

taneous emission from the $A^2\Pi_{1/2}(v = 0)$ state so with moderate pumping the number of molecules in the vibrational levels can be very low. Nevertheless, in order to gain an understanding of the power requirements needed to drive the repump transitions, we formulate here their own MLREs. We follow a similar procedure as that set out in ref [109] and ref [110]. Figure 4.4 shows a schematic of the model for repumping vibrational leaks via states that do not share an excited state with the main slowing transition. The main slowing transition here refers to the energy levels depicted in figure 4.2 and is treated as a single 'state'. The population in the main slowing cycle is denoted n_c. The role of the repump scheme is to maximise n_c. The main slowing cycle pumps population into N_g magnetic sublevels of a vibrational state at a rate $\alpha B_{\text{out}}\Gamma_A$, where α is the fraction of population in the main slowing cycle that is in the excited state, B_{out} is the branching ratio of decay from the excited state of the main slowing cycle to the loss state of interest and Γ_A is the linewidth of $A^2\Pi_{1/2}$. The population n_g in each magnetic sublevel is assumed to be the same. Similarly, the excited state consists of N_e magnetic sublevels with population n_e in each. The excited state of the repump transition returns population to the main slowing cycle at a rate $B_{\text{in}}\Gamma_{\text{repump}}$, where Γ_{repump} is the lifetime of the excited state in our repump transition. The spontaneous decay rate from the excited to the ground state of the repump transition is given by $B_{\text{repump}}\Gamma_{\text{repump}}$ where B_{repump} is the branching ratio of the excited state back to the ground state of the repump transition. R_a is the average excitation rate for all transitions. The total excitation rate from the ground to the excited level is given by $R_a\frac{N_eN_g}{3}$ since there are N_eN_g possible transitions between them and for every pair of states there are three times the number of routes for spontaneous decay as for stimulated absorption/emission due to a single laser polarisation. The rate equations and normalisation condition for such a system are as given below.

$$N_{\text{g}}\dot{n}_{\text{g}} = B_{\text{repump}}\Gamma_{\text{repump}}N_{\text{e}}n_{\text{e}} + \alpha B_{\text{out}}\,\Gamma_A n_{\text{c}} - R_a\frac{N_{\text{e}}N_{\text{g}}}{3}\left(n_{\text{g}} - n_{\text{e}}\right), \tag{4.9}$$

$$N_{\text{e}}\dot{n}_{\text{e}} = -\Gamma_{\text{repump}}N_{\text{e}}n_{\text{e}} + R_a\frac{N_{\text{e}}N_{\text{g}}}{3}\left(n_{\text{g}} - n_{\text{e}}\right), \tag{4.10}$$

$$\dot{n}_{\text{c}} = -\alpha B_{\text{out}}\,\Gamma_A n_{\text{c}} + B_{\text{in}}\,\Gamma_{\text{repump}}N_{\text{e}}n_{\text{e}}, \tag{4.11}$$

$$1 = n_C + N_e n_e + N_g n_g. \tag{4.12}$$

We now solve these scattering rate equations for the case of leaks to $X^2\Sigma^+(v = 2)$ and $X^2\Sigma^+(v = 3)$, additionally making the substitution that $R_a = \frac{\Gamma_{\text{repump}} B_{\text{repump}} I}{2 N_g I_{\text{sat}}}$, where I is the intensity of the driving laser and I_{sat}, the saturation intensity for the transition with wavelength λ, defined as $I_{\text{sat}} = \pi h c \Gamma_{\text{repump}} / (3\lambda^3)$. For our main slowing cycle, the maximum occupation fraction tends towards $\alpha = 1/7$ as the population is evenly distributed across all states. This is the value we assume here.

The fraction of molecules in the main slowing cycle, n_c, as a function of repump intensity for the lasers addressing the $[561] \leftarrow X^2\Sigma^+(v = 2)$ and $[557] \leftarrow X^2\Sigma^+(v = 3)$ is shown in figure 4.5. About 5 mW/cm^2 and ∼1 mW/cm^2 are needed to pump approximately 90% of the population back into the main slowing cycle for the $v = 2$ and $v = 3$ repump lasers respectively. This has not taken into account sideband frequencies or any frequency broadening of the laser light. These will increase power requirements.

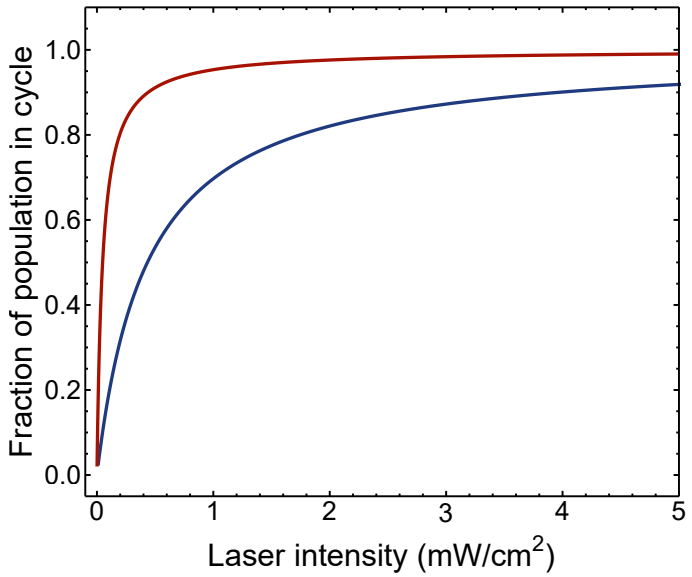

Figure 4.5: The fraction of molecules that are in the main slowing cycle as a function of laser intensity for the $v = 2$ repump (blue) and $v = 3$ repump (red). Adapted from [109].

4.3 Photon scattering

We now turn our attention to implementing laser slowing experimentally. As discussed in the previous sections, multiple laser frequencies are required to successfully scatter sufficient photons in order to reduce the velocity of the molecules. A separate laser is needed for every vibrational state that population can leak to. Additionally, within each vibrational level, sideband frequencies need to be added to address the hyperfine structure in these transitions. In this section we test longitudinal optical cycling by sequentially adding more repump lasers. We estimate the photon scattering rate by measuring the rate at which molecules are optically pumped into dark vibrational states. We later compare these measurements with the photon scattering rates observed by direct laser slowing.

4.3.1 Photon scattering on $A^2\Pi_{1/2}(v=0) \leftrightarrow X^2\Sigma^+(v=0)$

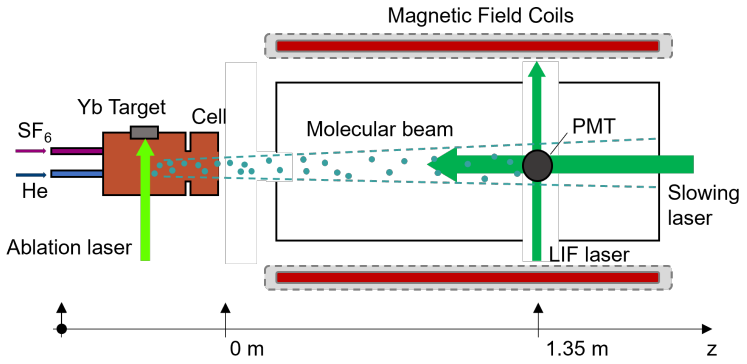

Figure 4.6: A schematic of the experimental setup used to measure the photon scattering rate from a longitudinal laser beam. A counter-propagating 'slowing laser' interacts with molecules exiting our cryogenic buffer gas source. The molecules downstream of the source are imaged by laser induced fluorescence (LIF) from a transverse probe beam. The beamline has been extended from that in chapter 3 to allow for additional interaction time with the laser (due to the long exit times of molecules out of the source).

Figure 4.6 shows a schematic of the setup used to measure the photon cycling rate. The setup is similar to that in chapter 3 used to detect the molecular beam. A 200 mW, 6 mm $1/e^2$ diameter laser ($I/I_{\text{sat}} = 160$) addressing the P(1) line in $A^2\Pi_{1/2}(v=0) \leftarrow X^2\Sigma^+(v=0)$ counter-propagates to the direction of the molecular beam. The laser beam has sideband

frequencies added to address the hyperfine structure in the $X^2\Sigma^+(v = 0, N = 1)$ state. We refer to this laser as the slowing laser. The slowing laser is turned on about 11 ms after the ablation pulse to allow molecules to exit the cryogenic buffer gas source, and turned off some variable time later. The timings of the laser are controlled by an AOM. To probe the molecules remaining in $X^2\Sigma^+(v = 0)$, a transverse laser, also addressing the P(1) line, intersects the molecular beam. The LIF is imaged onto a PMT as in previous setups.

The forward velocity, v, of the molecules will lead to a Doppler shift,

$$\Delta\nu = \frac{v}{\lambda}, \tag{4.13}$$

in the frequency of the laser as seen by the molecule. Here, λ refers to the wavelength of the laser light. Molecules travelling within a certain velocity range determined by the Doppler shifted resonance of the laser will be optically pumped into (vibrational) dark states. This causes a 'hole-burning' out of the time of flight profile when we pump with a longitudinal laser beam. It is the rate at which this hole burning occurs that we measure here. To ensure that we do not pump into dark m_F states, efficient destabilisation of dark states is required.

Destabilising dark states

The P(1) transition has less angular momentum in the upper state than in the ground state. For any given polarisation of light there will always be ground m_F states that do not couple to an excited state. For instance, if linearly polarised light is used to drive the P(1) line then the $X^2\Sigma^+(F = 2, m_F = \pm 2)$ states are dark. As a result, molecules will be optically pumped into one of these states after scattering only a few photons. To avoid this, dark states have to be destabilised. This can be solved in two ways. One way is to choose the polarisation such that we generate dark states which are superposition states of different m_F states in the quantisation axis of an applied magnetic field. The magnetic field introduces a Larmor precession of the dark state into bright states at an angular frequency,

$$\omega_B \approx \mu_B g_F m_F B, \tag{4.14}$$

where μ_B is the Bohr magneton, g_F is the magnetic g factor of state m_F and B is the magnitude of the applied magnetic field. The rate at which the dark states are destabilised should be such that the photon cycling rate is not limited by dark states, but not so large that the energy levels are Zeeman shifted out of resonance with the laser. Typically $\omega_B \sim \Gamma$. The second method is to leave dark states as stationary but instead modulate the polarisation at a rate $\sim \Gamma$. This is particularly useful for states that have small g factors. We investigate the use of both magnetic field remixing and polarisation modulation. Figure 4.7 displays a schematic of our

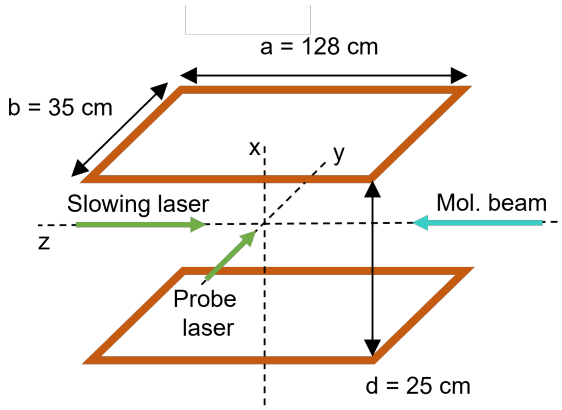

Figure 4.7: Magnetic field configuration on our beamline used to destabilise dark states. Two coils in Helmholtz configuration are used to produce a magnetic field of a few gauss.

magnetic field coils used to remix dark states in both the probe and slowing laser. Two parallel rectangular coils in Helmholtz-like configuration are used to generate a magnetic field of a few gauss (1 gauss = 10^{-4} Tesla) extending for about 20 cm in the y direction. Both the probe and slowing laser are linearly polarised at an angle $\theta_B = 60°$ to the direction of the magnetic field. This configuration was found optimal in [51] and successfully implemented in [107, 111]. For polarisation modulation the probe light is passed through an EOM mounted with its crystal axis at 45 degrees to the axis of polarisation of the laser light. The exit polarisation from the crystal is modulated from linear to circular to linear (90° rotated) at a modulation frequency of ∼1.3 MHz. In practice the transmitted light through the EOM is elliptical and the output fraction of light in the same polarisation state as that input can be modulated between 30% and 70%. Figure 4.8 shows the effect of magnetic field and polarisation modulation on the population pumped out of $X^2\Sigma^+(v = 0)$. The slowing laser is turned on for 50 μs and the time of flight profiles recorded. We find that both polarisation modulation and magnetic field

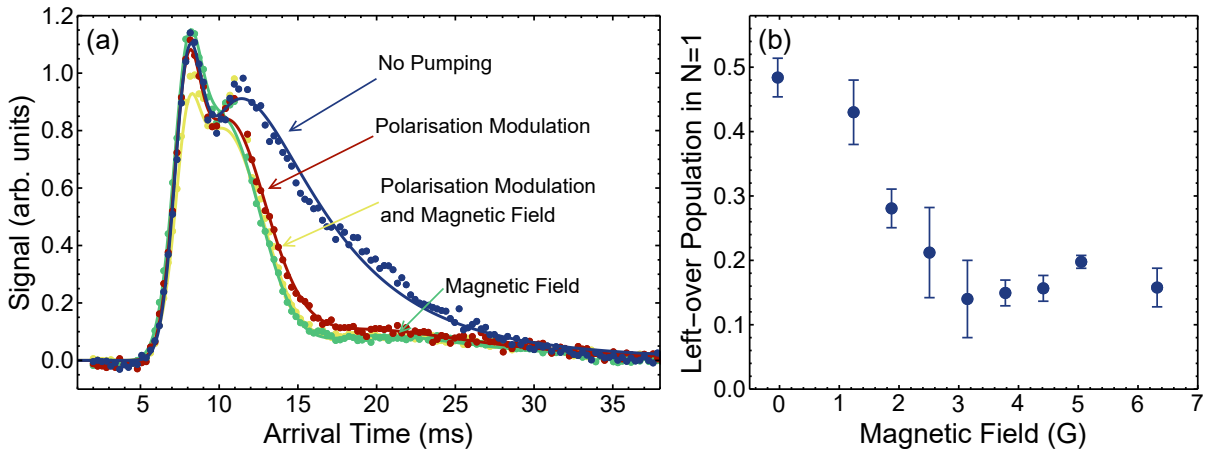

Figure 4.8: (a) Effect of optical pumping with a longitudinal laser addressing the P(1) rotational line of $A^2\Pi_{1/2} \leftarrow X^2\Sigma^+(v=0)$. Molecules within a certain velocity distribution, chosen by the detuning of the laser, are pumped to higher vibrational states. (b) The fraction of population left over in $X^2\Sigma^+(v=0, N=1)$ as a function of the magnetic field magnitude. Due to the Earth's field, even without a magnetic field we see non-zero pumping. 1 G = 10^{-4} T.

remixing enable pumping out $\sim$ 90% of the population out of $X^2\Sigma^+(v=0)$ for the targeted velocity class. Using both polarisation modulation and magnetic field remixing provides no further benefit. We note that even in the absence of any externally applied magnetic field, we observe $\sim$ 50% pumping. This is likely due to the Earth's field which is not cancelled. Figure 4.8(b) shows the fraction of left-over population as a function of magnetic field when only magnetic field remixing is used as a means to destabilise dark states. Successive shots are taken with and without the slowing laser at various magnetic fields. The time of flight profile is gated in a 1 ms wide window around the targeted velocity class. We find that beyond a magnitude of $B \sim 3$ G there is no further gain. The left-over population, even in the best case does not go below around 15%. This can be due to the targeted time bin consisting of molecules of various velocities, some of which won't be on resonance with our laser light. We see a similar situation in our simulations of laser slowing for a matching velocity and exit time distribution. Figure 4.3(a-b) show that not all molecules at a particular velocity or a particular arrival time are slowed to within 10 m/s.

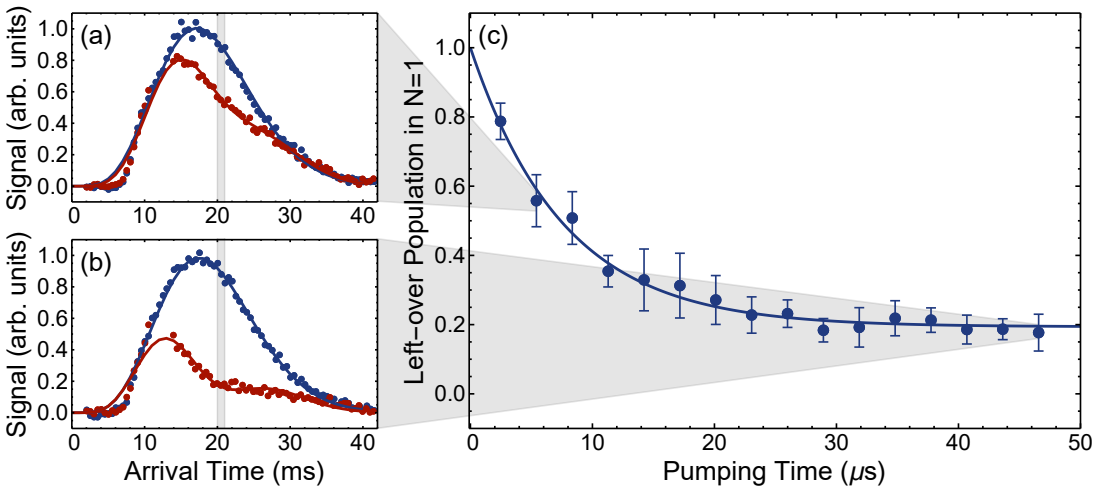

Figure 4.9: The left-over population in $X^2\Sigma^+(v = 0, N = 1)$ as a function of interaction time with a red-detuned counter propagating slowing laser addressing the $A^2\Pi_{1/2}(v = 0) \leftarrow X^2\Sigma^+(v = 0)$ transition. As molecules cycle on the P(1) transition, they are lost to higher vibrational levels. The pumped and unpumped molecular signals for two different pumping times are shown in blue and red respectively in (a)(b). The signal is integrated in a gated region from 20 ms to 21 ms indicated by a grey bar. The blue curve in (c) is a single exponential fit to the data.

Photon scattering rate

We now measure the photon scattering rate by varying the duration the slowing laser is turned on for. Figure 4.9 shows the left-over population in $X^2\Sigma^+(v = 0)$ as a function of pumping time. For each duration step, we record alternating time of flight profiles with and without the slowing laser. The signal within a 1 ms wide gate centered at 20.5 ms is integrated and the ratio of the pumped:unpumped signal is plotted on the y axis. We fit a single exponential to the data presented in figure 4.9(c). The photon scattering rate, R, is related to the decay time, τ, by N/τ where $N = 1/(1-B)$ is the estimated number of photons scattered by a molecule before it leaves the photon cycle, based on the branching ratio, B. We measure a decay time of $\tau = 7.6 \pm 0.4$ μs. Taking a branching ratio of 0.932 for the decay from $A^2\Pi_{1/2}(v = 0) \rightarrow X^2\Sigma^+(v = 0)$ gives a scattering rate of $R = 1.9(1) \times 10^6$ s^{-1}. This is approximately five times smaller than the maximum scattering rate ($\Gamma/4$) we might expect at maximum saturation. This method for determining the scattering rate neglects, however, that a particular time bin will be composed of multiple velocity classes of molecules, some of which won't be on resonance with the slowing laser. In addition, the scattering rate will be a spatial average of molecules inside the detection

volume, some of which will be interacting with laser light of lower intensity in the wings of the beam. Indeed, if the signal is gated for a shorter period and a smaller area is imaged by reducing the size of the field stop in the imaging optics, a higher scattering rate is observed. This, however, comes at the cost of signal.

4.3.2 Adding repump lasers. Scattering rate with $v = 0$, $v = 1$, $v = 2$

With just a single laser addressing the $A^2\Pi_{1/2}(v = 0) \leftarrow X^2\Sigma^+(v = 0)$ transition, each molecule will cycle only 14 photons and most of the population is lost to higher vibrational levels after only 50 μs of pumping. In order to increase the number of scattered photons we need to add vibrational repump lasers to pump population back into the main slowing cycle. In this section, we describe the frequency spectra used to address the hyperfine structure in each of our vibrational repump transitions. We then proceed to measure the photon scattering rate with lasers addressing the first three vibrational levels of $X^2\Sigma^+$.

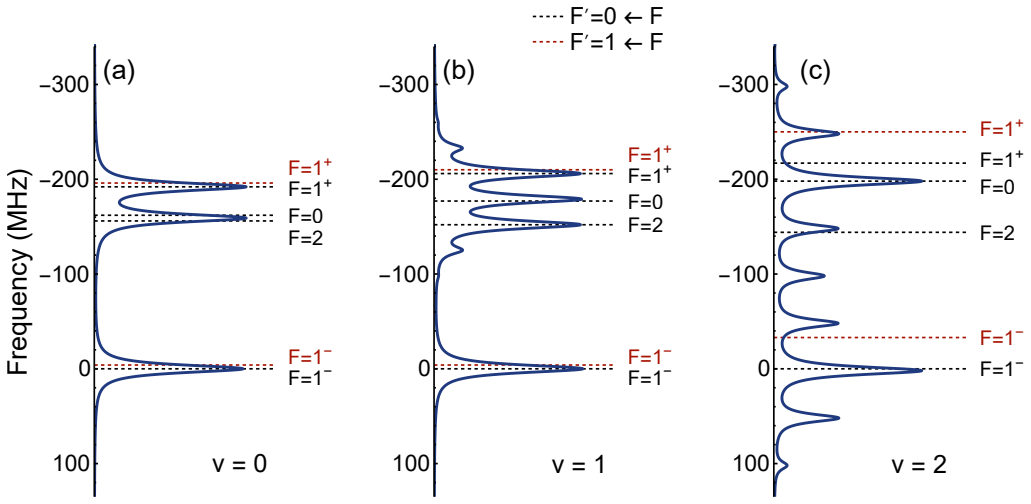

Figure 4.10: Sideband frequencies used to address hyperfine transitions in $X^2\Sigma^+(v = 0, 1, 2)$. Dashed lines represent transitions to F'.

Figure 4.10 shows the frequencies used to address the hyperfine structure of the various vibrational states. The spacing for each of the vibrational repumps is different so custom sideband frequency generation schemes are required for each of the repump transitions. We couple all of the laser frequency components into the same fiber which takes the light to the experiment. A shutter is used to turn the laser addressing $v = 0$ on and off before it is combined with the

other beams. The frequency sideband structure used to address the $X^2\Sigma^+(v = 0)$ transition is the same as that presented in other sections. To address the transitions from $X^2\Sigma^+(v = 1)$ we have used two lasers over the course of the experiment. The first is a fiber amplifier, seeded by Toptica DL Pro and subsequently frequency doubled. This system is produced by MPB and was shared with another experiment. We later inherited a Toptica DLC TA-SHG pro solid state system. This combines a seed laser, tapered amplifier and frequency-doubling resonant cavity to generate light at 568 nm. The laser beam is split into two paths. The first path is passed through an EOM at 27 MHz. This addresses the $F = 1^+$, $F = 0$ and $F = 2$ levels. The remaining light is shifted by an AOM to +170 MHz to address the $F = 1^-$ level. Although specified for use at 552 nm, we operate this laser at 568 nm. Due to water absorption lines near 1136 nm, the power output of the laser is limited to ∼140 mW at the experiment. For the $X^2\Sigma^+(v = 2)$ repump we initially used a Toptica DL ECDL at 1130 nm combined with a homebuilt tapered amplifier. The amplified light is fiber-coupled to a waveguide PPLN frequency doubler outputing approximately 20 mW. This was recently replaced by a Vexlum vertical external cavity surface emitting laser (VECSEL). An optically pumped gain chip emits light at 1130 nm which is intra-cavity frequency doubled to 565 nm. This laser is capable of ∼1 W output power. To address the sideband structure, we use a single EOM driven at 50 MHz. Each of the ground F states coincides with at least one of the frequencies generated by the EOM.

We now measure photon scattering rates with incrementally added repump lasers by the same method described in section 4.3.1. The $X^2\Sigma^+(v = 1)$ and $X^2\Sigma^+(v = 2)$ repump lasers are turned on together with the $X^2\Sigma^+(v = 0)$ laser but remain on for the duration of the molecular pulse (about 50 ms). The duration of the $X^2\Sigma^+(v = 0)$ laser is varied using an AOM as before. The number of photons scattered per molecule is limited by the leak probability out of the optical cycle, l. For every scattering event, the fraction of molecules remaining in the optical cycle will have a probability $r = (1 - l)$ of decaying back to the optical cycle such that the average number of photons scattered per molecule is given by

$$N = \frac{1}{1 - r}. \tag{4.15}$$

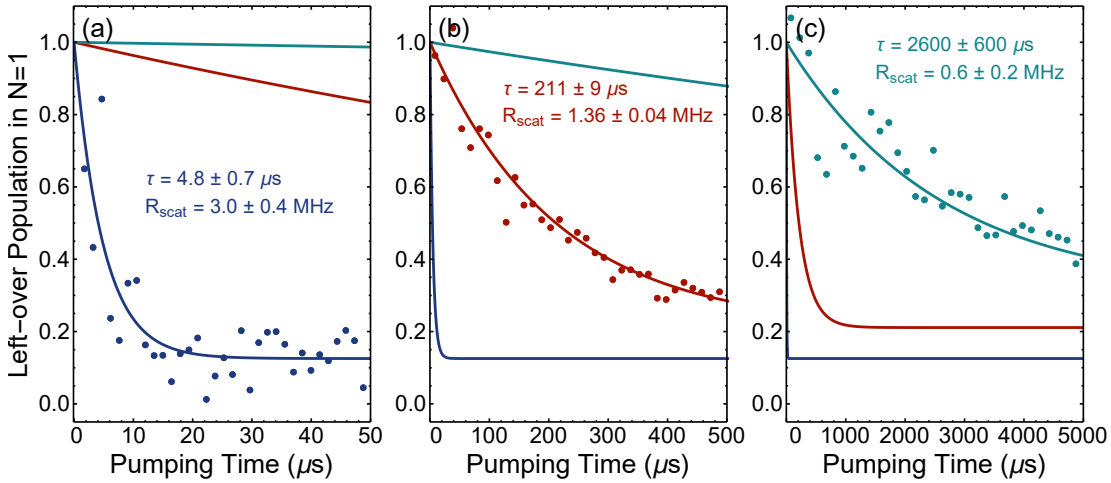

Figure 4.11: Population in $X^2\Sigma^+(v = 0, N = 1)$ as a function of pumping time by counter-propagating light comprising of (a): just a laser addressing the (0-0) transition, (b): a laser driving (0-0) and a $v = 1$ vibrational repump, (c): a laser driving (0-0), a $v = 1$ vibrational repump and a $v = 2$ vibrational repump. For these data, the time-of-flight profiles were integrated between 19.5 and 20.5 ms.

With the addition of a repump laser addressing the $v = 1$ transitions, the average number of photons scattered is $N_1 = 290$. Figure 4.11(b) shows the fraction of population left in $X^2\Sigma^+(v = 0)$ as a function of pumping time. The addition of the $v = 1$ repump has increased the time molecules scatter photons for, the population in $X^2\Sigma^+(v = 0)$ is lost with a time constant $\tau_1 = 211 \pm 9$ μs. The estimated scattering rate is given by $R_{\text{scat}} = N_1/\tau_1 = 1.36(4) \times 10^6$ s^{-1}. With the addition of the $v = 2$ repump the scattering rate decreases further to $R_{\text{scat}} = N_2/\tau_2 = 1600/2600 = 0.6(2) \times 10^6$ s^{-1} as shown in figure 4.11(c). The scattering rates are reduced by a factor 0.45(5) and 0.44(3) between the additions of a $v = 1$ and then subsequently the $v = 2$ repump laser. As discussed in section 4.2.1, we expect the scattering rate will decrease by a factor $4/7 \approx 0.57$ with the addition of the $v = 1$ laser due to the repump scheme sharing an excited state with the main (0-0) transition. This is consistent with our observation of the scattering rates in figure 4.11. The addition of the $v = 2$ laser should have a very small effect on the photon scattering rate, provided the repump transition is saturated. The observation here may point to insufficient power in the $v = 2$ laser or inefficient remixing of dark states which is limiting the scattering rate.

4.4 Laser slowing

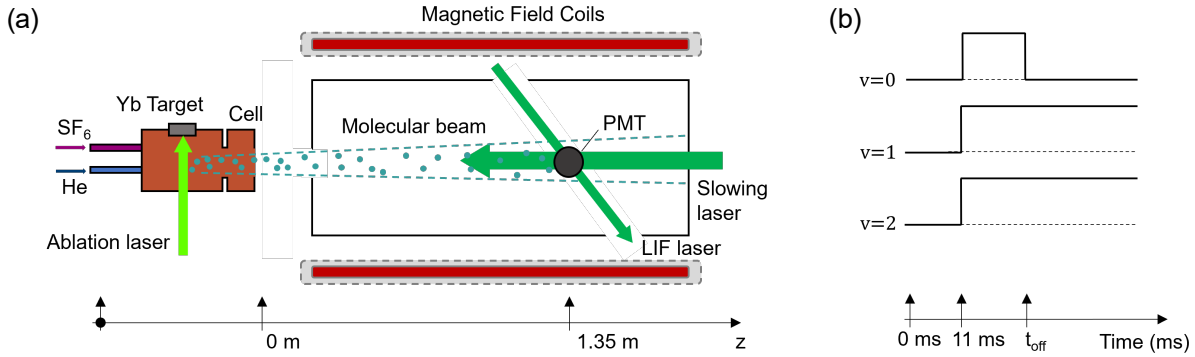

Figure 4.12: (a) Experimental setup for measuring the forward velocity change of molecules by a counter-propagating laser beam. The experimental setup is modified from that in figure 4.6 by detecting the molecules using an angled probe beam at 60° to the direction of propagation of the molecules. (b) Timing sequence for the experiment. The $v = 0$, $v = 1$ and $v = 2$ lasers are turned on simultaneously. The repump lasers remain on for the duration of the shot. The $v = 0$ laser duration is varied.

The next step towards laser slowing is to demonstrate a measurable change in the forward velocity of the molecular beam. This method also provides an unambiguous way to determine the photon scattering rate. Figure 4.12 shows a schematic of the experimental setup. The configuration is similar to that used above and in section 4.3.1, only the probe is incident at an angle. A counter-propagating slowing laser, comprised of the laser addressing the (0-0) transition and the first two vibrational repumps described in the previous section, is used to exert radiation pressure onto the molecular beam. The power of the $v = 0$ laser is 190 mW, whilst that of the $v = 1$ and $v = 2$ lasers is 150 mW and 8 mW respectively. The detuning of the slowing laser is set such that it is on resonance with the velocity class of molecules that arrive at 19 ms. A single angled probe beam is used to detect the changing Doppler shift of molecules. The probe beam has 8 mW of power evenly split across the sideband frequencies as shown in figure 4.10 and a $1/e^2$ diameter of 3.4 mm. The probe laser is scanned across the P(1) transition and the slowing beam is turned on and off on alternate shots. The Doppler shifted resonance positions between the data with slowing light on and off is used to infer a velocity change. The measured velocity change as a function of slowing time is shown in figure 4.13. The time-of-flight profiles were gated between 18.5 and 19.5 ms for these data. The inset shows the measured Doppler shift after 5 ms of longitudinal slowing. We observe a 3(1) MHz

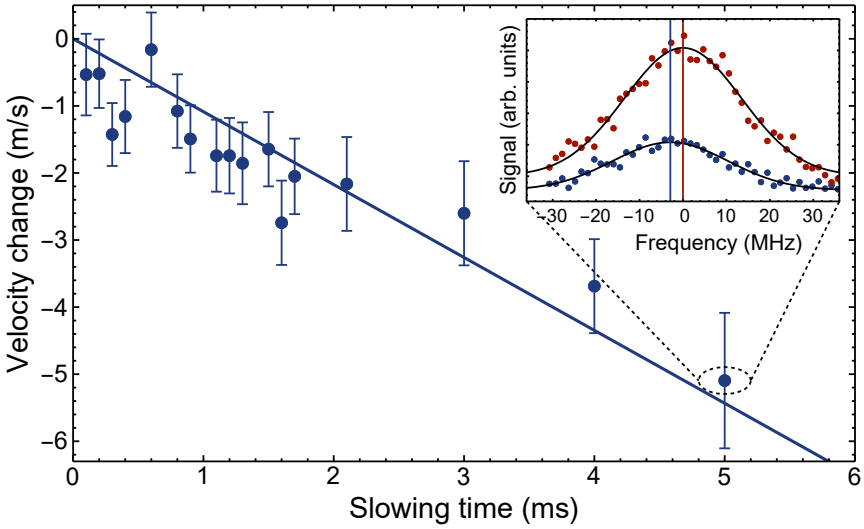

Figure 4.13: Forward velocity change of the molecular beam by radiation pressure from a counter-propagating laser. A probe laser tuned to the P(1) rotational line of YbF and angled at 60° to the forward direction of the molecules is used to detect the molecules. The inset shows the frequency shifted position of the P(1) resonance with (blue) and without (red) laser slowing. The time-of-flight profiles were gated between 18.5 and 19.5 ms for these data.

shift corresponding to a velocity change of -5(1) m/s. A linear fit to the data presented in figure 4.13 gives the average deceleration as 1090(80) m/s^2. The molecules scatter on average ∼1400 photons giving a mean scattering rate of 0.29(5) × 10^6 s^{-1}. This is within relatively good agreement with the value derived from the longitudinal optical pumping experiments in the previous section. Figure 4.14 shows the mean deceleration of the molecules as a function of the gate center. The gate width is 1 ms in each case. Only those molecules which are on resonance with our laser, are slowed. Before and after that, laser slowing is worse. The slowing laser saturates the PMT signal so no molecules are detectable before approximately 18 ms.

The scattering rates are still much smaller than those predicted from the MLRE. Under current conditions and, conservatively assuming an initial velocity of 80 m/s, the distance required to slow molecules to below 10 m/s is more than 1 m. At this distance we anticipate the divergence of the beam may significantly affect the captured number into the MOT. In addition, the observed acceleration is low compared to the trapping force needed for a molecular MOT. We also note that after 5 ms of slowing and ∼ 1400 photons scattered, 44(3)% of molecules remain in the optical cycle. The error here is estimated from the fit to figure 4.11(c). This corresponds to a leak rate out of our optical cycle of ∼ 6 × 10^{-4}. This can be detrimental to laser slowing

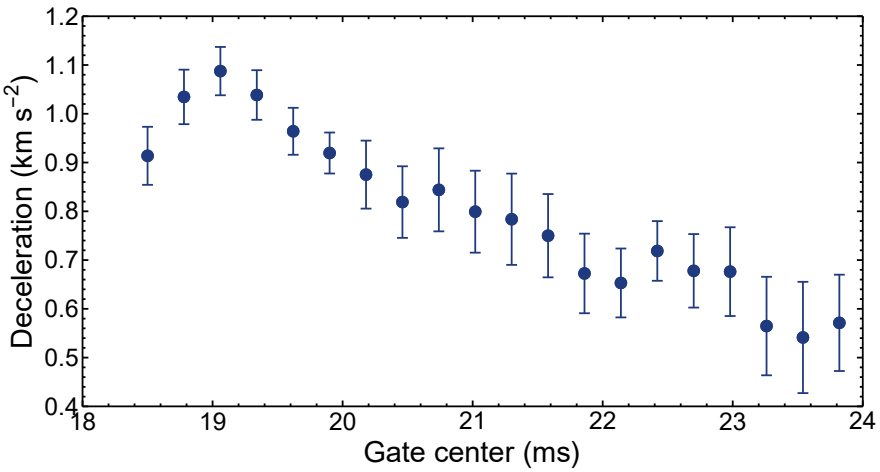

Figure 4.14: The mean deceleration as a function of gate center. For each data point, the gate width is 1 ms. The largest deceleration is observed at a gate center of 19 ms.

but is critical for the MOT where the lifetime of molecules in the MOT will be dramatically limited by the remaining leaks. In order to improve both the slowing and make a MOT feasible, higher scattering rates and plugging of the remaining vibrational leaks are needed. The higher scattering rates could be limited by either power limitations of the lasers driving the transitions or slow remixing of dark states. In the following sections we turn our attention to plugging remaining leaks out of the optical cycle.

4.5 Vibrational leak to $v = 3$

In order to repump vibrational losses to $X^2\Sigma^+(v = 3)$ and determine the magnitude of this leak, we carry out a pump-probe experiment on the $[557] \leftarrow X^2\Sigma^+(v = 3)$ transition. These experiments help us to determine the hyperfine structure of the transition and inform appropriate sideband frequencies to be added to the repump laser as well as determine the branching ratio of the leak. The experimental setup is shown in figure 4.15. It is the same as that shown in figure 4.6, only we now probe the molecules on the P(1) line of $X^2\Sigma^+(v = 3)$. The counter-propagating slowing light containing the main slowing laser plus the vibrational repump lasers for $v = 1$ and $v = 2$ interact with the molecules for 4 ms. This optically pumps population into $X^2\Sigma^+(v = 3, N = 1)$ as well as any further 'leak states' which have an allowed transition to $A^2\Pi_{1/2}(v = 0, J' = 1/2^+)$. The powers used for the pumping lasers are the same as in the pre-

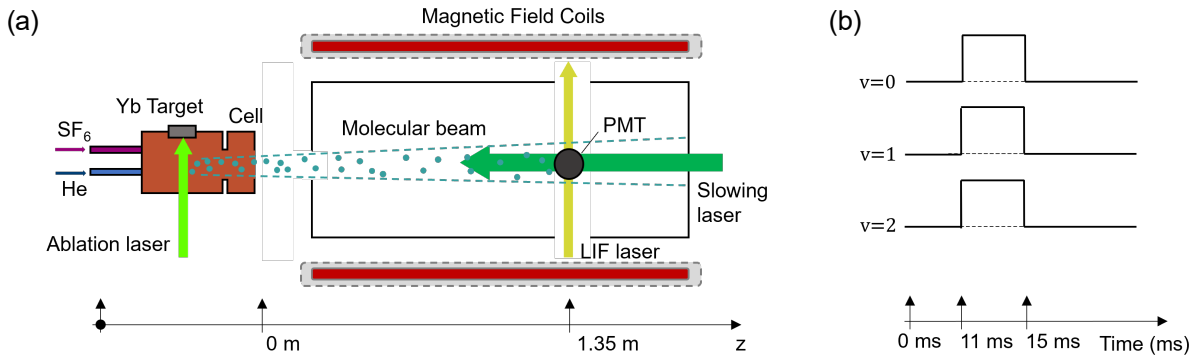

Figure 4.15: Experimental setup (a) and timing sequence (b) for pump-probe spectroscopy of $X^2\Sigma^+(v=3)$. Population is pumped into $X^2\Sigma^+(v=3)$ using $v=0$, $v=1$ and $v=2$. The population is detected by laser induced fluorescence from a transverse laser exciting the P(1) line of the $[557] \leftarrow X^2\Sigma^+(v=3)$ transition.

vious section. We probe the population in $X^2\Sigma^+(v=3, N=1)$ by driving the P(1) rotational line of $[557] \leftarrow X^2\Sigma^+(v=3)$. A probe laser intersecting the molecular beam excites population to [557] which predominantly decays to $X^2\Sigma^+(v=1)$. The fluorescence is collected and imaged onto a PMT as before. The expected signal is sufficiently low that the SNR is better when the PMT is used in photon counting. The probe laser has a $1/e^2$ diameter of 3.4 mm and is locked to our transfer cavity lock (TCL) described in the previous chapter. The frequency of the laser is stepped using TCL by changing the setpoint between the reference laser and our probe (see chapter 4). The voltage scan of the TCL cavity is separately calibrated by modulating the frequency spectrum of the probe laser at a known frequency using an EOM. We record the voltage positions of each sideband as the cavity is scanned. We find the cavity scan is linear across the scanned range and a fit yields a calibration of 232(1) MHz/V.

A scan of the probe laser frequency across the P(1) line of $[557] \leftarrow X^2\Sigma^+(v=3)$ is shown in 4.16. Previous measurements of the $[557] \leftarrow X^2\Sigma^+(v=3)$ transition have been made to MHz resolution in [104]. Our values for the hyperfine splitting in [557] differ slightly to that presented in [104]. Unlike in $A^2\Pi_{1/2}(v=0, J=1/2^+)$, the hyperfine splitting in [557] is sufficiently large that the six distinct P(1) transitions can be resolved. The assignment of the transitions from $F=2$ and $F=0$ in $X^2\Sigma^+(v=3, N=1)$ could in principle be the other way around to that indicated in figure 4.16. We take here the same assignment as in [104]. Transition to both $F'=0$ and $F'=1$ are allowed from $F=1^+$ and $F=1^-$. The spacing between these tells us

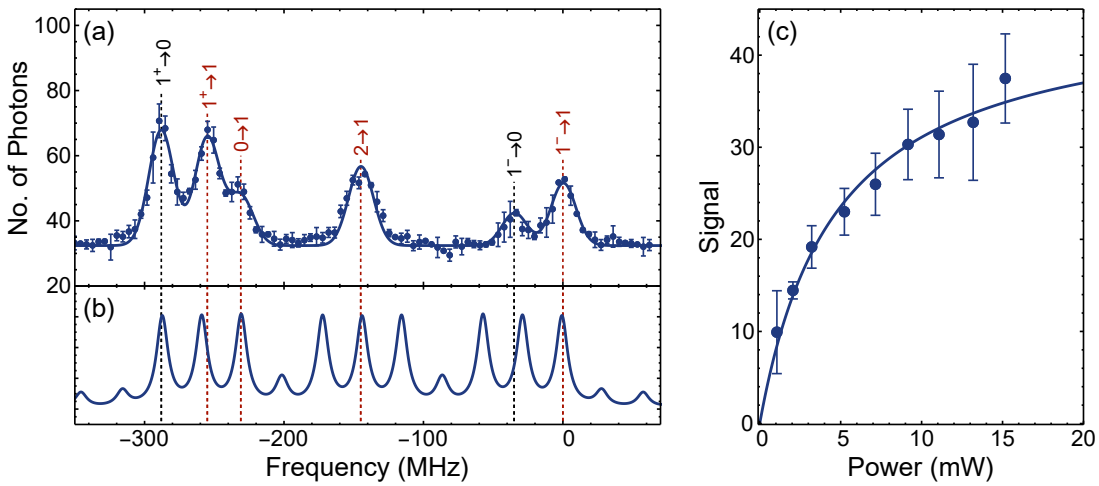

Figure 4.16: (a) Hyperfine structure of the [557] ← $X^2\Sigma^+(v = 3)$ P(1) transition. Dashed lines are assigned frequencies based on the peak positions of fitted Gaussian curves (blue line) to the data. Dashed black vertical lines indicate transitions to $F' = 0$ in [557] while red lines those to $F' = 1$. (b) The frequency spectrum generated by two EOMs driven at 115 MHz and 28 MHz respectively used to repump hyperfine transitions in $X^2\Sigma^+(v = 3)$. (c) Signal in a single hyperfine state as a function of probe power.

Table 4.1: Hyperfine splitting in the P(1) rotational line of [557] ← $X^2\Sigma^+(v = 3)$ relative to the $F = 1^+ \rightarrow F' = 0$ transition.

Transition	Value (MHz)
$F = 1^- \rightarrow F' = 1$	0
$F = 1^- \rightarrow F' = 0$	-35
$F = 2 \rightarrow F' = 1$	-145
$F = 0 \rightarrow F' = 1$	-231
$F = 1^+ \rightarrow F' = 1$	-255
$F = 1^+ \rightarrow F' = 0$	-288

the hyperfine splitting in [557]. We find this to be 34(2) MHz. The structure of the P(1) line is summarised in table 4.1.

Using this information, we were able to implement the optics to add frequency sidebands to address the hyperfine structure in our $v = 3$ repump laser. In order to repump effectively we do not need to hit every transition in figure 4.16 but at least a transition from every ground F state needs to be addressed. To achieve this, the light from the $v = 3$ laser is passed through two EOMs at 115 MHz and 28 MHz respectively. The resulting frequency spectrum is shown in figure 4.16(b). Figure 4.16(c) shows the photon signal in the largest hyperfine peak as a function of laser power. The maximum available laser power is around 15 mW which is near

saturation of the transition.

4.5.1 Branching ratio to $v = 3$

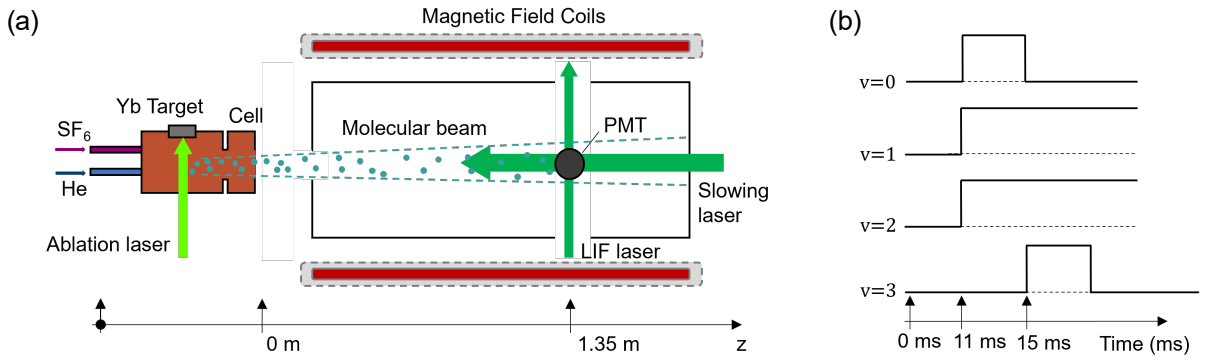

Figure 4.17: (a) Experimental setup used to measure the branching ratio to $X^2\Sigma^+(v = 3)$. The probe laser intersects the molecular beam transversely. The laser timings are shown in (b).

To test the closure of the optical cycle with $X^2\Sigma^+(v = 3)$ repumped we measure the ratio of population recovered when molecules are pumped into and then back out of $X^2\Sigma^+(v = 3)$. The timing sequence is shown in figure 4.17(b). The $v = 0$, $v = 1$ and $v = 2$ lasers longitudinally pump molecules into $v = 3$ and any other 'leak states' outside of the first three vibrational levels. We refer to this as the pumped away signal. The $v = 3$ laser now has its sideband frequencies added and is fiber coupled into the same fiber as that of the other slowing lasers. The slowing laser has a $1/e^2$ diameter of 4.5 mm. Every alternate shot, the $v = 3$ laser is turned on to return population to $X(v = 0)$. The $v = 0$, $v = 1$ and $v = 2$ lasers are set on resonance with molecules arrival at 25 ms. To set the frequency of the $v = 3$ laser on resonance with the same molecules, the laser is scanned across the P(1) line of $[557] \leftarrow X^2\Sigma^+(v = 3)$ and locked to the frequency of the largest peak corresponding to the the place where the sideband frequencies are on resonance. As a reference, we also record the time of flight profile without any pumping. The molecules are detected with a transverse probe beam on the P(1) line of $A - X$. The time integrated signal in a 1 ms wide gate centered on 25 ms is used to calculate the fraction of the signal pumped away that is returned from $X^2\Sigma^+(v = 3)$. This fraction of the total pumped population that is returned by the $v = 3$ laser is shown as a function of laser power in figure 4.18. The inset shows an example of the unpumped, pumped and returned signals.

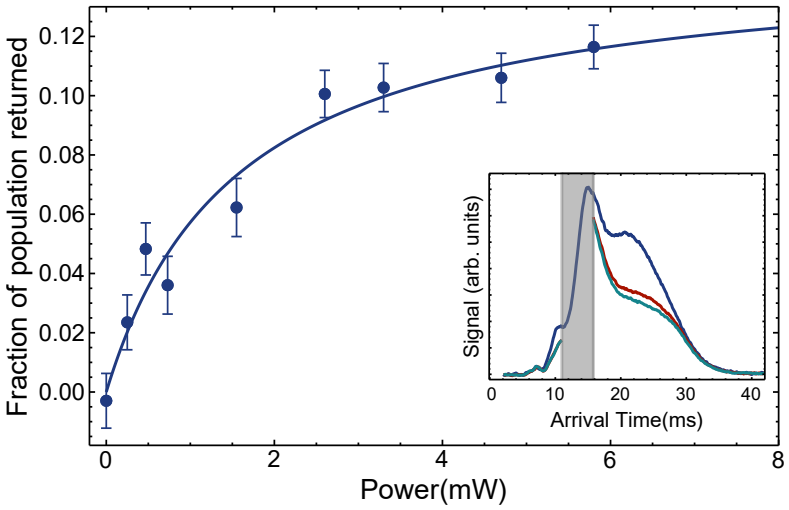

Figure 4.18: Fraction of population returned from $X^2\Sigma^+(v = 3)$ as a function of power in the $v = 3$ laser. The laser has sideband frequencies to address the hyperfine structure in $X^2\Sigma^+(v = 3)$. The inset shows the pumped (teal), unpumped (blue) and returned (red) signal. The $v = 0$ pumping laser saturates the PMT signal causing a discontinuity in the TOF profile, highlighted by a grey band.

The highest available $v = 3$ laser power during this experiment was 5.8 mW. At this power, the population returned from $X^2\Sigma^+(v = 3)$ is approaching saturation but we observe that only 11.6% of the lost population is returned. This indicates that missing population is not in $X^2\Sigma^+(v = 3)$ but has been pumped elsewhere.

To provide an estimate of the leak to $X^2\Sigma^+(v = 3)$ from these measurement, consider the fraction of lost population recovered from $v = 3$, which we denote p_3. This can be given by,

$$p_3 = \frac{B_{v=3}}{B_{v>2}}, \tag{4.16}$$

where $B_{v=3}$ is the branching ratio $A^2\Pi_{1/2}(v = 0) \rightarrow X^2\Sigma^+(v = 3)$ and $B_{v>2}$ is the branching ratio to all 'leak states' outside of $X^2\Sigma^+(v = 0, 1, 2)$. Prior experimental values for $B_{v>2}$ obtained by fluorescence measurements are consistent with zero and only quote an upper bound [102], so instead, as an estimate, we take a value of $B_{v>2} = 5 \times 10^{-4}$. This value is based on theoretical calculations [112] and is consistent with our measured value from section 4.4. Seeing in figure 4.18 that the returned fraction saturates at around 0.011 gives $B_{v=3} = 7 \times 10^{-5}$.

Figure 4.19 shows the population in $X^2\Sigma^+(v = 0, N = 1)$ as a function of pumping time when

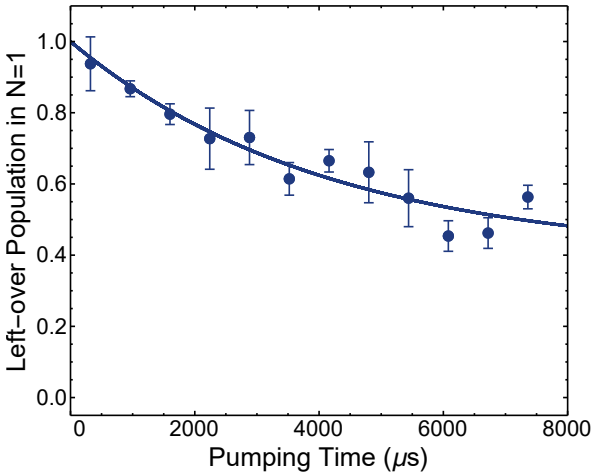

Figure 4.19: Population in $X^2\Sigma^+(v = 0, N = 1)$ as a function of pumping time by counter-propagating light comprising of the $v = 0$, $v = 1$, $v = 2$ and $v = 3$ lasers.

the counter-propagating light is comprised of four lasers addressing the $X^2\Sigma^+(v = 0, 1, 2, 3)$ states. The counter-propagating light has the same properties as described previously and we use the maximum available power in the $v = 3$ laser, about 6 mW split across the sidebands. The solid blue line is an exponential fit of the from $(1 - c)\exp(-t/\tau_{v=3}) + c$, where t is the pumping time and c a constant offset. The lifetime, $\tau_{v=3}$, of molecules in the slowing cycle has increased to 4.1 ± 1.2 ms compared to that without the $v = 3$ laser, $\tau_{v=2} = 2.6 \pm 0.6$ ms. Assuming the addition of the $v = 3$ laser has not affected the scattering rate, we can estimate the leak to $v = 3$ by this increase in the lifetime. When the two scattering rates are equal, we can write

$$\frac{N_3}{\tau_{v=3}} = \frac{N_2}{\tau_{v=2}}, \tag{4.17}$$

where N_2 and N_3 are the mean number of photons scattered before a molecule is pumped to a leak state $X^2\Sigma^+(v > 2)$ and $X^2\Sigma^+(v > 3)$ respectively. Using Eq. 4.15 we can then estimate the closure of the optical cycle with the addition of the $v = 3$ laser, r_3, as

$$r_3 = 1 - \frac{(1 - r_2)\tau_{v=2}}{\tau_{v=3}}, \tag{4.18}$$

where r_2 is the closure of the optical cycle with population in $X^2\Sigma^+(v = 0, 1, 2)$ repumped. Taking our value for r_2 as 0.9994 as determined in section 4.4, we find the observed increase in lifetime consistent with the optical cycle closure increasing to 0.99962. This suggests there is a

remaining leak of 3.8×10^{-4}. With the optical cycle closed to this extent, each molecule would be expected to scatter around 2500 photons. This would only be sufficient to slow molecules by around ∼10 m/s. To improve slowing significantly we still need to plug remaining losses out of the optical cycle.

4.6 Possible remaining loss channels

Vibrational loss channels are the dominant contribution to losses out of the slowing cycle. At the 10^{-5} level, however, there seem to be other leaks out of the optical cycle as indicated from the data presented above. Here we discuss some possible routes.

Intermediate electronic states

Heavy ions often have low lying states owing to an excitation of an inner-shell electron. Consider the Yb^+ ion. The ground state consists of a filled $4f$ shell and a single valence electron in the $6s$ shell. The lowest lying excited state, on the other hand, promotes a $4f$ electron to fill the $6s$ shell. These states also manifest themselves in molecules. In YbF, the ground state, $X\,^2\Sigma^+$, correlates to the $4f^{14}6s$ configuration of Yb^+, and the series of excited states $A\,^2\Pi$, $B\,^2\Sigma^+$ etc. arise from excitation of the $6s$ electron. However, the lowest-lying electronically excited state correlates to the $4f^{13}6s^2$ configuration of Yb^+ and is the first of a series of such states that we call the "$4f$ hole" states. These states mix with the nearby filled shell configurations and can introduce loss channels into our optical cycle. Recent theoretical studies [112] have predicted that a leak from $A^2\Pi_{1/2}$ to a $4f$ hole state is opened via a small mixing of the $X^2\Sigma^+$ state configuration in a $4f$ hole state. The branching ratio to this state is predicted to be about 5×10^{-4} [112], consistent with the magnitude of the leak observed in our experiments.

Off-resonant rotational excitation

Another possible leak mechanism is off-resonantly driving transitions from the ground state to a different excited state that is rotationally open. The nearest rotational line from P(1) is the Q(1) transitions ∼4.4 GHz away. Although relatively far away, both laser slowing and the MOT light will require large powers and long interaction time. Scattering rate equation and OBE models by J.Lim indicate that interaction times of a few ms would result in approximately ∼10% of molecules pumped to $N = 3$.

Hyperfine decay to $N = 3$

The selection rule $\Delta J = 0, \pm 1$ is only an approximation, albeit for most cases this is a good one. When exciting the P(1) line, the $F' = 1$ hyperfine state in $A^2\Pi_{1/2}$ could decay to the $F = 2$ state in $X^2\Sigma^+(N = 3)$ via the selection rule $\Delta F = -1$. This is expected to be very weak since it has $\Delta J = 2$ and violates the ΔJ selection rule. Calculations by M. Tarbutt expect this decay to be much smaller than our observed leak.

Rotational losses due to parity mixing

Optically cycling on the P(1) line relies on parity and angular momentum selection rules. A small electric field can mix opposite parity states. This can break the parity selection rule, and molecules can end up in rotational levels in the ground state that are dark. Such loss mechanisms have been reported for SrF [108] and AlF [113]. For such a leak to be introduced in our slowing cycle, opposite parity states in the $A^2\Pi_{1/2}$ state would need to mix in order to cause population to be lost to $N = 0$ and $N = 2$. The spacing between opposite parity states in $A^2\Pi_{1/2}$ is relatively large at 12 GHz and so this effect is likely to be small. A scan of Q_1 rotational lines with and without longitudinal pumping has so far not been able to identify any increase in population of rotational levels as a result of parity mixing, off-resonant rotational excitation, hyperfine decay or due to decay via the $4f$ hole states if they had a much smaller lifetime than the 8 ms predicted in [112].

Vibrational losses to $v > 3$

Although the vibrational branching ratio to $X^2\Sigma^+$ states with $v > 3$ have not been measured, the vibrational overlap between wavefunctions of the $A^2\Pi_{1/2}$ state and decreases with increasing vibrational number. The leak to $v = 4$ is therefore predicted to be an order of magnitude smaller than that to $v = 3$ [112]. Although it may contribute, it is not expected to be the primary leak in our optical cycle.

4.7 Summary

A measurement of the electron's electric dipole moment using YbF molecules can be greatly enhanced by trapping the molecules in a magneto-optical trap. In order to bring the molecules that exit from our cryogenic buffer gas source to within the capture velocity of such a MOT, we wish to implement radiation pressure slowing. We solve multi-level scattering rate equations for a 28 state system comprising of our main P(1) line of the $A^2\Pi_{1/2}(v = 0) \leftarrow X^2\Sigma^+(v = 0)$ transition and a $X^2\Sigma^+(v = 1)$ repump addressing the same excited state. Monte-Carlo simulations of longitudinal laser slowing show molecules are slowed to within 10 m/s in ∼8 ms and experience a maximum scattering rate of 4×10^6 photons/s. The addition of two repump lasers to address vibrational losses $X^2\Sigma^+(v = 2)$ and $X^2\Sigma^+(v = 3)$ has only a small effect on the scattering rate since population from these states are returned to the optical cycle via different excited states. Using this optical cycling scheme, which was previously used to demonstrate 2D transverse cooling [106], we estimate the photon scattering rate from molecules counter-propagating to the laser light. Using this configuration, we demonstrate a change in the forward velocity of the molecules on the order of 5 m/s. With three lasers addressing the first three vibrational levels of $X^2\Sigma^+$ we find that molecules scatter ∼1400 photons before ∼43% of molecules are lost to dark states. Compared to previous work optically cycling YbF [105, 106], longitudinal laser slowing requires more photon scattering events than Sisyphus cooling so we additionally add a $v = 3$ repump laser. Although repumping population from $X^2\Sigma^+$ has closed a leak with branching ratio $7(3) \times 10^{-5}$, a leak $\sim 4 \times 10^{-4}$ remains. At present, decay to

inner-shell excitations are believed to be the primary loss mechanism. We turn our attention to these states in the next chapter.

Chapter 5

Inner-shell excitations in YbF

This chapter primarily reproduces, and adds upon, the work published in [114] which was obtained in collaboration with the group of G.Meijer at the Fritz-Haber Institute of the Max-Planck Society. The author of the thesis wrote the first draft but acknowledges the input of others in producing [114].

5.1 Introduction

Atoms and ions in the lanthanide family have a rich spectrum of excited energy levels, one set arising from excitation of a $6s$ electron and another set due to excitation of a $4f$ electron. Transitions between the two sets of levels are strongly forbidden. These forbidden transitions serve as clock transitions as well as excellent testing grounds for physics beyond the Standard Model. Consider the Yb^+ ion for example. The ground state is $4f^{14}6s\ ^2S_{1/2}$ while the lowest-lying excited state is $4f^{13}6s^2\ ^2F_{7/2}$. The electric-octupole transition between these states is the basis of an optical clock [115] and is being used to search for new physics via isotope shift measurements [116], tests of local Lorentz invariance [117], and searches for variations of the fundamental constants [118]. Inner-shell transitions have also been studied in neutral Er, Dy and Tm [119–121].

Similar sets of inner-shell excited states must exist in *molecules* that contain atoms from the

lanthanide family, but very little is known about these states which have not received much attention so far. One such case is YbF, but another excellent example is YbOH which has also been laser cooled and has been proposed as a system for a measurement of the eEDM [75].

In YbF, the ground state, $X\,^2\Sigma^+$, correlates to the $4f^{14}6s$ configuration of Yb^+, and the series of excited states $A\,^2\Pi$, $B\,^2\Sigma^+$ etc. arise from excitation of the $6s$ electron. However, the lowest-lying electronically excited state correlates to the $4f^{13}6s^2$ configuration of Yb^+ and is the first of a series of such states that we call the "$4f$ hole" states. As mentioned in the discussion at the end of chapter 4, they are of particular relevance here, because the optical cycle we use, $A^2\Pi_{1/2} \leftrightarrow X^2\Sigma^+$, is suspected to leak to the low-lying $4f$-hole states. The branching ratio for this leak is predicted to be about 5×10^{-4} [112] which is too large for effective radiation pressure slowing or magneto-optical trapping of YbF. To make progress, it is necessary to address this leak, so a good understanding of the $4f$ hole states is needed. Recent theoretical studies [112, 122] have shed some light on these states, and their approximate energies have been determined by studying the fluorescence from high-lying states into the $4f$ hole states using a grating spectrometer [123], but there has been no previous laser spectroscopy of these states.

In this chapter, we present rotationally-resolved spectroscopy of a series of electronic states in YbF that have $4f$ hole character. These include, but are not limited to, the set of $4f$ hole states which provide our decay channel. We begin, in section 5.2, with a description of the energy levels and transitions we study and of the resonance-enhanced multi-photon spectroscopic methods we use. Then, in section 5.3, we introduce a simple and intuitive physical model for describing these states based on Hund's case (c).

There is no direct spectroscopic pathway to the $4f$ hole states from the ground state or any of the excited states arising from excitation of the $6s$ electron, as transitions between the two manifolds are strongly forbidden. Fortunately, there is a high-lying electronic state of mixed character, denoted [31.05], that connects strongly to both the ground state and the $4f$ hole states. In section 5.4 we characterise [31.05] using direct excitation from the ground-state and excitation from the ground-state via the $A^2\Pi_{1/2}$ state. We obtain a complete understanding

of the rotational structure of [31.05], which is key to interpreting the spectrum obtained when exciting from the $4f$ hole states to [31.05]. This spectrum is complicated, so to help decipher it we devise a fingerprinting method that, for each spectral line, identifies the rotational angular momentum and parity of the upper state. The method exploits a set of very strong resonances *above* the ionisation limit of the molecule, corresponding to auto-ionising states that have unusually long lifetimes. We attribute the long lifetime to the states being $4f$ hole states that are only weakly coupled to the ground state of the YbF^+ cation, which has a filled $4f$ shell. These strong auto-ionising states are themselves an interesting topic for study, and we characterise them in section 5.5.

Section 5.6 presents the spectroscopy of the three $4f$ hole states of lowest energy. Decays to two of these states are possible from our optical cycle. We use the information obtained in sections 5.4 and 5.5 to assign quantum numbers to each line in these spectra, and thus determine their rotational level structures and their absolute energies. We show how these conform to the model introduced in section 5.3, and note near degeneracies between certain levels of the same parity and between levels of opposite parity. In section 5.7 we look briefly at the structure of the [18.58] and [18.71] states which we use as repump states in our optical cycle[1]. These states arise from a near degeneracy of a $4f$ hole level with a level of $A^2\Pi_{1/2}$, resulting in states of completely mixed character. We show that these states also conform to our Hund's case (c) model.

Finally, in section 5.8, we discuss the implications of this work and consider a specific repumping scheme for addressing leaks to the $4f$ hole states so that magneto-optical trapping of the molecule can be achieved.

[1]These states have been referred to as [557] and [561] in previous chapters, in keeping with previous work in the group. Here we refer to them as [18.58] and [18.71] to maintain the naming convention used for this set of $4f$ hole states

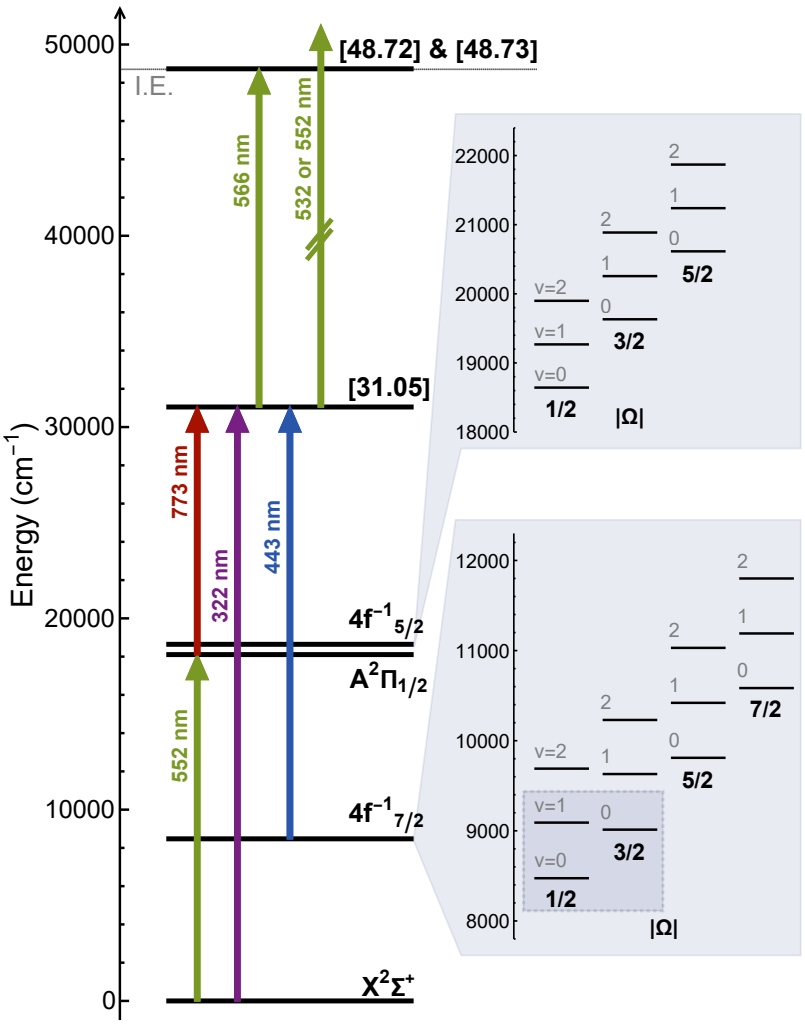

Figure 5.1: ^{174}YbF energy levels and transitions relevant to this work. Pulsed dye lasers are used to drive the transitions shown here. A pulsed 532 nm Nd:YAG laser can in addition be used for ionisation. Light grey boxes show the structure of the $4f$ hole states, and darker grey box indicates the $4f^{-1}_{7/2}$ states studied in this work.

5.2 Experimental configuration

5.2.1 Relevant energy levels

Figure 5.1 presents the energy levels and transitions relevant to this chapter. The main optical cycling transition we use is between $X^2\Sigma^+$ and $A^2\Pi_{1/2}$. The lowest energy $4f$ hole states correlate to the $4f^{13}6s^2$ configuration of Yb^+, which has orbital angular momentum $L = 3$ and spin $S = 1/2$. There is a very large spin-orbit interaction that splits this configuration into a pair of states with total atomic angular momentum $J_a = 5/2$ and $7/2$, with $J_a = 7/2$ having lower energy. Each of these states is further split by the electric field of the F^- ion

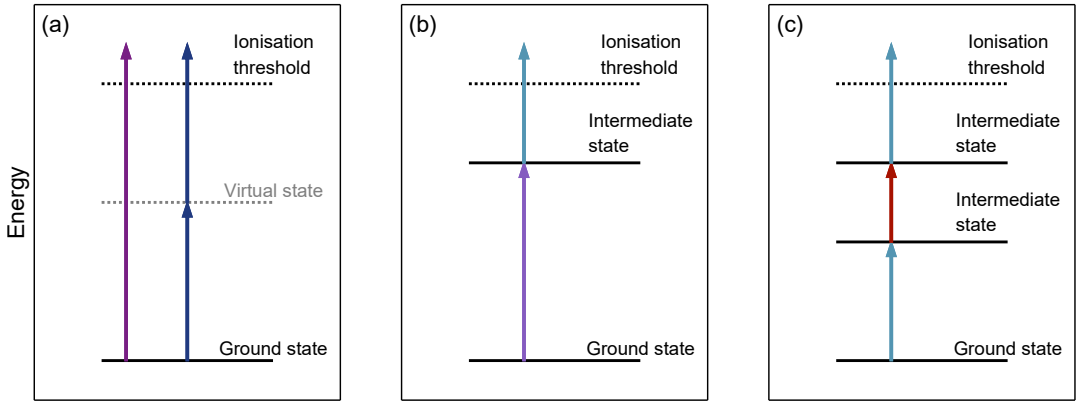

Figure 5.2: Illustration of photo-ionisation schemes. (a): Single photon ionisation (purple) and two-photon ionisation (blue). (b) $(1+1')$ resonantly-enhanced multi-photon ionisation (REMPI). (c) $(1+1'+1)$ REMPI scheme.

into a set labelled by the projection of the total angular momentum onto the internuclear axis, Ω. We use the notation $4f^{-1}_{J_a,|\Omega|}$ to label these states, omitting $|\Omega|$ when we want to refer to the entire manifold of states. The manifold $4f^{-1}_{7/2}$ lies about half way between $X^2\Sigma^+$ and $A^2\Pi_{1/2}$. The manifold $4f^{-1}_{5/2}$ lies close to $A^2\Pi_{1/2}$. Indeed, $A^2\Pi_{1/2}(v=1)$ is so close in energy to $4f^{-1}_{5/2,1/2}(v=0)$ that the pair mix almost completely [112].

We also use three higher-lying states of the molecule. The first was identified by Persinger et al. [123], who called it [31.05], where the label is the term energy in thousands of cm^{-1}. We will continue to use this notation. This state is convenient because it has strong transitions from both the ground state (at 322 nm) and from the $4f^{-1}_{7/2}$ states (near 443 nm). The remaining high-lying states are newly identified states at 48720 cm^{-1} and 48729 cm^{-1}, both less than 30 cm^{-1} above the ionisation energy. Continuing with the same notation, we label these as [48.72] and [48.73].

5.2.2 REMPI methods

In this chapter, we use resonantly-enhanced multi-photon ionisation (REMPI) schemes to study the rotational structure of various states in YbF. Figure 5.2 illustrates various photo-ionisation schemes. One way to ionise from the ground state is via a single photon with energy greater than the ionisation threshold. If the energy of the photon is insufficient to ionise, the atom or

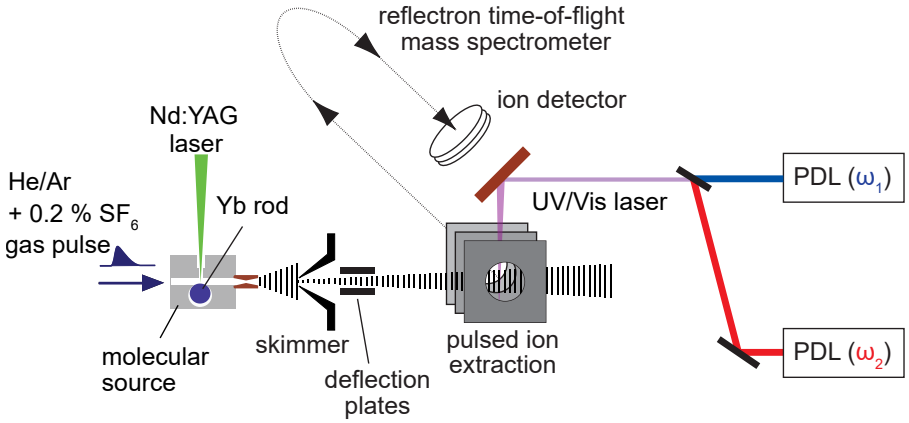

Figure 5.3: Schematic of the experimental setup. YbF molecules are produced by laser ablation of a Yb rod of natural isotopic abundance in the presence of a mixture of SF_6 and a carrier gas. The gas mixture is introduced via a pulsed valve. The molecules interact with pulsed dye lasers (PDLs). Ion detection is carried out by pulsed ion extraction and then measured on a time-of-flight mass spectrometer in either reflectron or linear configuration.

molecule can still reach the ionisation threshold through multi-photon absorption via a virtual state. These two cases are illustrated in figure 5.2(a). One can also ionise using multiple lasers via excitation to an intermediate state. This is known as resonantly-enhanced multi-photon ionisation (REMPI). Figure 5.2(b) shows such a REMPI scheme. A first photon excites an intermediate state then a second photon ionises the atom or molecule. The required pulse energy per photon is much smaller when ionising via REMPI compared to direct ionisation. REMPI schemes are denoted $(n_e + n_i)$, where, n_e, is the number of photons needed to excite to the intermediate state and, n_i, the number of photons needed to ionise. REMPI schemes via multiple intermediate states are also possible such as the $(1 + 1' + 1)$ scheme shown in figure 5.2(c). In this case, the number of photons required to reach the second intermediate state is also included in the labelling of the scheme. Additionally, a dash is used to indicate photons of different energies.

5.2.3 Beamline and experimental setup

Figure 5.3 illustrates the experiment [124]. We produce a supersonic beam of YbF and characterize the states of interest using resonance enhanced multi-photon ionisation (REMPI) spectroscopy. This figure illustrates the apparatus at the Fritz-Haber Institute and is reproduced

from [124].

The molecules are generated by pulsed laser ablation of a solid Yb rod (natural isotopic abundance) in the presence of SF_6 diluted in either a He or Ar carrier gas. The gas mixture is released into the source using a pulsed valve (R.M. Jordan Co., Inc.) operating at 10 Hz. The resulting supersonic beam first passes through a skimmer, then between a pair of plates where an applied electric field deflects away any ions generated by ablation that remain in the beam, and finally into the REMPI detection region. We find that the beam has significant population in approximately the first 18 rotational levels of $X^2\Sigma^+$, corresponding to a rotational temperature of about 40 K. We also find that there is substantial population in the $4f_{7/2}^{-1}$ states.

Two pulsed dye lasers are used during this study: a Sirah PrecisionScan laser with a linewidth of 0.04 cm^{-1} and a Radiant Dyes NarrowScan laser with a linewidth of 0.05 cm^{-1}. Their frequencies are measured with a wavemeter (HighFinesse WS6-600, absolute accuracy 600 MHz). In addition, a 532 nm pulsed Nd:YAG laser can be used for ionisation. The lasers interact with the molecules in a field-free environment. In most cases, the excitation laser pulse energy was such that there was little or no spectral broadening and transition widths were limited by the laser linewidths. The ionisation laser pulse energy was set low enough that no one-colour multi-photon ionisation was observed. After the laser pulses, a field is turned on to extract the ions. The cations are detected in a Wiley-McLaren type time-of-flight mass spectrometer whose resolution is sufficient to resolve the different YbF isotopologues. Although data for the various isotopologues has been obtained, we limit our discussion to the isotope most relevant to us in this thesis, ^{174}YbF.

5.3 Spectroscopic model: Hund's case (c)

The states studied in this chapter conform well to a Hund's case (c) model, as described by Veseth [125]. Figure 5.4 shows a vector diagram of Hund's case (c). The electronic orbital angular momentum $\vec{L}$ strongly couples to the electronic spin $\vec{S}$ to form $\vec{J}_a = \vec{L} + \vec{S}$. $\vec{J}_a$ and the rotational angular momentum $\vec{R}$ couple to form $\vec{J} = \vec{J}_a + \vec{R}$. The projection of $\vec{J}$ (and also

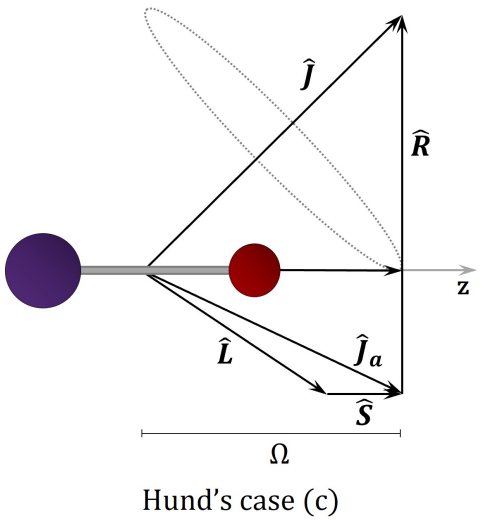

Figure 5.4: Vector diagram for Hund's case (c).

$\vec{J}_a$) onto the internuclear axis is Ω, and the basis states are $|J_a, J, \Omega\rangle$. We may think of $\vec{J}_a$ as the angular momentum of the underlying atomic state, which in this case is the state of the Yb^+ ion. The state is split by the electrostatic interactions of the molecule into components labelled by Ω. We think of this as the Stark splitting of the atomic state, which in this model is small compared to the spin-orbit interaction. In addition to the electronic structure, each of these states is split into smaller vibrational structure and even smaller rotational structure. The rotational structure is our main concern.

The rotational Hamiltonian in Hund's case (c) is

$$H_{\mathrm{r}} = B\vec{R}^2 = B(\vec{J} - \vec{J}_a)^2 = B(\vec{J}^2 + \vec{J}_a^2 - 2\vec{J}\cdot\vec{J}_a). \tag{5.1}$$

The matrix elements of H_{r} in the $|J_a, J, \Omega\rangle$ basis are

$$\begin{aligned}\langle J_a, J, \Omega|H_{\mathrm{r}}|J_a, J, \Omega'\rangle = & B[J(J+1)+J_a(J_a+1)-2\Omega^2]\delta_{\Omega,\Omega'} \\ & - 2B(-1)^{J_a+J-2\Omega}\sum_{q=\pm1} g_q(J_a)g_q(J),\end{aligned} \tag{5.2}$$

where

$$g_q(x) = \sqrt{x(x+1)(2x+1)}\begin{pmatrix} x & 1 & x \\ -\Omega & q & \Omega' \end{pmatrix}. \tag{5.3}$$

We introduce the basis set of symmetric and anti-symmetric combinations of Ω, denoted by e/f:

$$|J_a, J, |\Omega|, {}^{e}_{f}\rangle = \frac{1}{\sqrt{2}} \left(|J_a, J, \Omega\rangle \pm |J_a, J, -\Omega\rangle \right). \tag{5.4}$$

The diagonal elements of $H_{\rm r}$ in the e/f basis give energies

$$\begin{aligned} E_{f}^{e} &= BJ(J+1) + BJ_a(J_a+1) - 2B\Omega^2 \\ &\mp \frac{B}{4}(2J_a+1)(2J+1)\delta_{|\Omega|,1/2}. \end{aligned} \tag{5.5}$$

The terms, $BJ_a(J_a+1)$ and $2B\Omega^2$ are constants for each electronic state and do not contribute to the rotational structure. We incorporate these terms into the term energy, T. The final term in Eq. (5.5), which depends on the e/f symmetry and is only non-zero for $|\Omega| = 1/2$, comes from the off-diagonal matrix element in Eq. (5.2) which connects $\Omega = 1/2$ and $\Omega = -1/2$. We see that, for $|\Omega| = 1/2$, rotational level J of the f manifold is degenerate with level $J + (J_a + 1/2)$ of the e manifold, while for $|\Omega| > 1/2$ levels of the same J are degenerate in the two manifolds. There can also be degeneracy *within* the e manifold when $|\Omega| = 1/2$: levels J and J' are degenerate if they satisfy $J + J' = J_a - 1/2$. Figure 5.5(a) shows the energy level structure described by Eq. (5.5) for the case where $|\Omega| = 1/2$ and $J_a = 7/2$. We see the degeneracy between level J of the f manifold and level $J + 4$ of the e manifold. We also note the unusual behaviour of the e manifold at low J – the lowest level is $J = 1.5$, while $J = 0.5$ and $J = 2.5$ are degenerate. Figure 5.5(b) shows the case where $|\Omega| = 3/2$, where the rotational energies are simply $BJ(J+1)$ for both manifolds. All the states studied in this work have a rotational structure similar to the ideal case illustrated here, so we use this Hund's case (c) picture to describe them all.

Next, we consider two corrections that go beyond this simple model. The first is a small correction to the energy due to the off-diagonal matrix elements in Eq. (5.2) that couple states of different $|\Omega|$, differing by ± 1. This correction can be obtained using second order perturbation

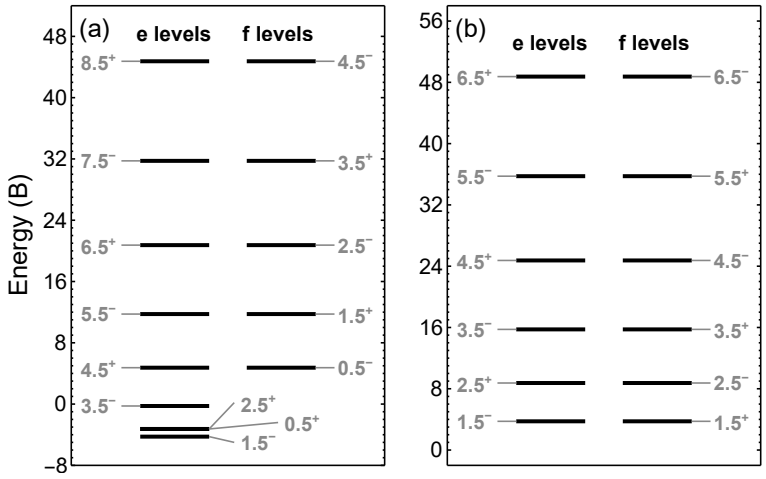

Figure 5.5: Rotational energy levels in Hund's case (c) for the case where $J_a = 7/2$ and (a) $|\Omega| = 1/2$ and (b) $|\Omega| = 3/2$. Levels are labelled by the total angular momentum J and the parity p using the notation J^p.

theory. For an $|\Omega| = 1/2$ state, the correction is

$$\begin{aligned}\Delta E &= \frac{\left|\left\langle J_a, J, 1/2, {}^e_f \right| H_\mathrm{r} \left| J_a, J, 3/2, {}^e_f \right\rangle\right|^2}{E_{1/2} - E_{3/2}} \\ &= \frac{15B^2 J(J+1)}{\Delta} - \frac{45B^2}{4\Delta}.\end{aligned} \tag{5.6}$$

The first term becomes a small correction to the coefficient of $J(J+1)$ in Eq. (5.5), while the second term is a constant that we absorb into the term energy T. The correction is small because $\Delta = E_{1/2} - E_{3/2}$, the energy difference between the $|\Omega| = 1/2$ and $|\Omega| = 3/2$ states, is large compared to B. Although ΔE is identical for the e and f manifolds, it depends on J, so slightly lifts the degeneracy for $|\Omega| = 1/2$ (but not for $|\Omega| > 1/2$). The equivalent correction for $|\Omega| = 3/2$ is

$$\Delta E = \frac{15(J(J+1) - 3/4)B^2}{E_{3/2} - E_{1/2}} + \frac{12(J(J+1) - 15/4)B^2}{E_{3/2} - E_{5/2}}. \tag{5.7}$$

Our second correction accounts for the fact that the molecular electric field responsible for the splitting by $|\Omega|$ can also mix configurations of different J_a, resulting in eigenstates of the form

$$|\psi\rangle = \sum_{J_a} c_{J_a} \left| J_a, J, |\Omega|, {}^e_f \right\rangle, \tag{5.8}$$

where the sum runs over the possible values of J_a, and $\sum_{J_a} |c_{J_a}|^2 = 1$. Since H_r does not couple states of different J_a, the only modification needed is to replace $\frac{1}{2}(2J_a + 1)$ by $\zeta = \sum_{J_a} \frac{1}{2}(2J_a + 1)|c_{J_a}|^2$ in the last term of Eq. (5.5).

Combining all of the above into a single expression, the energy of an $|\Omega| = 1/2$ state can be written as

$$E_f^e = T + \left(B + \frac{15B^2}{\Delta}\right) J(J+1) \mp \frac{B}{2}\zeta(2J+1). \tag{5.9}$$

The last term in Eq. (5.9) lifts the degeneracy between the e and f manifold noted above and illustrated in Fig. 5.5(a). It is equivalent to a lambda-type doubling term familiar from case (a) states, but here it is fully characterised by the rotational constant B and the wavefunction amplitudes $|c_{J_a}|^2$. Fitting to this model will return an optimal value of ζ, but the combination of $(2J_a + 1)|c_{J_a}|^2$ factors that give a certain ζ will, in general, not be unique.

5.4 The high-lying state: [31.05]

In this section, we analyse the rotational structure of [31.05]. This is a state of mixed character which provides a convenient pathway between the ground state and the $4f$ hole states [123]. Later, we use the structure of [31.05] in our analysis of the transition [31.05] $\leftarrow 4f_{7/2}^{-1}$.

Figure 5.6(a) presents the spectrum of the [31.05] $\leftarrow \mathrm{X}^2\Sigma^+(v = 0)$ band. The $(1 + 1')$ REMPI scheme used to obtain the spectrum is shown on the left of figure 5.6(a). The spectrum is obtained by scanning a laser at 322 nm. The laser is a RadiantDyes NarrowScan with DCM dye producing 644 nm light which is then frequency doubled. A second pulsed dye laser at 552 nm is used to ionise from [31.05]. There is a 10 ns delay between the two laser pulses. Each point in the scan is comprised of the ion intensity extracted from the average of 30 consecutive mass-spectra traces.

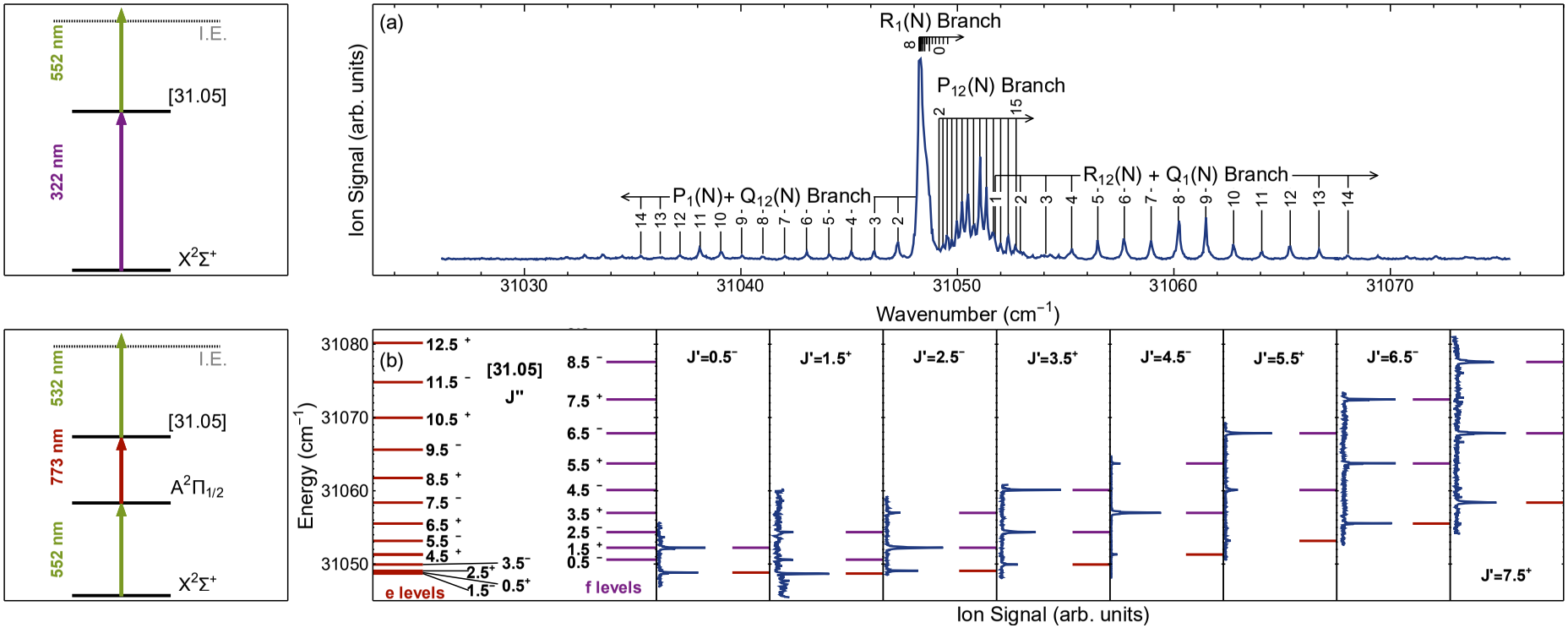

Figure 5.6: Study of [31.05]. (a) [31.05] $\leftarrow X^2\Sigma^+(v=0)$ spectrum, with assignments of rotational branches. The rotational branches are labeled in the same fashion as decribed in chapter 2. (b) Spectra of [31.05] $\leftarrow A^2\Pi_{1/2}(v'=0, J')$, where a single value of J' is used in each case and is determined by selective excitation on a known rotational transition from the X state. Each panel is labelled according to the value of J', with its parity indicated as a superscript. The vertical axis is the total excitation energy relative to the lowest energy level of $X^2\Sigma^+$. For each spectrum, this is obtained by adding up the energy of the initial rotational state of $X^2\Sigma^+$, the known energy of the $A^2\Pi_{1/2} \leftarrow X^2\Sigma^+$ excitation and the measured energy of the 773 nm photon, so that the vertical axis is the absolute energy. From these spectra we determine the rotational energy levels of [31.05], which are shown in the left panel and also as horizontal lines in the experimental spectra. The REMPI schemes used to obtain figures a) and b) are shown on the left of their respective spectra.

5.4.1 Assignment of spectral lines

Assignment of the spectral lines proved challenging because of the congestion of lines in the central region of the spectrum together with the irregular intensities observed. Instead, assignment of the rotational lines was made by excitation via a well characterised intermediate state. The $(1 + 1' + 1)$ two-colour REMPI scheme used to assign rotational levels in [31.05] is shown on the left of figure 5.6. The first step is to excite molecules to a known rotational level J' of $A^2\Pi_{1/2}(v = 0)$. We do this using a pulsed dye laser tuned to a selected rotational line in either the P_{12} or R_1 branches of the $A^2\Pi_{1/2}(v = 0) \leftarrow X^2\Sigma^+(v = 0)$ transition at 552 nm (branch notation is the same as described in the caption of Fig. 5.6). The rotational structure of these branches is well resolved and well characterised, so we can be sure to populate only one rotational state, J'. Then, we use a second pulsed dye laser at 773 nm to drive $[31.05] \leftarrow A^2\Pi_{1/2}(v = 0, J')$ transitions. There are, at most, three possible transitions, due to the angular momentum selection rule, so the spectrum is hugely simplified. We use a 532 nm pulsed Nd:YAG laser to ionise from [31.05], and then detect these ions. There is a 10 ns time delay between each of the laser pulses.

Figure 5.6(b) shows scans of the $[31.05] \leftarrow A^2\Pi_{1/2}(v = 0, J')$ transition for various values of J'. In each case, we add together the measured energy of the 773 nm photon with the known energy of the $A^2\Pi_{1/2} \leftarrow X^2\Sigma^+$ excitation and the known energy of the initial rotational level of $X^2\Sigma^+$, so that the vertical axis is the absolute energy. As expected, the method produces very simple and unambiguous spectra. For example, excitation of the $P_{12}(2)$ line prepares the negative parity component with $J' = 0.5$ of $A^2\Pi_{1/2}(v = 0)$. From here the only levels of [31.05] that can be excited are positive parity components with $J'' = 0.5$ and 1.5. We see only these two lines in the spectrum. The $J'' = 1.5$ line (but not $J'' = 0.5$) is observed again when we excite from the negative parity component of $J' = 2.5$, providing an unambiguous assignment. Continuing in this way, all lines can be assigned. Our method effectively measures the rotational energy levels directly, rather than the usual method of extracting the level structure from a fit to a spectrum.

The rotational energy levels determined this way are shown on the left of figure 5.6(b). We

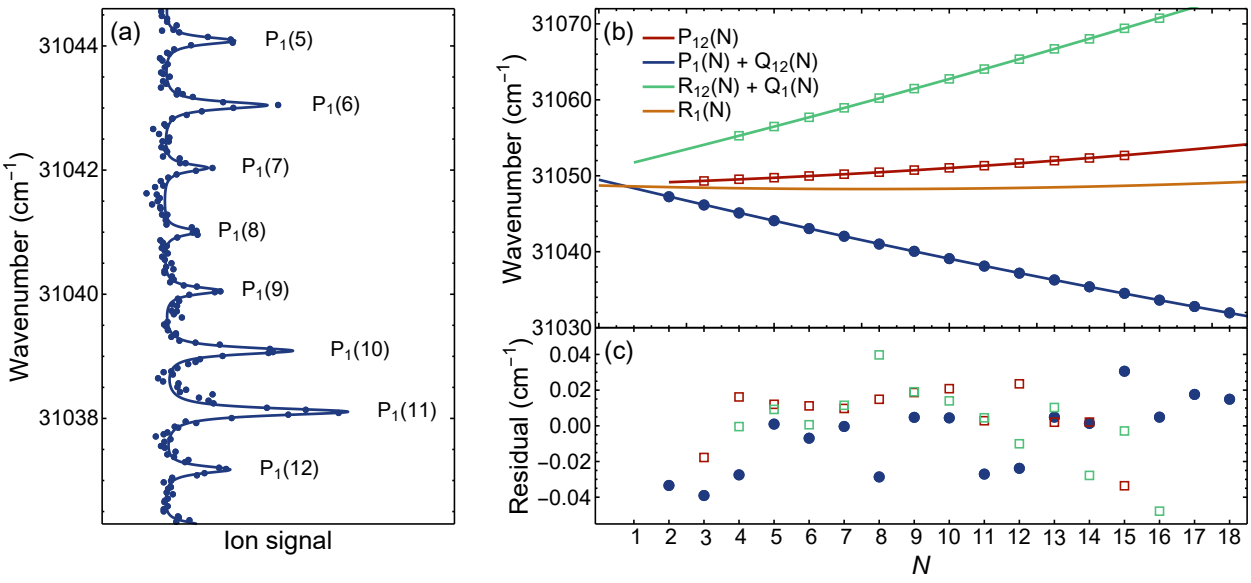

Figure 5.7: Fitting procedure for the $[31.05] \leftarrow X^2\Sigma^+(v = 0)$ spectrum. Spectral lines are fitted with Lorentzian curves to determine the line center as shown in (a). The line positions as a function of quantum number N for all fitted line positions is shown in (b). The solid lines in (b) show the result of a fit to our Hund's case (c) model. The residuals to the fit are displayed in (c).

immediately see the similarity to the structure illustrated in figure 5.5(a), clearly identifying that [31.05] is a state with $|\Omega| = 1/2$. We see that level J of the f manifold lies between levels $J + 3$ and $J + 4$ of the e manifold. A preliminary fit of these energy levels is used in order to assign the observed transitions in figure 5.6(a).

5.4.2 Fitting to the spectrum

In order to fit spectroscopic constants we first determine the central line positions by fitting a Lorentzian model to individual rotational lines in the spectrum where these do not overlap significantly. An example of this fit is shown for a selection of $P_1(N)$ lines in figure 5.7. The Lorentzians fit well, with a common linewidth of 0.06 cm^{-1}. Figure 5.7 shows the frequencies of the 43 rotational lines as a function of the rotational quantum number, N, identified in this way.

The energies of the rotational lines, $E_{\rm rot}(N)$, in [31.05] $\leftarrow$ X$^2\Sigma^+(v=0)$ can be given by

$$E_{\rm rot}(N) = E_{[31.05]} - E_{\rm X}, \tag{5.10}$$

Here, $E_{[31.05]}$, denotes the energies of rotational states in [31.05] given in Hund's case (c) by equation 5.9. $E_{\rm X}$ denotes the energies of the rotational states in $X^2\Sigma^+(v=0)$ as described in chapter 2 in Hund's case (b). We set the term proportional to B^2/Δ to zero for this fit. For completeness, the expressions we fit for all allowed rotational branches are given below.

$$\begin{aligned}
P_1(N) &= T_{[31.05]} + B_{[31.05]}(N-1/2)(N+1/2) - \frac{B_{[31.05]}}{2}\zeta_{[31.05]}(2N) - F_1(N) \\
Q_1(N) &= T_{[31.05]} + B_{[31.05]}(N+1/2)(N+3/2) + \frac{B_{[31.05]}}{2}\zeta_{[31.05]}(2N+2) - F_1(N) \\
R_1(N) &= T_{[31.05]} + B_{[31.05]}(N+3/2)(N+5/2) - \frac{B_{[31.05]}}{2}\zeta_{[31.05]}(2N+4) - F_1(N) \\
P_{12}(N) &= T_{[31.05]} + B_{[31.05]}(N-3/2)(N-1/2) + \frac{B_{[31.05]}}{2}\zeta_{[31.05]}(2N-2) - F_2(N) \\
Q_{12}(N) &= T_{[31.05]} + B_{[31.05]}(N-1/2)(N+1/2) + \frac{B_{[31.05]}}{2}\zeta_{[31.05]}(2N) - F_2(N) \\
R_{12}(N) &= T_{[31.05]} + B_{[31.05]}(N+1/2)(N+3/2) + \frac{B_{[31.05]}}{2}\zeta_{[31.05]}(2N+2) - F_2(N)
\end{aligned} \tag{5.11}$$

Here F_1 and F_2 are the spin multiplet energies in a Hund's case (b) molecule, as previously described in section 2, and are given by the expressions below.

$$\begin{aligned}
F_1(N) &= BN(N+1) - DN^2(N+1)^2 + \frac{\gamma_N}{2}N \\
F_2(N) &= BN(N+1) - DN^2(N+1)^2 - \frac{\gamma_N}{2}(N+1) \\
&\text{with } \gamma_N = \gamma_0 + \gamma_1 N(N+1) + \gamma_2 N^2(N+1)^2
\end{aligned} \tag{5.12}$$

The constants have the same meaning as described in chapter 2 and the previous section. A combined, non-weighted, non-linear fit of the 43 lines from this spectrum to the expressions in Eq. 5.11 is used to determine the spectroscopic constants for [31.05]. The spectroscopic constants for the $X^2\Sigma^+(v=0)$ state are fixed to their known values. The fitted branch lines

are shown as solid lines in figure 5.7(b) and the spectroscopic constants resulting from this fit are presented in table 5.1. The standard deviation of the residuals is 0.02 cm^{-1}. The value of $\zeta = 3.522$ corresponds to the case where the state is a 52:48 mixture of two electronic states with $J_a = 7/2$ and $J_a = 5/2$.

The isotope shift between the different YbF isotopologues can provide useful information about the vibrational band of the transition. We define the isotope shift between the ^{174}YbF and ^{176}YbF isotopologues as

$$\delta E = E_i\left(^{176}\text{YbF}\right) - E_i\left(^{174}\text{YbF}\right), \tag{5.13}$$

where $E_i(j)$ is the transition frequency of a single rovibrational transition, i, for some isotopologue, j. Recall that the vibrational energy is proportional to $\omega_e(v + 1/2)$. The vibrational constant, ω_e, will scale proportional to $1/\sqrt{\mu}$, where μ is the reduced mass of the molecule. From the difference in vibrational constants, and assuming that ω_e for [31.05] is similar to that in $X^2\Sigma^+$, we would expect a vibrational isotope shift of about -0.28 cm^{-1} between the ^{174}YbF and ^{176}YbF isotopologues for a 0-1 vibrational band. For the rotational spectra in [31.05] $\leftarrow X^2\Sigma^+(v = 0)$, we do not observe significant isotope shifts of the isotopologues and therefore assign this transition as a 0-0 vibrational band.

5.4.3 Lifetime of [31.05]

The lifetime of [31.05] is determined by time-resolved photo-ionisation using the same REMPI scheme as used to obtain the data in figure 5.6(b). The use of such time-resolved photo-ionisation to measure lifetimes of states was first reported in ref. [126]. We excite a single rotational state in $A^2\Pi_{1/2}$ by first driving a transition $A^2\Pi_{1/2} \leftarrow X^2\Sigma^+$ with 552 nm excitation and then populate a single rotational state in [31.05] with a 773 nm laser, delayed in time from the first by 10 ns. The ion signal is recorded as a function of the time delay between the 773 nm excitation and 532 nm ionisation laser pulses. The ion signal monitored in this manner, is representative of the population in the rotational state excited in [31.05]. We record a few points with negative time delay, meaning the 532 nm ionisation laser pulse comes entirely

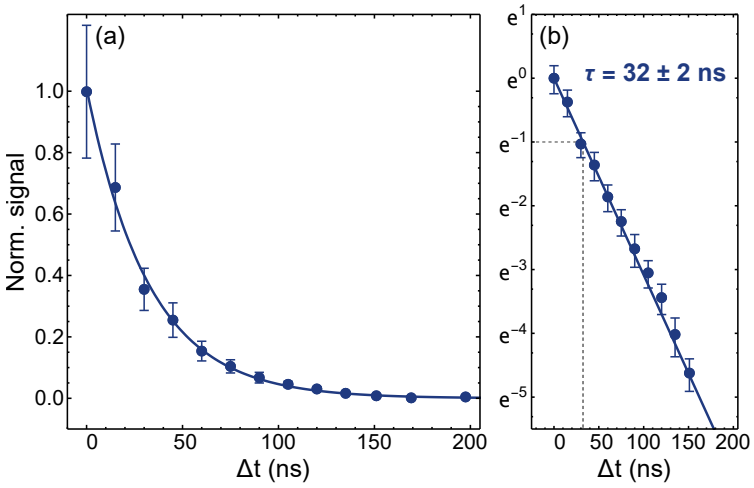

Figure 5.8: Lifetime measurement of [31.05]. (a) Normalised ion signal as a function of the time delay, Δt, between the excitation and ionisation laser pulses. The line is a fit to a single exponential decay. (b) The same data presented on a natural log scale. The error bars indicate the standard error on each measurement point.

before the 733 nm excitation laser pulse. The maximum signal occurs when the two laser pulses are overlapped and we take this as time $t = 0$. We made this measurement for six different rotational states of [31.05], namely the $J = 2.5^-, 3.5^-, 3.5^+, 5.5^-, 6.5^-, 7.5^-$ states, and saw no significant difference between them. Figure 5.8 shows the mean of these six measurements, along with a fit to a single exponential model. The rate of change of population for a single excited state with linewidth Γ is

$$\frac{dN}{dt} = -\Gamma N, \tag{5.14}$$

which integrates to

$$N = N_0\, e^{\frac{-t}{\tau}}, \tag{5.15}$$

where $\tau = 1/\Gamma$ and N_0 is the initial population. When plotted on a log scale, equation 5.15 has the form

$$\ln N(t) = -t/\tau + C, \tag{5.16}$$

where $C = ln(N_0)$ is an offset. Figure 5.8(b) shows the measured data plotted on a logscale. A fit to this data gives a lifetime of 32(2) ns.

Table 5.1: Spectroscopic parameters of the states studied in this work. The parameters of [31.05] are derived from a fit to the [31.05] $\leftarrow X^2\Sigma^+(v=0)$ spectrum. The parameters of [48.72] and [48.73] are derived by fitting the energy levels to Eq. (5.9). The parameters of the $4f^{-1}$ states are from a fit of [31.05] $\leftarrow 4f^{-1}_{7/2,|\Omega|}(v)$ spectra. The parameters of [18.58] and [18.71] are derived by fitting the data from Table 4 of Ref. [104] to Eq. (5.9). All energies presented in this paper are relative to the lowest rotational state of $X^2\Sigma^+$ [48].

Label	State composition	T (cm^{-1})	B (cm^{-1})	ζ
[8.47]	$4f^{-1}_{7/2,1/2}(v=0)$	8474.390(9)	0.26737(6)	3.8760(24)
[9.01]	$4f^{-1}_{7/2,3/2}(v=0)$	9012.541(6)	0.26597(8)	–
[9.09]	$4f^{-1}_{7/2,1/2}(v=1)$	9090.675(7)	0.2656(1)	3.8756(24)
[18.58]	$4f^{-1}_{5/2,1/2}(v=0)$ and $A^2\Pi_{1/2}(v=1)$	18580.574(2)	0.25466(6)	-1.7698(10)
[18.71]	$4f^{-1}_{5/2,1/2}(v=0)$ and $A^2\Pi_{1/2}(v=1)$	18705.007(2)	0.25687(6)	-1.9607(10)
[31.05]	$\|\Omega\|=1/2\,(v=0)$	31049.541(5)	0.24921(3)	3.5220(12)
[48.72]	$\|\Omega\|=3/2\,(v\approx 4)$	48720.277(3)	0.25162(3)	–
[48.73]	$J_a=3/2, \|\Omega\|=1/2\,(v\approx 2)$	48729.01(4)	0.2568(6)	2.016(12)

5.5 The autoionising states: [48.72] and [48.73]

We use [31.05] as the upper state in our spectroscopy of the $4f$ hole states, and the information obtained in the last section is crucial for understanding these spectra. Even with this information, the spectra were difficult to interpret. The relative intensities of rotational lines can be a great help in assigning quantum numbers in a spectrum, particularly when rotational lines overlap. In the present study, however, the observed intensities do not follow a thermal distribution or the expected Hönl-London factors as is already evident from the spectrum shown in figure. 5.6. Instead, the observed intensity pattern is skewed because we reach auto-ionising resonances above the ionisation energy of the molecule. These resonances prove to be both interesting and useful for understanding the $4f$ hole spectra. In this section we study these auto-ionising resonances, and in the next section we make use of them to help interpret the $4f$ hole spectra.

The ionisation energy of YbF is at 48703 ± 5 cm^{-1} [123]. Figure 5.9 shows scans above this ionisation energy. The excitation sequence is illustrated in the inset. First, a single rotational state (J) of [31.05] is populated by driving a single line of either the $P_1\,(N)$ or $R_{12}\,(N)$ branches

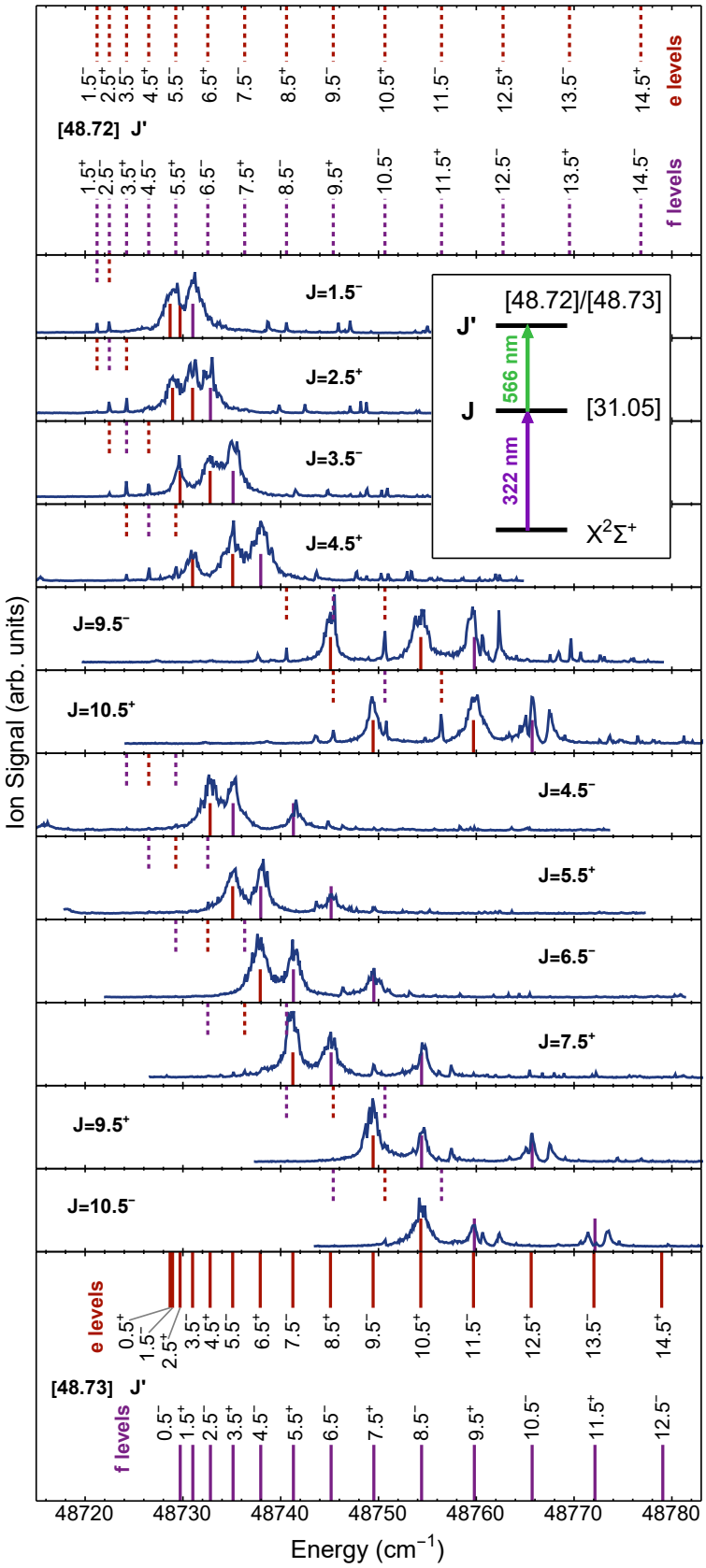

Figure 5.9: Spectroscopic study of [48.72] and [48.73]. The inset shows the selective ionisation scheme used. The first step prepares population in a single rotational level, J, of [31.05]. The rotational structure of [48.72] and [48.73] is then measured as the 566 nm laser is scanned. The set of middle panels show the spectra obtained for various J and for both parity components. The horizontal axis gives the total energy. The fitted energy levels are shown as red/purple vertical lines (dashed for [48.72], solid for [48.73]). The upper and lower panels show the complete set of energy levels determined by this spectroscopy.

of the [31.05] $\leftarrow X^2\Sigma^+(v=0)$ transition (see figure 5.6(a)). Then, a second laser at around 566 nm is scanned, resulting in ionisation of the molecule. The horizontal axis in figure 5.9 is the total energy relative to the lowest level of $X^2\Sigma^+$. We determine this for each spectrum by adding together the known energy of the initial level of $X^2\Sigma^+$, the fitted energy of [31.05] $\leftarrow X^2\Sigma^+$ and the energy of the 566 nm photon. The spectra in Fig. 5.9 contain a sequence of narrow resonances with Lorentzian widths limited by the laser linewidth, corresponding to states with remarkably long lifetimes of over 100 ps, and a series of broader resonances with Lorentzian widths (FWHM) of 1.4 cm^{-1}, corresponding to a lifetime of 3.7 ps. We first focus on these broad resonances and find that they correspond to the rotational structure of a state that we call [48.73] because its term energy is close to 48730 cm^{-1}. The uppermost spectrum in the figure corresponds to excitation from the negative parity, $J = 1.5$ level in [31.05]. This was excited by driving the $P_1(2)$ line of the [31.05] $\leftarrow X^2\Sigma^+(v=0)$ transition. The three allowed transitions to the positive parity $J' = 0.5, 1.5, 2.5$ levels are marked by vertical lines. The positive parity $J' = 2.5$ level is measured again in the spectrum where the selected lower level is the negative parity $J = 3.5$ level, confirming its assignment. The energy level structure of [48.73] is discerned by repeating this process for all the values of J shown in the figure. The resulting level structure is shown at the bottom of figure 5.9. Within our uncertainties, we find that level J' of the f manifold is degenerate with level $J' + 2$ of the e manifold, which tells us that [48.73] has $|\Omega| = 1/2$ and $J_a = 3/2$, and that it conforms exactly to the simple Hund's case (c) model described in section 5.3. Fitting the energy levels to equation (5.9)[1] gives the parameters summarised in Table 5.1. The standard deviation of the residuals from this fit is 0.1 cm^{-1}, which is commensurate with the increased uncertainty due to the width of the transitions. The residuals for this fit are shown in figure 5.10(b). By comparing our measured spectra for the various isotopologues of YbF, we find that the rotational lines of [48.73] $\leftarrow$ [31.05] show a significant isotope-dependent shift. This isotope shift is consistent with [48.73] having about 1000 cm^{-1} more vibrational energy than [31.05]. Since [31.05] has $v = 0$ and vibrational constants in YbF are typically around 500 cm^{-1}, we suggest that [48.73] has $v \approx 2$.

[1] We set the term proportional to B^2/Δ to zero in this fit

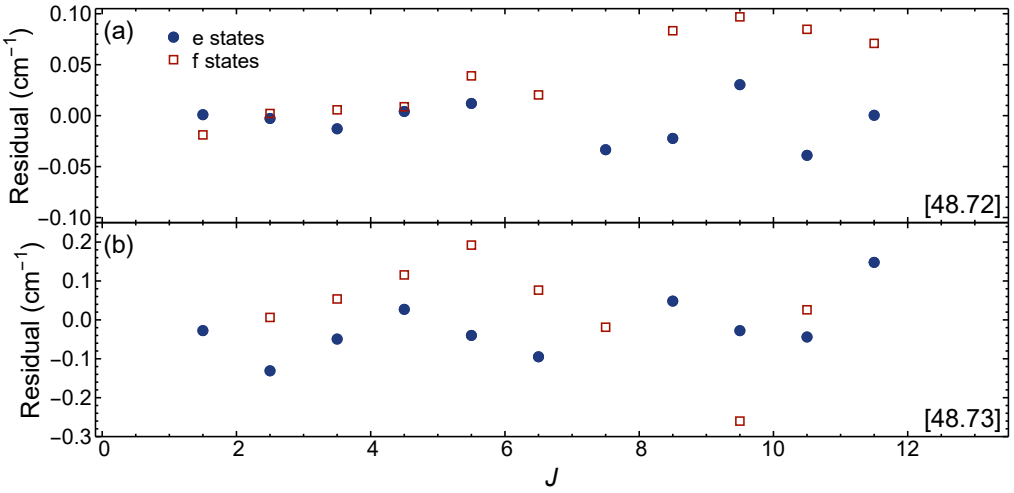

Figure 5.10: Error in the fit to our Hund's case (c) model of the observed [48.72] and [48.73] energy levels.

The structure of the narrow transitions can be discerned in much the same way. In keeping with the nomenclature above, we label the series of narrow peaks near 48720 cm^{-1} as [48.72]. Two key observations can be made about the structure of this state. First, we see that there are no excitations $J' = 0.5 \leftarrow J = 1.5$, i.e. $J' = 1.5$ is the first rotational state. Second, we find that levels with the same J' in the e and f manifolds are degenerate. In our Hund's case (c) model, this conforms well to a state of $|\Omega| = 3/2$. The term energy, T, and rotational constant, B, obtained by a weighted fit to Eq. (5.9) are presented in Table 5.1. For an $|\Omega| > 1/2$ state there is no ζ parameter, so only these two constants are relevant[1]. The residuals from this fit, shown in figure 5.10(a), all fall within their uncertainties. Transitions [48.72] $\leftarrow$ [31.05] show a large isotope shift consistent with [48.72] having almost 2000 cm^{-1} more vibrational energy than [31.05]. Such an isotope shift would be consistent with $v \approx 4$. We note that excitations to [48.72] via [31.05] $\leftarrow$ $X^2\Sigma^+(v = 0)$ R_{12} transitions are not as visible in figure 5.9 as those obtained via excitation on P_1 transitions.

Each ionisation spectrum in figure 5.9 is a unique 'fingerprint' of the rotational level prepared in [31.05]. We now use these fingerprints to help us characterise the $4f_{7/2}^{-1}$ states.

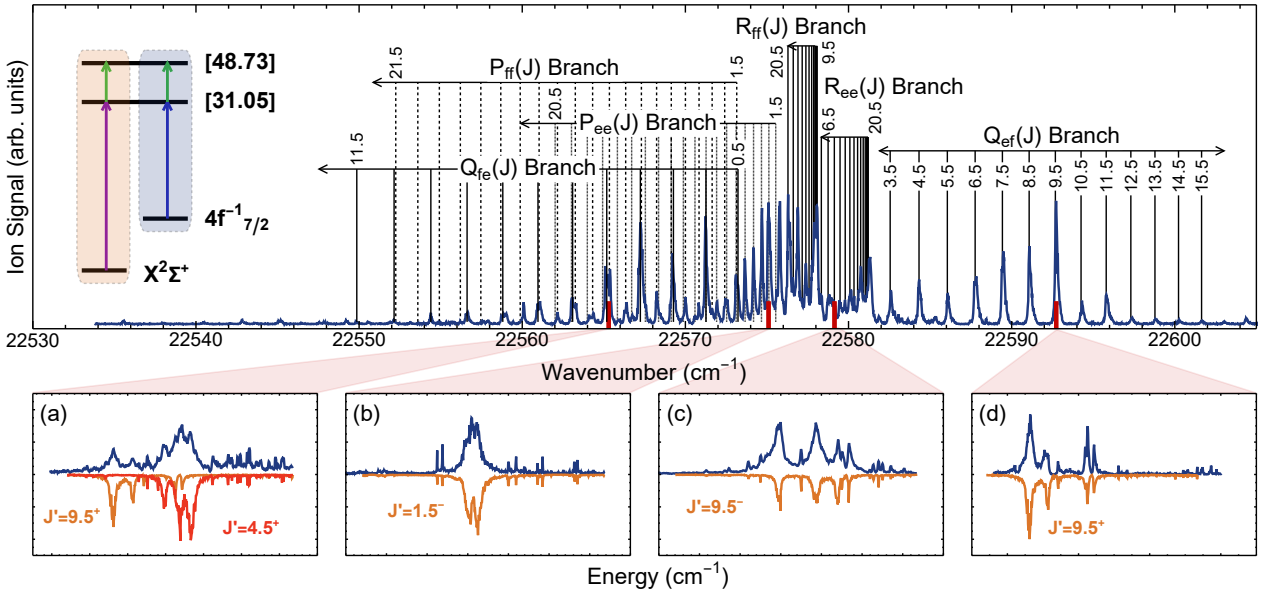

Figure 5.11: The rotational spectrum of the [31.05] $\leftarrow 4f^{-1}_{7/2,1/2}(v=0)$ transition. The branch labelling is described in the text. Example ionisation spectra are shown in (a) - (d). Characterisation of the rotational branches was made by recording ionisation spectra (blue) at selected excitation frequencies (red lines in top panel) and then comparing them to a reference spectrum (orange) obtained by starting from the $X^2\Sigma^+$ state. The REMPI schemes to obtain blue and orange curves are highlighted in the energy level diagram on the left.

5.6 The leak states: $4f^{-1}_{7/2}$

In this section we present rotationally resolved spectra of the [31.05] $\leftarrow 4f^{-1}_{7/2}$ transitions measured using two colour (1+1′) REMPI. The supersonic source produces sufficient population in the $4f^{-1}_{7/2}$ states to do this spectroscopy directly.

Figure 5.11 shows the observed spectrum of [31.05] $\leftarrow 4f^{-1}_{7/2,1/2}(v=0)$. The excitation scheme used to obtain the spectrum is shaded in blue. A first excitation laser driving the [31.05] $\leftarrow$ $4f^{-1}_{7/2}$ transition is scanned. A second 'ionisation' laser drives the [48.73] $\leftarrow$ [31.05] transition, producing ions which are then extracted and detected in the time-of-flight mass spectrometer. There is a 10 ns delay between the two laser pulses. The ion signal is much stronger when detected resonantly via [48.73], than when ionizing with 532 nm light. Since the auto-ionising states are broad, a single ionisation laser frequency is sufficient to observe many rotational lines in the [31.05] $\leftarrow 4f^{-1}_{7/2}$ spectrum. Note that the intensity of any given rotational line in the spectrum will depend on the strengths of the two excitation steps and also on the detuning of

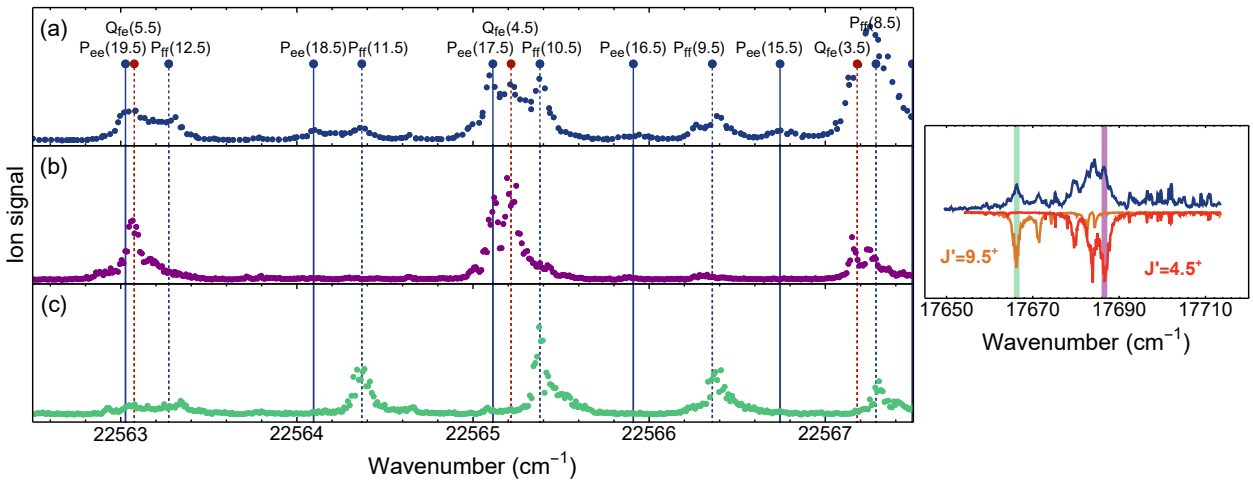

Figure 5.12: Selective ionisation permits resolving different rotational lines in the spectrum [31.05] $\leftarrow 4f^{-1}_{7/2,1/2}(v=0)$. A portion of the spectrum shown in figure 5.11 is repeated here in (a) alongside the ionisation spectrum when exciting at 22565.30 cm^{-1} (rightmost panel-replicated from figure 5.11(a)). By changing the ionisation frequency to either the purple or teal frequencies, we can select to view predominantly only Q_{fe} or P_{ff} lines respectively, as can be seen in (b) and (c).

the ionization laser from the resonance relevant to that rotational line. The intensity pattern can be very different if a different frequency is chosen for the ionisation laser, which makes it challenging to extract useful information from the intensities.

5.6.1 Assignment of rotational lines: "fingerprinting"

Assignment of the rotational lines was achieved with the help of the reference ionisation spectra (or 'fingerprints') noted above. We choose a particular line in the spectrum and fix the frequency of the excitation laser to the frequency of that line. This excites some particular rotational level J' of [31.05]. To determine J', we now scan the ionisation laser across the [48.73] state. The resulting ionisation spectrum is unique for each J' and can be compared to the 'reference' ionisation spectra in figure 5.9. Figure 5.11(a-d) shows four examples of this procedure, corresponding to the four positions marked by red lines in the upper panel. The blue lines are the ionisation spectra obtained after excitation from $4f^{-1}_{7/2,1/2}(v=0)$, while the orange lines are the reference spectra from figure 5.9. As an example, consider figure 5.11(d) where the excitation frequency is 22592.73 cm^{-1}. The ionisation spectrum matches that of the positive parity $J'=9.5$ level in [31.05]. This identifies the upper level for this line in the

spectrum, but not yet the lower level which could have $J = 8.5, 9.5$ or 10.5. The same level of [31.05] is reached again when we excite at 22565.30 cm^{-1}, as shown in figure 5.11(a). Here, the ionisation spectrum is more complicated, corresponding to the sum of two fingerprints, namely the positive parity components of $J' = 9.5$ (orange) and $J' = 4.5$ (red), meaning that two distinct lines are excited at this frequency. Following this procedure, each rotational level J of $4f^{-1}_{7/2,1/2}(v = 0)$ can in principle be observed three times, corresponding to the P, Q and R lines going to $J' = J - 1$, J and $J + 1$ of [31.05]. For each rotational line observed in the spectrum the absolute energy of the lower level can be calculated by subtracting the excitation frequency from the known energy of the [31.05] rotational level we are exciting to. A unique assignment of the rotational quantum number J can be made once a P and an R line coming from the same J (identified by having the same lower energy) have been measured. The energy level structure we determine this way is summarised in figure 5.15(a). The similarity to the level structure for the ideal $J_a = 7/2, |\Omega| = 1/2$ state is evident by comparison to figure 5.5(a).

5.6.2 Fitting to the spectra

The rotational bands in figure 5.11 are labelled using the notation $\Delta J_{p'p''}$ where p' and p'' are either e or f and denote the symmetry of the $4f^{-1}_{7/2}$ and [31.05] rotational states, respectively. We observe two bandheads in the R_{ff} and R_{ee} branches occurring at $J = 9.5$ and $J = 20.5$ respectively. As before, we fit Lorentzians to the rotational lines in the spectrum.

The low frequency side of the spectrum is congested with the P_{ff}, P_{ee} and Q_{fe} lines all overlapping. To better resolve this region of the spectrum, we set the ionisation frequency to selectively ionise only some rotational levels. This is illustrated in figure 5.12. For example, in figure 5.11(a) (which has been replicated on the right of figure 5.12) we see that there exist ionisation frequencies where only the $P_{ff}(10.5)$ line and $Q_{fe}(4.5)$ lines are respectively detected. These frequencies are indicated by vertical teal and purple lines respectively. Figure 5.12(b) shows a scan around the region of the spectrum containing the $P_{ff}(10.5)$ and $Q_{fe}(4.5)$ lines when the ionisation frequency is selectively chosen to detect the $Q_{fe}(4.5)$ line. We see that, predominantly, the Q_{fe} lines are visible. The same scan is repeated in figure 5.12(c) with the

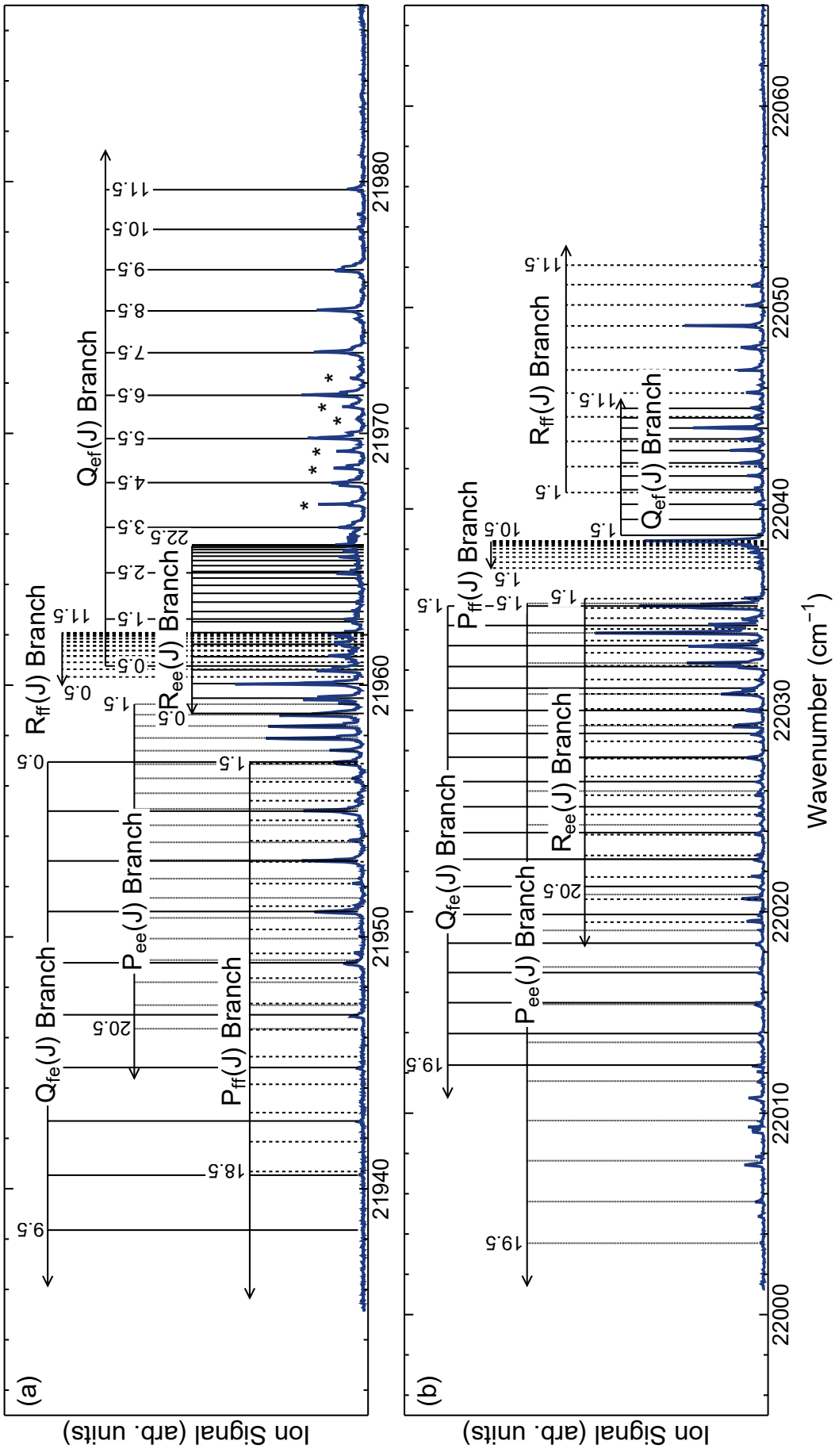

Figure 5.13: (a) Spectrum of the [31.05] $\leftarrow 4f^{-1}_{7/2,1/2}(v=1)$ transition. Note that there are a few unassigned lines near 21968 cm^{-1} (marked with an *) that do not belong to this transition. (b) Spectrum of the [31.05] $\leftarrow 4f^{-1}_{7/2,3/2}(v=0)$ transition. The notation is the same as in figure 5.11.

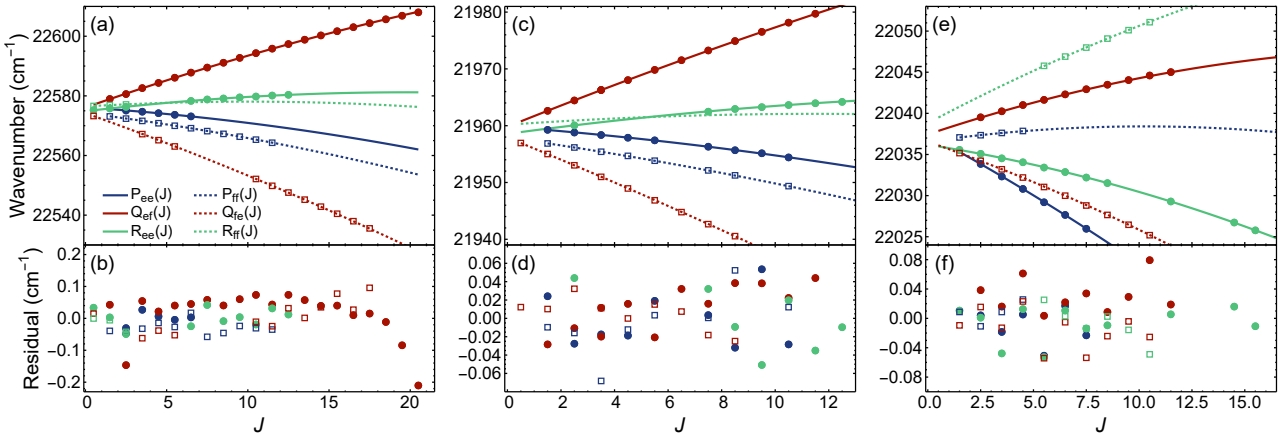

Figure 5.14: Rotational line frequencies as a function of quantum number J for (a): the $[31.05] \leftarrow 4f^{-1}_{7/2,1/2}(v=0)$ spectrum. (c): the $[31.05] \leftarrow 4f^{-1}_{7/2,1/2}(v=1)$ spectrum and (e): the $[31.05] \leftarrow 4f^{-1}_{7/2,3/2}(v=0)$ spectrum. Solid and dashed lines indicate the result of the fit. The fit residuals are shown beneath each plot.

ionisation frequency selectively chosen to detect the $P_{ff}(10.5)$ line. In this case, only the P_{ff} lines are visible. This procedure has been repeated for many of the overlapping peaks.

In total, we fit 61 rotational lines to a model where the rotational energy level structure in both the excited and ground state conform to Hund's case (c), as described by Eq. (5.9). The values for the excited state constants are fixed to those obtained from our fit of the $[31.05] \leftarrow X^2\Sigma^+(v=0)$ spectrum. In this fit, we fix Δ to our measured difference in term energies for $|\Omega| = 1/2$ and $3/2$, which is $\Delta = -538.151$ cm^{-1} (see Table 5.1 and next paragraph). Table 5.1 gives the best fit parameters. The rotational constant is in agreement with the value predicted from the bond length calculated in [112]. The value of ζ does not uniquely determine the coefficients c_{J_a} but is consistent with a dominantly $J_a = 7/2$ state; the upper bound on $|c_{7/2}|$ is 0.94.

Figure 5.13 shows our measured spectra for the $[31.05] \leftarrow 4f^{-1}_{7/2,1/2}(v=1)$ and $[31.05] \leftarrow 4f^{-1}_{7/2,3/2}(v=0)$ transitions. We use the same methodology as described above to assign quantum numbers to the lines in these spectra, and the same analysis methods to determine the spectroscopic constants, using 44 and 47 lines respectively. The energy difference, $E_{3/2} - E_{5/2}$, is set to -790 cm^{-1}, based on the work by Persinger et al. [123]. For the state with $|\Omega| = 3/2$, the ζ term is not relevant and we omit it.

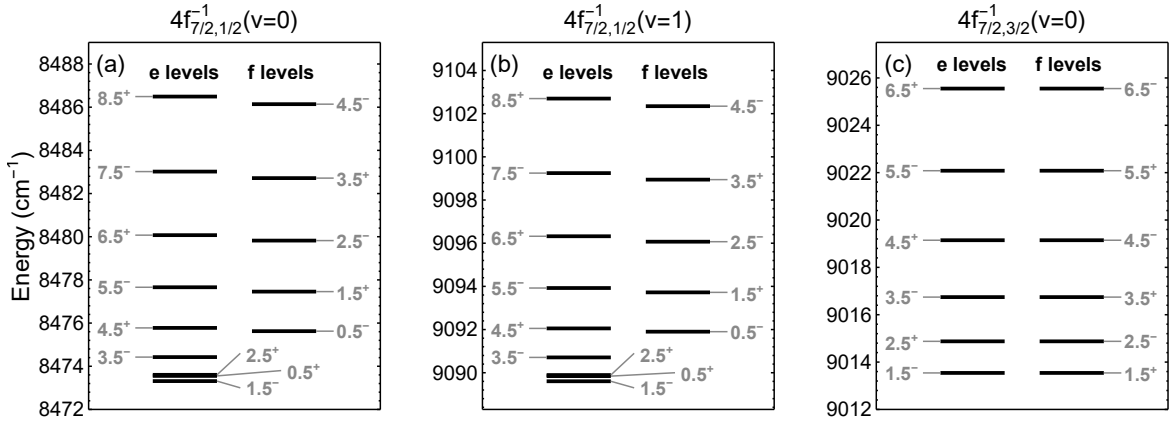

Figure 5.15: Summary of the energy level structures of the low-lying $4f$ hole states studied in this work: (a) $4f^{-1}_{7/2,1/2}(v=0)$, (b) $4f^{-1}_{7/2,1/2}(v=1)$, (c) $4f^{-1}_{7/2,3/2}(v=0)$.

Figure 5.14 shows the frequencies of the rotational lines of the three obtained $4f^{-1}_{7/2}$ spectra as a function of the angular momentum J. The results of the fit are shown as solid lines and the residuals are displayed beneath each figure. The spectroscopic constants we determine are reported in Table 5.1, and the energy level structures are summarized in figure 5.15.

5.7 The mixed character repump states: [18.58] and [18.71]

The $v = 0$ level of $4f^{-1}_{5/2,1/2}$ lies very close in energy to the $v = 1$ level of $A^2\Pi_{1/2}$, and they are strongly mixed. In our notation, the resulting eigenstates are labelled [18.58] and [18.71][2]. These two states have strong transitions to $X^2\Sigma^+$, and their rotational energy level structure has been measured previously by cw laser spectroscopy of the [18.58] $\leftarrow X^2\Sigma^+$ and [18.71] $\leftarrow X^2\Sigma^+$ transitions [104]. The states were characterized by modelling them as $^2\Pi_{1/2}$ states in Hund's case (a). By fitting the energy levels given in Table 4 of [104][3] to Eq. (5.9)[4] , we find that both states fit well to our model of an $|\Omega| = 1/2$ state in Hund's case (c). The residuals show some structure but are all below 0.01 cm^{-1}. The parameters of these fits are given in Table 5.1. For both states, the value of B is consistent with the value determined from the $^2\Pi_{1/2}$ model. The values of ζ are negative, consistent with the negative value of the Λ-doubling constant

[2]Elsewhere, e.g [104, 112], these states are instead labelled by their frequencies in THz: [557] and [561].
[3]There is an error in Table 4 of [104]: the e and f labels are the wrong way around.
[4]We set the term proportional to B^2/Δ to zero in this fit

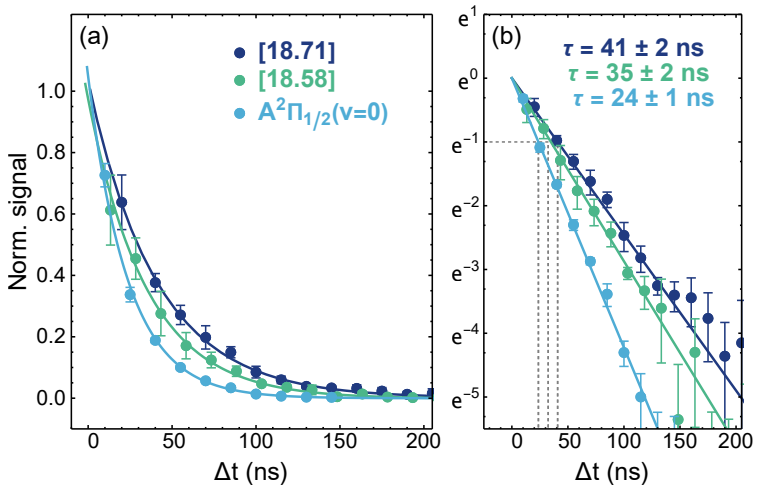

Figure 5.16: Lifetime measurements of [18.58], [18.71] and $A^2\Pi_{1/2}(v = 0)$ states of ^{174}YbF. The data are presented on a natural log scale in (b). The error bars indicate the standard error on each measurement point.

$(p + 2q)$ when modelled as a case (a) state. A discussion of the sign of this parameter is given by Hougen [127].

A previous deperturbation analysis [112] suggests that [18.58] has 52% $A^2\Pi_{1/2}(v = 1)$ character and 46% $4f^{-1}_{5/2,1/2}(v = 0)$ character, while for [18.71] the fractions are 47% and 51%. The remaining composition comes from other vibrational levels of the same electronic states and they are all at least an order of magnitude smaller. Below, we study these compositions by measuring the lifetimes of the two states.

5.7.1 Lifetimes of [18.58] and [18.71]

For a two level system, the lifetime, τ, of an excited state $|\psi\rangle$ is given by

$$\tau = \frac{3\pi\varepsilon_0\hbar c^3}{\omega^3|\langle\psi|d|g\rangle|^2}, \tag{5.17}$$

where ε_0 is the permittivity of free space, ω is the angular frequency of the transition, c is the speed of light, $\hbar$ is the reduced Planck constant and $\langle\psi|d|g\rangle$ is the transition dipole moment between the excited state $|\psi\rangle$ and the ground state $|g\rangle$. Consider the case where the excited state is a mixed state $|\psi\rangle = c_1|\phi_1\rangle + c_2|\phi_2\rangle$. In this case, the transition dipole moment squared

is

$$
\begin{aligned}
|\langle\psi|d|g\rangle|^2 &= \langle c_1\phi_1 + c_2\phi_2|d|g\rangle^2 \\
&= |c_1|^2\langle\phi_1|d|g\rangle^2 + |c_2|^2\langle\phi_2|d|g\rangle^2 + 2c_1c_2\langle\phi_1|d|g\rangle\langle\phi_2|d|g\rangle\,. \qquad (5.18)
\end{aligned}
$$

In our case, ψ denotes either [18.58] or [18.71] and ϕ_1 and ϕ_2 denote the A state and the perturbing stat, $4f^{-1}_{5/2,1/2}$. The transition dipole moment for the A-X transition is about 100 times larger than for the $4f^{-1}_{5/2,1/2}$-X transition. In this limit, where the mixing is strong and one transition dipole is much larger than the other, the transition dipole moment for the mixed character state can be approximated as

$$
|\langle\psi|d|g\rangle|^2 \approx |c_1|^2\langle\phi_1|d|g\rangle^2\,. \qquad (5.19)
$$

The lifetime of the mixed state whose A state amplitude is c_A is simply $\tau_\psi \simeq \tau_A/|c_A|^2$, where τ_A is the lifetime of the A state. We have measured the lifetimes of $A^2\Pi_{1/2}(v=0)$, [18.58] and [18.71] using the delayed ionisation method described in section 5.4. In each case, we measured the lifetime on three different rotational lines and averaged the data. Figure 5.16 shows our results. Fitting single exponential decays to these data we obtain the following lifetimes: $\tau_A = 24(1)$ ns, $\tau_{[18.58]} = 35(2)$ ns and $\tau_{[18.71]} = 41(2)$ ns. Our value of τ_A is consistent with the value of 28(2) ns measured previously [102]. These results imply that for [18.58] $|c_A|^2 = 69(5)\%$, while for [18.71] $|c_A|^2 = 58(4)\%$. These percentages are both a little larger than determined through the deperturbation analysis, but confirm that the two mixed states are indeed close to 50:50 mixtures.

5.8 Summary and discussion

In this chapter, we've studied the rotational structure of a series of states in YbF that have $4f$ hole character. The low-lying $4f$ hole states are of particular importance since our optical cycle is suspected to have a leak to these states. Our study of these low-lying $4f$ hole states in

YbF has determined the character of these states. They derive from the $4f^{13}6s^2$ configuration of Yb^+, which is split by a very large spin-orbit interaction into two terms, the one with $J_a = 7/2$ lying approximately 10000 cm^{-1} below the one with $J_a = 5/2$. Each of these is split by the electric field of the F^- ion into a set of states labelled by $|\Omega|$, but this splitting is much smaller, 500-1000 cm^{-1}. The rotational splitting is much smaller again, around 1 cm^{-1}, resulting in a convenient structural hierarchy conforming to Hund's case (c). The rotational structures of the $4f$ hole states fit very well to this model, requiring only 3 parameters – a term energy, a rotational constant, and an effective value of $J_a + 1/2$. In this chapter, we have determined these constants to high precision. In previous work, the energies, bond lengths and vibrational constants of the $4f$ hole states were calculated [112]. Taking our measured value for the rotational constant, $B = \frac{\hbar^2}{2\mu r_0^2} = 0.26737(6)$, where μ is the reduced mass of the YbF molecule, implies a bond length of $r_0 = 1.9187(2)$ Å. This is consistent with the calculations, which predict it to be around 1.93 Å. Similarly, the energy difference between $4f^{-1}_{7/2,1/2}(v = 0)$ and $4f^{-1}_{7/2,1/2}(v = 1)$, measured to be 616.285(11) cm^{-1}, is close to the calculated value of 614.3 cm^{-1}.

We consider the splitting between the $|\Omega|$ components of the $4f$ hole states to be the Stark splitting of the Yb^+ $4f^{13}6s^2\,{}^2F_{7/2}$ state. To support this picture, we estimate the polarisability of this configuration using second-order perturbation theory, summing over all relevant states of the ion. A table of the required transition frequencies and Einstein A-coefficients is given in [128]. We find the difference in polarisability between the $|\Omega| = 1/2$ and $|\Omega| = 3/2$ components to be $\alpha_{1/2} - \alpha_{3/2} = 1.19 \times 10^{-41}$ $J\,m^2\,V^{-2}$. Our measured splitting is $\Delta = E_{1/2} - E_{3/2} = -538.15$ cm^{-1}, implying an electric field of 4.25×10^{10} $V\,m^{-1}$ at the Yb^+ ion. This is the electric field produced by a charge placed 1.84 Å away. Given the simplicity of this picture, and the doubtful validity of using perturbation theory for such an enormous electric field, the result is remarkably close to the actual bond length of 1.92 Å.

As discussed in chapter 4, laser slowing and magneto-optical trapping of YbF using the $A^2\Pi_{1/2} \leftrightarrow X^2\Sigma^+$ transition will be hindered by small leaks from $A^2\Pi_{1/2}$ into $4f^{-1}_{7/2,1/2}(v = 0)$ and $4f^{-1}_{7/2,1/2}(v = 1)$. These small leaks open up because of a small mixing between the $4f^{-1}_{7/2,1/2}$ and $X^2\Sigma^+$ states [112]. Since the mixing preserves Ω, leaks to the $4f$ hole states with $|\Omega| > 1/2$ are thought

Table 5.2: Frequencies (in cm^{-1}) required to repump population from the relevant $4f$ hole states through either the [18.58] or [18.71] states. The uncertainty is mainly limited by the absolute accuracy of the wavemeter and is less than 0.03 cm^{-1}

	$[18.58](J = 1/2, e)$	$[18.71](J = 1/2, e)$
$[8.47](J = 1/2, f)$	10105.609	10230.091
$[8.47](J = 3/2, e)$	10107.956	10232.438
$[9.09](J = 1/2, f)$	9489.315	9613.797
$[9.09](J = 3/2, e)$	9491.612	9616.094

to be negligible. Leaks to $4f$ hole states with $v > 1$ are also sufficiently small due to small Franck-Condon factors. Given the upper state used for laser cooling, and the parity and angular momentum selection rules, leaks should only populate the negative parity components with $J = 0.5$ and $J = 1.5$. This population can be returned to the laser cooling cycle using additional repump lasers. Repumping via $A^2\Pi_{1/2}(v = 0)$ is not recommended since stimulated emission into the $4f$ hole states will reduce the photon scattering rate. Repumping via [31.05] is also a poor option, even though it connects strongly to both the $4f$ hole and X states, because this will transfer population to $4f^{-1}_{7/2,3/2}$. A better option is to repump via [18.58] and/or [18.71]. Our work establishes the required laser frequencies for this repump scheme, which are listed in table 5.2. The $J = 0.5^-$ and $J = 1.5^-$ states are separated by around 2.3 cm^{-1} in both $4f^{-1}_{7/2,1/2}(v = 0)$ and $4f^{-1}_{7/2,1/2}(v = 1)$. Closing the leaks to these states will therefore require either four separate lasers, or two lasers with high frequency modulators, alongside the four lasers used in chapter 4 to address $X^2\Sigma^+(v = 0, 1, 2, 3)$ [105, 106]. Based on previous measurements and calculations of branching ratios [102, 103, 112], it should then be possible to scatter about 10^5 photons, which is sufficient for radiation pressure slowing and magneto-optical trapping.

Although the low-lying $4f$ hole states have been primarily presented as a hindrance to laser slowing thus far, it is interesting to consider whether these low-lying $4f$ hole states may themselves be useful in measuring the eEDM. Electron EDM experiments measure the interaction energy between the EDM and an effective electric field, E_{eff}, which is enormous in heavy polar molecules. When the molecule has a pair of near-degenerate states of opposite parity, a small applied electric field fully polarises the molecule producing a pair of states where E_{eff} is equal and opposite. This ability to reverse the sign of the interaction through the choice

of state is exploited both two most precise eEDM measurements to date, ACME's experiment using ThO [29] and JILA's experiment utilising HfF^+ ions [26]. The ground states of laser coolable molecules do not have this structure, so attention has recently turned to polyatomic molecules [71]. The present work shows that the $4f$ hole states *do* have this structure providing long-lived states with closely-spaced parity doublets in a laser coolable molecule. The sensitivity to the EDM is proportional to E_{eff}, the value of which is not known for these sets of states and further work in calculating E_{eff} for this system would be of great interest. Furthermore, the $4f$ hole states may prove to be useful sensors of electric and magnetic fields, which is important for precision measurement. Closely-spaced parity doublets produce linear Stark shifts at low electric fields, and some of the $4f$ hole states should have strong Zeeman shifts. Measurements of these Stark and Zeeman shifts would be valuable. Finally, we note the considerable interest in developing molecular clocks, both as frequency standards and for measuring variations of fundamental constants [129, 130]. The transition from the ground state to one of the $4f$ hole states may be suitable for such a clock, similar to the Yb^+ clock based on the equivalent electric octupole transition [115]. A measurement of the lifetimes of the $4f_{7/2}^{-1}$ states would be valuable.

[31.05] and [48.73] have a very similar rotational structure to the low-lying $4f^{-1}$ states. It is likely that they also correspond to excitations out of the 4f shell, though we do not currently know their underlying configurations. [48.73] is especially notable as it conforms almost exactly to the Hund's case (c) model with $|\Omega| = 1/2$ and $J_a = 3/2$. A broad-band spectroscopic survey of the entire set of inner-shell excited states in YbF would be useful, as would quantum chemistry calculations of this set. Through this combination of spectroscopy and calculation, it should be possible to determine the character of each state.

We have found many electronic states above the ionisation energy, including [48.72] and [48.73] studied here. Some of them have remarkably long lifetimes, and we suppose that these also correspond to excitation of a $4f$ electron. We attribute the existence of such strong and narrow auto-ionising resonances to the weak coupling between the two series of electronically excited states. [48.73] has a $4f$ hole but does not have enough energy to auto-ionise to any $4f$ hole state of the YbF^+ cation or to dissociate to a state that has a $4f$ excitation in the atom or ion. Thus, [48.73] can only auto-ionise into the closed-shell ground-state of YbF^+, which requires a two-

electron Auger process. Indeed, the first core-hole excited state of the cation can be considered as the effective ionisation potential of the series of YbF $4f$ hole states, and is likely to lie approximately 8000-10000 cm^{-1} above the normal ionisation potential of the molecule. The existence of strong auto-ionising states may open a channel for efficient state-selective detection of YbF by CW laser excitation to an auto-ionizing state. So far, detection of YbF has utilised fluorescence detection which is often limited to an efficiency of about 10% [131], whereas ion detection can have almost unit efficiency if there is sufficient laser power for ionisation. Finally, we note that these resonances result in an ionisation spectrum that is different for each rotational state, which can be helpful in assigning quantum numbers to a spectrum. This method proved to be an extremely useful tool for elucidating the energy level structure of the $4f$ hole states from their complicated spectra.

Chapter 6

Setting up the MOT

6.1 Introduction

The magneto-optical trap [132] is often the workhorse of experiments with ultracold atoms. For us too it is the first step towards achieving trapped YbF molecules which can then be used to measure the eEDM. Molecular magneto-optical traps are still in their infancy compared to their atomic cousins. The first magneto-optical trap of molecules was achieved in 2014 using SrF molecules [69]. Since then, MOTs of CaF [65, 91], YO [90] and BaF [38] have additionally been developed and further molecular MOTs including those of AlF and MgF are currently under development [39, 63, 133]. YbF presents additional challenges compared to the molecular species that have been trapped so far. YbF is both heavier and has less favourable Franck-Condon factors, which in turn requires the use of a greater number of repump lasers. We wish to use the magneto-optical trap as a springboard towards loading an optical dipole trap. In order to do so we require efficient loading of the MOT, followed by compression and sub-Doppler cooling to well below the trap depth of a dipole trap, $\sim$200 μK. The time to load, cool and transfer the molecules out of the MOT is expected to be on the order of 50 ms, so we aim for a MOT lifetime on this order. In this section, we describe the progress in developing such a magneto-optical trap, which was carried out in parallel with the work in the previous chapters. We begin by describing the hardware used to construct the magneto-optical trap

chamber. We show that using a suitable frequency configuration for the MOT light we expect to achieve maximum accelerations of 6 km/s^2. We then proceed to carefully characterise the photo-detection setup in the MOT.

6.1.1 Background

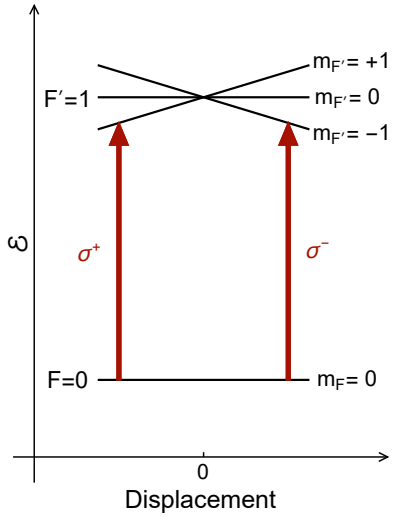

Figure 6.1: Operating principle of a magneto-optical trap in one dimension. Red detuned, counter-propagating laser beams driving $\Delta m_F = -1$ and $\Delta m_F = +1$ transitions respectively interact with an atom. As the displacement of the atom changes, a magnetic field preferentially brings the atom into resonance with the restoring beam.

We begin by considering the laser cooling and trapping forces in a magneto-optical trap. A MOT provides confinement using radiation pressure from three pairs of counter propagating laser beams and a magnetic field gradient that is zero at the center of the trap. Each pair of counter-propagating laser beams generally provides confinement along one of three orthogonal axes. Figure 6.1 illustrates this confinement in a single axis for the case of an atom with angular momentum $F' = 1$ in the excited state and $F = 0$ in the ground state. The excited and ground states have magnetic moments g' and g, respectively. In this case $|g'| \gg |g|$. The magnetic field applied is such that it is zero at the center of the trap and increases linearly with displacement. The increasing magnetic field causes the energies of m'_F energy levels of the excited state to similarly Zeeman shift increasingly. The two counter-propagating laser beams are both red-detuned. Both beams are left-hand circularly polarised such that the beam propagating from left to right drives transitions with $\Delta m_F = +1$ while the beam propagating

from right to left drives transitions with $\Delta m_F = -1$. We label these as σ^+ and σ^-, respectively. The combination of the laser polarisation and the linearly increasing magnetic field causes the scattering probability to vary spatially providing a restorative force. Consider an atom, initially in $m_F = 0$, at negative displacement from the center of the trap. Due to the Zeeman shift, the atom will come into resonance with the σ^+ beam. The restorative beam is closer to resonance, and therefore the atom is much more likely to scatter photons from the restorative beam than from the beam pushing it away from the trap (which is further from resonance).

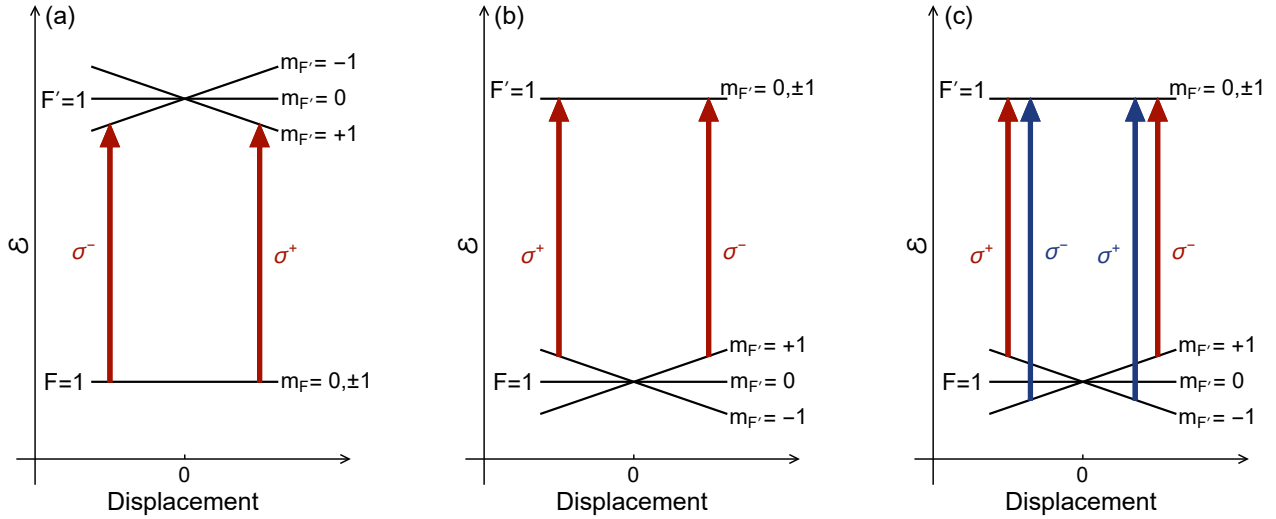

Figure 6.2: Angular momentum cases for which operating a magneto-optical trap is challenging. (a): Both the ground and excited states have $F' = F = 1$ and there is little to no Zeeman splitting in the ground state. (b): $F' = F = 1$ and there is greater Zeeman splitting in the ground state than the excited state. (c): A 'dual frequency' MOT can be used to restore a trapping force in configuration (b). Additional restoring beams of opposite handedness pump molecules back from dark states. For all cases here, $g' < 0$, as is the case for the $A^2\Pi_{1/2}$ state.

The situation is more complicated when using molecules. All molecules that have so far been confined in a MOT have the added complication that the excited state has much smaller Zeeman splitting than the ground state, and often have the same total angular momentum F. Figure 6.2(a-b) shows two situations for which magneto-optical trapping forces break down in one-dimension. These cases are discussed in greater detail in [134]. Our description here is for $g' < 0$ since this is the sign of g' for the $A^2\Pi_{1/2}$ state in YbF. Consider first the case where the upper state and ground state have equal angular momentum $F' = F = 1$. This case is shown in figure 6.2(a). Here, $|g'| \gg |g|$ as before, though this condition is not necessary for the following argument. In one-dimension there is no restoring force for this configuration. To understand

why, consider a molecule that is initially in $m_F = +1$ in the ground state. This molecule can only scatter photons from the σ^- beam and will be optically pumped to $m_F = -1$. A molecule in $m_F = -1$ can only scatter photons from the σ^+ beam and will be pumped to $m_F = +1$. On average, each molecule will scatter the same number of photons from each laser beam and there will be no net restoring force. The situation is somewhat ameliorated when considering confinement in three dimensions. For positive trap displacement, an $m_F = -1$ molecule will come into resonance with the restoring σ^+ beam. It is also possible for an $m_F = -1$ molecule to scatter photons from the orthogonal beams, however, this is less likely to occur as the orthogonal beams drive $\Delta m_F = 0$ transitions and are therefore further from resonance. As a result, photon scattering is more likely from the restoring beam. Similarly, let us consider a molecule at positive trap displacement but in the $m_F = +1$ state. The molecule can scatter from both the anti-restoring σ^- beam as well as the orthogonal beams. Since, however, the anti-restoring beam is Zeeman-shifted *away* from resonance, the molecule is more likely to scatter from the orthogonal beams. Finally, a molecule in $m_F = 0$ can scatter from both the restoring and anti-restoring beam but is more likely to scatter from the restoring beam since the transition to $m'_F = +1$ is closer to resonance. There is therefore an overall preference to excite from the restoring beam and a small restorative force is recovered.

The second case we consider is similar to the first, only now $|g'| \ll |g|$. This is shown in figure 6.2(b). Consider a positive trap displacement. Here, molecules in the $m_F = +1$ state can scatter from both the restoring and orthogonal beams. This occurs with equal probability since the $\Delta m_F = -1$ and $\Delta m_F = 0$ transitions are at the same detuning from resonance. Similarly molecules in $m_F = -1$ will only scatter from the anti-restoring and orthogonal beams. Molecules in the $m_F = 0$ state will scatter from both the anti-restoring and restoring laser with equal probability since both laser beams are now at the same frequency to excite both $\Delta m_F = \pm 1$ transitions. The scattering probability from $m_F = -1$ is lower than that from $m_F = +1$ since the light is further from resonance for the $m_F = -1 \rightarrow m'_F = 0$ transition than it is for the $m_F = +1 \rightarrow m'_F = 0$. This means that population will accumulate in $m_F = -1$. To get around this and recover a trapping force one of two options can be implemented. A second frequency component is added to the restoring beam on resonance with the $m_F = -1 \rightarrow m'_F = 0$

transition to preferentially scatter molecules in this state. This is known as a dual-frequency MOT and an example of this is shown in 6.2(c). Alternatively, both the magnetic field and polarisation of the laser beams can be modulated at the rate similar to which population accumulates in this state. This is known as an RF MOT [70]. Both RF [90, 91, 108] and dual frequency [65, 69, 87, 91, 135] MOTs have been successfully implemented for other molecules.

In this section we describe the progress towards the creation of a dual frequency MOT for YbF molecules.

6.2 MOT hardware

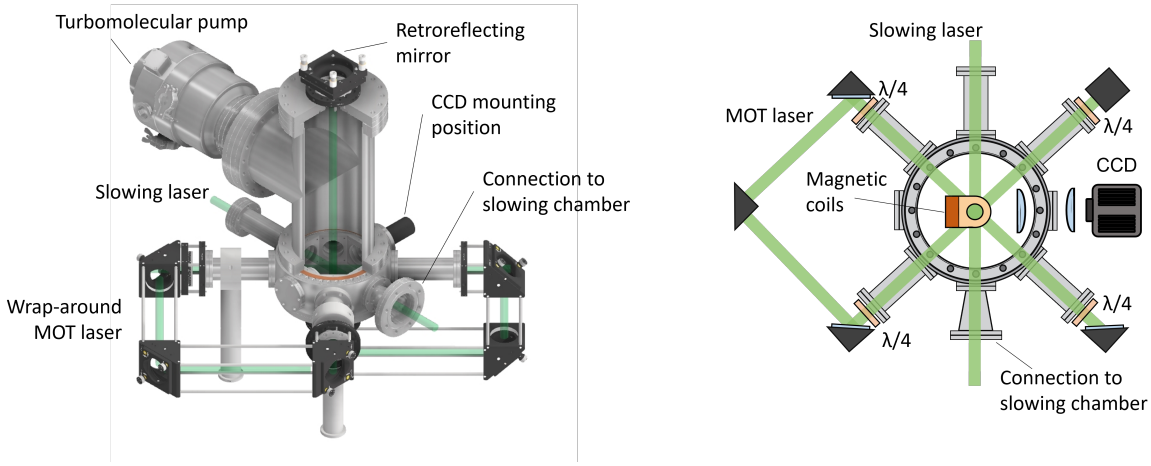

Figure 6.3: The MOT chamber assembly. The optics setup is shown on the right. The MOT light is formed from a single laser beam that wraps around the MOT chamber.

Figure 6.3 shows the design of the MOT chamber assembly. The MOT chamber itself was used to demonstrate magneto-optical trapping of CaF [95, 96, 136, 137] in our group before that experiment moved to a larger chamber with greater optical access. The MOT chamber is connected to the remainder of the beamline via an adapter flange. A 20 cm long, 20 mm diameter differential pumping tube limits the gas flow such that a higher vacuum can be achieved in the MOT chamber. A turbo molecular pump (250 l/s pumping speed) mounted to a cross-piece vacuum chamber is used to evacuate the MOT chamber. Optical access into the chamber is provided by eight windows. Six are used for the MOT light, one is used for the entry of the

slowing light and a final window allows for detection of the molecules. All the windows are anti-reflection coated for both light around 552 nm and 1100 nm. To reduce the power requirements, the MOT is formed of a single laser beam that wraps around the MOT chamber. Losses in power as the beam passes through the optical components can be mitigated by focusing the laser beam through the setup so that the intensity remains approximately constant. Quarter-wave plates at every entry and exit circularly polarise the beams to the appropriate handedness. In-vacuum coils (described below) provide the required magnetic field gradient to Zeeman shift molecules back into resonance. Current is provided to the coils via a set of high-current electrical feedthroughs. An aluminium cage coated in black soot surrounds the coils and acts as a baffle to reduce laser scatter.

6.2.1 Magnetic field coils

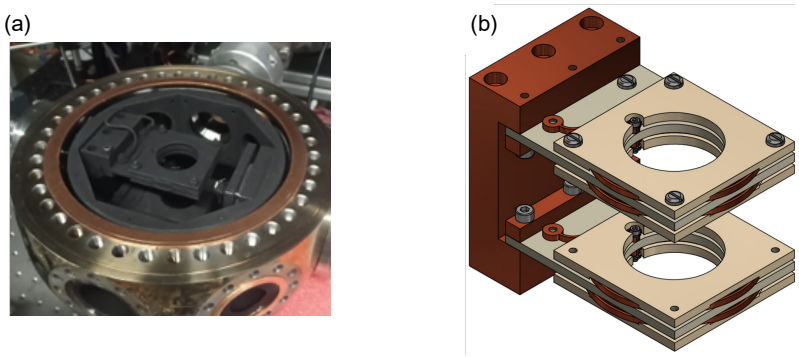

Figure 6.4: The in-vacuum MOT coils. The coils consist of two pairs of interconnected copper spirals each with 8 turns and separated by 40 mm. The spirals are each clamped between an aluminium nitride ceramic and a polymer (PEEK) plate. (a) shows the vacuum coils mounted inside the MOT chamber. The coils have been painted black to reduce laser scatter. This figure has been adapted from [138].

The design of the in-vacuum magnetic field coils is shown in figure 6.4. The coils were inherited alongside the chamber and their design is additionally described in [136, 138]. Two current-carrying coils in an anti-Helmholtz configuration are used to generate a magnetic field that is zero at the center of the MOT region and has a tunable radial magnetic field gradient of around 20 G/cm. Coils mounted outside the vacuum chamber can create fringe fields which can have adverse effects on the efficiency of laser slowing. In addition the necessarily large size

of externally mounted coils gives a large relaxation time to switching the coils on/off. To avoid this, the magnetic field coils in this design were placed inside of the chamber [136]. Usual designs for magnetic field coils consists of several turns of copper wire, where the wire is in contact. To prevent shorting, the coils require an insulating wrapper which in general is not vacuum compatible and can outgas, especially when hot. Instead, a more complicated design is used where two sets of two interconnected copper spirals form the electrodes of the electromagnet. Each spiral consists of 8 turns machined from a single piece of copper. To allow efficient heat dissipation, each spiral is placed between a shapal plate (ceramic aluminium nitride with boron nitride providing good thermal conductivity). In addition, to prevent the two spirals forming each electrode from touching, a PEEK plate is placed between them. Mounting the coils in vacuum means that good thermal dissipation is harder to achieve. Typical currents of 10 A are used. Given the resistance of the coils is around 0.04 Ω, the coils need to dissipate $P = I^2R = 4$ W of power [136, 138]. For heat dissipation, the shapal plates are connected to a copper block which is in turn anchored to the bottom flange of the MOT chamber. Nevertheless, heating of the coils still occurs which leads to outgassing into the MOT chamber increasing the operating pressure. To mitigate this, the coils are switched off between each shot. The relaxation time of these smaller coils is on the order of 1 ms, fast enough that they can be switched off between experimental shots. We map out the radial magnetic field on axis from

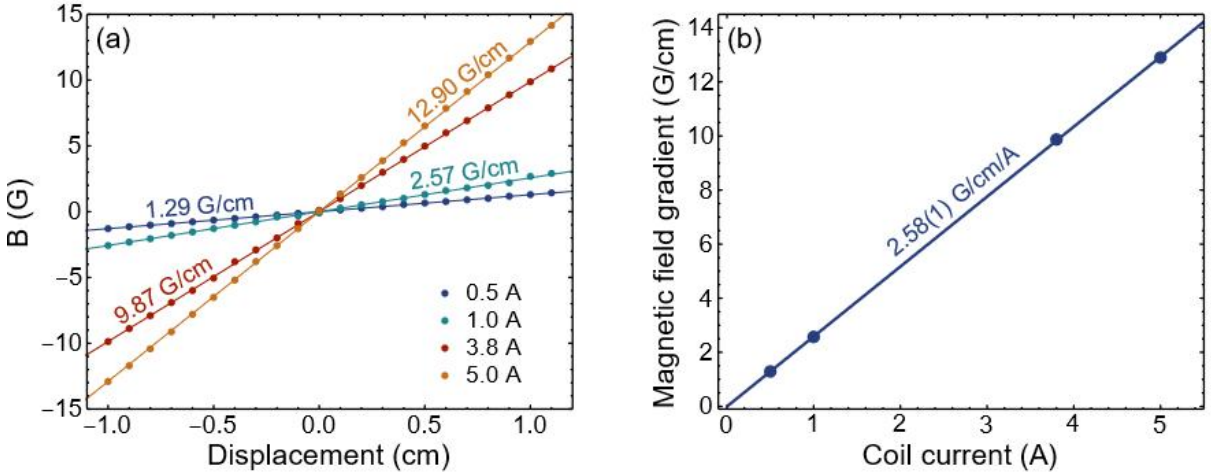

Figure 6.5: Magnetic field calibration as a function of coil current for the MOT coils. (a) The magnetic field as a function of displacement along one axis of the coils. The magnetic field gradient is measured for four different coil currents to give a calibration factor for the magnetic field gradient as a function of coil current shown in (b).

the center of the coil using a Hall probe. The results are summarised in figure 6.5. The coils produce a uniform magnetic field gradient of 2.58(1) G/cm/A across the measured range of 20 mm.

6.3 Frequency configuration and MOT optics

6.3.1 Sideband structure

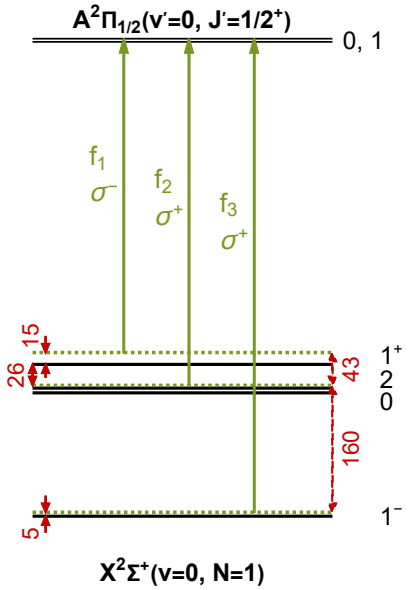

Figure 6.6: Proposed frequency components for a dual frequency MOT of YbF on the P(1) rotational line of $A^2\Pi_{1/2} \leftarrow X^2\Sigma^+$. Three frequency components are used to drive hyperfine transitions from $X^2\Sigma^+$. Two of the components are red and blue detuned, respectively, from the $F = 1^+$ level and of opposite polarisation to each other to generate a trapping force.

We plan to use the same optical cycling scheme for the magneto-optical trap as that described in chapter 4. The trapping laser, $\mathcal{L}_0^{\mathrm{MOT}}$, addresses the P(1) rotational line of the $A^2\Pi_{1/2}(v = 0, J = 1/2) \leftarrow X^2\Sigma^+(v = 0, N = 1)$ transition, the same transition we have used so far for detection and laser slowing. The proposed frequency configuration for $\mathcal{L}_0^{\mathrm{MOT}}$ is shown in figure 6.6. The hyperfine structure in the $X^2\Sigma^+(v = 0, N = 1)$ state is addressed by three frequency components. The polarisation of each component is also indicated in figure 6.6 along with its detuning. The $F = 1^+$ level is addressed by both a red and a blue detuned frequency component

of opposite polarisation to each other. This is the situation of a dual frequency MOT that is described in figure 6.2(c) and provides the main confining force. To evaluate the efficacy of such a trapping scheme, we calculate the acceleration of the molecules as a function of displacement along the axis of the magnetic field coils, z, as well as at the center of the MOT for various velocities along z, denoted v_z.

We use PyLCP [139], an open-source Python package that uses a rate equation approach to calculate the scattering force from arbitrary laser fields. PyLCP has built in functionality for solving molecular Hamiltonians in magnetic fields and has been used to model 3D-MOT geometries of CaF and MgF [140]. Here we use it to test the configuration described above in YbF. The model takes into account all of the hyperfine frequency components in each of the six MOT beams, the magnetic field produced by the quadrupole coils, all the relevant levels of the molecule in the $X^2\Sigma^+$ and $A^2\Pi_{1/2}$ states, their Zeeman shifts, and the transition strengths between all the levels for a given polarisation. The model is able to reproduce the results presented in [134] and provides good estimates for experimentally observed forces [95].

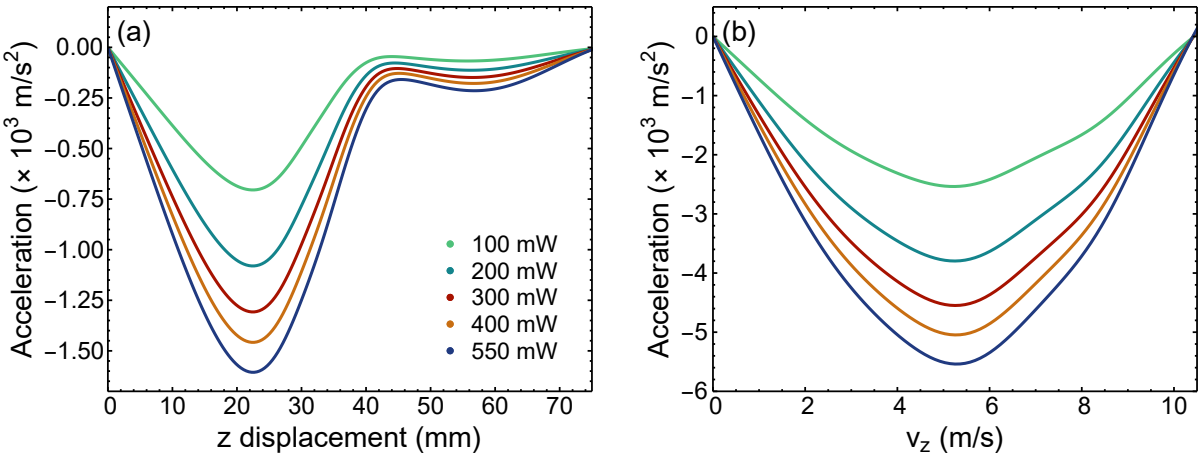

Figure 6.7: Simulated acceleration of a magneto-optical trap of YbF using the frequency components shown in figure 6.6. (a): Acceleration as a function of position experienced by a stationary molecule. (b): Acceleration as a function of velocity for a molecule at the center of the trap.

Figure 6.7 summarises the results of the simulation. The MOT beams are modelled as having constant laser intensity spread over a circle of radius 12 mm, and the magnetic field gradient is taken as 20 G/cm. Figure 6.7(a) shows the predicted acceleration for a stationary molecule as a function of displacement from the trap center along the z axis. We find that there is a confining

force for axial displacements up to ±40 mm. When using 550 mW of total power split across the three frequency components in the MOT as shown in figure 6.6, the maximum acceleration is for a stationary molecule is -1.6×10^3 m/s^2. Figure 6.7(b) shows the acceleration at the center of the trap as a function of velocity. There are strong decelerating forces, up to around -6×10^3 m/s^2 for molecules that are travelling below 10 m/s.

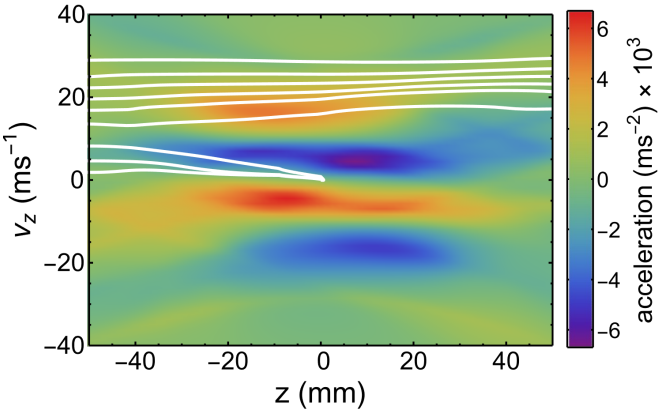

Figure 6.8: Acceleration as a function of velocity and displacement along the z axis. Simulated one dimensional phase-space trajectories of YbF molecules in the MOT are shown in white. Molecules travelling below 11 m/s are captured into the MOT.

To estimate the capture velocity of the MOT, v_c, we consider molecules entering along the axial direction. The acceleration as a function of the phase-space of the molecules along the z axis is shown in figure 6.8. This acceleration map is calculated using the same scattering rate model described above. Trajectories for molecules starting at a displacement -50 mm and with various initial velocities are shown in white. For each molecule, the local acceleration is sampled from the acceleration map shown in figure 6.8 and its motion under the influence of this acceleration propagated for a given time step. This is repeated until either successive positions of the molecule remain within the trap center or the molecule exceeds a displacement greater than 50 mm in either direction. Solving for the maximum velocity at which molecules become trapped, we find a capture velocity, $v_c = 11.1$ m/s. This estimate does not have a probabilistic treatment of absorption/emission events and neglects that the molecules will undergo a random motion due to spontaneous emission. Our approximation also neglects that molecules will enter the MOT chamber off-axis to the MOT beams.

6.3.2 MOT laser system and optics

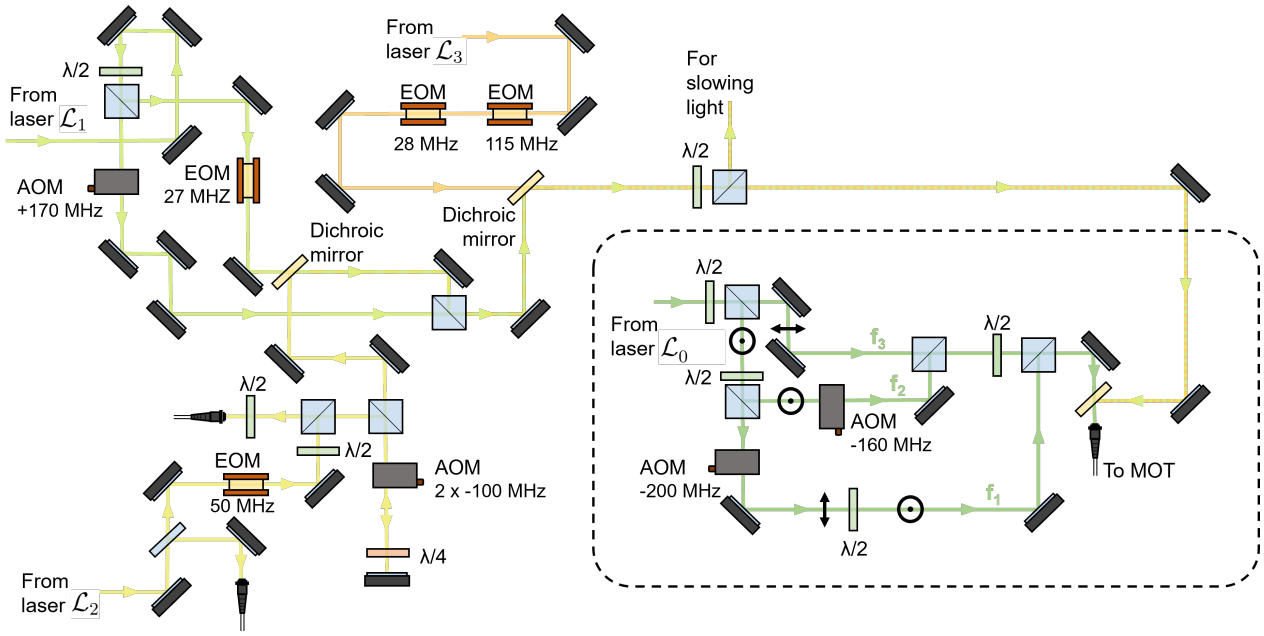

Figure 6.9: Schematic of the proposed optical setup for the magneto-optical trap. The sideband configurations for the repump lasers, $\mathcal{L}_1$, $\mathcal{L}_2$ and $\mathcal{L}_3$, used to repump population from $X^2\Sigma^+(v = 1, 2, 3)$, are the same as those used in chapter 4. The configuration for the main MOT light, $\mathcal{L}_0^{\mathrm{MOT}}$, addressing the $A^2\Pi_{1/2}(v = 0, J = 1/2) \leftarrow X^2\Sigma^+(v = 0, N = 1)$ transition is highlighted. Frequency components f_2 and f_3 are coupled to the MOT chamber with orthogonal polarisation to f_1. Here, $\lambda/2$ and $\lambda/4$ denote a half-wave plate and a quarter-wave plate respectively.

Figure 6.9 shows a schematic of the proposed MOT laser system. The configuration shown is such that light for both laser slowing and magneto-optical trapping is provided by the same lasers. The laser systems used to generate the light are therefore the same as those described in chapter 4. To generate the three sideband frequencies needed for $\mathcal{L}_0^{\mathrm{MOT}}$ the light from the laser is split into three paths using two polarising beam splitters (PBS). The proportion of light into each path can be controlled by adjusting half-wave plates placed before each PBS. Two AOMs placed in the paths of two of the beams provide the required frequency splitting. The beams are then recombined on PBSs. The trapping light requires that two frequency components, f_2 and f_3, have orthogonal circular polarisations to the remaining component, f_1. To ensure this, the beam recombination optics is designed such that f_2 and f_3 are combined first, and then transmitted through the last PBS which reflects f_1. Frequencies f_2 and f_3 are therefore coupled to the MOT chamber with orthogonal linear polarisation to f_1. A quarter-wave plate placed

at the MOT chamber can then be used to generate the required circular polarisations. Since f_1 and f_2 have orthogonal polarisation prior to their combination on the last PBS, not all of the light will be transmitted. A half-wave plate can be used to adjust the fractions of power from f_1 and f_2 that are sent to the MOT chamber. The sideband configurations for the repump lasers are the same as those outlined in chapter 4. A PBS together with a half-wave plate pick off some repump light after these have been combined with each other into one beam. The different wavelengths required to make the MOT are then combined on a dichroic mirror with a cut-off frequency near 560 nm before being coupled into the same fiber. Since the light is shared between the laser slowing and MOT, an additional double pass AOM may be needed to allow for independent adjustment of the laser frequencies between the slowing and MOT light.

6.4 Molecule detection in the MOT

We plan to detect the molecules in the MOT by imaging the fluorescence scattered by the molecules from the MOT beams onto a CCD camera. Since we're detecting the light at the same frequency as that of the MOT beams, a large source of background is expected to be light scatter from the MOT beams themselves. Under the circumstance where the light scatter is the dominant source of noise, the detectable signal will be limited by the shot noise from counting background photons. Consider the signal from 100 molecules scattering at a rate of 10^6 photons/s. In 1 ms of exposure time, 100 molecules will scatter 10^5 photons, of which we estimate the collection efficiency is around 4%. This gives 4×10^3 photons. In order to achieve a shot noise limited signal-to-noise ratio greater than 1, the photon shot noise from the background needs to be smaller than this, corresponding to $\sim 2 \times 10^7$ photons. For six MOT beams with a total power of 500 mW this is no trivial task since around 1.5×10^{18} photons enter the chamber each second. Prior to mounting the MOT chamber on the experiment it is therefore critical to characterise and reduce the background scatter. In the following we describe and characterise the detection optics and the measures taken to reduce the noise.

6.4.1 Reducing background noise

To give ourselves the best possible chance of detecting the fewest molecules we can, background scattered photons have to be prevented from reaching the detector. To limit this number, first the entire MOT chamber including connecting vacuum components and nipples are coated in soot from an oxygen-acetylene flame. The soot has a reflection of less than 0.02% [136]. The MOT coils, are spray painted with MH2200 black paint. Surrounding the MOT coils is an aluminium cylinder which is similarly coated in black MH2200 paint. This cylinder has 40 mm holes cut into it which act as baffles for the MOT beams. The windows for the MOT chambers are all anti-reflection coated. To prevent scatter from the windows reaching the detector, all nipples through which the MOT beams travel are fitted with baffles. The background against which the molecules are imaged is made from Acktar Spectral Black foil.

6.4.2 MOT detection optics

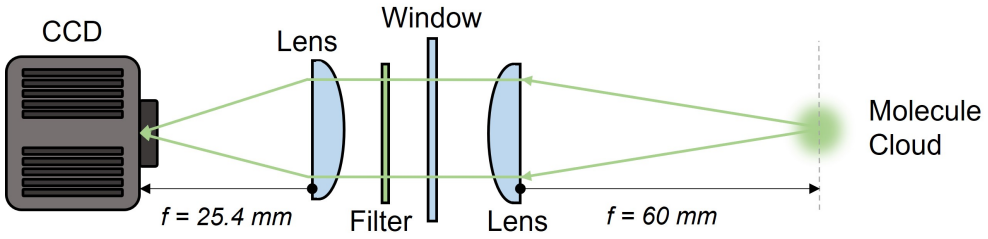

Figure 6.10: Optics for imaging laser induced fluorescence from the MOT chamber onto a CCD. LIF from the molecules is collected and collimated by an in vacuum lens. The light travels through an AR coated vacuum window flange and a band-pass interference filter to block out unwanted background light. A second lens projects an image onto a CCD.

Molecules in the MOT are imaged by collecting the laser induced fluorescence from the MOT beams onto a CCD. The optics setup used to do this is shown in figure 6.10. A plano-convex collection lens focuses emitted light from the MOT cloud. This lens is placed inside the vacuum chamber, 60 mm from the molecular cloud. It has diameter 50.8 mm and focal length 60 mm. The collimated light is focused onto a CCD (Hamamatsu C9100-23B) by a second lens placed outside the vacuum chamber with focal length 25.4 mm. This creates an imaging system with

a magnification of 0.42. The detector size of the CCD is 8.19 mm × 8.19 mm, which allows us to image an area of 19.5 mm × 19.5 mm. To limit background light, a bandpass filter centered at 550 nm is used to select the fluorescent light.

6.4.3 Smallest detectable signal in the MOT

In order to determine the smallest detectable signal, we measure the noise from our camera detection setup empirically and simulate the expected molecular signal. To measure the noise, we record N images of the background in the MOT chamber. The images are recorded with the MOT beam in situ. The MOT beam is formed of a 7.5 mm ($1/e^2$) diameter, 450 mW beam, slightly focused as it passes through the MOT. For these measurements each image is exposed for 20 ms. Alternate shots are designated as 'foreground' and 'background' shots. To simulate the signal from the MOT, the foreground shots each have signal photons added to the recorded background. Within the exposure time, $t_{\rm exp}$, a molecule will scatter $R_{\rm scat}t_{\rm exp}$ photons. We assume $R_{\rm scat} = 3 \times 10^6$ photons/s giving 6×10^4 photons in our 20 ms exposure time. Of these photons a fraction $\eta_{\rm col}\eta_{\rm t}$ will be imaged on the CCD, where $\eta_{\rm col}$ is the collection efficiency and $\eta_{\rm t}$ is the transmission efficiency through the optical imaging components. The collection efficiency is estimated as $\frac{\pi(25.4\ \rm mm)^2}{4\pi(60\ \rm mm)^2} \approx 0.04$, while $\eta_{\rm t} \approx 0.7$. The total number of photons imaged per molecule is then ≈ 1700. The photon positions on the image are drawn randomly from a Gaussian distribution,

$$n = n_0 e^{-r/2\sigma^2}, \tag{6.1}$$

where n is the number of photons at position r, n_0 is the total number of photons and σ is the width of the MOT cloud size. This signal photon count is added to the recorded photon count of the corresponding pixel of the foreground image. Finally, each 'foreground image' is subtracted from the subsequent 'background image' to generate a background subtracted signal image.

Figure 6.11 summarises the result. We model the expected signal from $n_0 = 200$, 100 and 50 molecules with a cloud size of 2 mm. The expected signal images are shown in figure 6.11(a),(c),(e). The

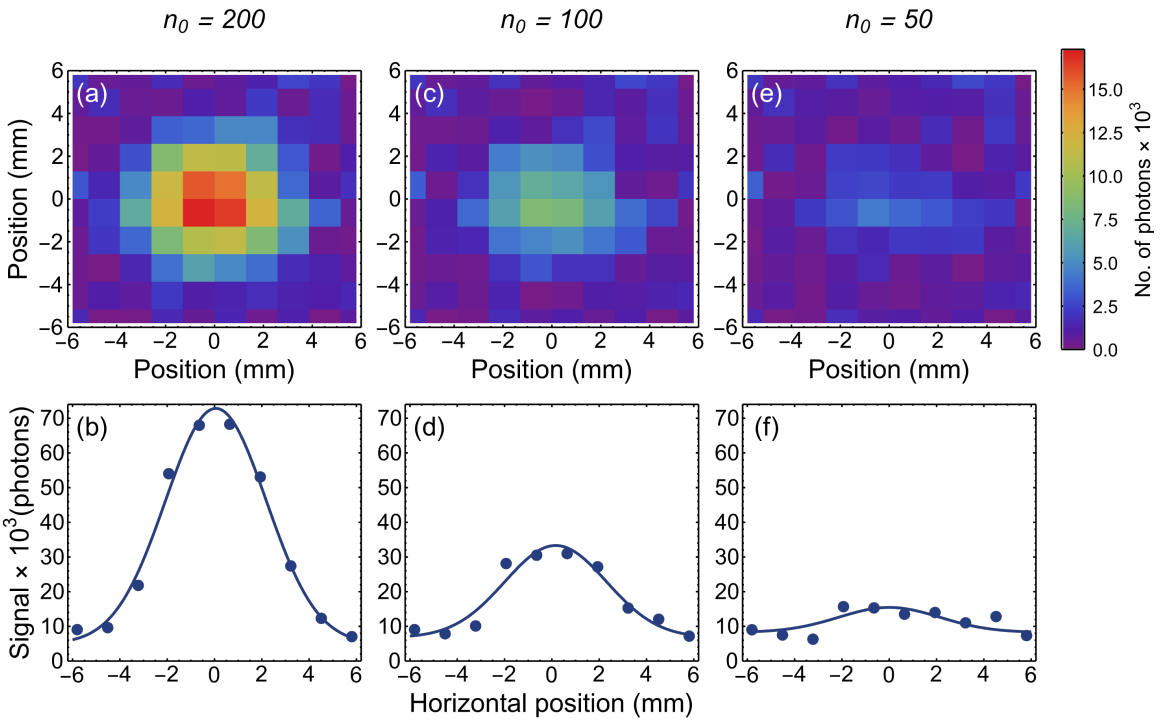

Figure 6.11: Simulated photon signal from a cloud of n_0 YbF molecules with a width of 2 mm. The lower panels show a summed cross-section of the images shown in the upper panels. Fewer than $n_0 = 50$ molecules can be detected with the current measured background. The images have been cropped to only the region of interest.

sum of all vertical counts as a function of horizontal position is shown in figure 6.11(b),(d),(f). Clouds with molecule numbers down to about 50 can still be seen with a single background subtracted shot. Each image on the CCD is recorded without any pixel binning but every 32 adjacent bins are summed in processing the data. The mean recorded background per post-processed bin is 950 counts while the standard deviation on the background is 700 counts. This corresponds to the signal generated by roughly 8 molecules.

6.4.4 Molecule detection in the MOT chamber

As an initial test of the fluorescence collection optics in the MOT chamber we image the passing molecular beam. Figure 6.12 shows the results of this measurement. In the frame of the image, the molecular beam moves from right to left. As the molecules traverse, they fluoresce from a single vertical intersecting probe beam. The probe beam has about 11 mW and 10 mm $1/e^2$ diameter. The fluorescence is imaged onto the CCD using 4×4 binning and an exposure time

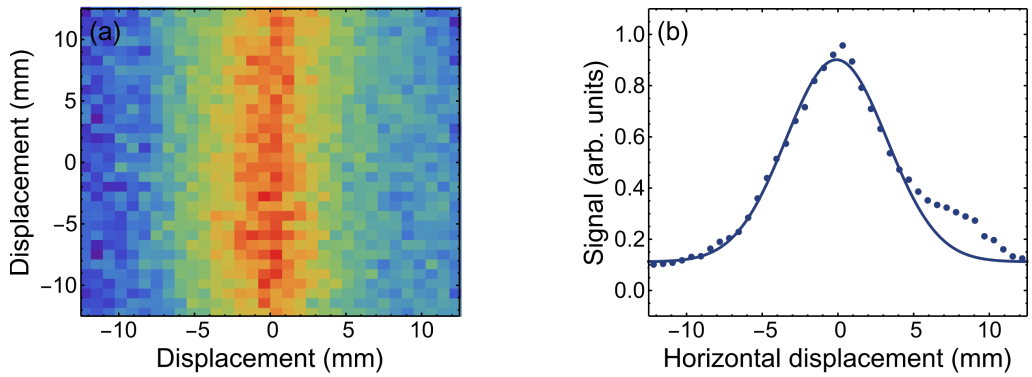

Figure 6.12: (a) Image of the laser induced fluorescence from the traversing molecular beam. The molecular beam passes from right to left and fluoresces when intersecting a probe laser crossing the image from top to bottom. (b) Horizontal position distribution of the LIF signal. Pixel counts are summed vertically from (a) and normalised. The horizontal distribution corresponds to the laser beam profile.

of 100 ms, sufficiently long that the entirety of the molecular pulse from the source has passed the detector. In the analysis of the image, further 2×2 binning is used. The molecules fill the whole field of view during their flight through the detector but only fluoresce when passing the probe beam. The profile seen in figure 6.12 is therefore that of the probe laser beam. The image is summed along the vertical axis to produce the horizontal one-dimensional signal profile shown in figure 6.12(b).

6.5 Summary

In this chapter we discussed the progress towards a magneto-optical trap of YbF. To understand the conditions needed to make a MOT of YbF we simulate the expected performance using a scattering rate equation model. Using three frequency sidebands, two red detuned from their nearest hyperfine state and one blue detuned, we can achieve confining forces for displacements ± 40 mm and peak accelerations of near 6 m/s^2. We estimate a capture velocity of 11 m/s. This chapter has also provided details on the hardware and optics for the magneto-optical chamber assembly. The vacuum, optical and imaging setups are all complete. The MOT chamber features in-vacuum coils that produce a uniform magnetic field gradient of 2.58(1) G/cm/A across a range of 20 mm. One of the biggest challenges is reducing the background scattered

light to a sufficiently low level that we can detect the fluorescence from a small number of molecules in the trapped cloud. We carefully characterise and reduce the background scattered light to a noise level estimated to be equivalent to the fluorescence from as few as 8 molecules. Although the work in this chapter has provided important practical advances, achieving a magneto-optical trap of YbF remains limited by leaks out of our optical cycle, both in laser slowing molecules to within the capture velocity of the MOT as well as limiting the lifetime of the MOT. To achieve a lifetime of 100 ms in a MOT with a scattering rate of 1×10^6 photons/s requires each molecule to scatter 100,000 photons. For this to occur, the optical cycle must be closed to 0.99999. To solve this requires plugging all leaks greater than 1×10^{-5}. Closing the suspected remaining leak to the $4f$ hole states therefore remains crucial.

Chapter 7

Conclusion

7.1 Summary of this thesis

The electron's electric dipole moment is a test of physics beyond the Standard Model. eEDM measurements use a Ramsey-type interferometer to measure the frequency shift induced by the interaction of the eEDM with an effective electric field. The sensitivity of such a measurement is proportional to the interaction time, the number of molecules detected and the size of the effective electric field. Heavy paramagnetic molecules offer increased sensitivity for measuring the eEDM due to a large effective electric field. To this extent, molecules, such as ThO, and molecular ions, such as HfF^+, have been used to measure the eEDM. The latter sets the current best limit, $|d_e| < 4.1 \times 10^{-30}\, e$ cm. It is difficult to combine large effective fields, long coherence times and a large number of molecules. The ThO experiment has large numbers of molecules but short coherence times, whilst the HfF^+ experiment has coherence times on the order of seconds but limited molecular ions. One way to increase all three is by using ultracold, trapped YbF in an optical lattice. The proposed aim of this project is to measure the eEDM of the electron with a precision at the $10^{-32}\, e$ cm level.

This thesis has presented significant progress towards such a measurement of the eEDM in an optical lattice. In order to be able to load the molecules into a lattice, they must first be trapped and cooled in a magneto-optical trap (MOT). Molecular MOTs have typical capture velocities

of around 10 m/s. To facilitate the loading of the trap, our study began with producing an already cold, slow beam of YbF. Our molecules are produced in a cryogenic buffer gas source comprising of a two-stage copper cell, cryogenically cooled to around 1.8 K. Using this source, we've demonstrated the production of 1.5×10^{10} molecules/sr/pulse travelling with a peak velocity of 50 m/s. Although, these lower velocities present a significant improvement compared to other cryogenic buffer gas sources of YbF, this is still above the capture velocity of a MOT.

To reduce the longitudinal velocity of the molecules further, we plan to implement radiation pressure slowing from a counter-propagating laser beam. We implemented the optical and laser hardware necessary for such slowing and demonstrated a modest reduction of the forward velocity by around 5 m/s in 5 ms of interaction time. This was achieved using three lasers, one to address the main (0-0) vibrational band of $A^2\Pi_{1/2} \leftrightarrow X^2\Sigma^+$, and two lasers to repump population lost to $X^2\Sigma^+(v = 1)$ and $X^2\Sigma^+(v = 2)$. Even with these repump lasers, we observe a leak out of the optical cycle of around 6×10^{-4}. We've shown that losses to $X^2\Sigma^+(v = 3)$ account for a leak around 1×10^{-4} and can be recovered with the addition of a fourth laser. Remaining potential loss channels will limit the ability to slow the molecules to within the capture velocity of the MOT and, indeed, the lifetime of the MOT itself.

A possible loss channel out of the optical cycle could be opened due to a weak decay from the $A^2\Pi_{1/2}$ state to low-lying electronically excited states. These states arise from the excitation of an inner-shell electron in the $4f$ shell of the Yb^+ ion and are called $4f$ hole states. The branching ratio for this leak is predicted to be 5×10^{-4}. As part of a spectroscopic study of these $4f$ hole states, we identified the rotational structure of these leak states as well as suitable repump transition frequencies. In addition to the leak states, we further characterised the rotational structure in a high-lying state denoted [31.05] and two newly identified states we denote [48.72] and [48.73]. These last two states lie *above* the ionisation threshold for YbF. We attribute these as being auto-ionising states of $4f$ hole character. These states may be useful for efficient detection of YbF.

Finally, we discussed our progress towards a MOT of YbF. Through simulation using a scat-

tering rate equation model, we identified a suitable sideband frequency scheme for the main MOT laser. We predict confining forces with peak accelerations of $-6\mathrm{m/s}^2$. The vacuum hardware and surrounding optics has been built. We reduced the background scattered light in the detection chamber to a noise level estimated to be equivalent to as few as 8 molecules.

The achievements in this work have paved the way for trapping of YbF but work remains in achieving the long-term goal of an eEDM measurement with long coherence times, in an optical lattice. In the next section we outline the steps needed to achieve this.

7.2 Outlook towards an eEDM measurement in a lattice

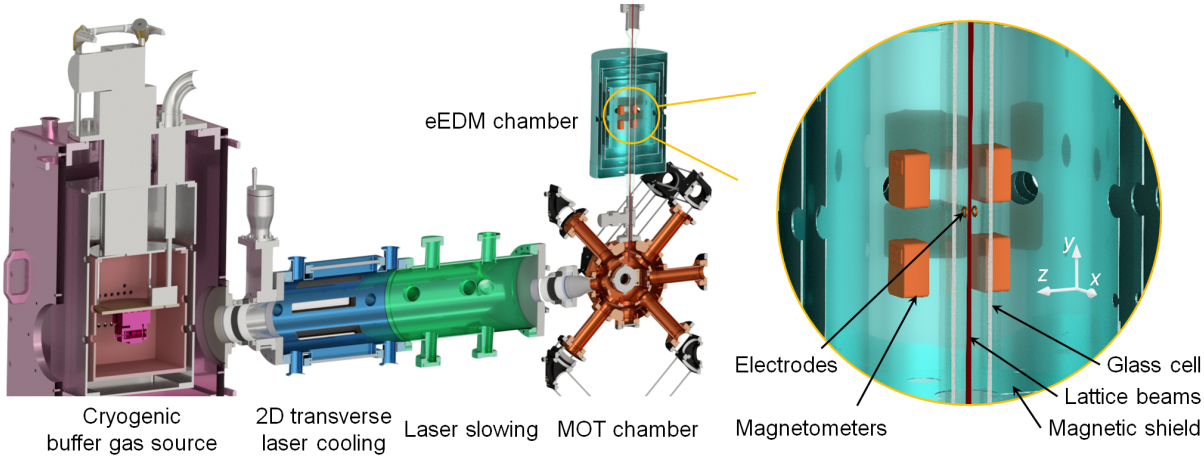

Figure 7.1: Illustration of the proposed beamline to measure the eEDM in an optical lattice. Figure produced by J. Lim.

Figure 7.1 shows an illustration of the proposed experiment. The source, slowing and MOT chamber have all been installed. Once the molecules are in the MOT chamber, the loading of the MOT can be improved by transversely collimating the molecular beam. Transverse cooling has not been implemented on our beamline yet, but is regularly operated on a different YbF source in the group [106]. The molecules can then be compressed and cooled before being transferred to an optical lattice. The molecules in the lattice will be moved to a region that is magnetically shielded, where the eEDM measurement can take place. Here we outline the path to achieving this goal.

In order to accomplish a MOT of YbF, the population that leaks out of the optical cycle has to be repumped. The dominant leaks are suspected to be into $4f^{-1}_{7/2,1/2}(v=0)$ and $4f^{-1}_{7/2,1/2}(v=1)$. We have already addressed the possible repump schemes in our discussion at the end of chapter 5. In order to be able to efficiently repump population from these states, their hyperfine structure must first be resolved. To do this requires the use of CW lasers. A pump-probe experiment using a 1038 nm laser to address the $A^2\Pi_{1/2} \leftarrow 4f^{-1}_{7/2,1/2}(v=0)$ transition is currently underway. The observed population size in the $4f$ states will determine the branching ratio from the $A^2\Pi_{1/2}$ state and therefore the size of leak.

Once all leaks at the level 10^{-4} or greater have been closed, there will be sufficient closure in the optical cycle to achieve the desired MOT lifetime of at least 50 ms. The parameter space of the MOT will be very large. The compression, lifetime and loading efficiency will all depend on the laser frequencies and detuning used for the MOT light, the magnetic field parameters as well as the laser slowing and source parameters. All of these parameters will need to be optimised. Using sub-Doppler cooling techniques, the temperature in the MOT can then be lowered to an expected temperature of less than 100 μK.

The molecules can be loaded into a 1D optical lattice formed by two counter-propagating 1064 nm lasers with a waist of 100 μm. The eEDM measurement will need to take place in a magnetically shielded region. In order to transfer the molecules to such an eEDM chamber, a frequency difference, $\Delta\nu$, is introduced between the two beams forming the lattice. To maintain the radial confinement, focus tunable lenses can be used to move the focus of the lattice together with the molecules [141]. The design of the eEDM apparatus is currently underway.

The statistical sensitivity of a quantum projection noise limited eEDM experiment is given by

$$\sigma_{d_e} = \frac{\hbar}{2\mathcal{E}_{\text{eff}}\mathcal{C}\tau\sqrt{N_{det}}}. \tag{7.1}$$

To estimate the shot-noise of a measurement in a lattice, we take an effective field of 18 GV/cm. This can be achieved with a laboratory field of around 20 kV/cm. At room temperature, the lifetime of the molecules in the lattice will be limited to around $\tau = 4$ s due to vibrational heating

by blackbody radiation. The contrast, $\mathcal{C}$, is a characterisation of experimental imperfections. We assume that these can be controlled to sufficient level such that $\mathcal{C} = 0.9$. Assuming 10^4 molecules captured in the lattice and a 100% detection efficiency we find $\sigma_{d_e} = 5.1 \times 10^{-29}\, e$ cm in a single shot. With a lifetime of 4 s in the lattice, a maximum of 14 shots can be taken in a minute. We therefore estimate that a sensitivity of below $1 \times 10^{-31}\, e$ cm can be reached in about 260,000 shots or 300 hours of operation. This could be further improved by increasing the number of molecules through means such as transverse cooling and improving the coherence time through cooling of the surroundings.

Appendix A

Line lists

This appendix lists the frequencies, in cm $^{-1}$, of observed rotational lines for the spectra [31.05] $\leftarrow X^2\Sigma^+(v=0)$, [31.05] $\leftarrow 4f^{-1}_{7/2,1/2}(v=0)$, [31.05] $\leftarrow 4f^{-1}_{7/2,1/2}(v=1)$ and [31.05] $\leftarrow 4f^{-1}_{7/2,3/2}(v=0)$. In addition, the observed rotational energy levels for the [48.72] and [48.73] states are listed in tables A.5 and A.6.

Table A.1: Rotational lines in [31.05] $\leftarrow X^2\Sigma^+(v = 0)$. All values presented are in cm^{-1}. $R_1(N)$ lines form a close bandhead and no individual lines were resolved for this branch.

Line	Measured	Fitted
$P_{12}(2)$	-	31049.157
$P_{12}(3)$	31049.317	31049.335
$P_{12}(4)$	31049.544	31049.528
$P_{12}(5)$	31049.749	31049.737
$P_{12}(6)$	31049.973	31049.962
$P_{12}(7)$	31050.213	31050.203
$P_{12}(8)$	31050.475	31050.460
$P_{12}(9)$	31050.752	31050.733
$P_{12}(10)$	31051.043	31051.022
$P_{12}(11)$	31051.330	31051.327
$P_{12}(12)$	31051.672	31051.649
$P_{12}(13)$	31051.988	31051.986
$P_{12}(14)$	31052.343	31052.340
$P_{12}(15)$	31052.677	31052.711

Line	Measured	Fitted
$R_1(0)$	-	31048.720
$R_1(1)$	-	31048.606
$R_1(2)$	-	31048.508
$R_1(3)$	-	31048.426
$R_1(4)$	-	31048.359
$R_1(5)$	-	31048.308
$R_1(6)$	-	31048.274
$R_1(7)$	-	31048.255
$R_1(8)$	-	31048.252
$R_1(9)$	-	31048.266
$R_1(10)$	-	31048.295
$R_1(11)$	-	31048.341
$R_1(12)$	-	31048.402
$R_1(13)$	-	31048.480
$R_1(14)$	-	31048.575
$R_1(15)$	-	31048.686

Line	Measured	Fitted
$P_1(1) + Q_{12}(1)$	-	31048.368
$P_1(2) + Q_{12}(2)$	31047.239	31047.273
$P_1(3) + Q_{12}(3)$	31046.155	31046.194
$P_1(4) + Q_{12}(4)$	31045.103	31045.130
$P_1(5) + Q_{12}(5)$	31044.084	31044.083
$P_1(6) + Q_{12}(6)$	31043.044	31043.051
$P_1(7) + Q_{12}(7)$	31042.035	31042.036
$P_1(8) + Q_{12}(8)$	31041.008	31041.036
$P_1(9) + Q_{12}(9)$	31040.057	31040.053
$P_1(10) + Q_{12}(10)$	31039.090	31039.085
$P_1(11) + Q_{12}(11)$	31038.107	31038.134
$P_1(12) + Q_{12}(12)$	31037.175	31037.199
$P_1(13) + Q_{12}(13)$	31036.285	31036.280
$P_1(14) + Q_{12}(14)$	31035.379	31035.378
$P_1(15) + Q_{12}(15)$	31034.522	31034.492
$P_1(16) + Q_{12}(16)$	31033.627	31033.622
$P_1(17) + Q_{12}(17)$	31032.787	31032.769
$P_1(18) + Q_{12}(18)$	31031.948	31031.933

Line	Measured	Fitted
$Q_1(0)$	-	31050.606
$Q_1(1) + R_{12}(2)$	-	31051.748
$Q_1(2) + R_{12}(2)$	-	31052.906
$Q_1(3) + R_{12}(3)$	-	31054.081
$Q_1(4) + R_{12}(4)$	31055.270	31055.271
$Q_1(5) + R_{12}(5)$	31056.486	31056.477
$Q_1(6) + R_{12}(6)$	31057.699	31057.698
$Q_1(7) + R_{12}(7)$	31058.948	31058.936
$Q_1(8) + R_{12}(8)$	31060.230	31060.190
$Q_1(9) + R_{12}(9)$	31061.479	31061.460
$Q_1(10) + R_{12}(10)$	31062.760	31062.746
$Q_1(11) + R_{12}(11)$	31064.052	31064.048
$Q_1(12) + R_{12}(12)$	31065.356	31065.366
$Q_1(13) + R_{12}(13)$	31066.711	31066.701
$Q_1(14) + R_{12}(14)$	31068.024	31068.052
$Q_1(15) + R_{12}(15)$	31069.416	31069.419
$Q_1(16) + R_{12}(16)$	31070.755	31070.803

Table A.2: Rotational lines in $[31.05] \leftarrow 4f^{-1}_{7/2,1/2}(v=0)$. All values presented are in cm^{-1}.

Line	Measured	Fitted
$P_{ee}(1.5)$	-	22575.538
$P_{ee}(2.5)$	22575.087	22575.117
$P_{ee}(3.5)$	22574.691	22574.664
$P_{ee}(4.5)$	22574.185	22574.179
$P_{ee}(5.5)$	22573.657	22573.661
$P_{ee}(6.5)$	22573.114	22573.111

Line	Measured	Fitted
$R_{ff}(0.5)$	22576.605	22576.606
$R_{ff}(1.5)$	22576.891	22576.897
$R_{ff}(2.5)$	22577.114	22577.156

Line	Measured	Fitted
$R_{ee}(0.5)$	22575.201	22575.168
$R_{ee}(1.5)$	22575.779	22575.776
$R_{ee}(2.5)$	22576.303	22576.352
$R_{ee}(3.5)$	-	22576.896
$R_{ee}(4.5)$	-	22577.408
$R_{ee}(5.5)$	-	22577.887
$R_{ee}(6.5)$	22578.309	22578.334
$R_{ee}(7.5)$	22578.790	22578.748
$R_{ee}(8.5)$	22579.122	22579.130
$R_{ee}(9.5)$	22579.484	22579.480
$R_{ee}(10.5)$	22579.778	22579.798
$R_{ee}(11.5)$	22580.114	22580.083
$R_{ee}(12.5)$	22580.347	22580.335

Line	Measured	Fitted
$Q_{ef}(0.5)$	-	22577.053
$Q_{ef}(1.5)$	22578.961	22578.919
$Q_{ef}(2.5)$	22580.605	22580.752
$Q_{ef}(3.5)$	22582.607	22582.553
$Q_{ef}(4.5)$	22584.343	22584.321
$Q_{ef}(5.5)$	22586.098	22586.057
$Q_{ef}(6.5)$	22587.806	22587.761
$Q_{ef}(7.5)$	22589.491	22589.433
$Q_{ef}(8.5)$	22591.112	22591.072
$Q_{ef}(9.5)$	22592.739	22592.679
$Q_{ef}(10.5)$	22594.327	22594.253
$Q_{ef}(11.5)$	22595.839	22595.795
$Q_{ef}(12.5)$	22597.379	22597.305
$Q_{ef}(13.5)$	22598.840	22598.783
$Q_{ef}(14.5)$	22600.267	22600.228
$Q_{ef}(15.5)$	22601.680	22601.640
$Q_{ef}(16.5)$	22603.031	22603.021
$Q_{ef}(17.5)$	22604.384	22604.369
$Q_{ef}(18.5)$	22605.673	22605.685
$Q_{ef}(19.5)$	22606.884	22606.968
$Q_{ef}(20.5)$	22608.009	22608.219

Line	Measured	Fitted
$P_{ff}(1.5)$	22573.109	22573.148
$P_{ff}(2.5)$	22572.368	22572.410
$P_{ff}(3.5)$	22571.608	22571.640
$P_{ff}(4.5)$	22570.823	22570.837
$P_{ff}(5.5)$	22569.975	22570.003
$P_{ff}(6.5)$	22569.152	22569.135
$P_{ff}(7.5)$	22568.178	22568.236
$P_{ff}(8.5)$	22567.258	22567.304
$P_{ff}(9.5)$	22566.316	22566.340
$P_{ff}(10.5)$	22565.312	22565.343
$P_{ff}(11.5)$	22564.279	22564.314

Line	Measured	Fitted
$Q_{fe}(0.5)$	22573.240	22573.225
$Q_{fe}(1.5)$	-	22571.263
$Q_{fe}(2.5)$	-	22569.268
$Q_{fe}(3.5)$	22567.178	22567.240
$Q_{fe}(4.5)$	22565.142	22565.181
$Q_{fe}(5.5)$	22563.036	22563.089
$Q_{fe}(6.5)$	-	22560.965
$Q_{fe}(7.5)$	-	22558.808
$Q_{fe}(8.5)$	-	22556.619
$Q_{fe}(9.5)$	-	22554.398
$Q_{fe}(10.5)$	22552.134	22552.144
$Q_{fe}(11.5)$	22549.834	22549.858
$Q_{fe}(12.5)$	22547.572	22547.540
$Q_{fe}(13.5)$	22545.191	22545.190
$Q_{fe}(14.5)$	22542.841	22542.807
$Q_{fe}(15.5)$	22540.469	22540.391
$Q_{fe}(16.5)$	22537.971	22537.944
$Q_{fe}(17.5)$	22535.559	22535.464

Table A.3: Rotational lines in [31.05] $\leftarrow 4f^{-1}_{7/2,1/2}(v=1)$. All values presented are in cm^{-1}.

Line	Measured	Fitted
$P_{ee}(1.5)$	21959.270	21959.246
$P_{ee}(2.5)$	21958.799	21958.827
$P_{ee}(3.5)$	21958.362	21958.379
$P_{ee}(4.5)$	21957.884	21957.903
$P_{ee}(5.5)$	21957.416	21957.397
$P_{ee}(6.5)$	-	21956.863
$P_{ee}(7.5)$	21956.304	21956.300
$P_{ee}(8.5)$	21955.676	21955.708
$P_{ee}(9.5)$	21955.141	21955.088
$P_{ee}(10.5)$	21954.410	21954.438

Line	Measured	Fitted
$R_{ee}(0.5)$	-	21958.877
$R_{ee}(1.5)$	-	21959.484
$R_{ee}(2.5)$	21960.053	21960.062
$R_{ee}(3.5)$	-	21960.611
$R_{ee}(4.5)$	-	21961.131
$R_{ee}(5.5)$	-	21961.623
$R_{ee}(6.5)$	-	21962.085
$R_{ee}(7.5)$	21962.469	21962.519
$R_{ee}(8.5)$	21962.944	21962.924
$R_{ee}(9.5)$	21963.266	21963.301
$R_{ee}(10.5)$	21963.638	21963.648
$R_{ee}(11.5)$	21963.951	21963.967
$R_{ee}(12.5)$	21964.188	21964.256

Line	Measured	Fitted
$Q_{ef}(0.5)$	-	21960.763
$Q_{ef}(1.5)$	21962.616	21962.626
$Q_{ef}(2.5)$	21964.442	21964.461
$Q_{ef}(3.5)$	21966.281	21966.268
$Q_{ef}(4.5)$	21968.024	21968.045
$Q_{ef}(5.5)$	21969.825	21969.793
$Q_{ef}(6.5)$	21971.529	21971.513
$Q_{ef}(7.5)$	21973.242	21973.204
$Q_{ef}(8.5)$	21974.904	21974.866
$Q_{ef}(9.5)$	21976.521	21976.499
$Q_{ef}(10.5)$	21978.148	21978.104
$Q_{ef}(11.5)$	21979.711	21979.679

Line	Measured	Fitted
$P_{ff}(1.5)$	21956.872	21956.884
$P_{ff}(2.5)$	21956.165	21956.162
$P_{ff}(3.5)$	21955.412	21955.411
$P_{ff}(4.5)$	21954.684	21954.631
$P_{ff}(5.5)$	21953.835	21953.823
$P_{ff}(6.5)$	-	21952.985
$P_{ff}(7.5)$	21952.129	21952.119
$P_{ff}(8.5)$	21951.257	21951.224
$P_{ff}(9.5)$	-	21950.300
$P_{ff}(10.5)$	21949.359	21949.348

Line	Measured	Fitted
$Q_{fe}(0.5)$	21956.949	21956.949
$Q_{fe}(1.5)$	21955.014	21954.998
$Q_{fe}(2.5)$	21953.027	21953.019
$Q_{fe}(3.5)$	21950.993	21951.011
$Q_{fe}(4.5)$	21948.950	21948.975
$Q_{fe}(5.5)$	21946.862	21946.909
$Q_{fe}(6.5)$	21944.782	21944.815
$Q_{fe}(7.5)$	21942.663	21942.692
$Q_{fe}(8.5)$	21940.554	21940.540

Line	Measured	Fitted
$R_{ff}(0.5)$	-	21960.329
$R_{ff}(1.5)$	-	21960.633
$R_{ff}(2.5)$	-	21960.908
$R_{ff}(3.5)$	-	21961.154
$R_{ff}(4.5)$	-	21961.371
$R_{ff}(5.5)$	-	21961.559
$R_{ff}(6.5)$	-	21961.719
$R_{ff}(7.5)$	-	21961.849
$R_{ff}(8.5)$	-	21961.951

Table A.4: Rotational lines in $[31.05] \leftarrow 4f^{-1}_{7/2,3/2}(v=0)$. All values presented are in cm^{-1}.

Line	Measured	Fitted
$P_{ee}(1.5)$	-	22035.309
$P_{ee}(2.5)$	22033.849	22033.844
$P_{ee}(3.5)$	22032.326	22032.345
$P_{ee}(4.5)$	22030.815	22030.810
$P_{ee}(5.5)$	22029.188	22029.239
$P_{ee}(6.5)$	22027.651	22027.633
$P_{ee}(7.5)$	22025.969	22025.992

Line	Measured	Fitted
$R_{ee}(0.5)$	-	22035.979
$R_{ee}(1.5)$	22035.558	22035.547
$R_{ee}(2.5)$	22035.080	22035.080
$R_{ee}(3.5)$	22034.529	22034.577
$R_{ee}(4.5)$	22034.051	22034.038
$R_{ee}(5.5)$	22033.412	22033.465
$R_{ee}(6.5)$	22032.866	22032.856
$R_{ee}(7.5)$	22032.198	22032.212
$R_{ee}(8.5)$	22031.522	22031.532
$R_{ee}(9.5)$	-	22030.817
$R_{ee}(10.5)$	-	22030.067
$R_{ee}(11.5)$	22029.287	22029.281
$R_{ee}(12.5)$	-	22028.460
$R_{ee}(13.5)$	-	22027.604
$R_{ee}(14.5)$	22026.729	22026.713
$R_{ee}(15.5)$	22025.775	22025.786

Line	Measured	Fitted
$P_{ff}(1.5)$	22037.073	22037.064
$P_{ff}(2.5)$	22037.345	22037.355
$P_{ff}(3.5)$	22037.620	22037.611
$P_{ff}(4.5)$	22037.857	22037.831

Line	Measured	Fitted
$Q_{ef}(0.5)$	-	22037.865
$Q_{ef}(1.5)$	-	22038.690
$Q_{ef}(2.5)$	22039.518	22039.479
$Q_{ef}(3.5)$	22040.249	22040.233
$Q_{ef}(4.5)$	22041.013	22040.952
$Q_{ef}(5.5)$	22041.639	22041.635
$Q_{ef}(6.5)$	22042.305	22042.283
$Q_{ef}(7.5)$	22042.930	22042.896
$Q_{ef}(8.5)$	22043.482	22043.474
$Q_{ef}(9.5)$	22044.045	22044.016
$Q_{ef}(10.5)$	22044.602	22044.522
$Q_{ef}(11.5)$	22045.013	22044.994

Line	Measured	Fitted
$Q_{fe}(0.5)$	-	22036.110
$Q_{fe}(1.5)$	22035.169	22035.179
$Q_{fe}(2.5)$	22034.228	22034.213
$Q_{fe}(3.5)$	22033.199	22033.211
$Q_{fe}(4.5)$	22032.198	22032.175
$Q_{fe}(5.5)$	22031.048	22031.103
$Q_{fe}(6.5)$	22029.990	22029.995
$Q_{fe}(7.5)$	22028.799	22028.853
$Q_{fe}(8.5)$	22027.651	22027.675
$Q_{fe}(9.5)$	22026.457	22026.461
$Q_{fe}(10.5)$	22025.187	22025.213

Line	Measured	Fitted
$R_{ff}(0.5)$	-	22039.490
$R_{ff}(1.5)$	-	22040.813
$R_{ff}(2.5)$	-	22042.101
$R_{ff}(3.5)$	-	22043.354
$R_{ff}(4.5)$	-	22044.571
$R_{ff}(5.5)$	22045.778	22045.753
$R_{ff}(6.5)$	22046.902	22046.899
$R_{ff}(7.5)$	22047.996	22048.010
$R_{ff}(8.5)$	22049.089	22049.086
$R_{ff}(9.5)$	22050.111	22050.127
$R_{ff}(10.5)$	22051.083	22051.132

Table A.5: Energy levels of [48.72] above the ground state of YbF, $X^2\Sigma^+(v = 0, N = 0, J = 0.5^+)$. All values given are in cm^{-1}.

J	e state measured	f state measured	Fitted
1.5	48721.222	48721.202	48721.221
2.5	48722.476	48722.481	48722.479
3.5	48724.227	48724.246	48724.240
4.5	48726.509	48726.513	48726.505
5.5	48729.284	48729.312	48729.273
6.5	-	48732.564	48732.544
7.5	48740.573	-	48736.318
8.5	48740.573	48740.679	48740.595
9.5	48745.407	48745.473	48745.376
10.5	48750.621	48750.745	48750.660
11.5	48756.448	48756.518	48756.447

Table A.6: Energy levels of [48.73] above the ground state of YbF, $X^2\Sigma^+(v = 0, N = 0, J = 0.5^+)$. All values given are in cm^{-1}.

J (e state)	Measured	Fitted	J (f state)	Measured	Fitted
0.5^+	-	48728.690	0.5^-	-	48729.725
1.5^-	48728.915	48728.942	1.5^+	-	48731.013
2.5^+	48729.578	48729.709	2.5^-	48732.821	48732.814
3.5^-	48730.939	48730.988	3.5^+	48735.183	48735.129
4.5^+	48732.809	48732.782	4.5^-	48738.073	48737.958
5.5^-	48735.048	48735.088	5.5^+	48741.492	48741.300
6.5^+	48737.814	48737.909	6.5^-	48745.231	48745.155
7.5^-	-	48741.242	7.5^+	48749.505	48749.524
8.5^+	48745.138	48745.090	8.5^-	-	48754.406
9.5^-	48749.423	48749.450	9.5^+	48759.542	48759.802
10.5^+	48754.281	48754.325	10.5^-	48765.738	48765.712
11.5^-	48759.860	48759.713	11.5^+	-	48772.135

Appendix B

Energy level diagrams

When looking at spectra, it is often useful to have the energy level drawn out to look at. Here, we present diagrams of the rotational energy levels for the relevant states all in one place. This is intended as a reference.

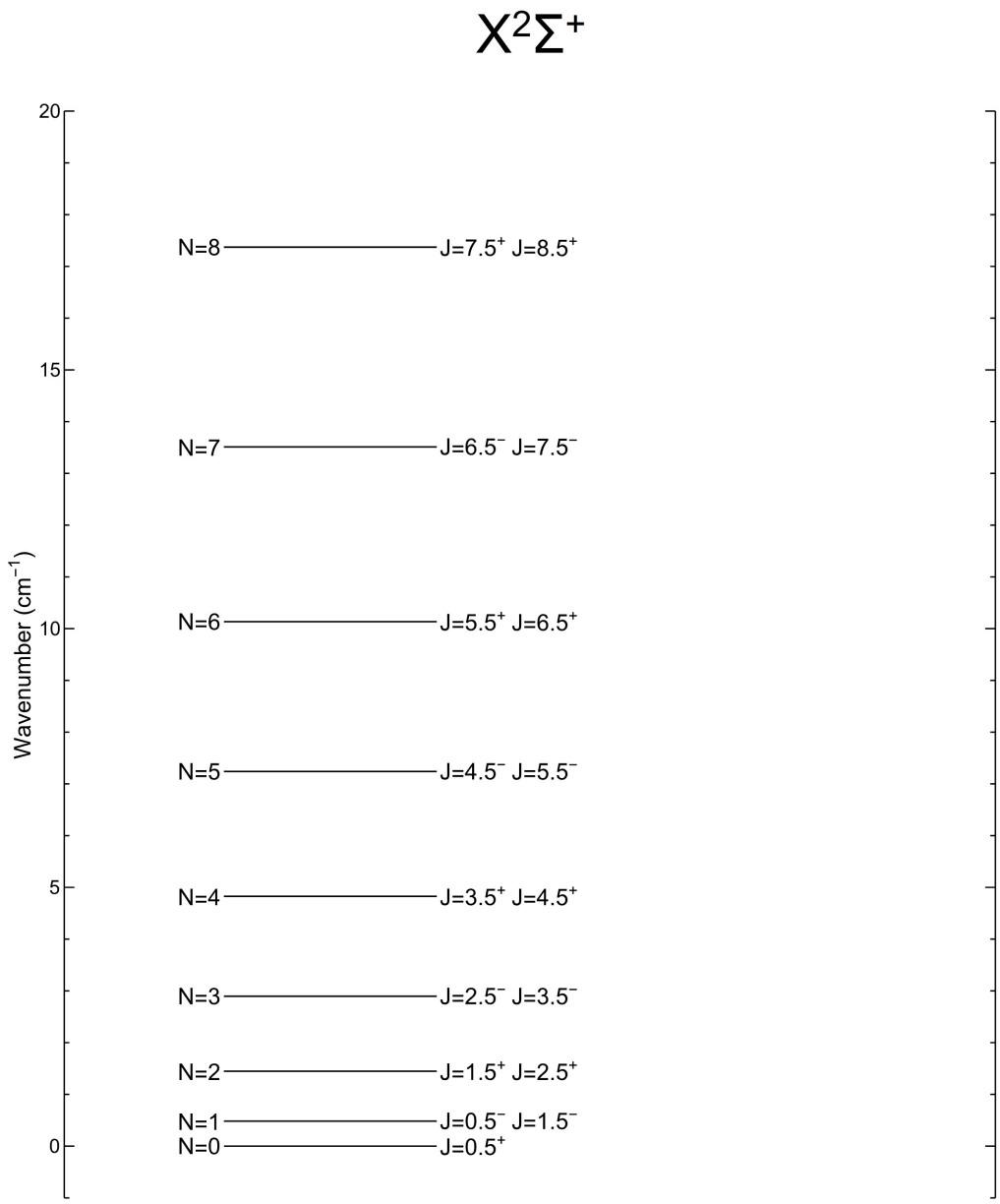

Figure B.1: Rotational levels of $X^2\Sigma^+(v = 0)$.

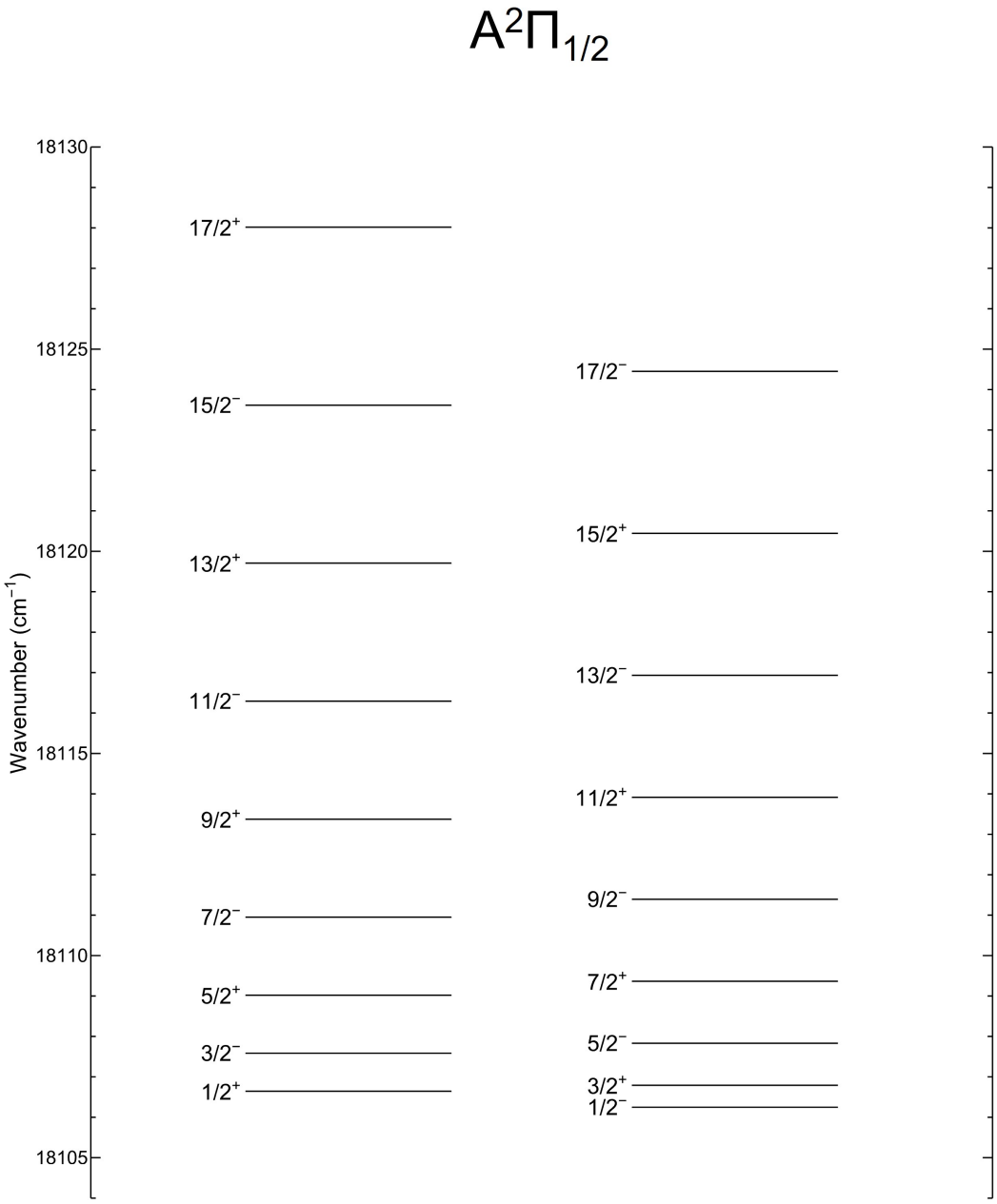

Figure B.2: Rotational levels of $A^2\Pi_{1/2}$.

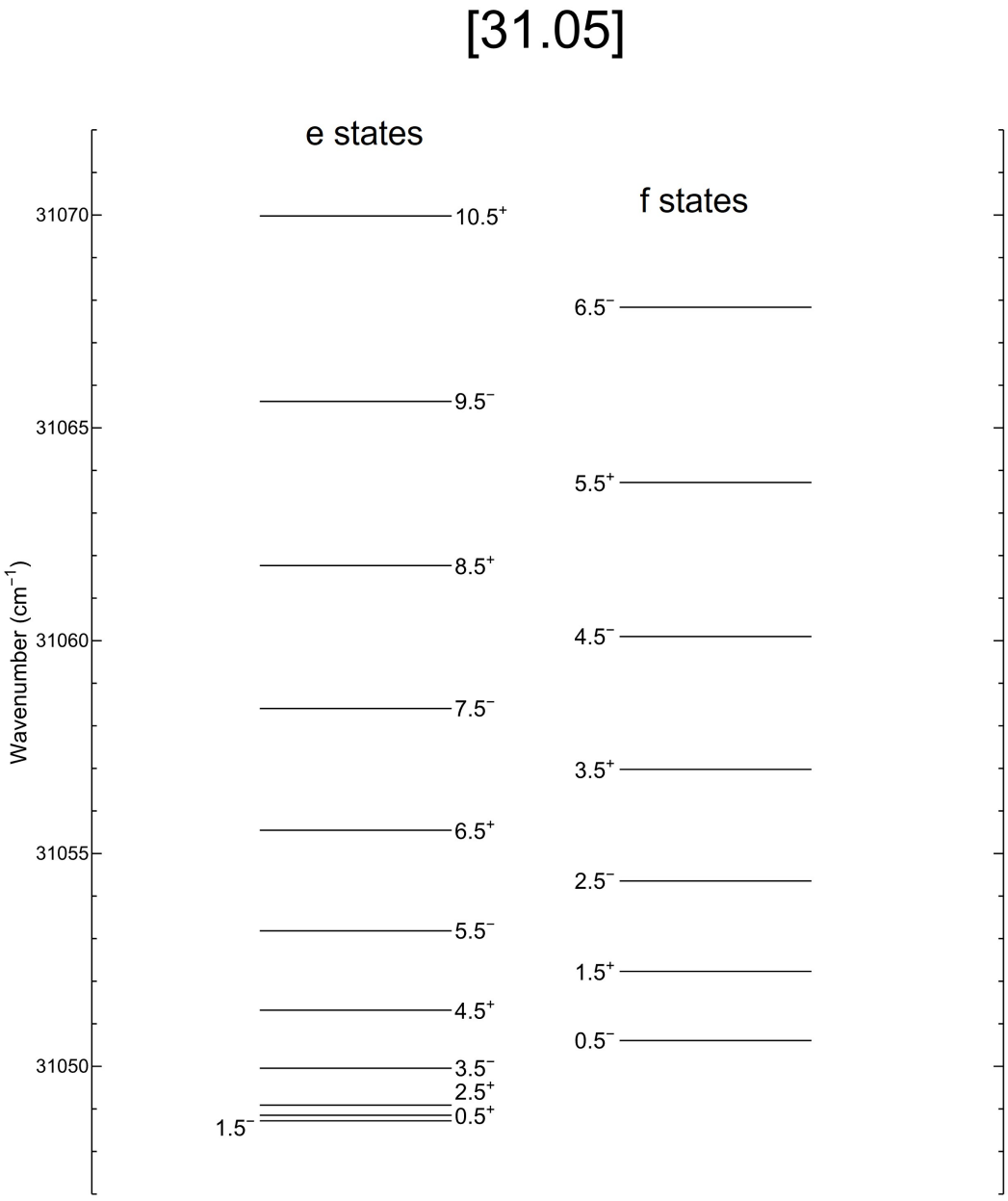

Figure B.3: Rotational levels of [31.05].

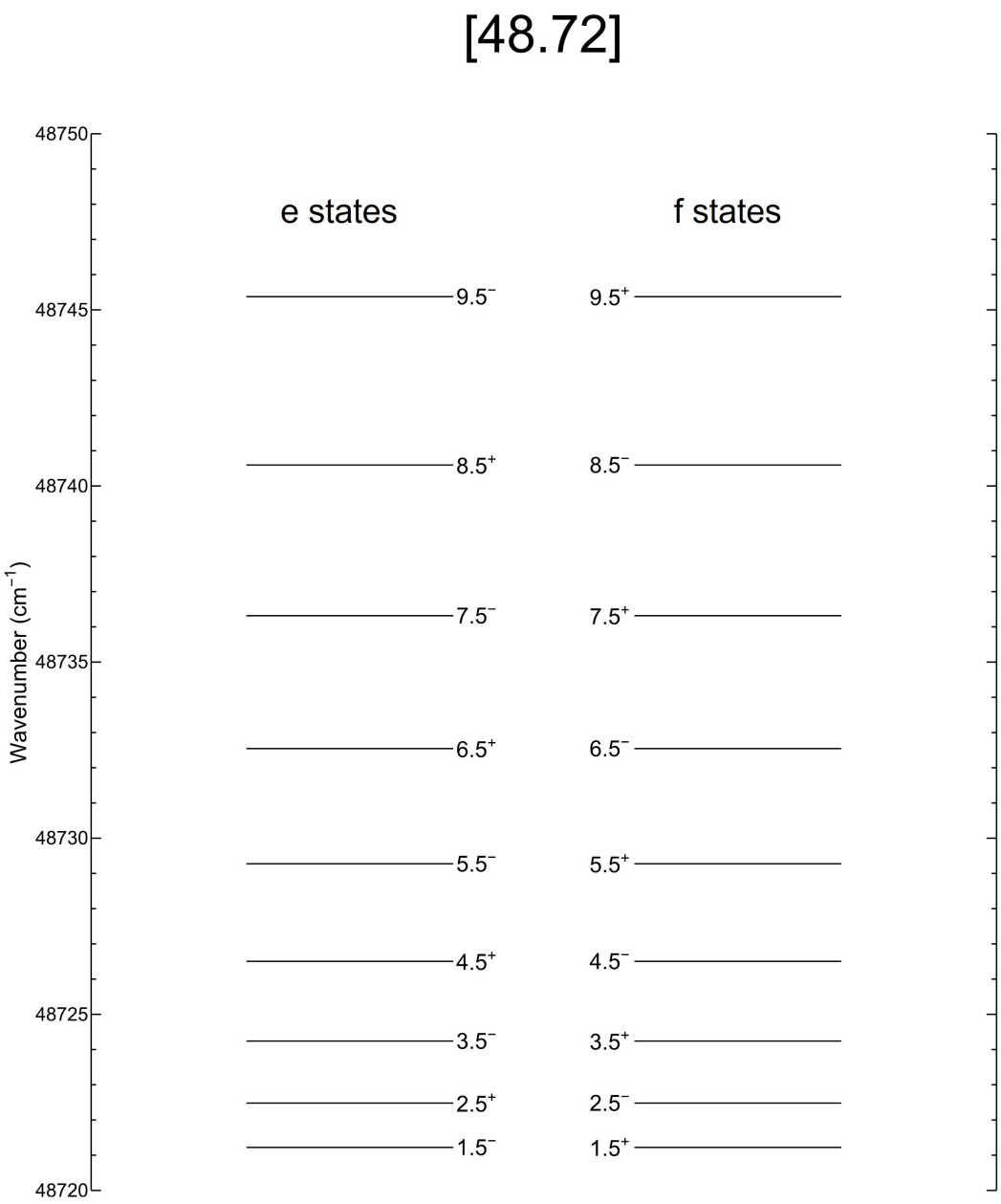

Figure B.4: Rotational levels of [48.72].

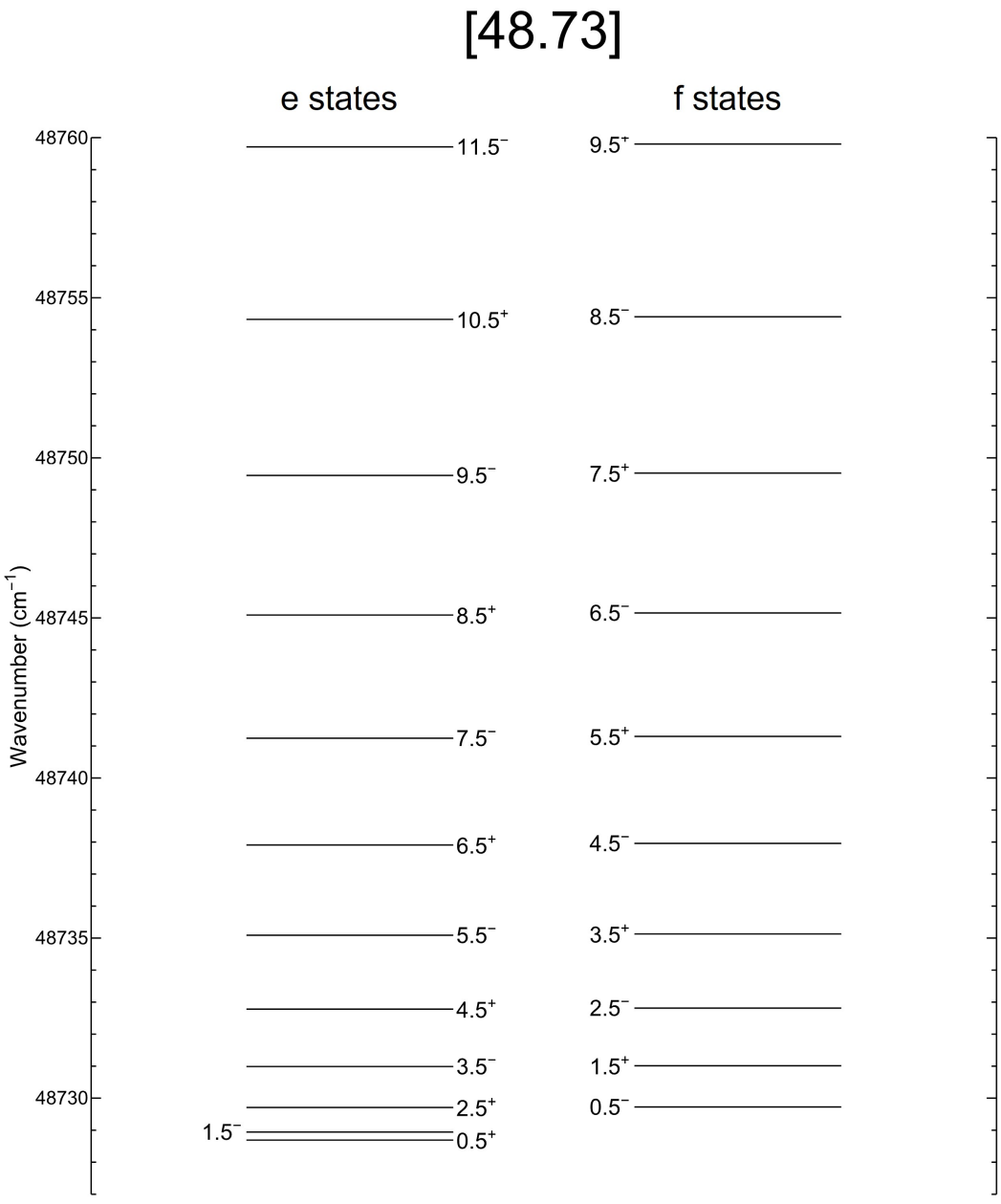

Figure B.5: Rotational levels of [48.73].

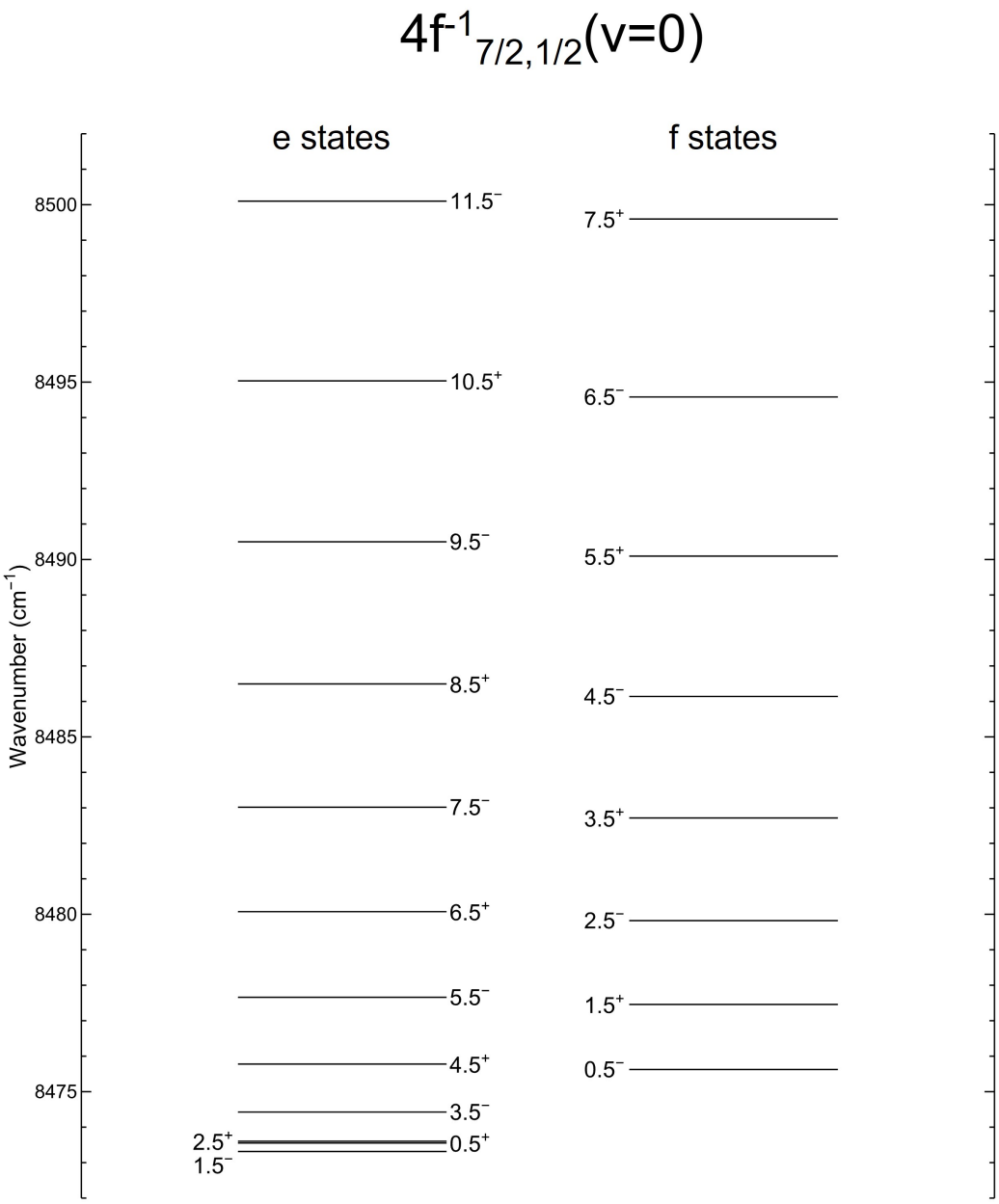

Figure B.6: Rotational levels of $4f^{-1}_{7/2,1/2}(v=0)$.

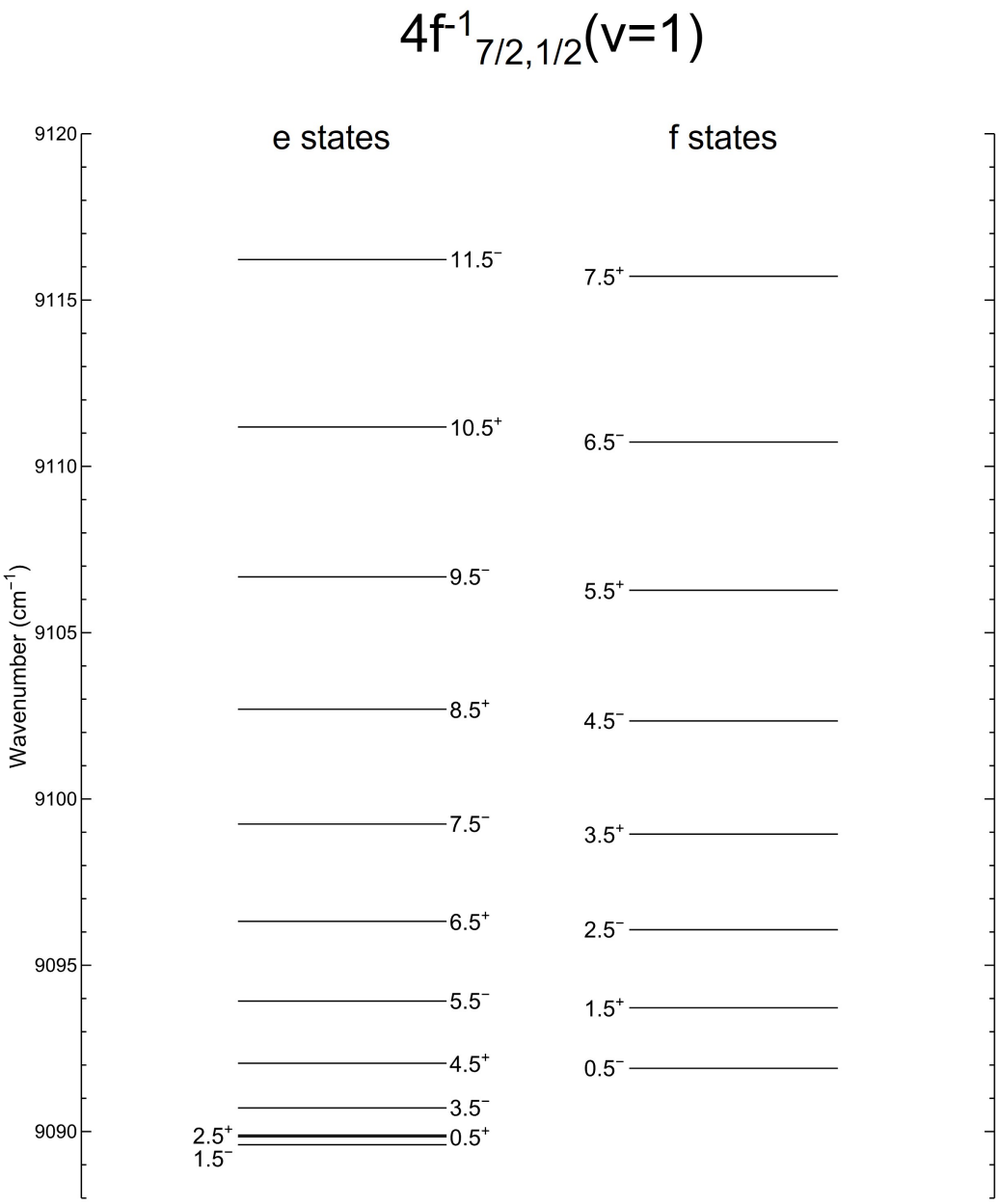

Figure B.7: Rotational levels of $4f^{-1}_{7/2,1/2}(v = 1)$.

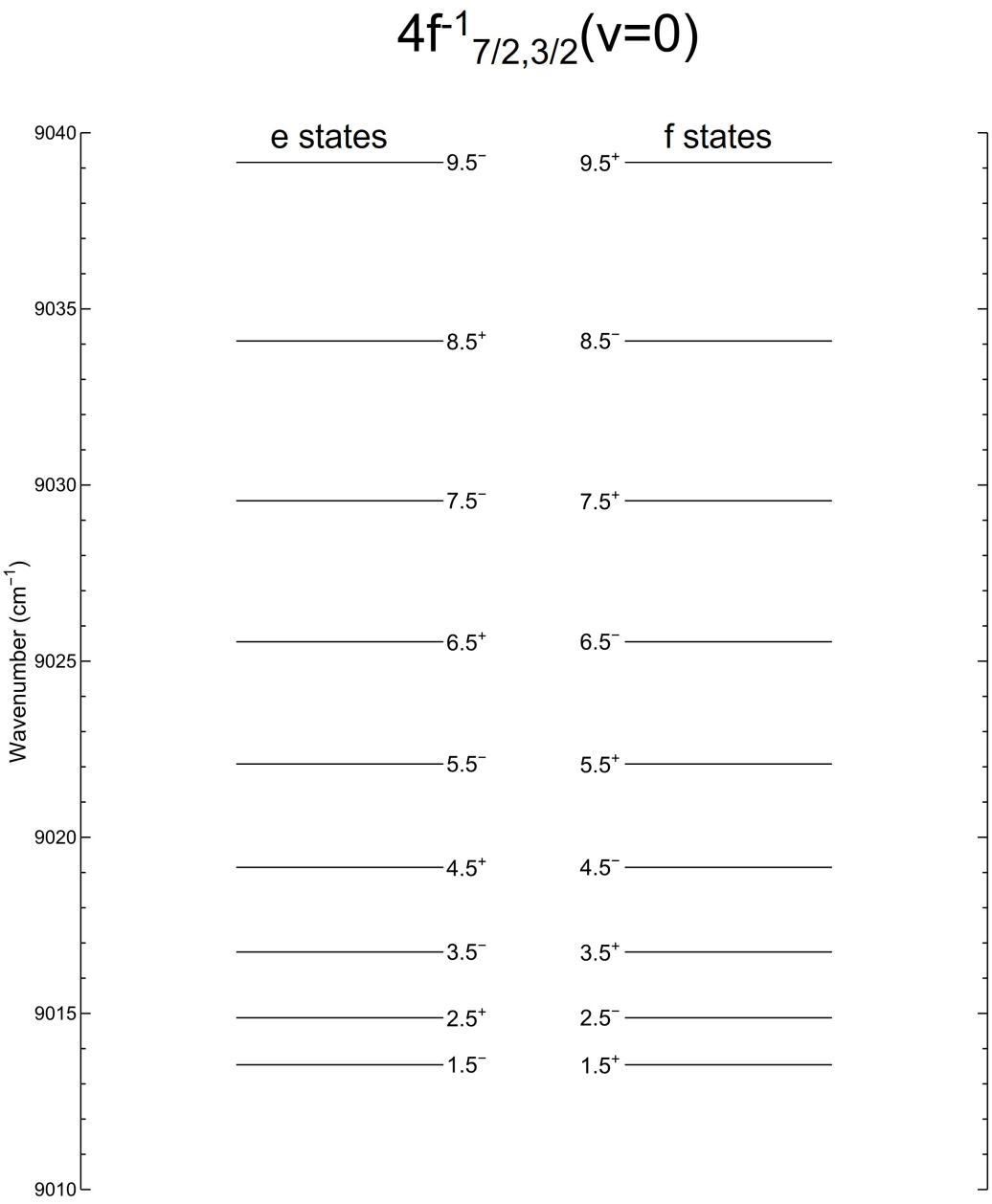

Figure B.8: Rotational levels of $4f^{-1}_{7/2,3/2}(v=0)$.

Bibliography

[1] I. B. Khriplovich and S. K. Lamoreaux, *CP Violation Without Strangeness: Electric Dipole Moments of Particles, Atoms, and Molecules*, Texts and Monographs in Physics (Springer, Berlin, Heidelberg, 1997) pp. 107–118.

[2] P. D. Group, P. Zyla, R. Barnett, J. Beringer, O. Dahl, D. Dwyer, D. Groom, C.-J. Lin, K. Lugovsky, E. Pianori, *et al.*, Progress of Theoretical and Experimental Physics **2020**, 083C01 (2020).

[3] E. M. Purcell and N. F. Ramsey, Phys. Rev. **78**, 807 (1950).

[4] C. S. Wu, E. Ambler, R. W. Hayward, D. D. Hoppes, and R. P. Hudson, Phys. Rev. **105**, 1413 (1957).

[5] J. H. Christenson, J. W. Cronin, V. L. Fitch, and R. Turlay, Phys. Rev. Lett. **13**, 138 (1964).

[6] H. Wahl, Physics Reports **403**, 19 (2004).

[7] K. Abe, R. Abe, I. Adachi, B. S. Ahn, H. Aihara, M. Akatsu, G. Alimonti, K. Asai, M. Asai, Y. Asano, *et al.*, Phys. Rev. Lett. **87**, 091802 (2001).

[8] R. Aaij, C. A. Beteta, B. Adeva, M. Adinolfi, C. A. Aidala, Z. Ajaltouni, S. Akar, P. Albicocco, J. Albrecht, F. Alessio, *et al.*, Phys. Rev. Lett. **122**, 211803 (2019).

[9] J. Lees, V. Poireau, V. Tisserand, J. G. Tico, E. Grauges, A. Palano, G. Eigen, B. Stugu, D. N. Brown, L. Kerth, *et al.*, Phys. Rev. Lett. **109**, 211801 (2012).

[10] J. Pendlebury and E. Hinds, Nuclear Instruments and Methods in Physics Research Section A: Accelerators, Spectrometers, Detectors and Associated Equipment **440**, 471 (2000).

[11] I. M. Rabey, *Improved shot noise limit of the YbF EDM experiment*, Ph.D. thesis, Imperial College London (2017).

[12] M. Dine and A. Kusenko, Reviews of Modern Physics **76**, 1 (2003), publisher: American Physical Society.

[13] L. Canetti, M. Drewes, and M. Shaposhnikov, New Journal of Physics **14**, 095012 (2012).

[14] M. Kobayashi and T. Maskawa, Progress of Theoretical Physics **49**, 652 (1973).

[15] Y. Ema, T. Gao, and M. Pospelov, Phys. Rev. Lett. **129**, 231801 (2022).

[16] C. Giganti, S. Lavignac, and M. Zito, Progress in Particle and Nuclear Physics **98**, 1 (2018).

[17] M. S. Safronova, D. Budker, D. DeMille, D. F. J. Kimball, A. Derevianko, and C. W. Clark, Rev. Mod. Phys. **90**, 025008 (2018).

[18] T. Fukuyama, International Journal of Modern Physics A **27**, 1230015 (2012).

[19] M. Pospelov and A. Ritz, Phys. Rev. D **89**, 056006 (2014).

[20] D. Nelson, A. Schupp, R. Pidd, and H. Crane, Phys. Rev. Lett. **2**, 492 (1959).

[21] D. T. Wilkinson and H. Crane, Physical Review **130**, 852 (1963).

[22] L. I. Schiff, Phys. Rev. **132**, 2194 (1963).

[23] P. G. H. Sandars, Phys. Lett. **14**, 196 (1965).

[24] E. A. Hinds, Physica Scripta **T70**, 34 (1997).

[25] E. D. Commins, J. D. Jackson, and D. P. DeMille, American Journal of Physics **75**, 532 (2007).

[26] T. S. Roussy, L. Caldwell, T. Wright, W. B. Cairncross, Y. Shagam, K. B. Ng, N. Schlossberger, S. Y. Park, A. Wang, J. Ye, *et al.*, Science **381**, 46 (2023).

[27] L. Caldwell, T. S. Roussy, T. Wright, W. B. Cairncross, Y. Shagam, K. B. Ng, N. Schlossberger, S. Y. Park, A. Wang, J. Ye, *et al.*, Physical Review A **108**, 012804 (2023).

[28] K. B. Ng, Y. Zhou, L. Cheng, N. Schlossberger, S. Y. Park, T. S. Roussy, L. Caldwell, Y. Shagam, A. J. Vigil, E. A. Cornell, *et al.*, Physical Review A **105**, 022823 (2022).

[29] V. Andreev, D. G. Ang, D. DeMille, J. M. Doyle, G. Gabrielse, J. Haefner, N. R. Hutzler, Z. Lasner, C. Meisenhelder, B. R. O'Leary, C. D. Panda, A. D. West, E. P. West, and X. Wu, Nature **562**, 355 (2018).

[30] J. J. Hudson, D. M. Kara, I. J. Smallman, B. E. Sauer, M. R. Tarbutt, and E. A. Hinds, Nature **473**, 493 (2011).

[31] N. J. Fitch and M. R. Tarbutt, in *Adv. At. Mol. Opt. Phys.*, Vol. 70 (Elsevier, 2021) pp. 157–262.

[32] M. Abe, V. Prasannaa, and B. Das, Physical Review A **97**, 032515 (2018).

[33] P. A. Haase, D. J. Doeglas, A. Boeschoten, E. Eliav, M. Iliaš, P. Aggarwal, H. L. Bethlem, A. Borschevsky, K. Esajas, Y. Hao, *et al.*, The Journal of Chemical Physics **155** (2021).

[34] S. Sasmal, H. Pathak, M. K. Nayak, N. Vaval, and S. Pal, Physical Review A **93**, 062506 (2016).

[35] V. Prasannaa, N. Shitara, A. Sakurai, M. Abe, and B. Das, Physical Review A **99**, 062502 (2019).

[36] M. Denis, Y. Hao, E. Eliav, N. R. Hutzler, M. K. Nayak, R. G. E. Timmermans, and A. Borschesvky, J. Chem. Phys. **152**, 084303 (2020).

[37] M. Rockenhäuser, F. Kogel, T. Garg, S. Morales, and T. Langen, "Laser cooling of barium monofluoride molecules using synthesized optical spectra," (2024), arXiv:2405.09427.

[38] Z. Zeng, S. Deng, S. Yang, and B. Yan, arXiv preprint arXiv:2405.17883 (2024).

[39] P. Aggarwal, H. L. Bethlem, A. Borschevsky, M. Denis, K. Esajas, P. A. B. Haase, Y. Hao, S. Hoekstra, K. Jungmann, T. B. Meijknecht, M. C. Mooij, R. G. E. Timmermans, W. Ubachs, L. Willmann, and A. Zapara, Eur. Phys. J. D **72**, 197 (2018).

[40] N. J. Fitch, J. Lim, E. A. Hinds, B. E. Sauer, and M. R. Tarbutt, Quantum Sci. Technol. **6**, 014006 (2021).

[41] J. Brown and A. Carrington, *Rotational spectroscopy of diatomic molecules* (Cambridge University Press, 2003).

[42] V. Aquilanti, S. Cavalli, and G. Grossi, Zeitschrift für Physik D Atoms, Molecules and Clusters **36**, 215 (1996).

[43] J. Brown and A. Merer, Journal of Molecular Spectroscopy **74**, 488 (1979).

[44] F. Hund, Zeitschrift für Physik **43**, 805 (1927).

[45] J. Van Vleck, Physical Review **33**, 467 (1929).

[46] B. E. Sauer, S. B. Cahn, M. G. Kozlov, G. D. Redgrave, and E. A. Hinds, J. Chem. Phys. **110**, 8424 (1999).

[47] B. E. Sauer, J. Wang, and E. A. Hinds, Phys. Rev. Lett. **74**, 1554 (1995).

[48] B. E. Sauer, J. Wang, and E. A. Hinds, J. Chem. Phys. **105**, 7412 (1996).

[49] A. G. Gaydon, *Dissociation energies and spectra of diatomic molecules* (Chapman and Hall, 1968).

[50] K. L. Dunfield, C. Linton, T. E. Clarke, J. McBride, A. G. Adam, and J. R. D. Peers, J. Mol. Spectrosc. **174**, 433 (1995).

[51] D. J. Berkeland and M. G. Boshier, Phys. Rev. A **65**, 033413 (2002).

[52] J. J. Hudson, *Measuring the electric dipole moment of the electron with YbF molecules*, Ph.D. thesis, University of Sussex (2001).

[53] M. R. Tarbutt, J. J. Hudson, B. E. Sauer, E. A. Hinds, V. A. Ryzhov, V. L. Ryabov, and V. F. Ezhov, J. Phys. B **35**, 5013 (2002).

[54] S. M. Skoff, R. J. Hendricks, C. D. J. Sinclair, M. R. Tarbutt, J. J. Hudson, D. M. Segal, B. E. Sauer, and E. A. Hinds, New Journal of Physics **11**, 123026 (2009).

[55] S. M. Skoff, R. J. Hendricks, C. D. J. Sinclair, J. J. Hudson, D. M. Segal, B. E. Sauer, E. A. Hinds, and M. R. Tarbutt, Phys. Rev. A **83**, 023418 (2011).

[56] M. R. Tarbutt, B. E. Sauer, J. J. Hudson, and E. A. Hinds, New J. Phys. **15**, 053034 (2013).

[57] N. R. Hutzler, M. F. Parsons, Y. V. Gurevich, P. W. Hess, E. Petrik, B. Spaun, A. C. Vutha, D. DeMille, G. Gabrielse, and J. M. Doyle, Physical Chemistry Chemical Physics **13**, 18976 (2011).

[58] T. E. Wall, J. F. Kanem, J. J. Hudson, B. E. Sauer, D. Cho, M. G. Boshier, E. A. Hinds, and M. R. Tarbutt, Phys. Rev. A **78**, 062509 (2008).

[59] T. E. Wall, Journal of Physics B: Atomic, Molecular and Optical Physics **49**, 243001 (2016).

[60] S. Truppe, M. Hambach, S. M. Skoff, N. E. Bulleid, J. S. Bumby, R. J. Hendricks, E. A. Hinds, B. E. Sauer, and M. R. Tarbutt, J. Mod. Opt. **65**, 246 (2017).

[61] X. Liu, W. Wang, S. C. Wright, M. Doppelbauer, G. Meijer, S. Truppe, and J. Perez-Rioz, J. Chem. Phys. **157**, 074305 (2022).

[62] S. C. Wright, M. Doppelbauer, S. Hofsäss, H. C. Schewe, B. Sartakov, G. Meijer, and S. Truppe, Molecular Physics **121**, e2146541 (2023).

[63] S. Truppe, S. Marx, S. Kray, M. Doppelbauer, S. Hofsäss, H. C. Schewe, N. Walter, J. Pérez-Ríos, B. G. Sartakov, and G. Meijer, Phys. Rev. A **100**, 052513 (2019).

[64] S. Y. T. van de Meerakker, H. L. Bethlem, N. Vanhaecke, and G. Meijer, Chem. Rev. **112**, 4828 (2012).

[65] S. Truppe, H. J. Williams, M. Hambach, L. Caldwell, N. J. Fitch, E. A. Hinds, B. E. Sauer, and M. R. Tarbutt, Nat. Phys. **13**, 1173 (2017).

[66] R. Albrecht, M. Scharwaechter, T. Sixt, L. Hofer, and T. Langen, Phys. Rev. A **101**, 013413 (2020).

[67] W. Bu, T. Chen, G. Lv, and B. Yan, Phys. Rev. A **95**, 032701 (2017).

[68] J. F. Barry, E. S. Shuman, E. B. Norrgard, and D. DeMille, Phys. Rev. Lett. **108**, 103002 (2012).

[69] J. F. Barry, D. J. McCarron, E. B. Norrgard, M. H. Steinecker, and D. DeMille, Nature **512**, 286 (2014).

[70] M. T. Hummon, M. Yeo, B. K. Stuhl, A. L. Collopy, Y. Xia, and J. Ye, Phys. Rev. Lett. **110**, 143001 (2013).

[71] N. R. Hutzler, Quantum Sci. Technol. **5**, 044011 (2020).

[72] I. Kozyryev, L. Baum, K. Matsuda, P. Olson, B. Hemmerling, and J. M. Doyle, New Journal of Physics **17**, 045003 (2015).

[73] I. Kozyryev, L. Baum, K. Matsuda, B. L. Augenbraun, L. Anderegg, A. P. Sedlack, and J. M. Doyle, Phys. Rev. Lett. **118**, 173201 (2017).

[74] L. Baum, N. B. Vilas, C. Hallas, B. L. Augenbraun, S. Raval, D. Mitra, and J. M. Doyle, Phys. Rev. Lett **124**, 133201 (2020).

[75] B. L. Augenbraun, Z. D. Lasner, A. Frenett, H. Sawaoka, C. Miller, T. C. Steimle, and J. M. Doyle, New J. Phys. **22**, 022003 (2020).

[76] N. R. Hutzler, H. I. Lu, and J. M. Doyle, Chem. Rev. **112**, 4803 (2012).

[77] H.-I. Lu, J. Rasmussen, M. J. Wright, D. Patterson, and J. M. Doyle, Phys. Chem. Chem. Phys. **13**, 18986 (2011).

[78] N. E. Bulleid, S. M. Skoff, R. J. Hendricks, B. E. Sauer, E. A. Hinds, and M. R. Tarbutt, Phys. Chem. Chem. Phys. **15**, 12299 (2013).

[79] D. Patterson and J. M. Doyle, The Journal of Chemical Physics **126**, 154307 (2007).

[80] C. J. Foot, *Atomic physics*, Vol. 7 (Oxford university press, 2005).

[81] S. M. Skoff, *Buffer gas cooling of YbF molecules*, Ph.D. thesis, Imperial College London (2011).

[82] H. Lu, *Magnetic trapping of molecules via optical loading and magnetic slowing*, Ph.D. thesis, Harvard University (2013).

[83] M. R. Tarbutt and T. C. Steimle, Phys. Rev. A **92**, 053401 (2015).

[84] B. Hemmerling, E. Chae, A. Ravi, L. Anderegg, G. K. Drayna, N. R. Hutzler, A. L. Collopy, J. Ye, W. Ketterle, and J. M. Doyle, J. Phys. B **49**, 174001 (2016).

[85] S. Xu, P. Kaebert, M. Stepanova, T. Poll, M. Siercke, and S. Ospelkaus, New Journal of Physics **23**, 063062 (2021).

[86] L. W. Cheuk, L. Anderegg, B. L. Augenbraun, Y. Bao, S. Burchesky, W. Ketterle, and J. M. Doyle, Phys. Rev. Lett. **121**, 083201 (2018).

[87] S. Ding, Y. Wu, I. A. Finneran, J. J. Burau, and J. Ye, Phys. Rev. X **10**, 021049 (2020).

[88] C. Monroe, W. Swann, H. Robinson, and C. Wieman, Phys. Rev. Lett. **65**, 1571 (1990).

[89] N. Radwell, G. Walker, and S. Franke-Arnold, Phys. Rev. A **88**, 043409 (2013).

[90] A. L. Collopy, S. Ding, Y. Wu, I. A. Finneran, L. Anderegg, B. L. Augenbraun, J. M. Doyle, and J. Ye, Phys. Rev. Lett. **121**, 213201 (2018).

[91] L. Anderegg, B. L. Augenbraun, E. Chae, B. Hemmerling, N. R. Hutzler, A. Ravi, A. Collopy, J. Ye, W. Ketterle, and J. M. Doyle, Phys. Rev. Lett. **119**, 103201 (2017).

[92] F. Kogel, M. Rockenh auser, R. Albrecht, and T. Langen, New J. Phys. **23**, 095003 (2021).

[93] M. Petzold, P. Kaebert, P. Gersema, M. Siercke, and S. Ospelkaus, New J. Phys. **20**, 042001 (2013).

[94] P. Kaebert, M. Stepanova, T. Poll, M. Petzold, S. Xu, M. Siercke, and S. Ospelkaus, New Journal of Physics **23**, 093013 (2021).

[95] H. J. Williams, S. Truppe, M. Hambach, L. Caldwell, N. J. Fitch, E. A. Hinds, B. E. Sauer, and M. R. Tarbutt, New J. Phys. **19**, 113035 (2017).

[96] S. Truppe, H. J. Williams, N. J. Fitch, M. Hambach, T. E. Wall, E. A. Hinds, B. E. Sauer, and M. R. Tarbutt, New J. Phys. **19**, 022001 (2017).

[97] T. P. Softley, Proceedings of the Royal Society A **479**, 20220806 (2023).

[98] N. B. Vilas, C. Hallas, L. Anderegg, P. Robichaud, A. Winnicki, D. Mitra, and J. M. Doyle, Nature **606**, 70 (2022).

[99] N. J. Fitch and M. R. Tarbutt, Chem. Phys. Chem. **17**, 3609 (2016).

[100] B. L. Augenbraun, A. Frenett, H. Sawaoka, C. Hallas, N. B. Vilas, A. Nasir, Z. D. Lasner, and J. M. Doyle, Phys. Rev. Lett. **127**, 263002 (2021).

[101] H. Sawaoka, A. Frenett, A. Nasir, T. Ono, B. L. Augenbraun, T. C. Steimle, and J. M. Doyle, Phys. Rev. A **107**, 022810 (2023).

[102] X. Zhuang, A. Le, T. C. Steimle, N. E. Bulleid, I. J. Smallman, R. J. Hendricks, S. M. Skoff, J. J. Hudson, B. E. Sauer, E. A. Hinds, and M. R. Tarbutt, Phys. Chem. Chem. Phys. **13**, 19013 (2011).

[103] I. J. Smallman, F. Wang, T. C. Steimle, M. R. Tarbutt, and E. A. Hinds, J. Mol. Spectrosc. **300**, 3 (2014).

[104] J. Lim, J. R. Almond, M. R. Tarbutt, D. T. Nguyen, and T. C. Steimle, J. Mol. Spectrosc. **338**, 81 (2017).

[105] J. Lim, J. R. Almond, M. A. Trigatzis, J. A. Devlin, N. J. Fitch, B. E. Sauer, M. R. Tarbutt, and E. A. Hinds, Phys. Rev. Lett. **120**, 123201 (2018).

[106] X. Alauze, J. Lim, M. A. Trigatzis, S. Swarbrick, F. J. Collings, N. J. Fitch, B. E. Sauer, and M. R. Tarbutt, Quantum Sci. Technol. **6**, 044005 (2021).

[107] J. F. Barry, *Magneto-optical trapping of a diatomic molecule*, Ph.D. thesis, Yale University (2014).

[108] E. B. Norrgard, D. J. McCarron, M. H. Steinecker, M. R. Tarbutt, and D. DeMille, Phys. Rev. Lett. **116**, 063004 (2016).

[109] J. R. Almond, *Laser cooling of YbF molecules for an improved measurement of the electron electric dipole moment*, Ph.D. thesis, Imperial College London (2017).

[110] J. A. Devlin, *Progress towards a more sensitive measurement of the electron electric dipole moment with YbF.*, Ph.D. thesis, Imperial College London (2020).

[111] E. S. Shuman, J. F. Barry, D. R. Glenn, and D. DeMille, Phys. Rev. Lett. **103**, 223001 (2009).

[112] C. Zhang, C. Zhang, L. Cheng, T. C. Steimle, and M. R. Tarbutt, J. Mol. Spectrosc. **386**, 111625 (2022).

[113] S. Hofsäss, M. Doppelbauer, S. C. Wright, S. Kray, B. G. Sartakov, J. Pérez-Ríos, G. Meijer, and S. Truppe, New Journal of Physics **23**, 075001 (2021).

[114] S. Popa, S. Schaller, A. Fielicke, J. Lim, B. G. Sartakov, M. R. Tarbutt, and G. Meijer, Phys. Rev. X **14**, 021035 (2024).

[115] N. Huntemann, M. Okhapkin, B. Lipphardt, S. Weyers, C. Tamm, and E. Peik, Phys. Rev. Lett. **108**, 090801 (2012).

[116] J. Hur, D. P. L. Aude Craik, I. Counts, E. Knyazev, L. Caldwell, C. Leung, S. Pandey, J. C. Berengut, A. Geddes, W. Nazarewicz, P.-G. Reinhard, A. Kawasaki, H. Jeon, W. Jhe, and V. Vuletić, Phys. Rev. Lett. **128**, 163201 (2022).

[117] H. A. Fürst, C.-H. Yeh, D. Kalincev, A. P. Kulosa, L. S. Dreissen, R. Lange, E. Benkler, N. Huntemann, E. Peik, and T. E. Mehlstäubler, Phys. Rev. Lett. **125**, 163001 (2020).

[118] R. Lange, N. Huntemann, J. M. Rahm, C. Sanner, H. Shao, B. Lipphardt, C. Tamm, S. Weyers, and E. Peik, Phys. Rev. Lett. **126**, 011102 (2021).

[119] A. Patscheider, B. Yang, G. Natale, D. Petter, L. Chomaz, M. J. Mark, G. Hovhannesyan, M. Lepers, and F. Ferlaino, Phys. Rev. Res. **3**, 033256 (2021).

[120] N. Petersen, M. Trümper, and P. Windpassinger, Phys. Rev. A **101**, 042502 (2020).

[121] A. Golovizin, E. Fedorova, D. Tregubov, D. Sukachev, K. Khabarova, V. Sorokin, and N. Kolachevsky, Nat. Commun. **10**, 1724 (2019).

[122] J. V. Pototschnig, K. G. Dyall, L. Visscher, and A. S. P. Gomes, Phys. Chem. Chem. Phys. **23**, 22330 (2021).

[123] T. D. Persinger, J. Han, A. T. Le, T. C. Steimle, and M. C. Heaven, Phys. Rev. A **106**, 062804 (2022).

[124] A. Fielicke, G. von Helden, and G. Meijer, Eur. Phys. J. D **34**, 83 (2005).

[125] L. Veseth, J. Phys. B **6**, 1473 (1973).

[126] M. Duncan, T. Dietz, M. Liverman, and R. Smalley, The Journal of Physical Chemistry **85**, 7 (1981).

[127] J. T. Hougen, J. Mol. Spectrosc. **267**, 23 (2011).

[128] E. Biémont, J.-F. Dutrieux, I. Martin, and P. Quinet, J. Phys. B **31**, 3321 (1998).

[129] S. S. Kondov, C.-H. Lee, K. H. Leung, C. Liedl, I. Majewska, R. Moszynski, and T. Zelevinsky, Nat. Phys. **15**, 1118 (2019).

[130] G. Barontini, L. Blackburn, V. Boyer, F. Butuc-Mayer, X. Calmet, C. L.-U. J. R., E. A. Curtis, B. Darquié, J. Dunningham, N. J. Fitch, E. M. Forgan, K. Georgiou, P. Gill, R. M. Godun, J. Goldwin, V. Guarrera, A. C. Harwood, I. R. Hill, R. J. Hendricks, M. Jeong, M. Y. H. Johnson, M. Keller, L. P. Kozhiparambil Sajith, F. Kuipers, H. S. Margolis, C. Mayo, P. Newman, A. O. Parsons, L. Prokhorov, B. I. Robertson, J. Rodewald, M. S. Safronova, B. E. Sauer, M. Schioppo, N. Sherrill, Y. V. Stadnik, K. Szymaniec, M. R. Tarbutt, R. C. Thompson, A. Tofful, J. Tunesi, A. Vecchio, Y. Wang, and S. Worm, EPJ Quantum Technol. **9**, 12 (2022).

[131] C. J. Ho, J. A. Devlin, I. M. Rabey, P. Yzombard, J. Lim, S. C. Wright, N. J. Fitch, E. A. Hinds, M. R. Tarbutt, and B. E. Sauer, New J. Phys. **22**, 043031 (2020).

[132] E. Raab, M. Prentiss, A. Cable, S. Chu, and D. Pritchard, Phys. Rev. Lett. **59**, 2631 (1987).

[133] S. Xu, M. Xia, R. Gu, Y. Yin, L. Xu, Y. Xia, and J. Yin, Physical Review A **99**, 033408 (2019).

[134] M. R. Tarbutt, New J. Phys. **17**, 015007 (2015).

[135] D. J. McCarron, E. B. Norrgard, M. H. Steinecker, and D. DeMille, New J. Phys. **17**, 035014 (2015).

[136] M. Hambach, *Development of a magneto-optical trap for CaF molecules*, Ph.D. thesis, Imperial College London (2017).

[137] S. Jurgilas, *Collisions between laser-cooled atoms and molecules*, Ph.D. thesis, Imperial College London (2021).

[138] L. Caldwell, *Deep laser cooling and coherent control of molecules*, Ph.D. thesis, Imperial College London (2020).

[139] S. Eckel, D. S. Barker, E. B. Norrgard, and J. Scherschligt, Computer physics communications **270**, 108166 (2022).

[140] K. J. Rodriguez, N. H. Pilgram, D. S. Barker, S. P. Eckel, and E. B. Norrgard, Physical Review A **108**, 033105 (2023).

[141] Y. Bao, S. S. Yu, L. Anderegg, S. Burchesky, D. Gonzalez-Acevedo, E. Chae, W. Ketterle, K.-K. Ni, and J. M. Doyle, New Journal of Physics **24**, 093028 (2022).